# PROPAGATION OF EN-ROUTE AIRCRAFT NOISE

A Dissertation

Submitted to the Faculty

of

Purdue University

by

Yiming Wang

In Partial Fulfillment of the

Requirements for the Degree

of

Doctor of Philosophy

December 2019

Purdue University

West Lafayette, Indiana

# THE PURDUE UNIVERSITY GRADUATE SCHOOL
# STATEMENT OF DISSERTATION APPROVAL

Dr. Kai Ming Li, Chair

School of Mechanical Engineering

Dr. J. Stuart Bolton

School of Mechanical Engineering

Dr. Marcial Gonzalez

School of Mechanical Engineering

Dr. Robert Nowack

Department of Earth, Atmospheric, and Planetary Sciences

**Approved by:**

Dr. Nicole L. Key

Head of the School Graduate Program

# ACKNOWLEDGMENTS

I would like to express my sincere gratitude to my major Professor Kai Ming Li for his continuous support of my PhD study and research, for his patience, motivation, enthusiasm, and immense knowledge. Without his guidance I cannot finish the writing of this thesis.

Besides my advisor, I would like to thank the rest of my thesis committee: Professor Stuart Bolton, Professor Robert Nowack and Professor Marcial Gonzales for their encouragement, insightful comments, and hard questions. I would also like to thank Professor Patricia Davies for the encouragement throughout my days at Herrick Lab.

A very special gratitude goes to Federal Aviation Administration for helping and providing the funding for the work (Grant Award No. 13-C-AJFE-PU). I would also like to thank Dr. Bill He, Professor Victor Sparrow, Eric Boeker and Juliet Page for encouragement and their many valuable suggestions.

I also want to thank Professor Yangfan Liu for letting me know how interesting my research is. Without him, I would never attend those difficult math courses.

I want to thank my friends Yixuan Qiu for his advice on statistic analysis and Zhongxiao Ma for his advice on cooking.

I would like to thank my parents for their love and guidance. Last but not the least, I would like to thank my wife for letting me know how beautiful my life is.

# TABLE OF CONTENTS

# LIST OF TABLES

# LIST OF FIGURES

Figure Page

Figure Page

Figure Page

Figure Page

# ABSTRACT

Wang, Yiming PhD, Purdue University, December 2019. Propagation of En-route Aircraft Noise. Major Professor: Kai Ming Li, School of Mechanical Engineering.

The prediction of the noise generated by en-route aircraft is gradually gaining in importance as the number of aircraft increases over the last few decades. While the studies of outdoor sound propagation have been focused on near ground propagation, the case when the sound source is high above the ground has not attracted much attention. At the same time there has been a lack of high-quality aircraft acoustic validation data sets that contain detailed acoustic, meteorology, and source-receiver position data. The DISCOVER-AQ data set, which was collected by Volpe in support of the Federal Aviation Administration (FAA), has greatly helped with studying the directivity and the Doppler effect in the comparison between simulation results and measurements.

To provide a more accurate prediction of en-route aircraft noise, we derived the analytic asymptotic solution of the sound field above a non-locally reacting ground due to a moving point source and a line source using the methods of the steepest descent and a Lorentz transform. The model predicts a much more accurate result for sound field above “soft” grounds, such as a snow-covered ground and sand-covered ground. At the same time, we derived a fast numerical algorithm based on Levin’s collocation for the prediction of the sound field in the presence of a temperature gradient, which can be applied to a wide range of acoustic problems involving integration. The achievements recorded in this thesis can be used to predict the sound field generated by aircraft, trains, and vehicles with a subsonic moving speed. In addition, the model can be used for detection and design of moving sound source.

# 1. AIRCRAFT NOISE PROPAGATION MODELING AND TECHNIQUES

The propagation of aircraft sound has been an important topic for several decades. Since the invention of the first aircraft, the noise emitted by an aircraft is gradually gaining more attention as the number of aircraft increases. Excess exposure to aircraft noise could compromise the mental health and cognition of human beings according to many related studies. [1–3]

An accurate prediction of aircraft noise requires the modeling of aircraft noise source and a detailed understanding of the effects during the propagation of aircraft noise. Although both areas have indisputable importance, the focus of this thesis is on the propagation part. Several important factors during the propagation of aircraft noise are listed in Section 1.1 with a review of related studies, and the main techniques used in the thesis are later listed in Section 1.2 of this chapter.

## 1.1 Propagation effects and Literature review

The propagation of outdoor noise is influenced by several different effects, [4] such as divergence effect, air absorption, temperature gradient, Doppler's effect, ground effect, barrier effect and turbulence—these effects all contribute to the attenuation of aircraft noise. Some of them are well studied with theoretical models and experiment validations, such as air absorption and the divergence effect. Others still require more research input and validation efforts.

### 1.1.1 Divergence effect

First, the sound is attenuated by distance due to the well-known divergence effect for spherical wave. For mono-pole sound source, the effect can be calculated using

$1/R$, where $R$ is the distance between the sound source and the receiver. If we use decibels to describe the attenuation, the divergence effect can be calculated with

$$L_{div} = 20log_{10}(1/R) \tag{1.1}$$

The model of divergence effect in Equation 1.1 is used in the Aviation Environmental Design Tool (AEDT), which is an aircraft noise prediction tool developed by the Federal Aviation Administration (FAA). The reflected wave, however, has different distances for divergence effect for aircraft noise prediction problems; due to the high elevation of en-route aircraft noise, the difference between the direct wave distance and the reflected wave distance is negligible, meaning that both $R_1$ (distance for direct wave) and $R_2$ (distance for reflected wave) can usually be treated as the same. The divergence effect is due to the nature of a spherical wave in Euclidean space, and it depends solely on the distance between the source and the receiver; this is the only frequency independent factor in the listed propagation effects.

### 1.1.2 Air absorption

The second factor to be discussed is air absorption, which is highly important at long range but is sometimes ignored in near field predictions. Air absorption for a narrow frequency band can be calculated according to ISO 9613, which is a widely used standard in outdoor sound propagation; the model is based on the equations by Bass and Attenborough [5] [6]. The air absorption coefficient is decided by the temperature, the pressure, and the humidity of air. During daytime, the temperature normally decreases with height, while during night time, the temperature can be more complicated. The pressure generally decreases with height linearly, and the humidity depends highly on weather and locations. The atmospheric profile, including temperature, pressure, and humidity are normally modeled into stratified profiles and are used in the prediction of air absorption attenuation. For a single frequency sound, the attenuation due to air absorption can be expressed as

$$L_{air} = \alpha(f, temp, pr, rh) \cdot R \tag{1.2}$$

where $f$ is the frequency of the noise source; $temp$ is the temperature; $pr$ is the pressure of air, which is different from the acoustic pressure $p$ used through the thesis; and $rh$ is the relative humidity.

### 1.1.3 Ground effect

The sound's propagation is influenced by the reflection of ground. The effect has been studied extensively for near ground propagation in the past few decades [4]. Most recently, the fast calculation and asymptotic solutions for the sound field above a locally and a non-locally reacting ground surface due to a point source have been studied in detail by Li, Liu, and Tao [7–9]. Many subcategories including moving source problems and mixed impedance problems are also studied with theoretical modeling and experiments [10–14]. The expression for the sound field of the most basic case with a homogeneous medium and a locally reacting ground due to a stationary source can be written as

$$p = \frac{e^{ikR_1}}{4\pi R_1} + [R_p + (1 - R_p)F(w)]\frac{e^{ikR_2}}{4\pi R_2}, \tag{1.3}$$

where $k$ is the wave number of the sound, $R_1$ and $R_2$ are the propagation distances for direct and reflected waves, and i is imaginary number. $F(w)$ is named as the boundary loss factor, the equation of which is as follows:

$$F(w) = 1 + i\sqrt{\pi}we^{-w^2}erfc(-iw), \tag{1.4}$$

The $erfc(z)$ function is known as the complimentary error function that is commonly used and implemented in many software programs such as MATLAB [15]. Here, $w$ is known as the numerical distance of the reflected wave, which can be expressed as

$$\frac{1}{2}(1 + i)\beta\sqrt{kr} \tag{1.5}$$

where $R_p$ is known as plane wave reflection coefficient

$$R_p = \frac{cos\theta - \beta}{cos\theta + \beta}, \tag{1.6}$$

where $\beta$ stands for the admittance of the ground and $\theta$ stands for the incident angle. The plane wave reflection coefficient is widely used in many acoustic problems. If the sound field is produced by plane wave sources or if the incident angle of the reflected wave is close to 0, the total sound field could be calculated with a much simpler equation instead of Equation 1.3 as follows:

$$p = \frac{e^{ikR_1}}{4\pi R_1} + R_p \frac{e^{ikR_2}}{4\pi R_2}. \tag{1.7}$$

The complicated expressions from Equation 1.3 to Equation 1.5 is mainly due to the ground wave term, which dominates the propagation at a large incident angle (above 85 degree). Equation 1.3 is the most basic equation for a sound field due to a mono-pole source. For aircraft noise prediction, the influence of the Doppler's effect has to be considered; several terms such as $\beta$ and $w$ have to be "Dopplerized" in order for us to take into account the effect of source motion. The detailed theoretical modeling process is presented in Chapters 2 and 3 for both a line source and a mono-pole sound source.

### 1.1.4 Refraction

Concerning the refraction effect, there has been studies for many years, especially since sound propagation outdoors is heavily influenced by meteorological conditions. The progress in the area has been summarized in a paper that contains benchmark cases with several common sound speed profiles [6].

In the presence of a sound speed gradient caused by a temperature gradient and a wind gradient, the path of the propagation will no longer be a straight line that connects the source and the receiver. Under upwind conditions, the sound ray bends upward, while under downwind conditions, the sound ray bends downward [16]. Several methods can be used in the prediction of the sound field above the ground with a sound speed gradient. The first type of method uses a ray tracing technique based on the geometric acoustic theory and the second type of method is based on inhomogeneous wave equations. Also, there is beam method to split the propagation area into smaller subsections where the property of the medium is a constant in each subsection. Ray tracing method is very efficient in the calculation of the sound field with any types of sound speed profiles, however, it is a high frequency approximation with relatively low accuracy at far range and cannot be used to calculate the sound field in the shadow zone since there are no possible ray paths connecting the sound source with any points in the shadow zone. The method based on wave theory is generally more accurate but requires much more calculation power. The calculation speed of the sound field in an upward refraction medium can be improved with a method based on residue theory. [17, 18] For downward refraction a similar approach can be used. [18, 19] However, the root searching process required in the calculation is troublesome and sometimes unstable; moreover, these methods cannot be used to predict near field propagation. In Chapter 7, a new technique based on Levin's collocation is introduced that can be used to obtain fast solutions for both upward and downward refraction problems.

## 1.2 Techniques used in the study

### 1.2.1 Steepest descent method

The application of the steepest descent method in the problem of point-to-point propagation was adapted from the studies of electromagnetic waves by Sommerfeld [20]. The topic was later studied in the outdoor acoustic field by Rudnick [21], Ingard [22], Chien and Soroka [23], and Li [24].

The steepest descent method can be used to solve the integral of the following type:

$$I = \int_{-\infty}^{+\infty} f(x) e^{ig(x)} dx. \tag{1.8}$$

If $f$ and $g$ functions are analytic in the region of interest, and $f$ changes much slower than the exponential term, the method of steepest descent could be applied to evaluate the whole integral along the integration path with only one point. The idea is to deform the path of integration from $-\infty$ $+\infty$ to the steepest descent path. According to Cauthy's theorem, if the start point and the end point are the same in the complex plane, the integral will provide the same value regardless which exact path is chosen during the integration. On the steepest descent path, the integrand is smooth and decreases with the fastest speed from the stationary point. The reason is that if we set the imaginary part of function $g$ to zero, the real part will have the maximum rate of decaying due to the feature of the exponential function in the complex plane.

The commonly used transformation is defined as

$$\frac{1}{2}W^2 = i\left[g(x_0) - g(x)\right] \tag{1.9}$$

where $x_0$ is the stationary point. At this point, the derivative of the phase function is equal to zero. With the help of Equation 1.9, Equation 1.8 can be transformed to

$$I = \int_{-\infty}^{+\infty} f e^{ig(x_0)} e^{-\frac{1}{2}W^2} \frac{dx}{dW} dW \tag{1.10}$$

where

$$\frac{dx}{dW} = \sqrt{\frac{i}{d^2g/dx^2}}. \tag{1.11}$$

The one-point asymptotic solution can be expressed in this way:

$$I = f(x_0)\frac{dx}{dW}(x_0)e^{ig(x_0)} \int_{-\infty}^{+\infty} e^{-\frac{1}{2}W^2} dW = f(x_0)\frac{dx}{dW}(x_0)e^{ig(x_0)}\sqrt{2\pi}. \tag{1.12}$$

Equation 1.12 is widely used in many asymptotic solutions in acoustics and physics. If the accuracy of Equation 1.12 cannot reach the requirement, an integration along the steepest descent path using the Gaussian quadrature could be formed with Equation 1.10. The integrand of Equation 1.10 is much smoother than that of Equation 1.8, which makes the integration much easier.

Depending on the form of the function $f$, both singularities and branch cuts could exist at times. The point singularity could be removed with the method of pole subtraction, which is used in the derivation of Equation 1.3. The branch cut contribution can also be calculated with a branch cut integral using the stationary phase method, which is slightly different from the stationary point method [25]. However, the evaluation of the branch cut integral is sometime unstable and inefficient, and it may not always give a good approximation for Equation 1.8.

The integral in Equation 1.8 can be approximated most of the time with only one point. For example, the direct wave $e^{ikR_1}/4\pi R_1$ for a homogeneous atmosphere can be derived with the stationary point method conveniently, and the reflected wave term can be approximated with a similar method with the help of the pole subtraction method. One of the reasons that the stationary point method is widely used in the derivation of acoustic waves is that the solution derived with the stationary point method can usually be expressed in a very neat form using parameters such as $k$ and $R_1$, which can be explained conveniently with ray acoustics. In Chapters 2, 3, and 6, the stationary phase method is used to derive the asymptotic solutions for several different acoustics problems.

### 1.2.2 Ray tracing method

The ray tracing method is a technique based on geometrical acoustics, where it approximates sound waves with sound rays. The method is widely used in the prediction of the sound field with influences of meteorological conditions such as the temperature gradient and wind speed gradient. The idea of the method is to find all the ray paths that connect the sound source and the receiver; if all paths are found, the total sound pressure is simply the sum of each $e^{ikR_n}/4\pi R_n$ term, where $R_n$ is the path length of the nth path. If reflection happened during the propagation of one of the rays, a reflection coefficient should be multiplied to that ray term. For a linear sound speed profile, an example of the ray theory solution can be found in [26].

Although the ray tracing method is not accurate under some circumstances, it does have a simple and convenient form. On the contrary, the solution based on wave theory is accurate but usually inefficient. Ray theory is mainly used in the thesis for comparisons with the other solutions derived in the research.

### 1.2.3 Levin's collocation method

Levin's collocation [27] [28] is a modification of Filon's method for the evaluation of an oscillating integral with a trigonometric oscillator [29]. Levin's method can be used efficiently to evaluate integrals of the type

$$\int f(x)e^{i\omega x}dx, \tag{1.13}$$

where $f$ is a smooth function along the path of integration. The evaluation of Equation 1.13 is very difficult using traditional methods such as the trapezoid rule or the Gaussian quadrature if the term $\omega$ is large. With Levin's collocation, only 10 to 15 points are required to obtain the same accuracy as the trapezoid rule with 10,000 points. The computational time of Levin's collocation does not rely on $\omega$, which is a huge advantage over the trapezoid rule or the fast field program (FFP) method . [30] In the evaluation of the sound field integrals with a linear sound speed gradient, the oscillation of Airy's function is extremely high, which makes an evaluation using any traditional method nearly impossible at a high frequency. The application of Levin's method in the evaluation of these integrals will save massive time compared to other integration algorithms . [31]

## 1.3 Overview of the thesis

The thesis has several subtopics under the scope of aircraft noise propagation. Chapter 2 and 3 give the theoretical models for a sound field above a locally and a non-locally reacting ground due to a line source and a point source. Chapter 4 gives the analysis of uncertainties and the influences of the Doppler's effect during the propagation of aircraft noise. Chapter 5 introduces a new technique for the integration of a reflected wave term. In Chapter 6, the asymptotic solution for the sound field in a medium with a temperature gradient is derived. Chapter 7 provides a fast integration algorithm for the prediction of a sound field with upward and downward refracting features. Chapter 8 serves as the conclusion for all the work in the thesis.

# 2. SOUND FIELD ABOVE GROUND DUE TO A MOVING LINE SOURCE

## 2.1 Introduction

The study of noise emanating from a moving source has become more imperative in the last several decades owing to the increasing speed of modern air-based and land-based transportation vehicles. Owing to the growth of computing power, time-domain numerical approaches such as the finite-difference time-domain (FDTD) method [32, 33] have gained popularity for applications in outdoor sound propagation. These approaches are particularly well-suited for use with moving sources, as they naturally account for the Doppler effect and can handle any source trajectory. Recent studies [32, 34] showed interest in such approaches. It is, therefore, expedient to develop an accurate and fast computational model in order to validate the ground effect predicted by the time-domain approaches [32]. In a recent study [35], an asymptotic formula was derived for predicting the sound fields from a source moving above a locally reacting ground. However, many outdoor ground surfaces are non-locally reacting in nature. For example, snow covered grounds [36, 37], forest floors [38], and railway ballast [39] are best modeled as non-locally reacting surfaces. Therefore, there is a need for generalizing the asymptotic formula to predict the sound fields from a source moving above a non-locally reacting ground.

Earlier research into moving source problems date back as early as the 1980s. Oie and Takeuchi [40] derived a much-simplified expression in which the ground wave term was ignored. This approximate solution can be inaccurate under near-grazing conditions. The current study aims to extend the prior studies [4, 10, 11, 35, 41] to offer a generalized expression that is simple yet accurate enough for the prediction of the sound fields above locally and non-locally reacting grounds.

It is notable that the general solution for the sound fields owing to a moving monopole in a free space is well recognized. [42] The Doppler effect is identified in the direct wave term. However, it is not properly included in the reflected wave term in which the ground's acoustical properties are calculated at a constant Depolarized frequency [4, 41]. An improved treatment of the Doppler effect on the spherical wave reflection coefficient was developed for a locally reacting ground [35, 40]. Here, the development of a generalized asymptotic formula for predicting sound fields from a source traversing horizontally at a constant speed above a non-locally reacting ground is presented.

An asymptotic analysis that centers on the use of contour integration where the steepest descent path is identified is proposed for obtaining an approximation solution in the present study. Indeed, Chien and Soroka [23] derived an asymptotic formula for the sound field owing to a stationary sound source above a locally reacting ground. Their approximate solution was expressed in terms of the direct wave term and the ground-reflected wave term. Subsequent studies (e.g., [7,43–48]) extended the steepest descent method for different ground types and various source characteristics.

This chapter has four sections. Section 2.2 shows a formulation of the problem. Using the standard transform for the physical space [23], the two-dimensional space-time wave equation can be adapted to yield a simpler analytical solution in the Lorentz space. By means of a convolution integral, the boundary condition can be simplified for the calculation of the ground-reflected wave. The steepest descent method is used and leads to an asymptotic solution for the boundary wave term in the Lorentz frame. It is further shown that the solution can be transformed back to the physical space, giving a closed-form solution. Section 2.3 discusses the ground model used in the validation process and explains how the surface wave pole can be determined. Section 2.4 validates the asymptotic formula by comparing the numerical results with those computed by the FDTD method. An approximation scheme for the asymptotic formula is discussed, and the condition for its validity is examined. Finally, concluding remarks are offered in Section 2.5.

## 2.2 Formulation of problem

### 2.2.1 Governing wave equation

In a two-dimensional rectangular coordinate system (x, z), a harmonic line source traverses horizontally in the x-direction. The airborne source has a subsonic constant speed of traveling at a constant height of $c_0M$ above an extended reaction ground that is situated at the z = 0 line. Here, M is the source Mach number, and $c_0$ is the sound speed in the upper medium ($z > 0$), with the subscript 0 representing their corresponding parameters in air. Since the sound fields are different for an approaching or receding source, a careful specification of the region for the receiver is needed to facilitate the modeling process, as follows. See Figure 2.1 for the geometry of the problem with the approaching source located in the $x > 0$ region. The upper and lower media are homogeneous with the sound speeds and densities of $c_j$ and $\rho_j$ ($j = 0, 1$), respectively, where the subscript 1 denotes the corresponding parameters in the lower medium ($z < 0$). Since air is modeled as a non-dissipative medium independent of frequency, $c_0$ and $\rho_0$ are real parameters. It is also important to note that the extended reaction ground is modeled as a dissipative medium. Hence, $c_1$ and $\rho_1$ are complex parameters that vary with frequency. The time-domain equations governing sound propagation within the ground would therefore involve convolutions. For the sake of simplicity, a frequency-domain approach is used in which the process of convolutions in the space-time domain is avoided initially.

For a sound source of unit strength, the wave equation above the ground is given in terms of the acoustic potential in the physical space-time domain by

$$\nabla^2\phi_0 - \frac{1}{c_0^2}\frac{\partial^2\phi_0}{\partial t^2} = \mathrm{e}^{-\mathrm{i}\omega_s t}\delta(x - c_0Mt)\delta(z - z_s) \tag{2.1}$$

where t is the time variable, $\omega_s$ is the angular frequency of the source in the stationary frame, the differential operator $\nabla^2 = \frac{\partial^2}{\partial x^2} + \frac{\partial^2}{\partial z^2}$, and is the Dirac delta function. Since

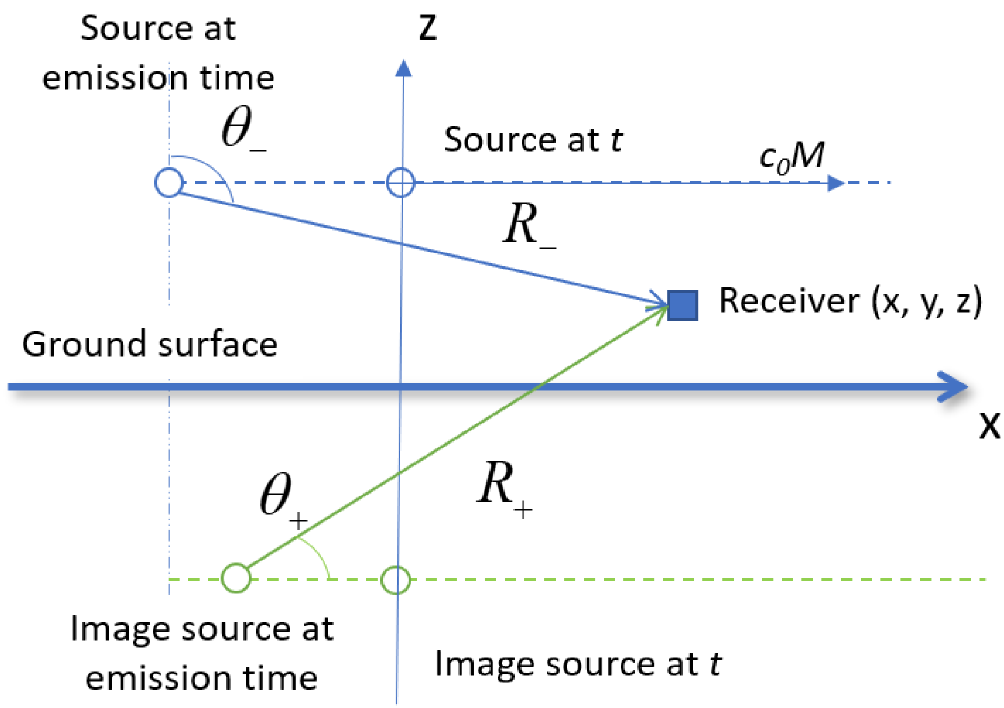


Figure 2.1. Geometry of problem

no source is placed below the ground, the corresponding wave equation in the lower medium is simply written as

$$\nabla^2\phi_1 - \frac{1}{c_1^2}\frac{\partial^2\phi_1}{\partial t^2} = 0 \tag{2.2}$$

where $c_1 \equiv c_1(\omega)$ varies with frequency of the sound waves transmitted through the lower medium. Given the acoustic potentials $\phi_j\,(x, z, t)$ (where j $=$ 0, 1), the corresponding sound pressures and vertical particle velocities in the upper and lower media are determined by

$$p_j(x, z, t) = -\rho_j\,(\omega)\,\partial_t\phi_j\,(x, z, t) \tag{2.3}$$

and

$$v_j(x, z, t) = \partial_z\phi_j\,(x, z, t)\,, \tag{2.4}$$

where $\partial_t = \partial/\partial t$ and $\partial_z = \partial/\partial z$. The boundary conditions for the problem are specified by requiring the continuity of pressure and normal particle velocity across the interface at z = 0, i.e.,

$$\rho_0 \partial_t \phi_0 (x, 0, t) = \rho_1 \partial_t \phi_1 (x, 0, t) \tag{2.5}$$

and

$$\partial_z \phi_0 (x, 0, t) = \partial_z \phi_1 (x, 0, t) \tag{2.6}$$

To solve for the sound fields in the upper medium, the Lorentz transformation can be used where the right side of Eq. 2.1 can be converted to a stationary line source problem by introducing a set of Lorentz variables $(x_L, z_L, t_L)$ such that

$$\begin{cases} x_L = \gamma^2 (x - c_0 M t), \\ z_L = \gamma z, \\ t_L = \gamma^2 (t - M x / c_0) \end{cases} , \tag{2.7}$$

where

$$\gamma = \left(1 - M^2\right)^{-\frac{1}{2}}, \tag{2.8}$$

and the subscript L symbolizes the corresponding variables in the Lorentz frame for the upper medium. Applying the Lorentz transformation, Eq. 2.1 can be converted to

$$\nabla^2{}_L \phi_L - \frac{1}{c_0^2} \frac{\partial^2 \phi_L}{\partial {t_L}^2} = \gamma e^{-\mathrm{i}\omega_s (t_L + M x_L / c_0)} \delta(x_L) \delta(z_L - z_{Ls}) \tag{2.9}$$

where $\phi_L \equiv \phi_0 (x_L, z_L, t_L)$ is the acoustic potential in the Lorentz frame.

The above step is analogous to the classic method for solving a moving source problem in the absence of boundary surfaces [14]. However, the imposition of the boundary conditions poses a challenge for determining the sound field owing to the extended reaction ground. This is because the wave equation in the upper medium is now transformed into the Lorentz frame, but that in the lower medium is still kept in the original physical frame. There is a need to match these two coordinate systems at the interface in order to ensure correct application of the boundary conditions as stipulated in Eqs. 2.5 and 2.6.

### 2.2.2 Integral representations of acoustic potentials

To correctly impose the boundary conditions, it is convenient to express the acoustic potentials $\phi_0$ and $\phi_1$ in their respective integral forms. This process can be facilitated by using the space-time transformation where their Fourier transform pairs for the respective acoustic potentials are defined as

$$\hat{\phi}_j(k_x, z, \omega) = \int_{-\infty}^{\infty} \int_{-\infty}^{\infty} \phi_j(x, z, t) \mathrm{e}^{-\mathrm{i}(k_x x - \omega t)} \mathrm{d}x \mathrm{d}t \tag{2.10}$$

and

$$\phi_j(x, z, t) = \frac{1}{4\pi^2} \int_{-\infty}^{\infty} \int_{-\infty}^{\infty} \hat{\phi}_j(k_x, z, \omega) \mathrm{e}^{\mathrm{i}(k_x x - \omega t)} \mathrm{d}k_x \mathrm{d}\omega, \tag{2.11}$$

where $j = 0, 1$. The variables $k_x$ and $\omega$, are the horizontal component of the wave vector and the varying angular frequency, respectively.

For the Lorentz space in the upper medium, the Fourier transform pair ($\phi_L$ and $\hat{\phi}_L$) is specified by

$$\hat{\phi}_L(L_x, z_L, \omega_L) = \int_{-\infty}^{\infty} \int_{-\infty}^{\infty} \phi_L(x_L, z_L, t_L) \mathrm{e}^{-\mathrm{i}(L_x x_L - \omega_L t_L)} \mathrm{d}x_L \mathrm{d}t_L \tag{2.12}$$

and

$$\phi_L(x_L, z_L, t_L) = \frac{1}{4\pi^2} \int_{-\infty}^{\infty} \int_{-\infty}^{\infty} \hat{\phi}_L(L_x, z_L, \omega_L) \mathrm{e}^{\mathrm{i}(L_x x_L - \omega_L t_L)} \mathrm{d}L_x \mathrm{d}\omega_L. \tag{2.13}$$

Note in Eqs. 2.12 and 2.12 that $L_x$ is the horizontal component of the wave vector, and $\omega_L$is the varying angular frequency for the Lorentz space.

Application of the Fourier transform pair in the Lorentz space leads to a simplification of Eq. 2.9 to give a second-order differential equation for $\hat{\phi}_L(L_x, z_L, \omega_L)$ in terms of $z_L$ as

$$\frac{\partial^2 \hat{\phi}_L}{\partial z_L^2} + L_z^2 \hat{\phi}_L = 2\pi\gamma\delta(z_L - z_{Ls})\delta(\omega_L - \omega_s), \tag{2.14}$$

where $L_z$ is the vertical component of the wave vector given by

$$L_z = +\sqrt{k_L^2 - L_x^2}, \tag{2.15}$$

and $k_L = \omega_s/c_0$ is the wave number in the Lorentz space. Strictly speaking, $\omega_L$ should be used instead of $\omega_s$ in defining $k_L$. However, the delta function $\delta(\omega_L - \omega_s)$ ensures that $\omega_L = \omega_s$ when the outer integral of Eq. (8b) is evaluated with respect to $\omega_L$. Hence, $\omega_s$is used for defining $k_L$, which facilitates the subsequent presentation of the theoretical results. The solution for Eq. 2.14 has the form

$$\hat{\phi}_L(L_x, z_L, \omega_L) = \frac{\gamma\pi}{\mathrm{i}L_z}\left[\mathrm{e}^{\mathrm{i}L_z\Delta z_-} + Ve^{\mathrm{i}L_z\Delta z_+}\right]\delta(\omega_L - \omega_s), \tag{2.16}$$

where $\Delta z_\mp$ are the respective height differences between the source and its image with the receiver, i.e., $\Delta z_\mp = |z_{Ls} \mp z_{Lr}|$, and V is the reflection factor to be determined from the boundary conditions given in Eqs. 2.5 and 2.6. By substituting Eq. 2.16 into Eq. 2.13, an integral expression for the acoustic potential in the upper medium in the Lorentz space can then be obtained.

For the lower medium, the acoustic potential in the physical space is used. By substituting Eq. 2.15 into Eq. 2.7, it is possible to obtain the following equation:

$$\frac{\partial^2\hat{\phi}_1}{\partial z^2} + \kappa_z^2\hat{\phi}_1 = 0, \tag{2.17}$$

where $\kappa_z$ is the vertical component of the wave vector given by

$$\kappa_z = +\sqrt{k_1^2 - k_x^2}, \tag{2.18}$$

and $k_1 = \omega/c_1$ is the wave number in the physical space. For a semi-infinite lower medium ($z < 0$), the transformed acoustic potential is the solution of Eq. 2.17 that can be expressed as

$$\hat{\phi}_1(k_x, z, \omega) = T\mathrm{e}^{-\mathrm{i}\kappa_z z}, \tag{2.19}$$

where $T$ is the transmission factor dependent on the boundary conditions.

### 2.2.3 Boundary condition for an extended reaction ground

Using Eq. 2.10, the boundary conditions given in Eqs. 2.5 and 2.6 can be modified to

$$\rho_0\hat{\phi}_0(k_x, 0, \omega) = \rho_1(\omega)\,\hat{\phi}_1(k_x, 0, \omega) \tag{2.20}$$

and

$$\partial_z \hat{\phi}_0(k_x, 0, \omega) = \partial_z \hat{\phi}_1(k_x, 0, \omega), \tag{2.21}$$

where $\partial_z$ is the differentiation with respect to z. It follows from Eqs. 2.19 and 2.4 that

$$\partial_z \hat{\phi}_0(k_x, 0, \omega) = -\mathrm{i}\kappa_z \hat{\phi}_1(k_x, 0, \omega). \tag{2.22}$$

Application of Eq. 2.22 to Eq. 2.3 leads to the following boundary condition:

$$c_0 \partial_z \hat{\phi}_0(k_x, 0, \omega) + \mathrm{i}\omega\beta\hat{\phi}_0(k_x, 0, \omega) = 0, \tag{2.23}$$

where $\beta\,[\equiv \beta(k_x, \omega)]$, which is the apparent surface admittance of the extended reaction ground, is given by

$$\beta = \zeta\sqrt{n^2 - (k_x/k_0)^2}, \tag{2.24}$$

$k_0\,(\equiv \omega/c_0)$ is the wave number in air, $\zeta$ is the complex density ratio:

$$\zeta \equiv \zeta(\omega) = \rho_0/\rho_1(\omega), \tag{2.25}$$

and $n$ is the index of refraction:

$$n \equiv n(\omega) = c_0/c_1(\omega). \tag{2.26}$$

Defining an impulse response in space-time for the apparent surface admittance:

$$\beta(k_x, \omega) = \int_{-\infty}^{\infty}\int_{-\infty}^{\infty} \hat{\beta}(x, t)\mathrm{e}^{\mathrm{i}(\omega t - k_x x)}\mathrm{d}x\mathrm{d}t, \tag{2.27}$$

the boundary condition [Eq. 2.23] can be converted to a twofold convolution integral in terms of the surface potential $\phi_g(x, t) \equiv \phi_0(x, 0, t)$:

$$c_0 \partial_z \phi_g(x, t) - \int_{-\infty}^{\infty}\int_{-\infty}^{\infty} \hat{\beta}(x', t')\partial_t \phi_g(x - x', t - t')\mathrm{d}t'\mathrm{d}x' = 0. \tag{2.28}$$

The space-time impulse response $\hat{\beta}(x, t)$ is introduced for the clarity of presentation. Its exact expression is not explicitly required in the present study. Nevertheless, more details for $\hat{\beta}(x, t)$ are discussed in Ref. [48].

The next step is to derive the corresponding boundary condition in the Lorentz space from Eq. 2.28. According to Eq. 2.7, the differentiations with respect to t, x, and z in the physical space can be written in the Lorentz space as

$$\partial/\partial t = \gamma^2 \left(\partial/\partial t_L - c_0 M \partial/\partial x_L\right) = -\mathrm{i}\omega_L \Omega, \tag{2.29}$$

$$\partial/\partial x = \gamma^2 \left[\left(-M/c_0\right) \partial/\partial t_L + \partial/\partial x_L\right] = \mathrm{i}k_L \Gamma, \tag{2.30}$$

and

$$\partial/\partial z = \gamma \partial/\partial z_L. \tag{2.31}$$

In Eqs. 2.29 and 2.30, the differential operators are applied to the acoustic potential $\phi_L(x_L, z_L, t_L)$ in the Lorentz space. Given the integral representation of $\phi_L$, viz. Eq. 2.13, $\Omega$ and $\Gamma$ can, therefore, be treated as algebraic functions in terms of $\omega_L$ and $L_x$ as follows:

$$\Omega\left(L_x, \omega_L\right) = \gamma^2 \left(1 + M L_x / k_L\right) \tag{2.32}$$

and

$$\Gamma\left(L_x, \omega_L\right) = \gamma^2 \left(M + L_x / k_L\right). \tag{2.33}$$

These two algebraic functions, $\Omega$ and $\Gamma$, are referred as the temporal and spatial Doppler terms, respectively. The reason for choosing these specific forms for the Doppler terms becomes apparent when the asymptotic solutions for the sound pressure are derived. In the Lorentz space, the two surface potentials in Eq. 2.28 can be expressed as

$$\phi_g(x, t) = \frac{1}{4\pi^2} \int_{-\infty}^{\infty} \int_{-\infty}^{\infty} \hat{\phi}_L(L_x, 0, \omega_L) \mathrm{e}^{\mathrm{i}(L_x x_L - \omega_L t_L)} \mathrm{d}L_x \mathrm{d}\omega_L \tag{2.34}$$

and

$$\phi_g(x - x', t - t') = \frac{1}{4\pi^2} \int_{-\infty}^{\infty} \int_{-\infty}^{\infty} \hat{\phi}_L(L_x, 0, \omega_L) \mathrm{e}^{\mathrm{i}(L_x x_L - \omega_L t_L) - \mathrm{i}(\Gamma k_L x' - \Omega \omega_L t')} \mathrm{d}L_x \mathrm{d}\omega_L. \tag{2.35}$$

where Eq. 2.35 is obtained by using the Lorentz transform [Eq. 2.7] with the temporal and spatial Doppler terms defined in Eqs. 2.32 and 2.33, respectively. Substituting

Eqs. 2.29 to 2.35 into Eq. 2.28, applying the convolution identity of Eq. 2.27, and manipulating the resulting expression, the boundary condition for an extended reaction ground in the Lorentz frame is then given by

$$\partial\hat{\phi}_L(L_x, 0, \omega_L) \Big/ \partial z_{_L} + \mathrm{i}k_L\,(\Omega/\gamma)\,\beta(\Gamma k_L, \Omega\omega_L)\hat{\phi}_L(L_x, 0, \omega_L) = 0, \tag{2.36}$$

where

$$\begin{aligned} \beta(\Gamma k_L, \Omega\omega_L) &= \zeta_L\sqrt{n_L^2 - (\Gamma/\Omega)^2}, \\ \zeta_L \equiv \zeta\,(\Omega\omega_L)\,; &\quad n_L \equiv n\,(\Omega\omega_L)\,. \end{aligned} \tag{2.37}$$

The above equation reveals that the boundary condition in the Lorentz frame has an analogous form comparable to the well-known impedance boundary condition. It is remarkable that Dragna et al. [35] used an impulse response in a onefold convolution integral for a locally reacting ground. For a source moving above an extended reaction ground, the apparent surface admittance varies both temporally and spatially; see Eqs. 2.32 and 2.33 for the temporal and spatial Doppler terms. Hence, Eq. 2.36 offers a generalization of Dragna's result by extending their analysis to a twofold convolution integral for an extended reaction ground. Indeed, Eq. 2.36 is one of the main results of the current study. To the best of our knowledge, this general form of the impedance boundary condition was not presented in any earlier studies.

### 2.2.4 Asymptotic solution for sound pressure in Lorentz frame

Substitution of Eq. 2.16 into 2.36 with $z_L = 0$ yields a solution for the reflection factor $V$ as follows:

$$V = \frac{L_z - k_L\Omega\beta(\Gamma k_L, \Omega\omega_L)/\gamma}{L_z + k_L\Omega\beta(\Gamma k_L, \Omega\omega_L)/\gamma}. \tag{2.38}$$

Using Eq. 2.16 in Eq. 2.13 with the reflection factor calculated by Eq. 2.38 and evaluating the outer integral with respect to $\omega_L$, the acoustic potential can be simplified to

$$\phi_L(x_L, z_L, t_L) = \int\limits_{-\infty}^{\infty} S_- \mathrm{d}L_x + \int\limits_{-\infty}^{\infty} S_+ \mathrm{d}L_x - \int\limits_{-\infty}^{\infty} \frac{2k_s\Omega_s\beta_{L,s}S_+/\gamma}{L_z + k_s\Omega_s\beta_{L,s}/\gamma}\mathrm{d}L_x, \tag{2.39}$$

where

$S_{\mp}\left[\equiv S\left(\Delta_{\mp}z\right)\right]$ is given by

$$S_{\mp} = S\left(\Delta_{\mp}z\right) = \frac{\gamma \mathrm{e}^{-\mathrm{i}\omega_s t_L}}{4\pi}\frac{\mathrm{e}^{\mathrm{i}\left[L_x x_L + L_z \Delta_{\mp} z\right]}}{\mathrm{i}L_z}, \tag{2.40}$$

and the vertical component of the wave vector is now evaluated with $k_L = \omega_L/c_0|_{\omega_L=\omega_s} = k_s$. Hence, $L_z = \sqrt{k_s^2 - L_x^2}$. In Eq. 2.39, the subscript s represents the evaluation of the corresponding parameters at $\omega_L = \omega_s$. For example,

$$\begin{cases} \Omega_s = \gamma^2\left(1 + ML_x/k_s\right) \\ \Gamma_s = \gamma^2\left(M + L_x/k_s\right) \\ \beta_{L,s} = \zeta_{L,s}\sqrt{n_{L,s}^2 - \left(\Gamma_s/\Omega_s\right)^2} \\ \zeta_{L,s} \equiv \zeta\left(\omega_s\Omega_s\right) \\ n_{L,s} \equiv n\left(\omega_s\Omega_s\right) \end{cases}$$

.

By using the identities in Eqs. 2.3, 2.12, and 2.14, the acoustic potential in the upper medium can be transformed from Eq. 2.39 to yield the sound pressure as

$$p_0(x_L, z_L, t_L) = p_- + p_+ + I_b, \tag{2.41}$$

where the first two integrals can be identified as the sound fields owing to the source and its image:

$$p_{\mp}(x_L, z_L, t_L) = i\rho_0\omega_s\int_{-\infty}^{\infty}\Omega_s S_{\mp}\mathrm{d}L_x, \tag{2.42}$$

and the third term is the wave contribution from the boundary surface:

$$I_b(x_L, z_L, t_L) = -\frac{\gamma\rho_0\omega_s \mathrm{e}^{-\mathrm{i}\omega_s t_L}}{2\pi}\int_{-\infty}^{\infty}\frac{k_s\Omega_s^2\beta_{L,s}/\gamma}{L_z + k_s\Omega_s\beta_{L,s}/\gamma}\frac{\mathrm{e}^{\mathrm{i}\left[L_x x_L + L_z \Delta z_+\right]}}{L_z}\mathrm{d}L_x. \tag{2.43}$$

Note that the first and second integrals of Eq. 2.41 are identical except for the difference in the height levels at $\Delta z_-$ and $\Delta z_+$, respectively. Consequently, their asymptotic solutions can be represented in a common form. Using the polar coordinate system $(k_s, \mu_L)$ to replace the wave vector $(L_x, L_z)$, Eq. 2.42 can be recast as

$$p_{\mp}(d_{\mp}, \Theta_{\mp}, t_L) = \mathrm{i}\rho_0\omega_s\frac{\gamma \mathrm{e}^{-\mathrm{i}\omega_s t_L}}{4\pi}\int_C \Omega_s\left(\mu_L\right)\mathrm{e}^{\mathrm{i}k_s d_{\mp}\cos(\mu_L - \Theta_{\mp})}\mathrm{d}\mu_L, \tag{2.44}$$

where $\Omega_s(\mu_L)$ can now be interpreted as the temporal Doppler factor given by

$$\Omega_s(\mu_L) = \gamma^2 \left(1 + \bar{M} \sin \mu_L\right), \tag{2.45}$$

$$\bar{M} = \mathrm{sgn}(x - c_0 M t) M, \tag{2.46}$$

and $d_\mp = \sqrt{{x_L}^2 + {\Delta z_\mp}^2}$ are the respective radial distances centered from the source (with the negative radical in the subscript) and its image (with the positive radical) to the receiver. The modified Mach number $\bar{M}$ is used in favor of M because it can lead to a more compact expression in Eq. 2.46 and in the subsequent expressions. A positive value of $\bar{M}$, $x > c_0 M t$, indicates an approaching source whereas a negative value represents a receding source.

The respective polar angles $\Theta_\mp$ in the Lorentz space are measured from the positive $z_L$-axis. The integration path C in Eq. 2.44 starts from $-\pi/2 + \mathrm{i}\infty$ in the complex $\mu_L$- plane, moves vertically downward to the point $-\pi/2 + 0\mathrm{i}$, horizontally to $\pi/2 + 0\mathrm{i}$, and vertically arrives at $\pi/2 - \mathrm{i}\infty$. By means of the steepest descent method [25], the integral of Eq. 2.44 can be evaluated asymptotically to offer approximate solutions for $p_\mp(d_\mp, \Theta_\mp, t_L)$ in the Lorentz space as

$$p_\mp(d_\mp, \Theta_\mp, t_L) \approx \rho_0 \omega_s \frac{\gamma}{4} \Omega_\mp \mathrm{e}^{-\mathrm{i}\omega_s (t_L - d_\mp / c_0)} \sqrt{2 / \mathrm{i}\pi k_s d_\mp}, \tag{2.47}$$

where $\Omega_-$ and $\Omega_+$ are the respective Doppler factors for the source and image source:

$$\Omega_\mp \equiv \Omega_s(\Theta_\mp) = \gamma^2 \left(1 + \bar{M} \sin \Theta_\mp\right). \tag{2.48}$$

An exact solution (expressed in terms of the Hankel function) can be identified for Eq. 2.44, see Eq. (29) of [35], but it is more convenient to use Eq. 2.47 in the following analysis.

Using the same polar coordinate system in the Lorentz frame, the boundary wave term can also be written analogously in an integral form as

$$I_b(d_+, \Theta_+, t_L) = -\rho_0 \omega_s \frac{\gamma \mathrm{e}^{-\mathrm{i}\omega_s t_L}}{2\pi} \int_C \frac{\left(\Omega_s^2 \beta_{L,s} / \gamma\right) \mathrm{e}^{\mathrm{i}k_s d_+ \cos(\mu_L - \Theta_+)}}{\cos \mu_L + \Omega_s \beta_{L,s} / \gamma} \mathrm{d}\mu_L, \tag{2.49}$$

where $\Omega_s$ is given by Eq. 2.46. The apparent admittance $\beta_{L,s}$ is derived from Eq. 2.37 to give

$$\beta_{L,s}(\mu_L) = \zeta_{L,s}\sqrt{n_{L,s}^2 - \left(\bar{M} + \sin\mu_L\right)^2 \Big/ \left(1 + \bar{M}\sin\mu_L\right)^2}, \tag{2.50}$$

where $\zeta_{L,s} \equiv \zeta(\omega_s\Omega_s)$ and $n_{L,s} \equiv n(\omega_s\Omega_s)$.

In the Lorentz space, the reflection factor $V(\mu_L)$ [see Eq. 2.38] can be transformed into the plane wave reflection coefficient:

$$V(\mu_L) = \frac{\cos\mu_L - (\Omega_s/\gamma)\,\zeta_{L,s}\sqrt{n_{L,s}^2 - \left(\bar{M} + \sin\mu_L\right)^2 \Big/ \left(1 + \bar{M}\sin\mu_L\right)^2}}{\cos\mu_L + (\Omega_s/\gamma)\,\zeta_{L,s}\sqrt{n_{L,s}^2 - \left(\bar{M} + \sin\mu_L\right)^2 \Big/ \left(1 + \bar{M}\sin\mu_L\right)^2}}. \tag{2.51}$$

The kernel function of the boundary wave term, viz. Eq. 2.49, can then be rearranged in a recognizable form as

$$(\Omega_s/2)\left[1 - V(\mu_L)\right] = \frac{(\Omega_s^2\beta_{L,s}/\gamma)}{\cos\mu_L + \Omega_s\beta_{L,s}/\gamma}. \tag{2.52}$$

To evaluate the integral of Eq. 2.49, it is necessary to find the pole $\mu_{L,p}$, say, in the Lorentz frame. This can be done readily by setting the denominator on the right side of Eq. 2.52 to zero, leading to a transcendental equation in terms of $\mu_{L,p}$ as

$$\cos\mu_{L,p} + \Omega_p\beta_{L,p}/\gamma = 0, \tag{2.53}$$

where the subscript p represents the corresponding parameters to be evaluated at the pole location, e.g., $\Omega_p \equiv \Omega_s(\mu_{L,p})$ and $\beta_{L,p} \equiv \beta_{L,s}(\mu_{L,p})$.

With the knowledge of the pole in the integrand, Li and Tao [49] used the steepest descent method in conjunction with the pole subtraction method to evaluate this type of diffraction integral. The details of this analysis will not be repeated here, but the asymptotic solution can be summarized as follows. In the Lorentz frame, the accurate asymptotic solution for Eq. 2.49 when $k_s d_+ \gg 1$ can be derived to yield

$$I_b(d_+, \Theta_+, t_L) = (V_+ - 1)\left\{1 - A_L F(w_{L,p})\right\} p_+(d_+, \Theta_+, t_L), \tag{2.54}$$

where $V_+ = V(\Theta)$ is the plane wave reflection coefficient (in the Lorentz frame) evaluated by Eq. 2.51 with $\mu_L = \Theta_+$, $A_L$ is referred to as the augmented diffraction factor [48], and $F()$ is the boundary loss factor defined by

$$F(w_{L,p}) = 1 + \mathrm{i}\sqrt{\pi} w_{L,p} \mathrm{e}^{-w_{L,p}^2} \mathrm{erfc}(-\mathrm{i} w_{L,p}). \tag{2.55}$$

$e^{-Z^2}\mathrm{erfc}(-\mathrm{i}Z)$ is the scaled complementary function with a complex argument Z [15], and $w_{L,p}$ is the apparent numerical distance determined by the following equation:

$$w_{L,p}^2 / \mathrm{i} k_s d_+ = 1 - \cos(\mu_{L,p} - \Theta_+). \tag{2.56}$$

The augmentation factor $A_L$ is calculated by

$$A_L = \left[\frac{\Omega_p \beta_{L,p}}{\Omega_+ \beta_{L,+}}\right] \left[\frac{w_{L,+}}{w_{L,p}}\right] \left[\frac{1}{\Delta_L}\right] \frac{\Omega_p}{\Omega_+}, \tag{2.57}$$

where

$$\Delta_L = -\frac{d}{d\mu_{L,p}} (\cos \mu_{L,p} + \Omega_p \beta_{L,p} / \gamma), \tag{2.58}$$

and$w_{L,+}$ is known as the approximate numerical distance:

$$w_{L,+} = \sqrt{\mathrm{i} k_s d_+ / 2} (\cos \Theta_+ + \Omega_+ \beta_{L,+} / \gamma). \tag{2.59}$$

$\Delta_L$ is the derivative of term $\cos \mu_L + \Omega \beta_L / \gamma$ at the pole location owing to L'Hôpital's rule. The Doppler terms and the admittance terms [see Eq. 2.50 for $\beta_{L,s}$] were defined earlier, but they are presented here again for convenience:

$$\left\{ \begin{array}{c} \Omega_p \equiv \Omega_s(\mu_{L,p}) = \gamma^2 \left(1 + \bar{M} \sin \mu_{L,p}\right) \\ \Omega_+ \equiv \Omega_s(\Theta_+) = \gamma^2 \left(1 + \bar{M} \sin \Theta_+\right) \\ \beta_{L,p} = \zeta_{L,p} \sqrt{n_{L,p}^2 - \left(\bar{M} + \sin \mu_{L,p}\right)^2 \Big/ \left(1 + \bar{M} \sin \mu_{L,p}\right)^2} \\ \beta_{L,+} = \beta_{L,s}(\Theta_+) \end{array} \right. , \tag{2.60}$$

where the arguments for $\zeta_{L,p}$ and $n_{L,p}$ are evaluated at a frequency of $\omega_{L,p} \equiv \omega_s \Omega_p$. The frequency term $\omega_{L,p}$ and admittance term $\beta_{L,p}$ are referred to respectively as the Dopplerized pole frequency and the apparent admittance in the Lorentz frame.

Replacing the diffraction term $I_b(d_+, \Theta_+, t_L)$ in Eq. 2.41 with that given by the right side of Eq. 2.54, the sound field in the upper medium can be determined by

$$p_0\left(x_L, z_L, t_L\right) = p_-(d_-, \Theta_-, t_L) + \left\{V_+ + A_L\left[1 - V_+\right] F\left(w_{L,p}\right)\right\} p_+(d_+, \Theta_+, t_L), \quad (2.61)$$

where $p_\mp(d_\mp, \Theta_\mp, t_L)$ are the direct and ground-reflected wave terms given by Eq. 2.47. All terms in Eq. 2.61 can be computed readily except for the factor involving $\Delta_L$ for the augmented diffraction factor $A_L$ [see Eq. 2.57]. Using the appropriate identities of Eq. 2.60 in Eq. 2.58, it is tedious but straightforward to derive an explicit expression for $\Delta_L$ leading to its numerical computations. For brevity, the lengthy algebraic expression for $\Delta_L$ is not presented here. Alternatively, the numerical values for $\Delta_L$ can be accurately obtained by means of the numerical differentiation of Eq. 2.58. In the limiting case of a locally reacting ground, $\beta_{L,p} = \zeta_{L,p} n_{L,p}$ in Eq. 2.60 because $n\left(\omega\right)$ becomes large for all frequencies. Hence, a relatively simple form for $\Delta_L$ can be derived from Eq. 2.58 to give

$$\Delta_L = -\sin\mu_{L,p} + \gamma\bar{M}\cos\mu_{L,p}\beta_{L,p} + \frac{\Omega_p}{\gamma}\beta'_{L,p} \quad (2.62)$$

where the prime in $\beta_{L,p}$ is the derivative with respect to $\mu_L$. Finally, all relevant functions can be assembled in Eq. 2.61 to arrive at the prediction of the sound fields owing to a line source moving at a constant height above a non-locally reacting ground. This is equivalent to the corresponding expression, which is Eq. (92) in Ref. [35], for the special case of a locally reacting ground.

### 2.2.5 Asymptotic formula in emission time geometry

Although Eq. 2.61 provides an accurate expression for computing the sound fields, it does not yield an appropriate interpretation in the physical frame for each term in the equation. It is more illuminating to present the results in a retarded time frame (i.e., the emission time geometry) instead of the Lorentz frame used in the derivation of Eq. 2.61. Starting from the standard two-dimensional Lorentz transformation [42], the following identities between the Lorentz space and the physical space can be established:

$$\begin{cases} x_L = \gamma^2 \left(\sin\theta_\mp - \bar{M}\right) R_\mp \\ \Delta z_\mp = \gamma \left|z_s \mp z_r\right| \\ d_\mp = \gamma^2 R_\mp / D_\mp \\ \cos\Theta_\mp = D_\mp \cos\theta_\mp / \gamma \\ \Omega_\mp = D_\mp \equiv D\left(\theta_\mp\right) \\ D\left(\theta_\mp\right) = 1 \big/ \left(1 - \bar{M}\sin\theta_\mp\right) \\ t_L - d_\mp / c_0 = t - R_\mp / c_0 \end{cases}, \tag{2.63}$$

where $(R_\mp, \theta_\mp)$ are the corresponding polar coordinates in the emission time geometry centered at the source and its image, and $D_\mp \equiv D\left(\theta_\mp\right)$ are the corresponding Doppler factors.

Using these identities, the sound fields owing to a moving source ($p_-$) and its image ($p_+$) can be rewritten from Eq. 2.47 to give

$$p_\mp(R_\mp, \theta_\mp, t) = \frac{\rho_0 \omega_s}{4} D_\mp^{3/2} \sqrt{2/\mathrm{i}\pi k_s R_\mp} \mathrm{e}^{-\mathrm{i}\omega_s (t - R_\mp/c_0)} \tag{2.64}$$

in the retarded time frame.

The kernel function of the boundary wave term, viz. Eq. 2.49, can then be rearranged in the physical frame as

$$\frac{(\Omega_s^2 \beta_{L,s}/\gamma)}{\cos\mu_L + \Omega_s \beta_{L,s}/\gamma} = \frac{\Omega_s \beta_s}{\cos\mu + \beta_s}, \tag{2.65}$$

where the polar angle  in the physical frame is introduced to replace $\mu_L$ by means of the following identities:

$$\beta_s\left(\mu\right) = \zeta_s \sqrt{n_s^2 - \sin^2\mu} \tag{2.66}$$

$$\cos\mu = \gamma \cos\mu_L / \Omega_s\left(\mu_L\right), \tag{2.67}$$

$$\sin\mu = \frac{\bar{M} + \sin\mu_L}{1 + \bar{M}\sin\mu_L}, \tag{2.68}$$

$$D\left(\mu\right) = 1 \big/ \left(1 - \bar{M}\sin\mu\right) = \Omega_s\left(\mu_L\right), \tag{2.69}$$

with $\zeta_s \equiv \zeta\left(\omega_s D\right)$ and $n_s \equiv n\left(\omega_s D\right)$. Eqs. 2.65 to 2.69 can be derived based on Eq. 2.63 with basic algebra.

Using Eqs. 2.65 to 2.69, it is possible to correlate the pole location in the Lorentz frame with that of the physical frame as follows:

$$\cos\mu_{L,p} = (D_p/\gamma)\cos\mu_p \tag{2.70}$$

and

$$\sin\mu_{L,p} = D_p\left(\sin\mu_p - \bar{M}\right), \tag{2.71}$$

where $\mu_p$ is the pole location in the physical frame, and $D_p \equiv D(\mu_p)$ is the Doppler term. The parameter $\mu_p$ will be referred to as the Dopplerized surface wave pole (or simply the Dopplerized pole), which indicates the effect of the source motion on the location of the pole.

To determine the Dopplerized pole, it is convenient to set the denominator on the right side of Eq. 2.65 to zero. Explicit expressions for $\cos\mu_p$ and $\sin\mu_p$, which can be obtained by noting Eq. 2.66, are given as follows:

$$\cos\mu_p = -\zeta_p\sqrt{\left(n_p^2 - 1\right)/\left(1 - \zeta_p^2\right)} \tag{2.72}$$

and

$$\sin\mu_p = \sqrt{\left(1 - \zeta_p^2 n_p^2\right)/\left(1 - \zeta_p^2\right)}, \tag{2.73}$$

where $\zeta_p \equiv \zeta(\omega_p)$, $n_p \equiv n(\omega_p)$, $\omega_p \equiv \omega_s D_p$, and the subscript p represents the parametric values evaluated at the Dopplerized pole.

The asymptotic solution for the boundary wave term can now be simplified considerably in the emission time geometry by applying the following identities for the apparent numerical distance $w_p$ and effective numerical distance $w_+$:

$$w_{L,p}^2 \equiv w_p^2 = \mathrm{i}R_+\left(\omega_p/c_0\right)\left[1 - \cos\left(\mu_p - \theta_+\right)\right] \tag{2.74}$$

and

$$w_{L,+}^2 \equiv w_+^2 = \left(\mathrm{i}R_+/2\right)\left(\omega_+/c_0\right)\left[\cos\theta_+ + \beta_+\right]^2, \tag{2.75}$$

where the effective admittance $\beta_+\left[\equiv \beta_s(\theta_+)\right]$ and apparent admittance $\beta_p\left[\equiv \beta_s(\mu_p)\right]$ in the emission time geometry are given respectively by

$$\beta_{L,+} = \beta_+ \tag{2.76}$$

and

$$\beta_{L,p} = \beta_p, \tag{2.77}$$

and $\beta_s\,()$ is defined in Eq. 2.66.

Using the identities given in Eqs. 2.63, 2.74, 2.74, 2.76 and 2.77, the boundary wave term can be transformed from Eq. 2.54 into

$$I_b(R_+, \theta_+, t) = -\left(1 - Q\right) p_+(R_+, \theta_+, t), \tag{2.78}$$

where $Q$ is the spherical wave reflection coefficient:

$$Q = V_+ + A\left[1 - V_+\right] F\left(w_p\right), \tag{2.79}$$

and $V_+$ is the plane wave reflection coefficient in the emission frame:

$$V_+ = \frac{\cos\theta_+ - \beta_+}{\cos\theta_+ + \beta_+}, \tag{2.80}$$

$V_+$ is equal to the plane wave reflection coefficient $V(\Theta)$ in the Lorentz frame in Eq. 2.54.

Starting from Eq. 2.57, the augmented diffraction factor A becomes

$$A = \frac{r_\beta / r_w}{\delta_\mu \Delta} \tag{2.81}$$

in the physical frame where $r_\beta$ is the admittance ratio:

$$r_\beta = \frac{D_p \beta_p}{D_+ \beta_+} = \frac{D_p \zeta_p \sqrt{n_p^2 - \sin^2\mu_p}}{D_+ \zeta_+ \sqrt{n_+^2 - \sin^2\theta_+}}, \tag{2.82}$$

and $r_w$ is the ratio of numerical distances:

$$r_w = \frac{w_p}{w_e} = 2\sqrt{D_p / D_+}\left[\sin\tfrac{1}{2}(\mu_p - \theta_+)/(\cos\theta_+ + \beta_+)\right], \tag{2.83}$$

where $\zeta_+\,[\equiv \zeta(\omega_+)]$ and $n_+\,[\equiv n(\omega_+)]$ in Eq. 2.81 are, respectively, the density ratio and the index of refraction calculated at the Doppler frequency $\omega_+\,[\equiv D_+\omega_s]$ with the Doppler factor for the image source as $D_+\left[\equiv 1/(1 - \bar{M}\sin\theta_+)\right]$. It is also possible to show that the factor $\Delta$ in Eq. 2.81 can be expressed as

$$\Delta \equiv -\partial\left(\cos\mu_p + \beta_p\right)/\partial\mu_p = \sin\mu_p - \beta_p' \tag{2.84}$$

where the prime in $\beta_p$ represents its derivative with respect to $\mu_p$, and $\delta_\mu$is defined as

$$\delta_\mu \equiv (D_+/\gamma)\,\partial\mu/\partial\mu_L|_{\mu=\mu_p} = \frac{D_+}{D_p}. \tag{2.85}$$

It is important to note that $\Delta$ is different from $\Delta_L$ in Eq. 2.57 and their ratio is

$$\Delta_L/\Delta = \frac{D_p}{D_+}\delta_\mu \tag{2.86}$$

The rather lengthy algebraic expression for $\beta_p'$ will not be presented here as it can be obtained readily with the help of the symbolic toolboxes available in MATLAB, Maple, or Mathematica.

Summing Eqs. 2.64 and 2.78 and rearranging the resulting terms, the total sound pressure in the physical space (retarded time) can now be recast in a familiar Weyl-van der Pol (WVDP) form as

$$p_0\,(x_{L,}z_L, t_L) = p_-(R_-, \theta_-, t) + Q\; p_+(R_+, \theta_+, t), \tag{2.87}$$

where $p_-$ and $p_+$ are given by Eq. 2.64. The above equation, which is one of the main results of the present study, generalizes WVDP for the sound field from a source moving horizontally at a constant speed above an extended reaction ground. This formula is referred to as the Dopplerized Weyl-Van der Pol (D-WVDP) formula in the following section. The first term in Eq. 2.87 is identified as the direct wave term, the second term is referred to as the ground reflected wave term, and Q is the spherical wave reflection coefficient.

It is worth pointing out that Eq. 2.87 is expressed in an asymptotic form with all terms written in the emission time geometry. In fact, the asymptotic solution for the boundary wave term, $I_b$, was only expressed in the Lorentz frame in most, if not all, previous studies [4, 10, 11, 35]. Subsequent transformations are therefore needed to convert these numerical solutions from the Lorentz frame to the physical time frame.

## 2.3 Impedance model and Dopplerized surface wave pole

Based on the D-WVDP formula [see Eq. 2.87], several analyses are discussed in the following sections. Although most impedance models for a non-locally reacting ground [50] can be used in our analyses, a phenomenological model (referred to as the Hamet and Bérengier model [51]) is chosen in the present study. Three adjustable parameters, known as the airflow resistivity $\sigma_0$, tortuosity $q^2$, and porosity of the air-filled connected pores , are used to model a rigid porous medium in which the density ratio $\zeta(\omega)$ and the index of refraction $n(\omega)$ are calculated by

$$\zeta(\omega) = \rho_0/\rho_1 = \varphi/\left(q^2\Gamma_\mu\right) \tag{2.88}$$

and

$$n(\omega) = k_1/k_0 = q\Gamma_\mu^{1/2}[\upsilon - (\upsilon - 1)/\Gamma_\theta]^{1/2}, \tag{2.89}$$

where $\nu$ is the ratio of specific heat for air. The functions $\Gamma_\mu$ and $\Gamma_\theta$ are respectively used to model the viscous and thermal effects on the interaction of sound with the ground surface. They are determined by

$$\Gamma_\mu(\omega) = 1 + \mathrm{i}\varphi\sigma_0/\left(\omega\rho_0 q^2\right) \tag{2.90}$$

and

$$\Gamma_\theta(\omega) = 1 + \mathrm{i}\sigma_0/(\omega\rho_0\,\mathrm{Pr}), \tag{2.91}$$

where Pr is the Prandtl number of air. The respective numerical values of 1.22 kg m-3, 1.4, and 0.72 for $\rho_0$, $nu$, and Pr are used in all computations described below.

When the Dopplerized pole $\mu_p$ is determined, both $\xi$ and $n$ [calculated respectively by Eqs. 2.88] and 2.89]] are dependent on the complex frequency $\omega_p$ instead of the constant source frequency $\omega_s$. These ground characteristic functions $xi$ and $n$ vary with the Dopplerized frequency $\omega_+$ when the effective admittance [see Eq. 2.76]] is determined. Consequently, the Doppler effect causes an apparent change in the acoustical properties of the ground surface as a result of the source motion. These subtle changes have significant impacts on the calculation of the ground reflected wave term.

The excess attenuation ($EA$), which is introduced to facilitate the presentation of numerical results, is defined as

$$EA = 20\log_{10}(p_0/p_-) \tag{2.92}$$

where $p_0$ is the total sound field calculated by Eq. 2.61], and $p_-$ is the direct wave term given in Eq. 2.64]. The sound pressure level ($SPL$), which is used in some of the plots of the current study, is defined as

$$\text{SPL} = 20\log_{10}(p_0/p_{ref}) \tag{2.93}$$

where the reference pressure, $p_{ref}$, is set at 20 $\mu$Pa.

Since $\zeta_p$ and $n_p$ are functions of the Dopplerized pole, the solution to Eq. 2.72 can be found straightforwardly by a simple iterative scheme for a given value of$\bar{M}$. Note here that a positive value of $\bar{M}$ gives the condition of an approaching source, while a negative $\bar{M}$ represents the condition of a receding source. A close examination of Eq. 2.72 reveals that the Dopplerized pole does not change with the source/receiver geometry but is only dependent on the acoustical property of the ground and the convection speed of the source. The Newton–Raphson method is used to find the pole location. If $\mu_p^{(j)}$ is the jth iterative solution, then the sequence $\mu_p^{(0)}$, $\mu_p^{(1)}$, $\mu_p^{(2)}$, ... converges to the required pole. The recursive formula becomes

$$\mu_p^{(j+1)} = \mu_p^{(j)} - \left(\cos\mu_p^{(j)} + \beta_p^{(j)}\right)\Big/\Delta^{(j)}, \tag{2.94}$$

where the superscript j indicates the corresponding function values at the jth iteration. The iteration starts with an initial guess where $\omega_p = \omega_s$ and $D_p = 1$ are used for calculating $\zeta_p^{(0)}$, $n_p^{(0)}$, and $\Delta^{(0)}$. Their use provides the first iterative solution for the Dopplerized pole in Eq. 2.72. The first estimated $\mu_p^{(1)}$ is then used to calculate a revised $\zeta_p^{(1)}$, $n_p^{(1)}$, and $\Delta^{(1)}$, where the respective variables are set to $\omega_p^{(1)} = \omega_s D_p^{(1)}$ and $D_p^{(1)} = 1\Big/\left(1 - \bar{M}\sin\mu_p^{(1)}\right)$. The "new" Dopplerized pole, $\mu_p^{(2)}$, is then determined from Eq. 2.94. This iterative process repeats until this surface wave pole converges to the required accuracy. Typically, fewer than 10 iterations are needed to arrive at a converged solution accurate to within 10-16 for $|\mu_p|$.

Using the above numerical scheme, Figure 2.2a demonstrates a tracing of the pole locations with $\bar{M}$ varying between 0 and $\pm 0.8$ for an approaching and receding source. An airflow resistivity of 5 kPa m s$^{-2}$, tortuosity of 0.6, porosity of 0.6, and source

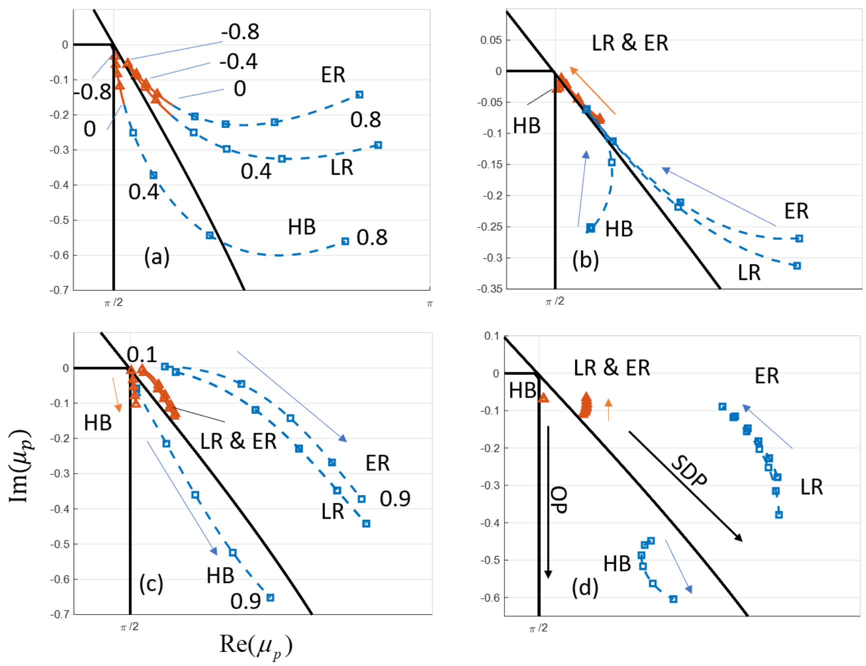


Figure 2.2. Variation in pole locations with changes in Mach number and ground properties. Source frequency is set at 100 Hz and source/receiver heights at 0.3 and 0.6 m, respectively. Other symbols are as follows. SDP: steepest descent path, OP: original path of integration, LR: locally reacting ground, ER: extended reaction ground, and HB: hardback layered ground. SDP and OP are shown in all graphs and are only marked explicitly in 2(d). (a) $\bar{M}$ varies from -0.8 to 0 (solid lines with triangles) and from 0 to 0.8 (dashed lines with squares) at a step of 0.2. Ground property is kept unchanged at $\sigma_0$ . $q^2$ and $\varphi$ of 5 kPa m s-2 are 1.22 and 0.6, respectively. (b) $\sigma_0$ varies from 10 to 500 kPa m s-2. Other ground properties $q^2$ and $\varphi$ are set at 1.22 and 0.6, respectively. Dashed lines with squares (approaching source): $\bar{M}$= 0.5, and solid lines with triangles (receding source): $\bar{M}$ = -0.5. Arrows indicate direction of increasing $\sigma_0$. (c) $\varphi$ varies from 0.1 to 0.9. Other ground properties $\sigma_0$ and $q^2$ are set at 5 kPa m s-2 and 1.22, respectively. dashed lines with squares (approaching source): $\bar{M}$ = 0.5, and solid lines with triangles (receding source): $\bar{M}$= -0.5. Arrows indicate directions of increasing $\varphi$. (d)$q^2$ varies from 1.0 to 4.0. Other ground properties $\sigma_0$ and $\varphi$ are set at 5 kPa m s-2 and 0.6, respectively. dashed lines with squares (approaching source): $\bar{M}$= 0.5, and solid lines with triangles (receding source): $\bar{M}$= -0.5. Arrows indicate directions of increasing $q^2$.

frequency of 100 Hz are used in the plot. Figures 2.2 show the respective numerical results for a fixed $\bar{M} = \pm 0.5$. However, two of the three ground parameters are held constant at the same nominal values used in Fig. 2a, but the third parameter is allowed to vary over a useful parametric range. These three additional figures, which are self-explanatory, serve to highlight the effect of each ground parameter $\sigma_0$, q$^2$, and $\varphi$ on $\mu_p$.

For comparison, the respective locations of the surface wave pole for the locally reacting (LR), extended reaction (ER), and hardback (HB) ground with a layer thickness of 0.12 m are also traced in the figures. Details for modeling the HB ground can be found in the appendix of [52] for information. In addition to the pole locations, the original integration path and steepest descent path are shown in all subplots. These two paths are referred to, respectively, as OP and SDP, and are marked explicitly in 2.2d for information. It is well-known that surface waves are triggered if and only if the pole location is sandwiched between OP and SDP [4]. Since the SDP differs as the source traverses horizontally, only the most critical one (i.e., the grazing propagation with the saddle point located at $\pi/2$) is shown in these figures for reference.

The primary aim of the present study is to provide a generalization of the asymptotic formula for predicting the sound fields due to a monopole source moving close to an outdoor ground surface. In the numerical simulations shown in section 2.4, the source speeds and the ground parameters are chosen to ensure a non-negligible presence of a surface wave component in the predicted sound fields. Furthermore, a realistic geometrical configuration of the source and receiver positions are selected for presenting the numerical results. These results allow thorough examinations of the relative importance of the direct wave term and various components of the ground reflected wave term. The impact on the prediction of sound fields due to the change in ground parameters, which is a subject of future studies, will not be pursued here for succinctness.

## 2.4 Validity of asymptotic formula and its approximations

### 2.4.1 Numerical validation

As described in 2.3, the Dopplerized pole can be determined numerically and can subsequently be used in Eq. 2.87 for calculating the sound field above a non-locally reacting ground. In order to confirm the validity of the D-WWDP formula [cf. Eq. 2.87], comparisons are carried out with a direct numerical solution of Eqs. 2.1 and 2.2 using a FDTD approach. For this, an FDTD solver [35, 53] is used. The computational domain in the FDTD solver is split into two subdomains. The linearized Euler equations are solved for the acoustic pressure in air for the upper domain. The lower computation domain corresponds to the ground in which time-domain equations associated with the Hamet and Bérengier model are solved. As in Ref. [35], a Gaussian source is employed to model the theoretical Dirac delta function source. The width of the Gaussian B should be as small as possible in order to avoid non-compacity effects [34] and consider that the Gaussian source behaves as a point source. In all simulations, the parameter $k_s B/(1-M)$ is kept below 0.3. Hence, the validity of the D-WWDP formula [cf. Eq. 2.87] can be confirmed by comparing its numerical solutions with those obtained by the FDTD methods.

Comparisons were conducted for a range of different values of M, $\sigma_0$, $q^2$, and$\varphi$. Typical time histories for the predicted sound pressure levels (SPL) are summarized for a source moving above an ER ground and an HB ground with a layer thickness of 0.15 m in Fig. 2.3a and 2.3b, respectively. In Fig. 2.3a, M = 0.5, $\sigma_0 = 1.0$ kPa s $m^{-2}$, $q^2 = 1.82$, and $\varphi = 0.5$ are used in the numerical simulations. On the other hand, M = 0.3, $\sigma_0 = 10.0$ kPa s $m^{-2}$, $q^2 = 1.252$, and $\varphi = 0.5$ are selected for the HB ground in Fig. 2.3b. A source frequency of 300 Hz is used in both plots, where the solid lines indicate the numerical results according to the FDTD method, and the circles (o) are those obtained by the asymptotic formula. The source moves at respective heights of 2 m and 0.5 m above the ER and HB grounds. The receiver is placed at different heights of 0, 2, and 5 m above the ground in both cases. The predicted

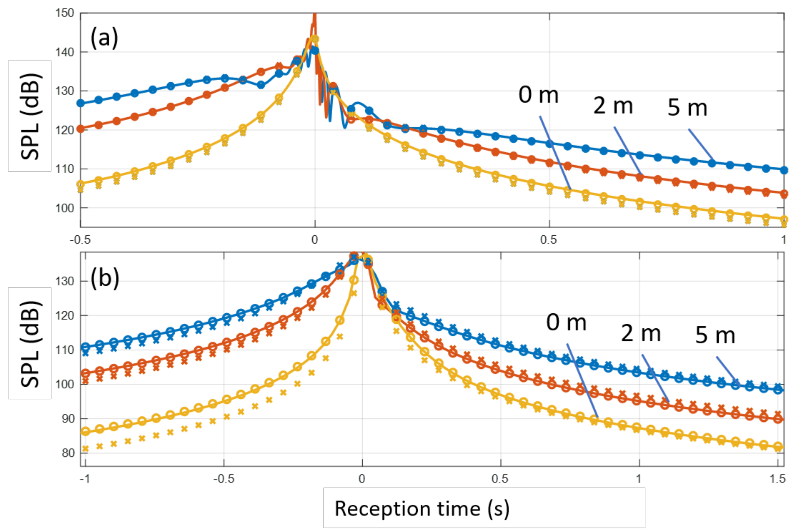


Figure 2.3. Comparisons between asymptotic solutions of locally reacting model (x) and non-locally reacting model (o) with time-domain finite difference solutions (solid lines). Reference sound pressure is 20 µPa for SPL calculation. Receiver is located at 0, 2, and 5 m above the ground. $x$ coordinates of source and receiver are both 0 when reception time is 0. Harmonic source has frequency of 300 Hz. (a) Semi-infinite extended reaction ground: source moves at constant height of 2 m above the ground with Mach number of 0.5. Ground has $\sigma_0$ , $q^2$, and $\varphi$ of 1 kPa m s − 2, 1.82, and 0.5, respectively. (b) Hard-back ground with layer thickness of 0.15 m: source moves at constant height of 0.5 m above the ground with Mach number of 0.3. Ground has $\sigma_0$ , $q^2$, and $\varphi$ of 10 kPa m s − 2, 1.252, and 0.5, respectively.

sound fields emitted by a source moving above an LR ground (using the identical ground parameters and the same source/receiver geometry) are also presented. They are shown as crosses (x) in these two figures for the purpose of illustration. It is worth noting that the ground wave term plays a more important role in predicting the total sound fields for the near-grazing propagation. Use of an LR ground model for the ER and HB grounds therefore becomes increasingly inadequate when the receiver is located in the vicinity of the ground surface.

In the predicted sound fields above the non-locally reacting ground, outstanding agreements between the D-WVDP formula and those obtained by the FDTD method are evinced in Figures 2.3a and 2.3b. The levels of agreement between these two numerical schemes are excellent for all other source/receiver geometries and ground surfaces. These comparisons mutually validate the adequacy of either method as a tool to predict the sound fields from a source moving above a non-locally reacting ground.

### 2.4.2 Validity of different approximate schemes

In 2.79 , the D-WVDP formula was derived for predicting sound fields owing to a source moving horizontally at a constant speed above a non-locally reacting ground. The accuracy of the D-WVDP formula was confirmed in the validation with Dragna's data, and the validity of various approximate schemes will be examined in this section. By using Eqs. 2.79 and 2.87, the D-WVDP formula can be re-arranged as follows:

$$p_0 = [p_- + V_+ p_+] + A\,[1 - V_+]\,F\,(w_p)\,p_+, \tag{2.95}$$

for facilitating discussion. The first two terms in Eq. 2.95 are grouped together in square brackets. They are known as a sum of the contributions from the direct and specularly reflected waves. The third component, which is known as the ground wave (GW) term, is needed for accurate prediction of near-grazing situations. [54]

For non-near-grazing propagation (i.e., $|\theta_+|$ is less than around 85°), the steepest descent path lies away from the surface wave pole. In this case, the pole has minimal effects on the evaluation of the integral of Eq. 2.50. The Dopplerized boundary loss factor term $F\,(w_p)$ becomes negligibly small. This implies that the GW term has an insignificant contribution to the D-WVDP formula. If a further approximation is made such that $\bar{M}\sin\theta_+ \to 0$, then $\omega_+ \approx \omega_s$ because $D_+ \to 1$. The acoustical characteristics of the ground can therefore be evaluated at the source frequency. The D-WVDP formula can then be approximated by

$$p_0 = p_- + \frac{\cos\theta_+ - \beta_s}{\cos\theta_+ + \beta_s} p_+, \tag{2.96}$$

and $\beta_s = \zeta_s\sqrt{n_s^2 - \sin^2\theta_+}$ for an ER ground. This approximate solution is analogous to the expression given in Ref. [40]. It is clear in Eq. 2.96 that $\beta_s = \zeta_s n_s$ for an LR ground, and $\beta_s = -\mathrm{i}\zeta_s\sqrt{n_s^2 - \sin^2\theta_+}\tan\left(k_s d\sqrt{n_s^2 - \sin^2\theta_+}\right)$ for an HB ground.

Equation 2.96 has a limited range of applicability owing to the assumption of a small $\bar{M}\sin\theta_+$. An improvement was highlighted by Ochmann [11], who argued that the Dopplerized frequency $\omega_+$ should be used instead of the source frequency $\omega_s$. A heuristic modification can simply be obtained by using the "Dopplerized" plane wave reflection coefficient [cf. Eq. 2.80 for the emission time frame and Eq. 2.51 for the Lorentz frame] in Eq. 2.96. The resulting formula is essentially the sum of the direct and specular wave terms, i.e., the first square-bracketed term in Eq. 2.95.

A further improvement can be identified by using a pseudo-stationary source approach as follows. First, the source frequency is kept constant at $\omega_+$ instead of $\omega_s$. Second, a retarded-time algorithm [10] is used at each time step for determining the relative positions of the receiver and the moving source. The source is then "frozen" at the spatial position corresponding to each time step where $\omega_+$ is different in each position. Finally, a saddle path integral is set up using this information for the source/receiver locations to arrive at an approximate solution as [48]

$$p_0 = p_A + [1 - V_+]\, F\left(w_+\right) p_+, \tag{2.97}$$

where A is approximated as 1 in the GW term for a stationary source. The sum of contributions from the direct and specularly reflected waves is given by

$$p_A = p_- + \frac{\cos\theta_+ - \beta_+}{\cos\theta_+ + \beta_+} p_+. \tag{2.98}$$

For a near-grazing sound propagation, Eq. 2.97 is identical to the approximate solution presented by Dragna and Blanc-Benon [their Eq. (100)] [35]. They demonstrated the adequacy and necessity of using Eq. 2.97 for computing the sound fields owing to a moving source placed above an LR ground. Nevertheless, it is reassuring to show that the same approximate scheme, as shown in Eq. 2.97, can be modified straightforwardly to compute the sound fields above a non-locally reacting ground.

Generally speaking, Eq. 2.97 gives sufficiently accurate solutions for the cases of LR and ER grounds. The difference in the computational results using Eqs. 2.95 and 2.97 is typically less than 0.5 dB for all time steps with a traversing source and a host of different ground parameters. For brevity, these comparisons are not shown here. However, this is not precisely the case when the numerical results for an HB ground are considered. Figure 2.4 shows two sets of comparisons for an ER ground and an HB layered ground. The time histories of the excess attenuation ($EA$) are plotted to illustrate the accuracy of the approximate formula [Eq. 2.97] compared with the D-WVDP formula [Eq. 2.95]. To have a clear presentation of these sets of results, the time scale is shown in the lower abscissa for Fig. 2.4a. The upper abscissa, which is shifted to the left by 0.2 s, is used for Fig. 2.4b. The following parameters are used in Fig. 2.4a. The HB ground has a layer thickness of 0.5 m, source frequency of 400 Hz, and source and receiver heights of 0.5 and of 0.2 m, respectively. The respective parameters of 0.12 m, 100 Hz, 0.6 m, and 0.3 m are used in Fig. 2.4b. For all plots in Fig. 2.4, the same source speed (M = 0.3) and identical ground parameters ($\sigma_0 =$ 5.0 kPa s m $-$ 2, $q^2 = 1.252$, and $\varphi = 0.9$) are used in the numerical simulations. As demonstrated in Ref. [35], the error of using Eq. 2.97 is negligibly small for predicting the sound fields above an LR ground. However, it can be observed from Figs. 2.4a and 2.4b that there are noticeable discrepancies when Eq. 2.97is used to predict the acoustic pressures above an ER ground, but the error is generally less than 0.5 dB for all time steps. The level of discrepancies becomes more acute at some time steps for an HB layered ground. The maximum discrepancy reaches an order of about 3 dB at some time steps, although the approximate solution [Eq. 2.97] agrees quite well with the general trend in the EA predicted by Eq. 2.95.

It is beneficial to isolate the possible bases of errors in Eq. 2.97 when it is used in lieu of Eq. 2.95. Comparisons of Eqs. 2.95 and 2.97 make it clear that both equations have identical $p_A$. The source of errors comes solely from the computation of the GW, the third term in both equations. In fact, the first error is caused by the substitution of the augmented diffraction term A with 1 in Eq. 2.97. The second

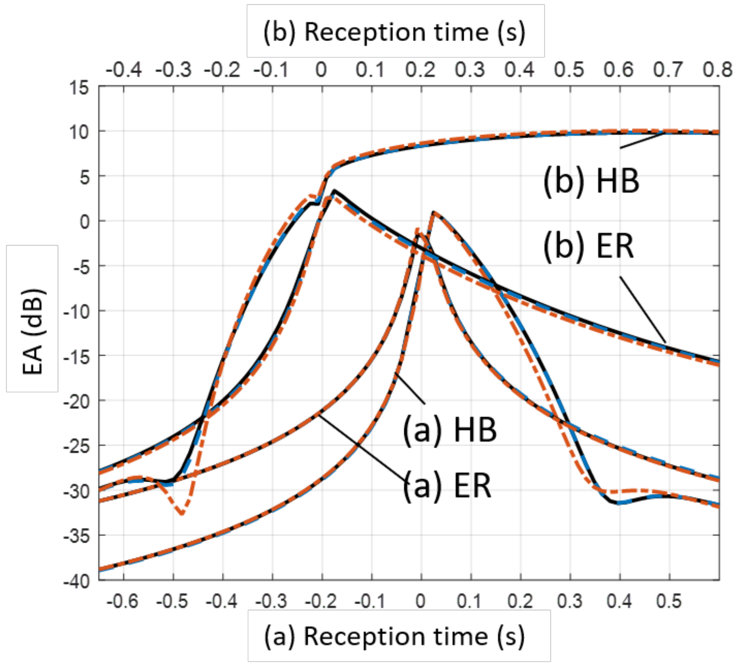


Figure 2.4. Comparisons between time histories of excess attenuation (EA) function of asymptotic solution (dashed lines), approximated solution (dash-dotted lines) and accurate numerical integration solution (solid lines). ER: extended reaction, and HB: hardback layered ground. The x-coordinates of source and receiver are both 0 when reception time is 0. (a) M = 0.3 and source frequency is 400 Hz. The source and receiver heights are set at 0.2 and 0.5 m above the ground. The ground has $\sigma_0$ , $q^2$, and $\varphi$ of 5 kPa m $s-2$ , 1.44, and 0.9, respectively. The HB ground has a layer thickness of 0.05 m. (b) Same Mach number as (a) but the source frequency is 100 Hz. The source and receiver heights are set differently at 0.3 and 0.6 m above the ground. The HB ground has a layer thickness of 0.12 m. The ground parameters are the same as (a) above. Reception time of (b) is shifted left by 0.2 s and uses top abscissa as the scale for reception time.

error is introduced in $F\left(w_p\right)$ because the effective numerical distance w+ is used to replace the apparent numerical distance $w_p$ in the approximation. By defining these two errors as

$$E_1 = 20\log_{10}|A| \tag{2.99}$$

and

$$E_2 = 20\log_{10}\left|F\left(w_p\right)/F\left(w_+\right)\right|, \tag{2.100}$$

respectively, it is instructive to plot the time histories of $E_1$ (dotted lines) and $E_2$ (dash-dotted lines) in Fig. 2.5. The corresponding incident angle in the physical frame, $\theta_+$, is marked at the top abscissa for ease of reference. Three sets of graphs are displayed for (a) an HB ground with a layered thickness of 0.05 m, (b) an ER ground, and (c) an LR ground. In these graphs, the same M, zs, z, and ground parameters are chosen for illustration (see the captions for their details). The EA predictions of $p_A$ (dashed lines) and the GW term (solid) are presented in Fig. 2.6.

To have an obvious error in the approximation calculated with Eq. 2.97, two conditions must be met at the same time. First, the pole must be badly predicted with the approximation, which means E1 or E2 must be at least 1 dB. Second, the magnitude of the GW component must be comparable to that of $p_A$. These two conditions can be easily met for the HB layered ground at frequencies between 100 Hz and 500 Hz. However, for the ER and LR grounds, the contribution of the surface wave component is often too small to influence the total sound fields, although the GW term and A are often poorly approximated.

Validation of the above statements can be found in Fig. 2.5 and Fig. 2.6. The GW contributions, which are considerably smaller in magnitude than $p_A$ in the region of $|\theta_+| < 80°$, can be ignored when the sound fields are calculated. This is illustrated in their respective EA time histories shown in Fig. 2.6. This means that the impacts of $E_1$ and $E_2$ on the calculations of the total fields are not important, although their absolute values can exceed 3 dB in this near-overhead region. The term A can usually be approximated as 1 in the region of $|\theta_+| > 80°$ for a locally reacting ground and an extended reacting ground. However, numerous simulations have suggested that a better agreement can be achieved if $A$ is used instead of 1, especially for a hardback layered ground.

The error $E_2$ deserves more explanation as it involves calculation of the ground wave contributions. The range of variations in $E_2$ is greater when it is compared with that of $E_1$. As noted in Ref. [54], the surface wave is a separate component in the GW term, and it travels parallel and close to the porous ground. Its presence (as long as the surface wave pole is sandwiched between OP and SDP, see Fig. 2.2)d can impact the overall sound fields. As shown in Fig. 2.2a–d, the surface waves are not expected for a source moving above an LR and an ER ground if Eqs. 2.88 and 2.89 are used to model their acoustical characteristics. In the absence of the surface wave, the errors caused by the evaluation of GW components are limited. On the other hand, when the surface wave is present, the error E2 can play a significant role in the prediction of the total fields; see Fig. 2.4a and b. As shown in Fig. 2.5a, a peak is observed in $E_2$ at $\theta_+ \approx -88°$ for the HB layered ground, but there are no obvious peaks for the ER and LR grounds (see Figs. 2.5b and 2.5c) because there are no surface wave components in these two types of ground surfaces.

The magnitude of the GW component is another important factor that influences the total error of the approximation. An example is shown in Fig. 2.6 as follows. The contribution of the GW component is in excess of 10 dB higher for the HB layered ground than those for the ER and LR grounds when the reception time $t > 0$, i.e., the sound field for a receding source. As a result, $E_2$ causes a noticeable error in the total sound field when the approximation scheme is used. This is particularly the case when the reception time is between 0.3 s and 0.4 s; see Fig. 2.4a for the prediction of HB layered ground. As shown in Fig. 2.5b and 2.5c, $E_1$ and $E_2$ have large errors for the ER and LR grounds. However, these errors are not important since the contributions of the GW component are much smaller than $p_A$. Hence, the overall errors in predicting the sound fields for the ER and LR grounds are usually less than 0.5 dB.

It is also noteworthy that the errors in the total sound fields are dependent on the relative locations of the Dopplerized poles and SDP paths. There are cases when the errors in approximating the GW components are higher in the approaching region (i.e., $t < 0$) than the receding region ($t > 0$); see Fig. 2.4b. In general, it is found necessary to use Eq. 2.95 instead of Eq. 2.97 in calculating the sound fields, especially

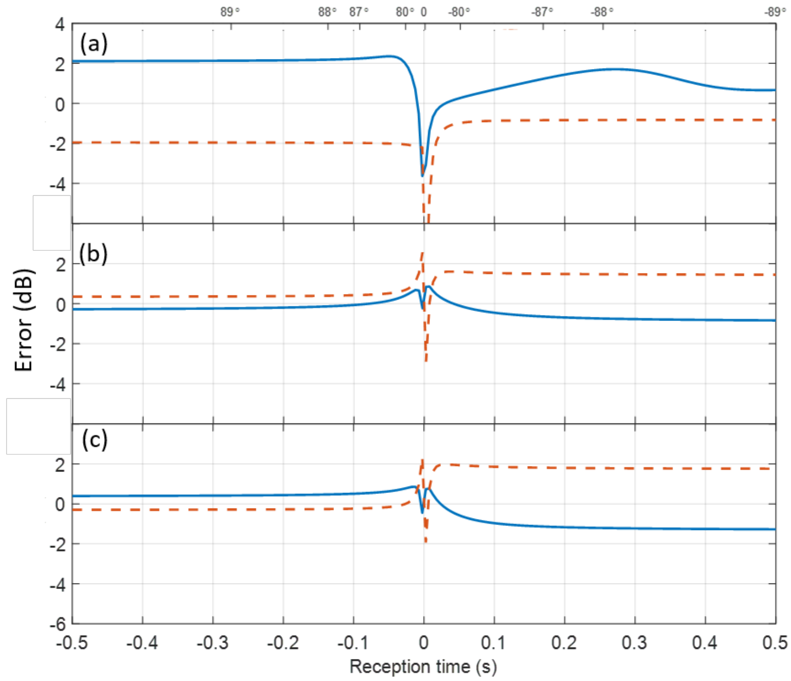


Figure 2.5. Predicted time histories of E1 (dashed lines) and E2 (solid lines) for (a) hard-backed ground, (b) extended reaction ground, and (c) locally reacting ground. Source frequency is 400 Hz. M = 0.3. Source and receiver heights are set, respectively, at 0.2 and 0.5 m above the ground. The x-coordinates of the source and receiver are both 0 when reception time is 0. The layer thickness of hardback ground is 0.05 m. Ground has $\sigma_0$ , $q^2$, and $\varphi$ of 5 kPa m s $-$ 2, 1.44, and 0.9, respectively.

for the case when the surface wave is present. Indeed, it was demonstrated by Albert et al [55,56] for the significance of the surface wave component when they studied the propagation of sound generated by a piston shot over a thin layer of snow. Hence, it becomes evident that the use of the D-WVDP equation is particularly importance for the case when the source translates above a snow-covered ground, forest floors and railway ballast.

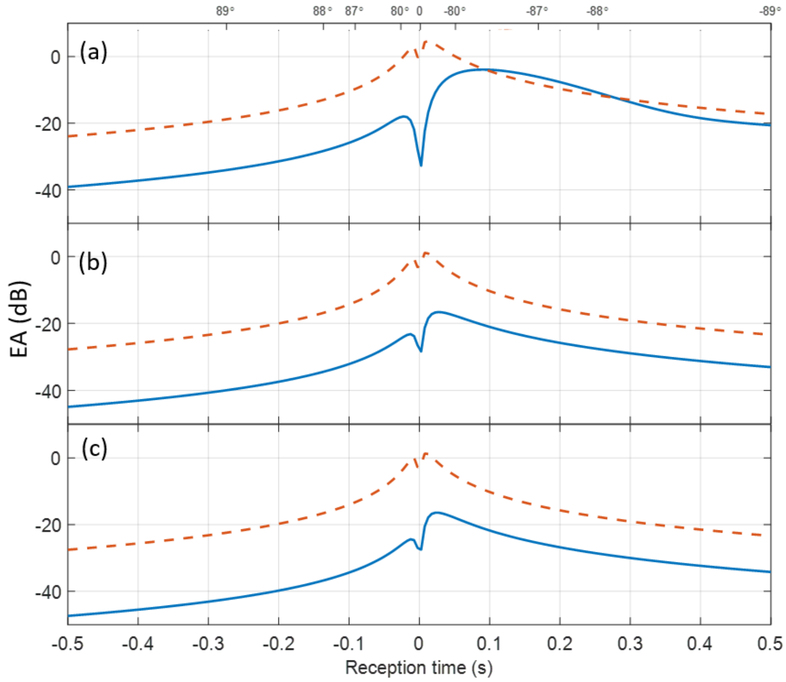


Figure 2.6. Predicted time histories of pA (dashed lines) and the ground wave term (solid lines) for (a) hard-backed ground, (b) extended reaction ground, and (c) locally reacting ground. The geometry, source speed, Mach number and ground properties are the same as those given in Fig. 2.5

## 2.5 Conclusion

An asymptotic formula, which is referred to as the Dopplerized Weyl-Van der Pol (D-WVDP) formula, was derived for predicting sound fields from a line source moving at a constant height above non-locally reacting grounds. Although a Lorentz frame formulation was used in the derivation, the final asymptotic solution was transformed back in the physical frame with no further approximations. The solution was written in emission time geometry where the ground effect was incorporated in the formulation. The Doppler effect not only affects the source frequency but also impacts the acoustical properties of the non-locally reacting ground. In the current study, the Doppler effect on the ground wave term was elucidated, and the surface wave pole was examined for an approaching and receding source. The numerical solutions obtained by the D-WVDP formula were compared with the corresponding numerical solutions calculated by a heuristic approach that assumes a pseudo-stationary source. It was demonstrated that this heuristic approach yields sufficiently accurate numerical solutions for all time steps in the case of a locally reacting or an extended reaction ground. The heuristic approach can predict the general trend of the pressure time histories reasonably well in the case of a hardback layered ground. However, there are regions of disagreement in the predictions of sound fields between the D-WVDP formula and the heuristic formula. The errors in approximating the Dopplerized surface wave pole are the main "culprit" causing these disagreements (up to 3 dB) in the prediction of the total sound fields owing to a source moving at a constant speed.

In this chapter, the sound field due to a line source above non-locally reacting ground is derived with asymptotic method as the first step for other moving source problems. In the next step, the sound field due to a point source is to be found with a similar approach.

# 3. SOUND FIELD ABOVE GROUND DUE TO A MOVING POINT SOURCE

In the last chapter, the sound field above non-locally reacting ground due to a moving line source was solved with method of steepest descent. In this chapter, the line source is change to a point source and the ground surface is changed to both locally reacting and non-locally reacting. The dimension is changed from 2d to 3d, which has much wider applications such as aircraft noise prediction with side-line distance and vehicle noise prediction away from the traveling path. A similar approach is used to solve these problems with a few additional techniques such as invariant of phase function to mach the boundary conditions in the frequency domain. First, the asymptotic model above locally reacting ground is derived. Then, the solution is extended to non-locally reacting ground.

## 3.1 Sound field generated by a 3-dimensional moving mono-pole point source above a locally reacting surface

The sound field generated by a harmonic mono-pole noise source traveling at a constant speed above an impedance ground surface is derived using the method of steepest descent. A Doppler shift (which represents the instantaneous wavefront experienced at particular point on the ground surface due to source motion) is applied to modify the frequency dependent ground impedance. The Doppler factor varies continuously as the source moves past a ground-based receiver. The evaluation of the analytic solution is performed via a modified trapezoid rule summation. An asymptotic solution similar to the classical Weyl-Van der Pol formula for grazing incidence is also proposed and validated against the results obtained in the Fast Field Program (FFP) approach. Due to the asymmetry of the moving source problem, a two-dimensional sound field is desired at each plane of constant elevation. The computationally intensive 2D-FFP algorithm (order N2) can be applied directly to model the full wave equation. But for high elevation sources or at high frequencies, the "exact" method becomes unfeasible. As an alternative, a radial slice approximation can be applied to reduce the computational demands to order N, while achieving similar results. A more efficient solution obtained via asymptotic analysis is proposed in this paper.

### 3.1.1 Introduction

The adverse effect of aircraft noise has been one of the important environmental issues for many decades. High aircraft noise levels can cause hearing impairments, hypertension and sleep disturbances. Recent studies have also suggested that aircraft noise may increase the risk of ischemic heart disease. To better understand the en-route aircraft noise, an accurate numerical model is needed to predict its impact on neighborhood communities. Most of the previous models for the sound fields above a locally reacting ground are based on the assumption that the source is stationary. [4] The ground admittance is therefore constant for a given source frequency. Extending this solution to a moving source, Buret et [57] derived an asymptotic solution assuming that the acoustical properties of the ground surface is only dependent on the source frequency. However, the Doppler effect causes a frequency shift as the source moving past a stationary receiver. Indeed, the wavelength of the harmonic source appears to be 'compressed' for an approaching source. It becomes 'stretched' for a receding source. The well-known Doppler effect has a detrimental effect on the sound waves reflected from a locally reacting ground because its specific normalized admittance will be modified due to the source motion. Ignoring such effect will inevitably introduce a significant error in the prediction of the sound fields, especially for a source traveling at high speeds and locating at low elevations above the ground surface. In a recent study, Ochmann [11] used a simplified ground model and derived an alternative solution for a point source moving above a flat ground with varying admittance. On the other hand, Dragna and Blanc-Benon [35] considered the sound fields due to a line source moving above a locally reacting ground. They obtained a two-dimensional asymptotic solution analogous to those given by Buret but their solution provides a correct interpretation of the frequency-dependent ground model. In this paper, we endeavor to extend Dragna and Blanc-Benon model to three-dimensions, i.e. we consider a point source moving above a locally reacting ground. The Lorentz transform will be used again that converts the moving source problem into a 'standard' monopole located at a stationary point. Section 3.1.2 addresses the formulation and the asymptotic analysis for the sound fields due to a moving source. A brief discussion of the radial-slice fast field formulation (FFP) will also be presented. In Section 3.1.3, we present the numerical validation of the asymptotic formula. Finally, conclusion is offered in Section 3.1.4.

### 3.1.2 Theoretical analysis

Consider a point monopole source of unit strength moving at a constant speed at a constant height z = $z_s$ in the positive x-direction where $c_0$ is the sound speed and M is the Mach number. Suppose that, at time t = 0, the source and receiver are situated, respectively, at rs = (0, 0, $z_s$) and r = (x, y, z). Figure 3.1.2 shows the geometrical configuration of the problem. The ground is located at the z = 0 plane. A similar method based on Dragna and Blanc-Benon [35] is used to include the varying admittance in the theoretical analysis for the three-dimensional sound fields. The governing wave equations for the source moving above a locally reacting plane is given by

$$\frac{\partial p}{\partial t} + \rho_0 c_0 \nabla \cdot u = \rho_0 c_0^2 \delta(x - c_0 M t)\delta(y)\delta(z - z_s)e^{-i\omega_0 t} \tag{3.1}$$

$$\rho_0 \frac{\partial u}{\partial t} + \nabla p = 0 \tag{3.2}$$

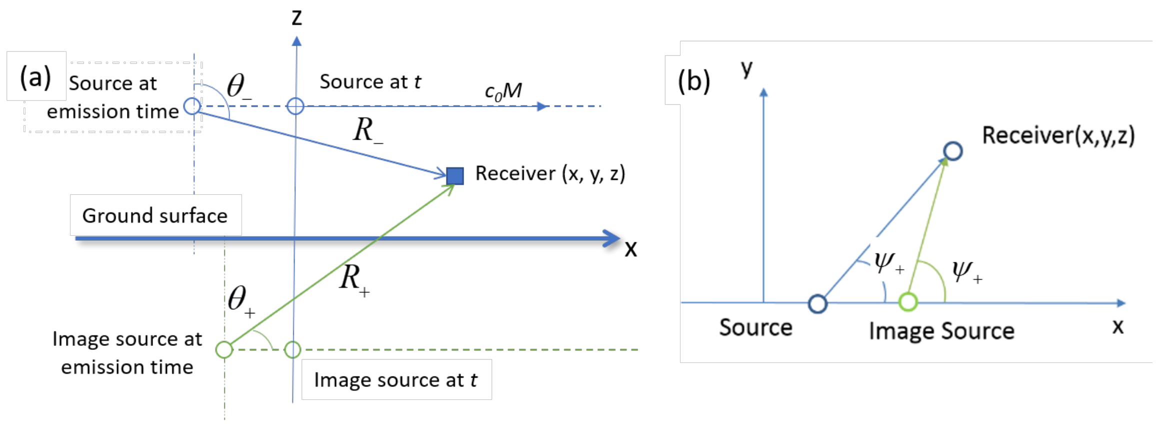


Figure 3.1. A weighting adjusted SPL for different frequencies sound

where p is acoustic pressure, u= (ux, uy, uz) is the particle velocity, $\omega_0$ is the angular frequency of the sound source and $\rho_0$ is the air density. The boundary condition at the ground surface, i.e. at z = 0, is specified by

$$\rho_0 c v_z(x, y, z = 0, t) + \int_{-\infty}^{+\infty} b(u) p(x, y, z = 0, t - u) du = 0 \tag{3.3}$$

where the impulse response b(t) is determined by

$$\beta(\omega) = \int_{-\infty}^{+\infty} b(t) e^{i\omega t} dt \tag{3.4}$$

with $\beta(\omega)$ as the specific normalized admittance of the locally reacting ground, and f is the frequency. We find it more convenient to use an acoustic potential $\phi$ which is defined as $p = -\rho \partial\phi/\partial t$ and $u = \nabla \cdot \phi$ . Using $\phi$ in Eqs. 3.1 and 3.2, we can show that

$$\Delta\phi - \frac{1}{c^2}\frac{\partial^2\phi}{\partial t^2} = \delta(x - cMt)\delta(y)\delta(z - z_s)e^{-i\omega_0 t} \tag{3.5}$$

$$\rho c \frac{\partial}{\partial z}\phi(x, y, z = 0, t) + \int_{-\infty}^{+\infty} b(u) \frac{\partial}{\partial t}\phi(x, y, z = 0, t - u) du = 0 \tag{3.6}$$

Applying the standard Lorentz transform:

$$\begin{aligned}
x_L &= \gamma^2(x - Mct),\\
y_L &= \gamma y,\\
z_L &= \gamma z,\\
t_L &= \gamma^2(t - Mx/c),\\
\gamma &= (1 - M^2)^{-\frac{1}{2}}
\end{aligned} \tag{3.7}$$

and introducing a two-dimensional Fourier transform, the wave equation in Eq. 3.5 can be reduced to a one-dimensional Helmholtz equation:

$$\frac{d^2\hat{\phi}}{d{z_L}^2} + \left({k_0}^2 - {k_x}^2 - {k_y}^2\right)\hat{\phi} = \gamma^2\delta(z_L - z_{Ls}) \tag{3.8}$$

where the subscript L denotes the variables in the Lorentz space, and form the Fourier transform pair:

$$\phi_L(x_L, y_L, z_L) = \frac{1}{4\pi^2}\int_{-\infty}^{+\infty}\int_{-\infty}^{+\infty}\hat{\phi}\left(k_x, k_y, z_L\right)e^{ik_x x_L + ik_y y_L}dk_x dk_y \tag{3.9}$$

$$\hat{\phi}\left(k_x, k_y, z_L\right) = \int_{-\infty}^{+\infty}\int_{-\infty}^{+\infty}\phi_L(x_L, y_L, z_L)e^{-i(k_x x_L + k_y y_L)}dxdy \tag{3.10}$$

The impedance boundary condition, Eq. 3.6, becomes

$$\frac{d\hat{\phi}}{dz_L}(k_x, k_y, z_L = 0) + i(k_0 + k_x M)\gamma\beta[(\omega_0 + k_x cM)\gamma^2]\hat{\phi}(k_x, k_y, z_L = 0) = 0 \tag{3.11}$$

It is tedious but straightforward to show that the solution for the velocity potential has a rather simple form as

$$\hat{\phi} = \frac{\gamma^2}{2ik_z}\left[e^{ik_z|z_L - z_{Ls}|} + R(k_x)e^{ik_z(z_L + z_{Ls})}\right] \tag{3.12}$$

where

$$R(k_x) = \frac{k_z - U}{k_z + U} = 1 - \frac{2U}{k_z + U} \tag{3.13}$$

$$U = (k_0 + Mk_x)\gamma\beta[(\omega_0 + c_0 Mk_x)\gamma^2] \tag{3.14}$$

$$k_z = +\sqrt{k^2 - k_x^2 - k_y^2} \tag{3.15}$$

Substitution of Eq. 3.12 into Eq. 3.9, we can obtain an integral representation of $\varphi$ which can further be split into three terms. The first two terms can be identified as the Sommerfeld integrals for the direct and the image wave contribution. Consequently, the velocity potential $\phi$ becomes

$$\phi(x_L, y_L, z_L) = -\gamma^2 \frac{e^{ik_0 R_{1L}}}{4\pi R_{1L}} - \gamma^2 \frac{e^{ik_0 R_{2L}}}{4\pi R_{2L}} + I_\phi \tag{3.16}$$

where $R_{1L}$ and $R_{2L}$ are the direct distances measured from the source and its image to the receiver in the Lorentz frame. The third term of Eq. 3.16 is often referred as the diffraction integral given by

$$I_\phi = -\frac{1}{2\pi^2} \int\limits_{-\infty}^{+\infty} \int\limits_{-\infty}^{+\infty} \frac{\gamma^2}{ik_z} \frac{k_0 U}{k_z + k_0 U} e^{ik_x x_L + ik_y y_L + ik_{zL}(z+z_s)} dk_x dk_y \tag{3.17}$$

Changing the variables from the rectangular domain to their respective spherical-polar forms [i.e. (kx, ky, kz) $\rightarrow$ (k0, $\mu$, $\psi$) and ($x_L$, $y_L$, $z_L$ ) $\rightarrow$ ( $R_{2L}$, $\theta_L$, $\psi_L$)]:

$$\begin{cases} k_x = k_0 \sin\mu \cos\psi \\ k_y = k_0 \sin\mu \sin\psi \\ k_z = k_0 \cos\mu \end{cases} \tag{3.18}$$

$$\begin{cases} x_L = r_L \cos\psi_L \\ y_L = r_L \sin\psi_L \\ z_L = R_{2L} \cos\theta_L \end{cases} \tag{3.19}$$

making use of $r_L = R_{2L} sin\theta_L$ and the integral expression for the Bessel function, we can simplify the diffraction integral as follows:

$$\begin{aligned} I_\phi = -\frac{\gamma^2}{4\pi i} \int_{-\pi/2+i\infty}^{\pi/2-i\infty} & \frac{\gamma D_L \beta\left(\omega_L\right) \sin\mu}{\cos\mu + \gamma D_L \beta\left(\omega_L\right)} {H_0}^{(1)}(k_0 r_L \sin\mu) \\ & e^{-ik_0 r_L \sin\mu} e^{ik_0 R_{2L} \cos(\mu - \theta_L)} d\mu \end{aligned} \tag{3.20}$$

$$\omega_L = \gamma^2 D_L \omega_0 \tag{3.21}$$

$$D_L(\mu) = 1 + M \sin\mu \cos\psi_L \tag{3.22}$$

Figure 3.1a and 3.1b show the schematic diagram for the corresponding polar and azimuthal angles, $\theta_L$ and $\psi_L$.

The acoustic pressure for the diffraction wave term can then be expressed by using Eq. 3.11 and noting

$$p = -\rho_0 \frac{\partial \phi}{\partial t} = -\rho_0 \gamma^2 \frac{\partial \phi}{\partial t_L} + \rho_0 c_0 M \gamma^2 \frac{\partial \phi}{\partial x_L} \tag{3.23}$$

In the Lorentz frame, the diffraction integral can then be written as

$$I_p = \frac{-\rho_0 \omega_0 \gamma^4 k_0}{4\pi} \int\limits_{-\pi/2+i\infty}^{\pi/2-i\infty} \frac{\gamma {D_L}^2 \beta(\omega_L) \sin\mu}{\cos\mu + \gamma D_L \beta(\omega_L)} {H_0}^{(1)}(k_0 r \sin\mu) e^{ik_0 R_{2L} \cos\mu \cos\theta_L} d\mu \tag{3.24}$$

where the integration path starts at $-\pi/2 + i\infty$, moves through the points $-\pi/2$, $\pi/2$ and ending at $\pi/2 - i\infty$. In the special case of M $\to 0$ and $\gamma^2 \to 1$ , the specific admittance of the ground surface is only dependent on the source frequency $\omega_0$ which remains constant throughout the integration path. A modified Miki model is used to calculate the acoustical properties of the ground surface in which the normalized admittance is calculated by

$$\begin{aligned} &\beta(\omega) = \beta_\infty \tanh(-ik_c l) \\ &\beta_\infty(\omega) = 1/[1 + 0.459(\tfrac{\sigma_0}{-i\rho_0\omega})^{0.632}], \\ &k_c(\omega) = \tfrac{\omega}{c_0}[1 + 0.643(\tfrac{\sigma_0}{-i\rho_0\omega})^{0.632}]. \\ &\omega_L(\mu) = (1 + \sin\mu \cos\psi M)\omega_0\gamma^2 \end{aligned} \tag{3.25}$$

where $\sigma$ is the effective flow resistivity of the ground surface.

There is a pole in the integrand of Eq.3.24 which gives rise to the surface wave pole contribution. The pole location, $\mu_p$ say, is determined by solving a non-linear equation:

$$\cos\mu_p + \gamma\left[1 + M \sin\mu_p \cos\psi_L\right] \beta(\omega_L) = 0 \tag{3.26}$$

where $\beta(\omega_L)$ is calculated by Eq. 3.25. The equation can be solved by means of the Newton-Raphson method. Only the pole lies near the integration path is of interest in our problem, and the other poles have negligible effect on the total sound fields. The diffraction integral, Eq. 3.24, cannot be evaluated analytically to yield an exact solution. However, it can be approximated asymptotically by the method of steepest descent. The details for approximating Eq. 3.24 can be found elsewhere [48] and the details will not be repeated here for brevity. To present the analytic results for validation, it is more expedient to cast the formula in the emission time geometry. Here, the Doppler factor in the emission time $\tau$ (also known as the retarded time) is denoted by $D(\theta_\tau, \psi_{tau})$ where $\theta_t au$ and $\psi_t au$ are the corresponding polar and azimuthal angles in the retarded time $\tau$. Since $D(\theta_{1\tau}\tau, \psi_t au) = D(\theta_L, \psi_L)$, it is possible to show that

$$D\left(\theta_\tau, \psi_\tau\right) = \frac{1}{1 - M \sin\theta_\tau \cos\psi_\tau} = \gamma^2 \left(1 + M \sin\theta_L \cos\psi_L\right) \tag{3.27}$$

We can then specify the Doppler factors for the direct and reflected wave term as $D_1 = D(\theta_{r1}, \psi_L r1)$ and $D_1 = D(\theta_{r2}, \psi_L r2)$ where the subscripts 1 and 2 signify the corresponding parameters for the direct and reflected waves. Application of the inverse Lorentz transform in Eq. 3.16, substitution in Eq. 3.23 and manipulation of the resulting equation yield the acoustic pressure in the emission time geometry:

$$p = p_d + p_i + I_p \tag{3.28}$$

where

$$p_d = -i\rho_0\omega_0 D_{1t}^2 e^{-i\omega_0 t} e^{ik_0 R_{1\tau}} / 4\pi R_{1\tau} \tag{3.29}$$

$$p_i = -i\rho_0\omega_0 D_{2\tau}^2 e^{-i\omega_0 t} e^{ik_0 R_{2\tau}} / 4\pi R_{2\tau} \tag{3.30}$$

The diffraction integral, i.e. the 3rd term of Eq. 3.28, can be evaluated asymptotically to give

$$I_p = -i\rho_0\omega_0 D_{2\tau}^2 e^{-i\omega_0 t}[V_{\theta\tau} - 1 + C(1 - V_{\theta\tau})F(w_a)]\frac{e^{ik_0 R_{2\tau}}}{4\pi R_{2\tau}} \tag{3.31}$$

where

$$V_{\theta\tau} = \frac{\cos\theta_{2\tau} - \beta(\omega_0 D_{2\tau})}{\cos\theta_{2\tau} + \beta(\omega_0 D_{2\tau})} \tag{3.32}$$

$$C = \frac{r_\beta}{r_w} \frac{\sin\mu_p}{\sin\mu_p - \frac{d\beta}{d\mu}\Big|_{\mu=\mu_p}} \frac{1}{\sqrt{\sin\theta_L \sin\mu_p}} \frac{1 + M\cos\psi_L \sin\mu_p}{1 + M\cos\psi_L \sin\theta_L} \tag{3.33}$$

$$\begin{aligned} F(w_a) &= 1 + i\sqrt{\pi} w_a e^{-w_a^2} \mathrm{erfc}\,(-iw_a) \\ w_a^2 &= ikR_{2L}[1 - \cos(\mu_p - \theta_L)] \end{aligned} \tag{3.34}$$

with $\mu_p$ as the solution of Eq. 3.27. The function $F(w_a)$ is often referred as the boundary loss factor and $w_a$ is termed as the numerical distance. In a recent work, [58] C in Eq. 3.31 is approximated as 1. In the current paper, a more accurate value for C is given in Eq. 3.33 where

$$r_\beta = -\cos\mu_p/[\gamma(1 + M\sin\theta_L\cos\psi_L)\beta(\omega_0 D_{2\tau})] \tag{3.35}$$

$$r_\omega = w_a/w_\theta \tag{3.36}$$

$$\omega_\theta = \sqrt{ik_0 R_{2\tau} D_{2\tau}/2}\,[\cos\theta_{2\tau} + \beta(\omega_0 D_{2\tau})] \tag{3.37}$$

Substitution Eqs. 3.29, 3.30 and 3.31 into 3.28 and rearrangement of terms yield an analytical formula for the acoustic pressure of a moving source:

$$p = -i\rho_0\omega_0 e^{-i\omega_0 t}\left\{D_{1\tau}^2 e^{ik_0 R_{1\tau}}/4\pi R_{1\tau} + D_{2\tau}^2\left[V_{\theta\tau} - 1 + C(1 - V_{\theta\tau})F(w_a)\right] e^{ik_0 R_{2\tau}}/4\pi R_{2\tau}\right\} \tag{3.38}$$

For an en-route aircraft, the boundary loss factor $F(w_a)$ is typically negligibly small. Furthermore, the second term in the convective source strength is small compared with the first term. Hence, the acoustic pressure above a locally-reacting ground may be simplified

$$p = \left(-i\rho_0\omega_0 e^{-i\omega_0 t}/4\pi\right)\left[D_{1\tau}^2 e^{ik_0 R_{1\tau}}/R_{1\tau} + V_{\theta\tau} D_{2\tau}^2 e^{ik_0 R_{2\tau}}/R_{2\tau}\right] \tag{3.39}$$

Equations 3.38 and 3.39 are the main results of the current work. They provide an extension to allow predictions of sound fields due to a moving point source. To validate the asymptotic formulas, a radial-slice fast field formulation (FFP) has been developed which follows the suggestions of Wilson [59] who calculated an approximate numerical solution for the three-dimensional sound fields due to a moving point

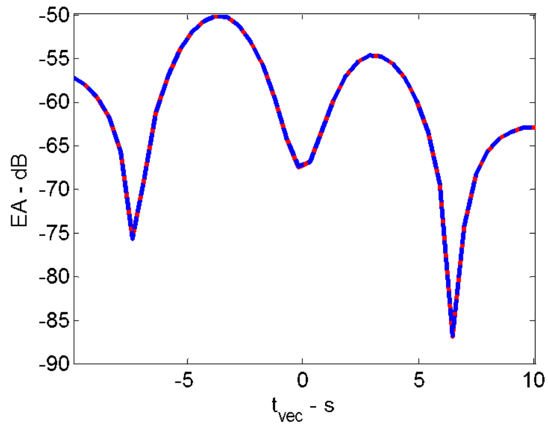


Figure 3.2. (a) and (b) Asymptotic solution compare with radial-slice FFP formulation. Solid (blue): FFP solution; Dash (red): asymptotic solution. The Miki one parameter model for hard-backed ground is used. The effective flow resistivity is 100 kPa sm-2; Mach number is 0.5; sound source frequency is 300 Hz; zs = 1000 m; zr = 1.2 m; material depth=0.01 m. (a) y = 10 m (left plot); (b) y =200 m (right plot).

source. In particular, we apply to the polar representation of the wave equation. The integration over the azimuthal angle is then collapsed into an evaluation at a single angle corresponding to the direct line of sight between the source and the receiver. Thus, the time-consuming two-dimensional integral can then be reduced to a simpler one-dimensional integral. Using this radial-slice approach, we can obtain accurate numerical solutions for validating Eq. 3.38.

### 3.1.3 Result and comparison

In presenting the numerical results, we shall use excess attenuation (EA) which is defined by

$$EA = 20\log_{10}\left[p\Big/\left(\frac{\rho\omega_0}{4\pi}\right)\right] \tag{3.40}$$

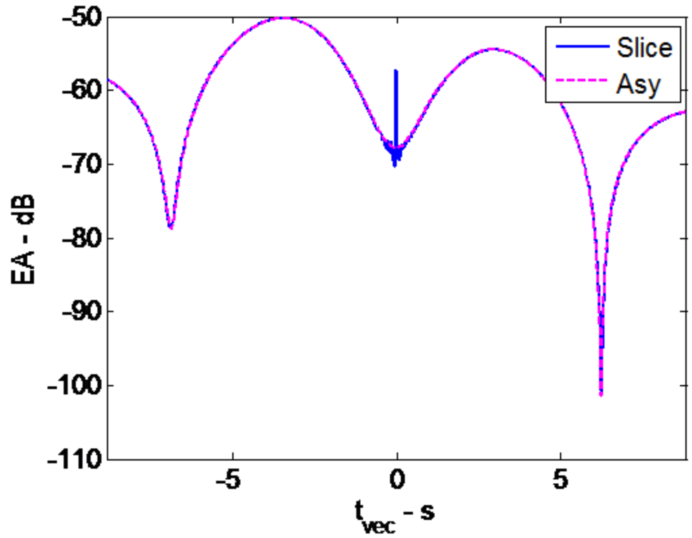


Figure 3.3. Asymptotic solution compare with radial-slice FFP formulation. Solid: FFP solution; Dash: asymptotic solution. The same ground surface and geometry as Fig 1 are used except the offset distance, y = 0.

Figure 3.2(a), 3.2(b) and 3.3 show good agreements between the asymptotic solution Eq. 3.38 and the radial-slice FFP solutions. In the plots, the source and receiver are located at 1000 m and 1.2 m respectively. The source moves with a Mach number of 0.5 and the Miki model hard-back layered model is used to calculate the admittance of the ground surface. The receiver is located at an offset distance of 10 m and 200 m for Fig. 3.2(a) and 3.2(b) but the offset distance is set at y = 0. In this case, the move source is located directly above the receiver at t = 0. We see that the prediction schemes agree in the majority of the time range but the FFP results show significant discrepancies with that predicted by the asymptotic solution. This is because of the assumption used in the FFP formulation that it cannot give accurate solutions when the horizontal range r is close to zero, i.e. at t = 0.

The disagreement in Fig 3.4 shows the difference between frequency varying admittance model and the constant admittance model. The error is neglectable with Mach number 0.1, however, significant with Mach number 0.5. The dashed line ig-

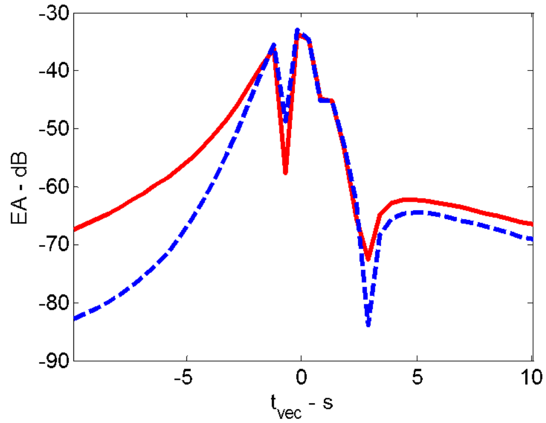


Figure 3.4. Asymptotic result compare with constant ground admittance result. Solid: asymptotic solution; Dash: constant ground admittance result. The Miki one parameter model for hard-backed ground is used. The effective flow resistivity is 100 kPa sm-2; Mach number is 0.5 on the left, 0.1 on the right; sound source frequency is 300 Hz; zs=100 m; zr=1.2 m; y=0; material depth=0.01.

nores the surface wave and the solid line results are based on Equation 3.38. High elevation degenerate the influence of the surface wave term quickly.

An assumption is often made on the admittance of the ground surface: it is evaluated at the source frequency which is kept constant for different time steps. However, the well-known Doppler effect has caused a frequency shift for the moving source. In fact, the source frequency appears to be higher for an approaching source and this apparent frequency is lower when the source recedes. As a result, the apparent admittance of the ground surface varies at different time steps for the source traversing past the receiver. This assumption leads to two approximations in the asymptotic formula. First, the pole location, $\mu_p$, has been approximated by reducing Eq. 3.28 to

$$cos\mu_p + \gamma^2[1 + Msin\mu_p cos\psi_L]\beta(\omega_0) = 0 \tag{3.41}$$

These two approximations in Eq. 3.38 can lead to significant errors in calculating the diffraction integrals especially for the situations with high source speeds and low

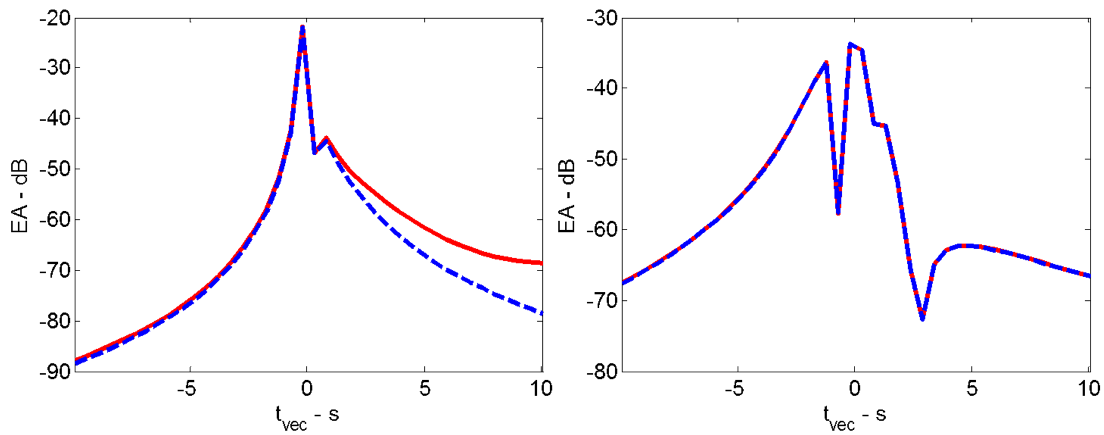


Figure 3.5. Asymptotic solution compare with 1D direct-numerical integration solution. Dash: asymptotic solution without ground wave term; Solid: asymptotic solution. The Miki one parameter model for hard-backed ground is used. The effective flow resistivity is 100 kPa sm-2; Mach number is 0.5; sound source frequency is 300 Hz; zs=10 m in (a) and zs=100 m in (b); y=0; zr=1.2 m; material depth=0.01 m.

source heights.

To illustrate the impact of ignoring the Doppler effect on the apparent ground admittance, we display in Fig. 3.5 the numerical results by using the constant ground admittance model and our new model. In these two plots, the source has Mach numbers of 0.5 and 0.1 respectively. All other parameters are the same as Fig. 3.3. As shown in Fig. 3.2 (the left plot), there are significant errors in predicting the acoustic pressure especially when the source is located at longer ranges. On the other hand, the Doppler effect on the apparent admittance is insignificant if the source speed is low which is shown in Fig. 3.4b (the right plot) with the Mach number of 0.1.

We end this section by showing significance of the ground wave term by comparing the numerical solution obtained by the direct numerical integration scheme with the results predicted by Eq. 3.39. The same ground admittance model and source frequency as Fig. 3.2 are used in the following numerical simulations. The receiver is located at (0, 0, 1.2) m. The source travels at a constant speed at a Mach number of 0.5. Two numerical simulations are presented in Fig. 3.5 with source height at 10 m and 100 m. It can be seen that when the source is close to the ground, the ground wave term becomes important when the receiver is located at a long distance from the moving source, i.e. near-grazing propagation. In addition, there is no numerical instability for the direct numerical scheme (near the region of t = 0) as compared with the FFP solution shown in Fig. 3.3.

### 3.1.4 Conclusion

An asymptotic model for homogeneous 3D moving source above a locally reactive ground has been derived with Lorentz transform and steepest descent method. The frequency varying ground property has been implemented. The good agreement with results calculated from direct numerical integration and the radial slice approximation validates the asymptotic model. A further approximation has been shown to be valid for high elevation condition, which is enough for prediction of the noise emitted by en-route aircraft. The comparison between the approximation and the direct numerical integration proved the accuracy of the model. A suggestion for the future work is the analysis of the extended-reaction ground. The boundary condition for extended-reaction requires different treatment from the current method due to the complicated boundary condition equation in the Lorentz frame.

## 3.2 Sound field generated by a 3-dimensional moving mono-pole point source above a non-locally reacting surface

In the derivation of the asymptotic solution for moving source above locally reacting ground, the solution is derived mostly in the Lorentz frame. In Section 3.2, the analysis for non-locally reacting ground has several important improvements. First, the new model makes the fast evaluation of the sound field above non-locally reacting ground due to a moving mono-pole source possible. Second, a new technique is used to match the boundary condition, which can be useful in other studies as well. Third, the Doppler's factors in each frame (ordinary frame, Lorentz frame and emission frame) are expressed with a unified expression, which makes each expression much easier to understand.

### 3.2.1 Difference between locally reacting and non-locally reacting ground for moving source

The only difference between a locally reacting ground and non-locally reacting ground is that for locally reacting ground, the ground admittance is independent of the incident angle, however, for non-locally reacting ground, the ground admittance depends on the incident angle. It means that in the modeling of the non-locally reacting problems, both the above ground medium and below ground medium need to be modeled with Helmholtz equations. And for moving source problems, the boundary condition of non-locally reacting ground becomes even more complicated due to the change of sound frequency.

One of the most challenging problem in the modeling process is that the boundary condition above the ground is usually written in the Lorentz frame to simplify the governing equation and the boundary condition below the ground is usually written in the ordinary reception time frame. The method to match the boundary conditions used for a stationary source cannot be used here since the above and below ground parts are in different frames. In Chapter 2, the boundary condition was matched with method of convolution. In this chapter, a different method based on 'invariant of phase function' [60, 61] is used to couple the above and below ground mediums on the air-ground interface. This method gives more physical understandings compared to the method of convolution and can be applied to other types of even more complicated problems such as the sound field above multi-layered ground.

### 3.2.2 Theory

**Formulation of the problem**

In a 3-dimensional space-time rectangular coordinate system $(x, y, z, t)$, a point mono-pole source of unit strength translates horizontally in the x direction at a constant velocity of $c_0 M$. Here, $M = (M, 0, 0)$ and $c_0$ is the speed of sound above the ground, while $M\ (< 1)$ is the magnitude of the Mach number. A rigid porous ground is assumed to be homogeneous and located at the $z = 0$ plane. Suppose that the source, which moves at a constant height $z_s$ in the upper medium, passes through the point (0, 0, zs) at the time $t = 0$. Air has a constant density $\rho_0$ in the upper medium $(z > 0)$ and the rigid porous ground has complex density, and sound speed of $\rho_1$ and $c_1$, respectively, in the lower medium $(z < 0)$. Figure 1 shows the geometrical configuration of the problem. Also shown in the diagram, $R_\mp$ are the respective distances measured from the moving source and its image to the receiver at the respective retarded (emission) times, $\tau_\mp$. In the following paragraphs, the subscripts – and + will be used to denote the corresponding parameters for the source and image source.

Introducing an acoustic potential function $\phi(r, z, t)$ in the upper medium, the acoustic pressure $p(r, z, t)$ and particle velocity $u(r, z, t)$ are defined by

$$p(r, z, t) = -\rho_0\, \partial\phi(r, z, t)/\partial t, \tag{3.42}$$

and

$$u(r, z, t) = \nabla\phi(r, z, t), \tag{3.43}$$

where $r[\equiv (x, y)]$ represents the horizontal position vector at the reception time t and $\nabla$ is the spatial derivatives in the physical frame. With the point mono-pole source located at $S = (c_0 M t, 0, z_s)$, the space-time wave equation can be written in terms of $\phi_0$ as [4]

$$\nabla^2\phi_0 - \frac{1}{c_0^2}\frac{\partial^2\phi_0}{\partial t^2} = \mathrm{e}^{-i\omega_s t}\delta(x - c_0 M t)\delta(y)\delta(z - z_s) \tag{3.44}$$

where $\nabla^2 \equiv \partial^2/\partial x^2 + \partial^2/\partial y^2 + \partial^2/\partial z^2$ is the Laplacian operator, $\delta$ is the Dirac delta function and $\omega_s$ is the angular frequency of the source. In addition to the governing wave equation, the boundary conditions at the ground (i.e. $z = 0$) also affect the final form of the solution for Eq. 3.44. The appropriate boundary conditions will be presented after the discussions of the integral solution for Eq. 3.44.

The following linear transformations are used between the physical frame $(r, z, t)$ and the Lorentz frame $(r_L, z_L, t_L)$:

$$(r_L, z_L, t_L)^T = \gamma^2 \begin{pmatrix} 1 & 0 & 0 & -c_0 M \\ 0 & 1/\gamma & 0 & 0 \\ 0 & 0 & 1/\gamma & 0 \\ -M/c_0 & 0 & 0 & 1 \end{pmatrix} (r, z, t)^T, \tag{3.45}$$

$$(r, z, t)^T = \begin{pmatrix} 1 & 0 & 0 & c_0 M \\ 0 & 1/\gamma & 0 & 0 \\ 0 & 0 & 1/\gamma & 0 \\ M/c_0 & 0 & 0 & 1 \end{pmatrix} (r_L, z_L, t_L)^T \tag{3.46}$$

where $\gamma = 1/\sqrt{1-M^2}$ and the subscript L denotes the corresponding parameters in the Lorentz frame, and the solution for

$$\phi_0(r, z, t) \, [\equiv \phi_L(r_L, z_L, t_L)]$$

can be written in an integral form as

$$\phi_0 = \frac{1}{(2\pi)^3} \int_{-\infty}^{\infty} \int_{-\infty}^{\infty} \int_{-\infty}^{\infty} \hat{\phi}_0 e^{i(k_x x + k_y y - \omega t)} dk_x dk_y d\omega \tag{3.47}$$

or

$$\phi_L = \frac{1}{(2\pi)^3} \int_{-\infty}^{\infty} \int_{-\infty}^{\infty} \int_{-\infty}^{\infty} \hat{\phi}_L e^{i(L_x x_L + L_y y_L - \omega_L t_L)} dL_x dL_y d\omega_L, \tag{3.48}$$

where $\phi_0(r, z, t)$ and $\hat{\phi}_0(k_r, z, \omega)$ form a Fourier transform pair in the physical frame with $k_r \equiv (k_x, k_y)$ as the horizontal wave vector, $k_r$ as its magnitude and $\omega \in [0, \infty)$ as the angular frequency. Similarly, $\phi_L(r_L, z_L, t)$ and $\hat{\phi}_L(L, z, \omega_L)$ are the Fourier transform pair in the Lorentz frame where the associated horizontal wave vector, its magnitude, and angular frequency are $Lr \equiv (L_x, L_y), L_r$ and $\omega_L$, respectively. These two transform variables, $\hat{\phi}_0(k_r, z, \omega)$ and $\hat{\phi}_L(L_r, z, \omega_L)$, can be expressed respectively as

$$\hat{\phi}_0 = \int_{-\infty}^{\infty}\int_{-\infty}^{\infty}\int_{-\infty}^{\infty} \phi_0 e^{-i(k_x x + k_y y - \omega t)} dx dy dt \tag{3.49}$$

$$\hat{\phi}_L = \int_{-\infty}^{\infty}\int_{-\infty}^{\infty}\int_{-\infty}^{\infty} \phi_L e^{-i(L_x x_L + L_y y_L - \omega_L t_L)} dx_L dy_L dt_L. \tag{3.50}$$

Applying the Lorentz transform [Eq. 3.45] in Eqs. 3.42 and 3.46 and using the Fourier transformation [Eq. 3.50], it is straightforward to reduce the space-time wave equation to a second-order ordinary differential equation in terms of $z_L$ as an independent variable:

$$\frac{\partial^2 \hat{\phi}_L}{\partial z_L^2} + L_z^2 \hat{\phi}_L = 2\pi\gamma^2 \delta(z_L - z_{Ls})\delta(\omega_L - \omega_s), \tag{3.51}$$

where $k_L$ $(= \omega_L/c_0)$ is the wave number, $L_z$ $\left(= +\sqrt{k_L^2 - L_r^2}\right)$ is the vertical component and $L_r$ is the horizontal component of the wave vector in the Lorentz frame. The solution for Eq. 3.51 is simply given by

$$\hat{\phi}_L = \frac{\pi\gamma^2}{iL_z}\left[e^{iL_z \Delta z_{L-}} + V_L(L_r, \rho_1, c_1)e^{iL_z \Delta z_{L+}}\right]\delta\left(\omega_L - \omega_s\right) \tag{3.52}$$

where $\Delta z_{L\mp} = |z_L \mp z_{Ls}|$ is the vertical height difference from the source and its image to the receiver , and $V_L(L_r, \rho_1, c_1)$ refers to the plane wave reflection factor in the Lorentz frame. The plane wave reflection factor can be determined from the boundary conditions stipulated at $z = 0$ where the acoustical properties of the ground ($\rho_1$ and $c_1$) are introduced to model the interactions of the sound waves within the air/ground interface.

An substitution of Eq. 3.52 into Eq. 3.48 and an evaluation of the inverse Fourier integral lead to an expression for determining $\phi_L(r_L, z_L, t_L)$. Applying the linear transformation [Eq. 3.46] and using Eq. 3.42, the acoustic pressure from a source moving above a rigid porous ground can then be determined in the physical frame, i.e., $p(r, z, t)$. However, the plane wave reflection factor $V_L$ [see Eq. 3.51] is required in order to use this scheme. The determination of $V_L$ will be addressed in the next section.

**Imposition of the boundary conditions**

In the rigid porous ground at the lower medium (z ¡ 0), the corresponding acoustic potential $\phi_1(r, z, t)$ can be obtained from the space-time wave equation:

$$\nabla^2 \phi_1 - \frac{1}{c_1^2} \frac{\partial^2 \phi_1}{\partial t^2} = 0. \tag{3.53}$$

Furthermore, $\phi_1(k_r, z, \omega)$ can also be written in terms of its Fourier transform, $\hat{\phi}_1(k_r, z, \omega)$, as

$$\phi_1 = \frac{1}{(2\pi)^3} \int_{-\infty}^{\infty} \int_{-\infty}^{\infty} \int_{-\infty}^{\infty} \hat{\phi}_1 e^{i(k_x x + k_y y - \omega t)} dk_x dk_y d\omega. \tag{3.54}$$

The subscript 1 is used to denote the variables for the rigid porous ground in Eqs. 3.53 and 3.54. The acoustic pressure $p_1(r, z, t)$ and particle velocity $u_1(r, z, t)$ can be found by using Eqs. 3.42 and 3.42 analogously, i.e. the subscript 0 is replaced with 1 in the related equations if the rigid porous ground is considered. It is remarkable that $\phi_1$ and $\hat{\phi}_1$ are the Fourier transform pair of the acoustic potential for the rigid porous ground, are are comparable to $\phi_0$ and $\hat{\phi}_0$ [Eqs. 3.47 and 3.49] for air in the upper medium. Using a similar approach according to the last section, the solution for $\phi_1$ (with $z \leq 0$) in Eq. 3.53 can be written as

$$\hat{\phi}_1 = T(k_r, \rho_1, c_1) e^{-i\sqrt{k_1^2 - k_r^2} z} \tag{3.55}$$

where $k_1\,(= \omega/c_1)$ is the wave number of the rigid porous ground and $T(k_r, \rho_1, c_1)$ refers to the plane wave transmission factor in the physical frame. [4]

The unknown parameters $V_L$ in Eq. 3.52 and $T$ in Eq. 3.55 can now be determined by matching (i) the acoustic pressure, and (ii) the vertical particle velocity, across the air/ground interface at z = 0. The acoustic potential for the upper medium is given in the Lorentz frame (see Eqs. 3.50 and 3.52]. Consequently, there is a need to transform its wave vector from the Lorentz space of $(L_r, \omega_L)$ to that of the physical space, i.e., $(k_r, \omega)$ so that the boundary conditions can be matched accurately at the z = 0 plane.

The property of the phase invariant of waves among different inertial frames, [60, 61] requires that

$$k_x x + k_y y - \omega\, t = L_x x_L + L_y y_L - \omega_L t_L, \tag{3.56}$$

for the plane waves in the z = 0 plane. By using Eq. 3.46, $x, y$ and $t$ on the right side of Eq. 3.56 can be replaced with $x_L$, $y_L$ and $t_L$. It follows then immediately that

$$\begin{pmatrix} k_x \\ k_y \\ \omega \end{pmatrix} = \gamma^2 \begin{pmatrix} 1 & 0 & M/c_0 \\ 0 & 1/\gamma & 0 \\ c_0 M & 0 & 1 \end{pmatrix} \begin{pmatrix} L_x \\ L_y \\ \omega_L \end{pmatrix} \tag{3.57}$$

and the inversion of Eq. 3.57 yields

$$\begin{pmatrix} L_x \\ L_y \\ \omega_L \end{pmatrix} = \begin{pmatrix} 1 & 0 & -M/c_0 \\ 0 & 1/\gamma & 0 \\ -c_0 M & 0 & 1 \end{pmatrix} \begin{pmatrix} k_x \\ k_y \\ \omega \end{pmatrix}. \tag{3.58}$$

Hence, the Jacobian of the transformation, $|\partial(k_x, k_y, \omega)/\partial(L_x, L_y, \omega_L)|$, can be evaluated to give $\gamma^{-3}$. The vertical wave vector in the Lorentz space, $L_z$ can then be expressed in a simplified form in terms of the physical space as:

$$L_z = +\sqrt{k_L^2 - L_r^2} = k_z/\gamma, \tag{3.59a}$$

where

$$k_z = +\sqrt{k_0^2 - k_r^2} \tag{3.59b}$$

and $k_0 = \omega/c_0$ is the total wave number in the physical space. The use of the Lorentz transformation in the wavenumber spaces [Eqs. 3.57 and 3.58] will benefit the subsequent formulation of the problem of a moving source above a rigid porous ground surface.

The acoustic potential, $\phi_0(r,z,t)\,[\equiv \phi_L(r_L,z_L,t_L)]$, can therefore be expressed in the physical space through by using Eqs. 3.50, 3.52, 3.58, 3.59 and the Jacobian of the transformation to yield

$$\phi_0(r,z,t) = \frac{1}{(2\pi)^2}\int\limits_{-\infty}^{\infty}\int\limits_{-\infty}^{\infty}\int\limits_{-\infty}^{\infty}\frac{\delta\left(\omega-\omega_s\Omega_k\right)\left[e^{ik_z\Delta z_-}+Ve^{ik_z\Delta z_+}\right]}{2ik_z}\,e^{i(k_x x+k_y y-\omega t)}\,dk_x dk_y d\omega, \tag{3.60}$$

where the respective height differences are $\Delta z_{\mp} = |z \mp z_s|$ in the physical frame, $V\left(k_r,\rho_1,c_1\right)[\equiv V_L\left(L_r,\rho_1,c_1\right)]$ is the plane wave reflection factor in the physical space, $k = (k_r,k_z)$ is the wave vector, $k_s = \omega_s/c_0$ is the wave number of the source in air and the Dopplerized function $\Omega_k$ is given by

$$\Omega_k = \Omega\left(k\right) = 1 + Mk_x/k_s \tag{3.61}$$

Here, it is convenient to define two associated Doppler functions, $\Omega(X)$ and $D(X)$, as follows:

$$\Omega_X = \Omega(X) = \left(1 + M\cdot\hat{X}\right), \tag{3.62}$$

and

$$D_X = D(X) = \left(1 - M\cdot\hat{X}\right)^{-1}, \tag{3.63}$$

where the caret in the argument X denotes its unit vector, i.e. $\hat{X} = X/|X|$. The Doppler function $\Omega_X$ is used in Eq. 3.61 and the other Doppler function $D_X$ will be used later when the solution is derived in the emission time frame.

At the $z = 0$ plane, the surface acoustic pressure $p_s(r,t)$ and the normal surface particle velocity $u_s(r,t)$ can therefore be written in terms of $\phi_0(r,0,t)$ as

$$p_s(r,t) = \frac{\rho_0}{(2\pi)^2}\int\limits_{-\infty}^{\infty}\int\limits_{-\infty}^{\infty}\int\limits_{-\infty}^{\infty}\frac{\omega\left(V+1\right)e^{i(k_z z_s+k_x x+k_y y-\omega t)}}{2k_z}\,\delta\left(\omega-\omega_s\Omega_k\right)dk_x dk_y d\omega, \tag{3.64}$$

$$u_s(r,t) = \frac{1}{(2\pi)^2}\int\limits_{-\infty}^{\infty}\int\limits_{-\infty}^{\infty}\int\limits_{-\infty}^{\infty}\frac{\left(V-1\right)e^{i(k_z z_s+k_x x+k_y y-\omega t)}}{2k_z}\delta\left(\omega-\omega_s\Omega_k\right)dk_x dk_y d\omega. \tag{3.65}$$

Considering the lower medium, $p_s(r,t)$ and $u_s(r,t)$ can also be evaluated in terms of Eq. 3.55 as

$$p_s(r,t) = \frac{1}{(2\pi)^3} \int_{-\infty}^{\infty} \int_{-\infty}^{\infty} \int_{-\infty}^{\infty} i\omega\rho_1 T e^{i(k_x x + k_y y - \omega t)} dk_x dk_y d\omega, \tag{3.66}$$

$$u_s(r,t) = -\frac{1}{(2\pi)^3} \int_{-\infty}^{\infty} \int_{-\infty}^{\infty} \int_{-\infty}^{\infty} \sqrt{k_1^2 - k_r^2} T e^{i(k_x x + k_y y - \omega t)} dk_x dk_y d\omega. \tag{3.67}$$

By comparing Eq. (17a) with Eq. (18a) and Eq. (17b) with Eq. (18b), V and T can be determined by equating the integrands of these two pairs of the associated equations. In particular, V can be determined from these equations for a rigid porous ground as follows:

$$V = \frac{L_z - k_s \Omega_k \beta(k_0, k_r)}{L_z + k_s \Omega_k \beta(k_0, k_r)}, \tag{3.68}$$

where $\beta(k_0, k_r)$ is the normalized admittance of the ground. The appropriate function for $\beta(k_0, k_r)$ used on different types of ground will be addressed later.

Substituting Eqs. 3.60, 3.61 and 3.68 into Eq. 3.42, the acoustic pressure in air can be written as a sum of contributions from three terms:

$$p_0(r,z,t) = p_-(r,z,t) + p_+(r,z,t) + I_b(r,z,t), \tag{3.69}$$

where

$$p_{\mp} = \frac{\rho_0}{8\pi^2} \int_{-\infty}^{\infty} \int_{-\infty}^{\infty} \int_{-\infty}^{\infty} \frac{\omega}{k_z} \delta\left(\omega - \omega_s \Omega_k\right) e^{i[k_x x + k_y y + k_z \Delta z_{\mp} - \omega t]}\, dk_x dk_y d\omega, \tag{3.70}$$

and

$$I_b = -\frac{\rho_0}{8\pi^2} \int_{-\infty}^{\infty} \int_{-\infty}^{\infty} \int_{-\infty}^{\infty} \frac{\omega}{k_z} \frac{2k_s \Omega_k \beta(k_0, k_r) \delta\left(\omega - \omega_s \Omega_k\right)}{[k_z + k_s \Omega_k \beta(k_0, k_r)]}\, e^{i[k_x x + k_y y + k_z \Delta z_{+} - \omega t]}\, dk_x dk_y d\omega. \tag{3.71}$$

The first two terms of Eq. 3.69 are the spherical wave contributions from the source and the image source (with the subscripts – and + respectively), which can be specified collectively in Eq. 3.70. The third term accounts for the effect of the finite impedance of the rigid porous ground.

An examination of Eq. 3.71 reveals that the outer integral with respect to $\omega$ can be evaluated immediately with $\omega$ replaced by $\omega_s\Omega_k$. Hence, $k_0$ becomes $k_s\Omega_k$. The normalized admittance of the ground is a parameter that is dependent on the density ratio, $\zeta(k_D) = \rho_0/\rho_1(k_D)$, the index of refraction, $n(k_D) = c_0/c_1(k_D)$ and the layer thickness, d, of the rigid porous ground. By employing use of a scalar argument X and another vector argument Y $\equiv (Y_1, Y_2)$ with its magnitude of Y, the normalized admittance can be expressed in a generalized form as [48]

$$\beta(X,Y) = -i\zeta(X)\sqrt{n^2(X) - (Y/X)^2}\tan(X\sqrt{n^2(Y) - (Y/X)^2}d) \tag{3.72}$$

for a hardback rigid porous ground with a layer thickness of $d$, and

$$\beta(X,Y) = \zeta(X)\sqrt{n^2(X) - (Y/X)^2} \tag{3.73}$$

for a semi-infinite rigid porous ground (or the so-called extended reaction ground) with $d \to \infty$. In the special case of a locally reacting ground where $n(\omega) \to \infty$, Eq. 3.73 can be reduced to

$$\beta(X,Y) = \zeta(X)n(X). \tag{3.74}$$

Thus $\beta(k_0, k_r)$ in Eq. 3.73 is now evaluated at $\beta(\omega_s\Omega_k, k_r)$. In the LR ground, the product of $\zeta(\omega_s\Omega_k)$ and $n(\omega_s\Omega_k)$ is independent of the wave vectors $k_r$.

### Asymptotic solution in the physical frame

As reported by Morse and Ingards, [42] the integrals 3.70 can be evaluated more conveniently in the Lorentz frame. The respective solutions can then be transformed back to the emission (retarded) time frame. To facilitate the presentation of the results, it is convenient to define a term related to the Doppler factors $D_\mp \equiv D(\hat{R}_\mp)$ at the retarded times where the Doppler function, $D(\hat{R}_\mp)$, is given in Eq. 3.63. The terms, $\hat{R}_-$ and $\hat{R}_+$, are the respective unit vectors pointing from the source, $S_-=$ $(c_0M\tau_-, 0, z_s)$, and the image source, $S_+=$ $(c_0M\tau_+, 0, -z_s)$, to the receiver $(r, z)$.

The corresponding retarded times, $\tau_\mp$, are related to the time $t$ (also referred as the reception time) as follows

$$\tau_\mp = t - R_\mp / c_0 \tag{3.75}$$

where $R_\mp$ are the path lengths of the ray linking the source and its image to the receiver. In Eq. 3.70, the acoustic pressures can therefore be expressed in a compact form as

$$p_\mp = -i\rho_0\omega_s D_\mp^2 e^{-i(\omega_s t - k_s R_\mp)} \big/ 4\pi R_\mp . \tag{3.76}$$

It is remarkable that $\tau_-$ is necessarily different from $\tau_+$ for the same reception time $t$ because $R_+ > R_-$unless either the moving source or the receiver is located on the ground at $z = 0$.

The next step involves the evaluation of the integral given in Eq. 3.71. Generally, there is no exact expression for the integral but it can be approximated accurately by means of the steepest descent method leading to a uniform asymptotic solution. Again, the derivation of the asymptotic solution is best addressed in the Lorentz frame. A substitution of Eq. 3.57 into Eq. 3.71, the evaluation of the outer integral with respect to $\omega_L$ and the rearrangement of the resulting expressions yield

$$\frac{I_b}{\rho_0 c_0} = \frac{-\gamma^2 k_s e^{-i\omega_s t_L}}{4\pi^2} \int\limits_{-\infty}^{\infty} \int\limits_{-\infty}^{\infty} \frac{\gamma^3 k_s \Omega_L^2 \beta(\gamma^2 k_s \Omega_L, \gamma^2 k_s \Gamma_r) e^{i(L_x x_L + L_y y_L + \gamma L_z \Delta z_+)}}{L_z \left[L_z + \gamma k_s \Omega_L \beta(\gamma^2 k_s \Omega_L, \gamma^2 k_s \Gamma_r)\right]} dL_x dL_y, \tag{3.77}$$

where the vertical component of the wave vector in the Lorentz frame becomes

$$L_z = +\sqrt{k_s^2 - L_r^2}, \tag{3.78}$$

and the Doppler function $\Omega_L \equiv \Omega(L)$ is defined in Eq. 3.62.

In Eq. 3.77, $\beta(\gamma^2 k_s \Omega_L, \gamma^2 k_s \Gamma_r)$is evaluated by using Eq. 3.72-3.74 accordingly, $\Gamma_r\,[\equiv (\Gamma_x, \Gamma_y)]$ is obtained by applying Eq. 3.57 and $\omega_L$is then replaced by $\omega_s$ to yield,

$$\begin{cases} \Gamma_x = (k_x/k_s)\big|_{\omega_L = \omega_s} = L_x/k_s + M \\ \Gamma_y = (k_y/k_s)\big|_{\omega_L = \omega_s} = L_y/(\gamma k_s) \end{cases}, \tag{3.79}$$

where $\Gamma_x$ and $\Gamma_y$ are referred to as the spatial Doppler functions in the Lorentz frame along the x and y axes respectively. [see 2d non-locally solution in the previous chapter]

For a fixed $t_L$, the evaluation of the integral in Eq. 3.77 can be facilitated using a spherical polar coordinate system centering on the location of the image source. In the Lorentz frame, the receiver location is specified by $d_+ = (d_+, \psi_L, \theta_L)$, where $d_+$ is the radial length, and $\psi_L$ and $\theta_L$ are the azimuthal angle and polar angle respectively. Similarly, the wave vector L $=(L_x, L_y, L_z)$ is represented as $(k_s, \varepsilon_L, \mu_L)$ in the spherical polar coordinates. Hence, $dL_x dL_y = k_s^2 \cos\mu_L \sin\mu_L d\varepsilon_L d\mu_L$ and the Doppler function, $\Omega_L$, can be expressed as

$$\Omega_L \equiv \Omega(L) = 1 + M\cos\varepsilon_L \sin\mu_L, \tag{3.80}$$

By changing the coordinate systems and evaluating the integral asymptotically with respect to $\varepsilon_L$, Eq. (24a) can be simplified to

$$\frac{I_b}{\rho_0 c_0} = \frac{-\gamma^2 {k_s}^2 e^{-i(\omega_s t_L - k_s d_+)}}{4\pi} \int\limits_{C_L} \sqrt{\frac{\sin\mu_L}{2i\pi k_s r_L}} F_L\left(\psi_L, \mu_L\right) e^{ik_s R_L(\cos(\mu_L - \theta_L) - 1)} d\mu_L \tag{3.81}$$

where $F_L\left(\psi_L, \mu_L\right)$ is referred to as the boundary function:

$$F_L\left(\psi_L, \mu_L\right) = \frac{2\gamma^3\,\Omega_L^2 \beta(\gamma^2 k_s \Omega_L, \gamma^2 k_s \Gamma_r)}{\cos\mu_L + \gamma\,\Omega_L \beta(\gamma^2 k_s \Omega_L, \gamma^2 k_s \Gamma_r)}, \tag{3.82}$$

$r_L = d_+ \sin\theta_L$, and the variables, $\Omega_L$and $\beta$, in the kernel function are now evaluated at $\varepsilon_L = \psi_L$, Taking $\Gamma_r \equiv |\Gamma_r|$ as the horizontal component of the spatial Doppler function, it can be expressed in terms of the polar coordinates as

$$\Gamma_r = \sqrt{\left(M + \cos\psi_L \sin\mu_L\right)^2 + \left(\sin\psi_L \sin\mu_L / gamma\right)^2}, \tag{3.83}$$

by noting Eq. 3.79. Generally, $\Gamma_r$ cannot be simplified further in the Lorentz frame. The integration path, $C_L$, of Eq. 3.81 follows the contour from $\mu_L = -\pi/2 + i\infty$ to $\pi/2 - i\infty$ via the points $(-\pi/2, 0)$, $(0, 0)$ and $(\pi/2, 0)$ in the complex $\mu_L-$ plane. The integral of Eq. 3.81 can be approximated asymptotically by means of the steepest descent method where the saddle path $C_S$ can be found by setting the real part of the phase function to zero, i.e., $\mathrm{Re}\left(1-\cos\left(\mu_p-\theta_L\right)\right)$. Details of the saddle path analysis can be found in Ref. [7, 48]

The emission time geometry is typically needed for a physically interpretable solution. At the emission time $\tau_+$, the physical path length of the reflected ray path can be established by centering at the location of the image source. Hence, the receiver can be specified in terms of the spherical polar coordinate as $R_+ = (R_+, \psi_+, \theta_+)$ where $\psi_+$ and $\theta_+$ are the respective azimuthal and polar angles in the emission time frame. By geometrical consideration, [57] $d_+$ and $R_+$ are related by

$$\cos\psi_L \sin\theta_L = D_+ \left(\cos\psi_+ \sin\theta_+ - M\right), \tag{3.84}$$

$$\sin\psi_L \sin\theta_L = D_+ \sin\psi_+ \sin\theta_+/\gamma, \tag{3.85}$$

$$\cos\theta_L = D_+ \cos\theta_+/\gamma, \tag{3.86}$$

and

$$d_+ = \gamma^2 R_+/D_+ \tag{3.87}$$

where the Doppler factor, $D_+$, in the emission time frame can be expressed in terms of the corresponding Doppler function, $\Omega_d \equiv \Omega\left(\hat{d}_+\right)$, in the Lorentz frame as

$$D_+ = \gamma^2 \Omega_d, \tag{3.88}$$

i.e.

$$\left(1 - M\cos\psi_+ \sin\theta_+\right)^{-1} = \gamma^2 \left(1 + M\cos\psi_L \sin\theta_L\right). \tag{3.89}$$

It should also be noted that

$$t - R_+/c_0 = t_L - d_+/c_0, \tag{3.90}$$

where this identity will be required in the following analysis. For a given pair of real variables for $\psi_L$ and $\theta_L$ in the Lorentz frame, any two of the three equations, Eqs. 3.84 to 3.83 can be used to map the corresponding pair of real angles, $\psi_+$ and $\theta_+$, in the emission time frame.

To obtain an appropriate asymptotic solution for Eq. 3.80, it is useful to express the kernel function from the Lorentz frame to the emission time frame for a fixed $t_L$.

This transformation is made easier by introducing the wave vector in the emission time frame as $\kappa \equiv (D_\kappa k_s, \varepsilon, \mu)$ where $\epsilon$ is the azimuthal angle, $\mu$ is the polar angle and the Doppler function $D_\kappa$ is defined in Eq. 3.63. For the spherical polar coordinate system, $D_\kappa = (1 - M\cos\varepsilon\sin\mu)$. The pair of angles in these two different frames are linked by

$$\cos\psi_L \sin\mu_L = D_\kappa \left(\cos\varepsilon\sin\mu - M\right), \tag{3.91}$$

$$\sin\psi_L \sin\mu_L = D_\kappa \sin\varepsilon\sin\mu/\gamma, \tag{3.92}$$

$$\cos\mu_L = D_\kappa \cos\mu/\gamma, \tag{3.93}$$

and the Doppler functions, $\Omega_d$ and $D_\kappa$, are connected by

$$\gamma^2\Omega_d = D_\kappa, \tag{3.94}$$

i.e.

$$\gamma^2 \left(1 + M\cos\psi_L\sin\mu_L\right) = \left(1 - M\cos\varepsilon\sin\mu\right)^{-1}. \tag{3.95}$$

To avoid the need to introduce another set of temporary variables, $\varepsilon_L$is replaced directly by $\psi_L$ in Eqs. 3.91 to 3.95 because all parameters in the integrand of Eq. 3.81 are to be evaluated at $\varepsilon_L = \psi_L$.

A mapping from $(\psi_L, \mu_L)$ to $(\varepsilon, \mu)$ can be obtained by using any two of the three equations [Eqs. 3.84 to 3.86] and the third is then subject to the condition laid down by Eq. 3.59a. By applying Eqs. (3.91 to 3.95) in the spatial Doppler functions, a rather simple form can be obtained in the emission time frame as

$$\begin{cases} \Gamma_x = \cos\varepsilon\sin\mu = M + \cos\psi_L\sin\mu_L \\ \Gamma_y = \sin\varepsilon\sin\mu = \sin\psi_L\sin\mu_L/\mu \\ \Gamma_r = \sin\mu = \sqrt{\left(M + \cos\psi_L\sin\mu_L\right)^2 + \left(\sin\psi_L\sin\mu_L/\gamma\right)^2} \end{cases} \tag{3.96}$$

The mapping from $\mu_L$ plane to $\mu$ plane is shown in Figure 3.6. The original path of $\mu_L$ is alone lines: $-\pi/2 + \infty$ to $-\pi/2$, $-\pi/2$ to $\pi/2$, $\pi/2$ to $\pi/2 - \infty$. The path for $\mu$ is very close to the original path of $\mu_L$. $\pi/2$ is mapped to $\pi/2$ and $-\pi/2$ is mapped to $-\pi/2$. However, when $\mu_L$ has imaginary component, the path in $\mu$ plane is slightly deviated from the original path.

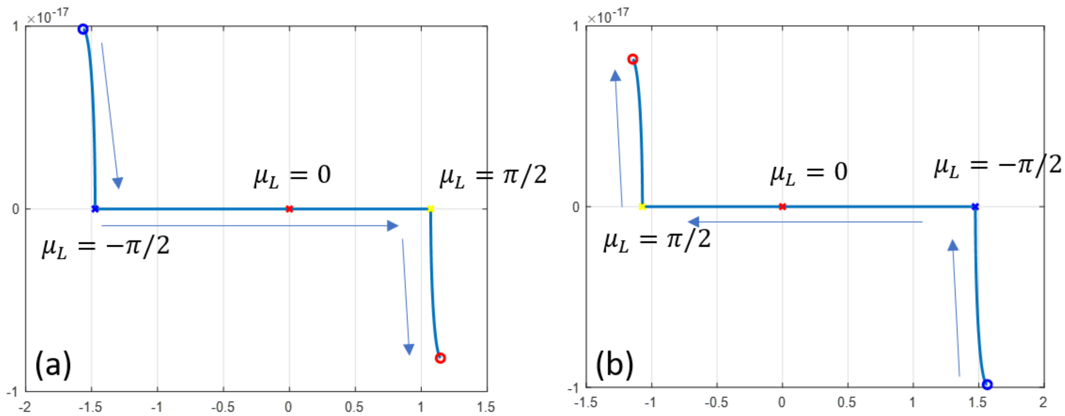


Figure 3.6. Mapping from $\mu_L$ to $\mu$. (a) Approaching case. (b) Receiding case.

Hence, the ratio of the Doppler functions, $\Gamma_r/\Omega_d$ is only dependent on $\mu$ in the emission time frame. Resulting from this simplification, the normalized admittance of the ground becomes $\beta(D_\kappa k_s, \kappa_r)$ as opposed to $\beta(k_0, k_r)$ in Eq. 3.68 in the physical frame. From Eqs. 3.72 to 3.74, it follows then that the normalized admittance for the hardback (HB), extended reaction (ER) and locally reacting (LR) ground are given respectively by

$$\beta(D_\kappa k_s, \kappa_r) = -i\zeta_s\sqrt{n_s^2 - \sin^2\mu}\tan(D_\kappa k_s d\sqrt{n_s^2 - \sin^2\mu}), \tag{3.97}$$

$$\beta(D_\kappa k_s, \kappa_r) = \zeta_s\sqrt{n_s^2 - \sin^2\mu}, \tag{3.98}$$

and

$$\beta(D_\kappa k_s, \kappa_r) = \zeta_s n_s, \tag{3.99}$$

where $\zeta_s \equiv \zeta(k_s D_\kappa)$ and $n_s \equiv n(k_s D_\kappa)$ are respectively the density ratio and the index of refraction to be evaluated at the Dopplerized frequency of $D_\kappa k_s$.

Using Eqs. 3.93 and 3.95, the boundary function in Eq. 3.82 can be transformed from $F_L(\psi_L, \mu_L)$ to $F(\varepsilon, \mu)$ as

$$F(\varepsilon, \mu) = \frac{2D_\kappa\beta(D_\kappa k_s, \kappa_r)}{\cos\mu + \beta(D_\kappa k_s, \kappa_r)}. \tag{3.100}$$

The location of the Dopplerized pole in the emission time frame can therefore be identified by requiring the denominator of the right side of Eq. 3.100 to be zero, i.e.,

$$\cos\mu_p + \beta_p = 0 \tag{3.101}$$

where the subscript p denotes the corresponding parameters to be evaluated at the Dopplerized pole location, $\kappa_r = \kappa_p \equiv (D_p k_s, \varepsilon_p, \mu_p)$ with the Doppler function given by

$$D_p = (1 - M\cos\varepsilon_p \sin\mu_p)^{-1}, \tag{3.102}$$

and $\beta_p \equiv \beta(D_p k_s, \kappa_p)$. On its own, Eq. 3.101 is not sufficient to determine $\varepsilon_p$ and $\mu_p$ uniquely for an arbitrary location of the moving source and the stationary receiver at a fixed emission time, $\tau_+$. It is recognized that the integral of Eq. 3.81 is evaluated at a constant $\psi_L$ when the Dopplerized pole is determined. Hence, the elimination of $\sin\mu_L$ from Eqs. 3.91 and 3.92 lead to the second equation supplementing Eq. 3.101 to determine $\varepsilon_p$ and $\mu_p$:

$$\cos\varepsilon_p = \frac{ME_2 + \operatorname{sgn}(x - c_0Mt)\sqrt{{E_1}^2M^2 - (E_1+E_2)(E_1M^2 - E_2\sin{\mu_p}^2)}}{(E_1+E_2)\sin\mu_p} \tag{3.103}$$

where $E_1$ and $E_2$ are two constants defined as

$$\begin{aligned} E_1 &= (\sin\psi\sin\theta_+)^2 \\ E_2 &= (\cos\psi\sin\theta_+ - M)^2 \end{aligned} \tag{3.104}$$

In the 2-dimensional case or a direct overhead flight with no off-set distances (y = 0) for the 3-dimensional situation, Eq. 3.103 simply implies that $\cos\varepsilon_p = 1$, i.e., $\varepsilon_p = 0$. Equation (32a) is now reduced to a transcendental equation with $\mu_p$ as the only unknown. This can then be solved numerically by using the standard Newton Raphson method described in the previous chapter.

The recursive scheme can be extended easily to handle the case when an offset location$y \neq 0$ is considered. Suppose $\cos\varepsilon_p^{(j)}$ and $\mu_p^{(j)}$ are used as the pair of jth iterative solutions for the transcendental equations, Eqs. 3.101 and 3.103. To facilitate the subsequent analysis, a variable $\Delta$ is introduced:

$$\Delta \equiv -\partial\,(\cos\mu_p + \beta_p)/\partial\mu_p = \sin\mu_p - \beta_p', \tag{3.105}$$

where the prime denotes the derivative with respect to $\mu_p$. The iterative scheme is centered on the acquisition of the solution for $\mu_p^{(j+1)}$ by using the Newton Rasphson method:

$$\mu_p^{(j+1)} = \mu_p^{(j)} + \left(\cos\mu_p^{(j)} + \beta_p^{(j)}\right)/\Delta^{(j)} \tag{3.106}$$

where the superscript (j) signifies the corresponding parameters evaluated at the jth iteration. When calculating Eq. 3.106, $\cos\varepsilon_p^{(j)}$ [which is readily available from Eq. 3.103] is needed because $\beta_p^{(j)}$ and $\Delta^{(j)}$ are implicit functions of $D_p^{(j)}$. Regardless of the ground types, $\mu_p^{(0)} = \cos^{-1}\left(\zeta_p^{(0)} n_p^{(0)}\right)$ is used as an initial value where $\zeta_p^{(0)}$ and $n_p^{(0)}$ are calculated at the Doppler frequency, $D_p^{(0)} = 1$. The variation in the azimuthal component, $\cos\varepsilon_p^{(0)}$ is then calculated by applying Eq. 3.103. These initial values, $D_p^{(0)}$, $\mu_p^{(0)}$ and $\cos\varepsilon_p^{(0)}$ are used to calculate $D_p^{(1)}$ from Eq. 3.102, $\mu_p^{(1)}$ from Eq. 3.106 and $\cos\varepsilon_p^{(1)}$ from Eq. 3.103. The process is repeated in the next iterations until the computed results converge to the required accuracy. The solutions for $\varepsilon_p$ and $\mu_p$ are typically accurate to within $1.0 \times 10^{-16}$ in less than 10 iterations.

By following the steepest descent analysis, [4, 48] the integral in Eq. 3.81 can be approximated asymptotically. The approximate solution can subsequently be transformed back to the emission time frame. The solution for $I_b$ can then be used together with $I_\mp$ [cf Eq 3.76] in Eq. 3.69 to give an asymptotic solution for the total sound field in the retarded time frame as

$$p_0(r, z, t) = p_-(r, z, t) + Q\, p_+(r, z, t), \tag{3.107}$$

where $Q$ is the spherical wave reflection coefficient,

$$Q = V_+ + A(1 - V_+)F(w_p), \tag{3.108}$$

$V_+$ is the plane wave reflection coefficient,

$$V_+ = \frac{\cos\theta_+ - \beta_+}{\cos\theta_+ + \beta_+}, \tag{3.109}$$

$\beta_+ \equiv \beta(D_+k_s, \hat{R}_+)$ is the effective admittance which has been 'Dopplerized'. According to Eq. 3.72 to 3.74, it can be specified as

$$\beta_+ = -i\zeta_+\sqrt{n_+^2 - \sin^2\theta_+}\tan\left(D_+k_sd\sqrt{n_+^2 - \sin^2\theta_+}\right), \tag{3.110}$$

$$\beta_+ = \zeta_+ \sqrt{n_+^2 - \sin^2\theta_+}, \tag{3.111}$$

and

$$\beta_+ = \zeta_+ n_+, \tag{3.112}$$

for the HB, ER and LR grounds respectively. The density ratio $\zeta_+$ and index of refraction $n_+$ are the respective ground parameters evaluated at the Doppler frequency, $D_+ k_s$. In Eq. 3.108, A is the augmented diffraction factor: [48]

$$A = \frac{(r_\beta / r_w)}{\delta_\mu \Delta} \sqrt{\frac{\sin \bar{\mu}_p}{\sin \theta_L}}, \tag{3.113}$$

where $\bar{\mu}_p$ is related to $\mu_p$ by

$$\cos \bar{\mu}_p = D_p \cos \mu_p / \gamma, \tag{3.114}$$

$\theta_L$ can be expressed in terms of $\theta_+$ using Eq. 3.86, $r_\beta$ is the Dopplerized admittance ratio:

$$r_\beta = D_p \beta_p / D_+ \beta_+, \tag{3.115}$$

and $r_w$ is the ratio of Dopplerized numerical distances:

$$r_w = (2\gamma / D_+) \sin \tfrac{1}{2} \left(\bar{\mu}_p - \theta_L\right) \big/ (\cos \theta_+ + \beta_+), \tag{3.116}$$

$\Delta$ is defined in Eq. 3.105 and $\delta_\mu \equiv (D_+/\gamma)\, \partial\mu / \partial\mu_L|_{\mu=\mu_p}$ can be found as follows:

$$\delta_\mu = \frac{D_+ \left(1 - D_p \cos^2 \mu_p\right)}{D_p \sin \mu_p \sin \bar{\mu}_p}. \tag{3.117}$$

Equation 3.107 is a generalized form for the 3-dimensional sound fields due to a point monopole source moving above flat ground surfaces. In the special case of M = 0, it reduces to the classic form of the Weyl-Van der Pol formula, which can be used to identify the contribution of the sound fields due to the direct and the specularly reflected wave terms. The asymptotic solution is referred to as the Dopplerized Weyl-van der Pol Formula in three dimensions, or simply, the D-WVDP formula in the following sections.

### 3.2.3 Validation of the D-WVDP formula

In an earlier study, Wang et. al [previous chapter] derived an asymptotic solution for the sound fields due to a line source moving horizontally above a non-locally ground. Their two-dimensional asymptotic solution was validated by comparing the numerical results with those obtained by the finite-difference time-domain (FDTD) method. At the expense of more computational resources, the FDTD method can be extended readily to calculate the three-dimensional sound fields. These numerical results are used to authenticate the D-WVDP formula as follows. The details of numerical implementations of the FDTD method are discussed elsewhere [35] and will not be reiterated here.

Figure 3.7 shows the comparison between asymptotic solutions and finite difference solution of locally reacting model (FDTD) provided by Dilder Dragna. Two different types of ground are used in the comparison: semi-infinite ground and hard-backed ground with a layer thickness of 0.05 m. The side line distance is set to 5 m to allow the azimuthal angle to be non-zero. Source frequency are chosen as 200 Hz and 100 Hz respectively and is set to 1 m above the ground to verify the prediction of the near grazing case. The agreement between the asymptotic solution of the extend reacting model and FDTD solution is great for both types of ground as we can see in Figure 2(ab) with the maximum error less than 0.2 dB. The comparison is expected to have good agreement because the flow resistivity is large enough to ignore the difference between locally and non-locally reacting models.

For ease of comparisons, the Hamet and Bérengier phenomenological model [51] is selected to estimate the acoustical impedance of the grounds. Three adjustable parameters, namely the airflow resistivity $\sigma_0$, tortuosity $q^2$, and porosity of the air-filled connected pores $\varphi$, are used to model a rigid porous medium, which is same as the model used in 2d comparison.

Figure 3.8 shows the comparison between direct numerical integration solution and asymptotic solution for both semi-infinite case and hard-backed case. More than

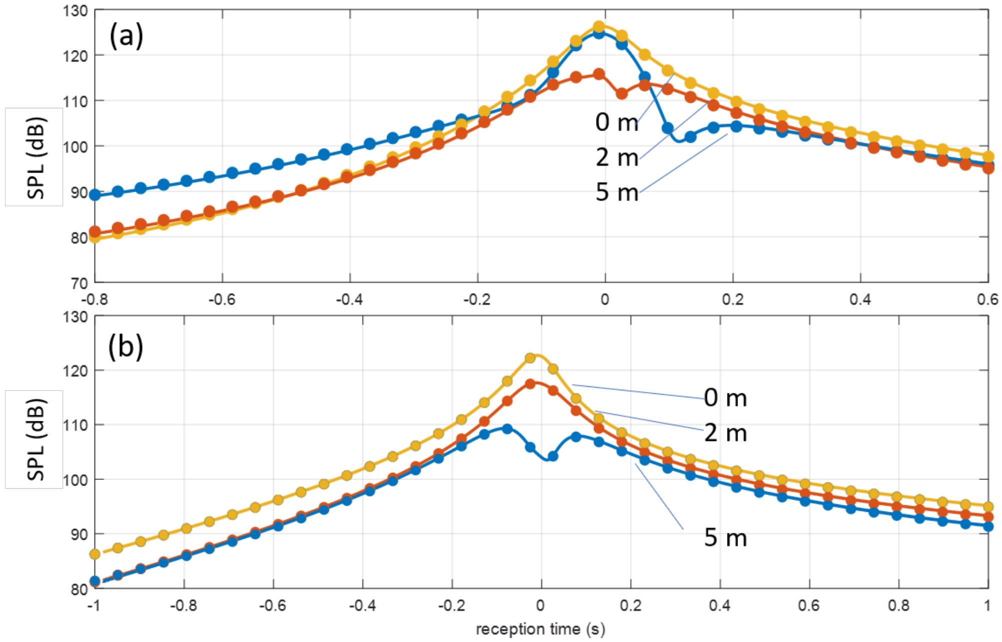


Figure 3.7. Comparisons between direct numerical integration solutions of non-locally reacting model (*) and asymptotic solution of nonlocally reacting model (o) with time-domain finite difference solutions of locally reacting model (solid lines) based on locally reacting model. Receiver is located at 0, 2, and 5 m above the ground. Side line distance y = 5 m. Source moves at constant height of 1 m above the ground with Mach number of 0.3. Ground has $\sigma_0$ , $q^2$, and $\varphi$ of 100 kPa m s-2, 1.0, and 1, respectively. (a) Semi-infinite extended reaction ground. Source frequency = 200 Hz. (b) Hardback ground with layer thickness of 0.05 m. Source frequency = 100 Hz.

$10^4$ points are used in the direct numerical integration for each sampling point to get better accuracy. The agreement is great even the flow resistivity is very low (less than 10 kpa m $s^{-2}$), which is the parameters chosen to simulate the behaviors of snow covered hard-backed ground. We can conclude that the asymptotic solution has great accuracy. There is still no available results based on finite difference numerical experiment for non-locally reacting ground when the asymptotic solution id derived. So the comparison will be not shown here but possibly will be shown and published in the near future.

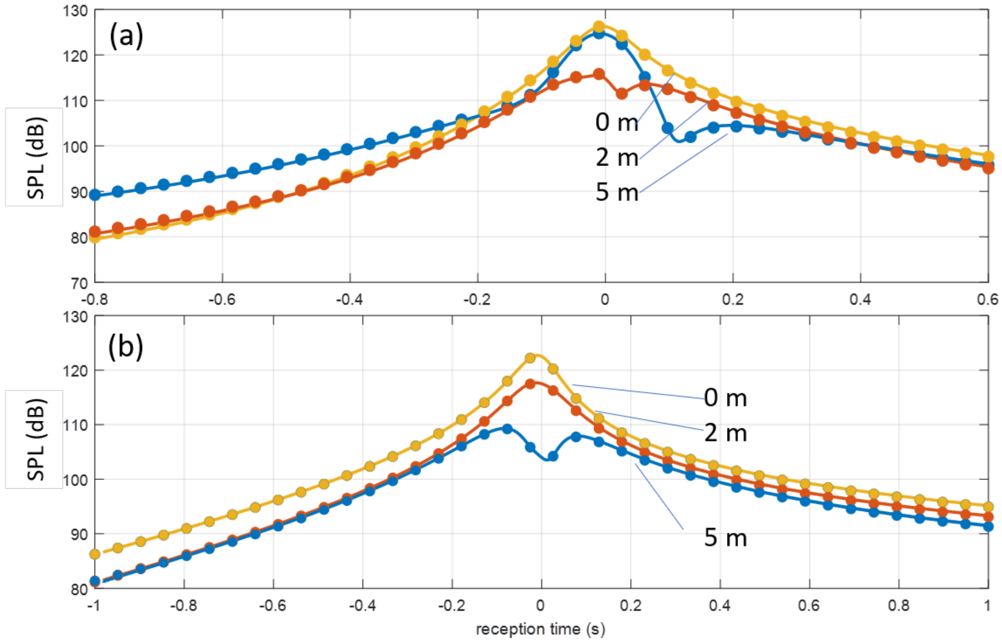


Figure 3.8. Comparisons between direct numerical integration solutions of non-locally reacting model (solid) and asymptotic solution of nonlocally reacting model (o). Receiver is located at 0, 2, and 5 m above the ground. Side line distance y = 5 m. Source moves at constant height of 1 m above the ground with Mach number of 0.3. Ground has $\sigma_0$ , $q^2$, and $\varphi$ of 10 kPa m $s^{-2}$, 1.0, and 0.9, respectively. Source frequency = 300 Hz. (a) Semi-infinite extended reaction ground. (b) Hardback ground with layer thickness of 0.05 m.

**Validity of the simple approximated model and the asymptotic solution**

A simple asymptotic solution was widely used in many references for stationary source and moving source, which is given as

$$Q = V_+ + (1 - V_+)F(w_+), \tag{3.118}$$

where

$$w_+ = \sqrt{\frac{ik_0 R_+ D_+}{2}}(cos\theta_+ + \beta_+) \tag{3.119}$$

and $A$ is treated as 1. Using Eqs. 3.118 and 3.119 doesn't require any interetation to find the pole location, which is one of the more difficult task in the evaluation. This approximation has great accuracy for stationary source [4, 48] and was widely used in the past in many applications. In a recent paper [35] the approximation is also shown to be great for moving source with a locally reacting ground. However, with a 'soft' ground and a moving source, the accuracy of the approximation could be very bad at grazing cases when the source and receivers and both very close to the ground surface. Results can be concluded from Fig. 3.9 and Fig. 3.10. In Fig. 3.9 the excess

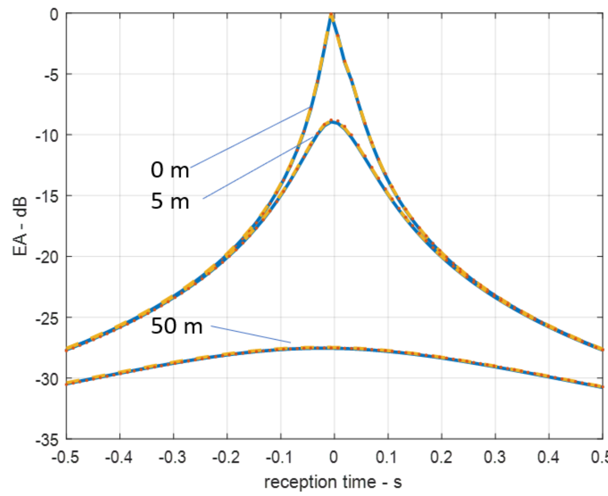


Figure 3.9. Comparisons between time histories of excess attenuation (EA) function of direct numerical integration solution (solid lines), simple approximated solution (red, dotted lines) and asymptotic solution (yellow, dashed) for hard-backed extend reacting model. (a) M = 0.3. Source frequency is 400 Hz. Source and receiver heights are set at 0.3 and 0.6 m above the ground. Ground has $\sigma_0$ , $q^2$, and $\varphi$ of 10 kPa m s-2, 1.2, and 0.9, respectively. Sideline distance is set to 0, 50 and 50 m from the source respectively.

attenuation of the sound field above locally reacting ground is plotted using direct numerical integration solution, asymptotic solution and simple approximation. The accuracy of both the asymptotic solution and approximated solution are great with error less than 0.2 dB. However, in Fig. 3.10, the advantage of using the asymptotic solution is obvious. In 3.10(a) and 3.10(b), the location of the interference effect predicted by approximated solution if off by around 0.03 s. As a result, the error at the dip is larger than 5 dB in 5(b). The parameter (Ground has $\sigma_0$ , $q^2$, and $\varphi$ of

10 kPa m s-2, 1.2, and 0.9, respectively) used in the prediction is close of those of snow [Prem Datt], and the speed M = 0.3 can be reached by modern high speed rails, which means the prediction could possible happen in real scenario during winter time in the open area.

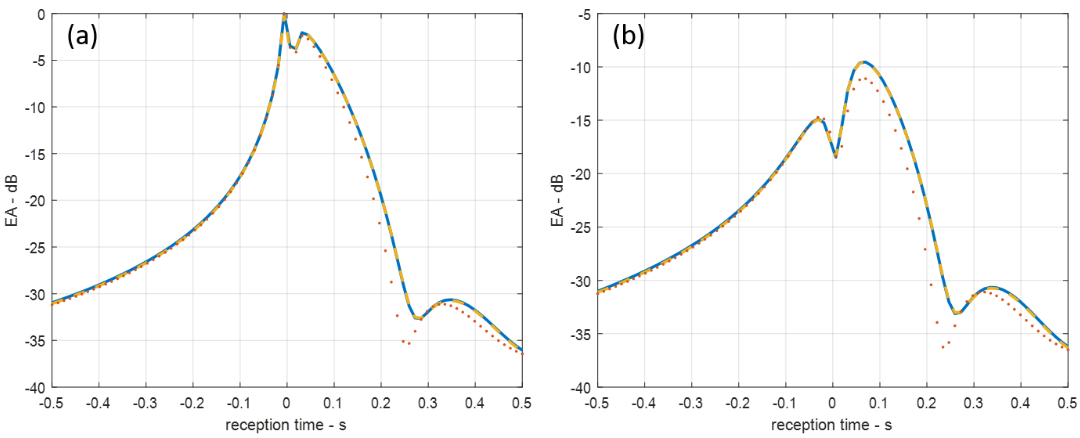


Figure 3.10. Comparisons between time histories of excess attenuation (EA) function of direct numerical integration solution (solid lines), simple approximated solution (red, dotted lines) and asymptotic solution (yellow, dashed) for hard-backed extend reacting model. (a) M = 0.3. Source frequency is 400 Hz. Source and receiver heights are set at 0.3 and 0.6 m above the ground. Ground has $\sigma_0$ , $q^2$, and $\varphi$ of 10 kPa m s-2, 1.2, and 0.9, respectively. Sideline distance is set to 0 m from the source. (b) Sideline distance is set to 5 m from the source. Ground parameters, source speed and other geometries are same as (a) above. Thickness of the hard-backed layered is 0.05 m.

In Fig. 3.11, the advantage of using asymptotic solution is more obvious when a much lower flow resistivity is used in the simulation. The prediction of the locations of interference effect by approximated model has poorly agreement with the accurate solution. At some location (-0.26 s reception time) the error is larger than 20 dB. The choice of the ground parameters is based on a study of ballast along the railroad. We can conclude that in a lot of scenarios with low resistivity ground, such as for high speed rail traveling above ballast or in the winter with snow covered ground, the advantage of using the asymptotic model could be huge if interference effect and

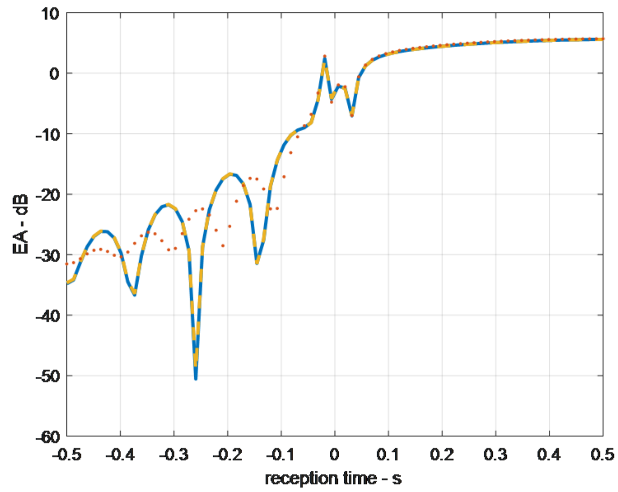


Figure 3.11. Comparisons between time histories of excess attenuation (EA) function of direct numerical integration solution (solid lines), simple approximated solution (red, dotted lines) and asymptotic solution (yellow, dashed) for hard-backed extend reacting model. M = 0.3. Source frequency is 1000 Hz. Source and receiver heights are set at 0.3 and 0.6 m above the ground. Ground has $\sigma_0$ , $q^2$, and $\varphi$ of 0.2 kPa m s-2, 1.3, and 0.5, respectively. Sideline distance is set to 0 m from the source.

surface wave exist. The error of the approximated model is more than 5 dB for snow covered ground and could be more than 20 dB for ballast covered ground with low flow resistivity. The reasons for the error reside in both the prediction of $A$ and the estimation of surface wave pole. A more detailed studied was conducted for line source and will not be repeated here. However, one can see that the difference between D-WVDP solution and simple approximation is more noticeable for point source than for line source. This is mainly due to the exist of sideline distance for 3d problems, which makes the surface wave easier to be seen in the comparisons.

### Monopole source vs. line source

Before talking about moving source, we can start from stationary source problems first. For a stationary source, the reflection coefficient $Q$ for a point source can be approximated by that of a line source with very small error. [4] The only difference is a $\sqrt{sin\mu_p/sin\theta}$ term in the augmentation factor $A$. [48]. One can substitute any point source problems with a equivalent line source problem by borrowing the reflection coefficient of line source. For a moving source, there is no one-to-one mapping from a point source problem to a line source problem for none-zero sideline distance due to the source motion and the coefficient of reflection must to solved separately for a line source and a point source.

However, it is interesting to compare the 2-d and 3-d solution with zero sideline distance. The excess attenuation of 2-d solution can be written as

$$EA_{2-d} = 10\log_{10}\left(1 + 2\Gamma_{2-d}\cos\left[k_s\left(R_+ - R_-\right) + \Phi_{2-d}\right] + \Gamma_{2-d}^2\right), \tag{3.120}$$

and for 3-d, the expression is

$$EA_{3-d} = 10\log_{10}\left(1 + 2\Gamma_{3-d}\cos\left[k_s\left(R_+ - R_-\right) + \Phi_{3-d}\right] + \Gamma_{3-d}^2\right), \tag{3.121}$$

where $\Gamma_{2-d}$ and $\Gamma_{3-d}$ are given

$$\Gamma_{2-d} = \left(D_+/D_-\right)\Lambda^{\frac{1}{2}}|Q|_{2-d}, \tag{3.122}$$

and

$$\Gamma_{3-d} = \left(D_+/D_-\right)\Lambda|Q|_{3-d}, \tag{3.123}$$

with $\Lambda$ referred as the ratio of the Dopplerized divergence factor:

$$\Lambda = \frac{R_-}{D_-}/\frac{R_+}{D_+} \tag{3.124}$$

The variables, $Q_{2-d}$ and $Q_{3-d}$ are the cylindrical (2-d) and spherical (3-d) reflection coefficients which can be calculated according to Eq. 3.108. Figure 3.12 presents typical comparisons of the $\mathrm{EA}_{2-d}$ and $\mathrm{EA}_{3-d}$ time histories for ER and HB grounds with $\sigma_0$, $q^2$, and $\varphi$ values of 10 kPa m s−2, 1, and 0.9, respectively. Furthermore, the HB ground has a layer thickness of 0.05 m. To compute the 3D sound fields, the sideline distance is set to 0 because the direct overhead flight path is considered. The source and receiver are fixed at respective heights of 0.3 and 0.6 m above the ground, and the Mach number of 0.3 is chosen in the numerical simulations presented in the two plots shown in Figs. 3.12a and 3.12b. The time history of $EA_{2-d}$ is illustrated in solid lines, and that of the $EA_{3-d}$ is displayed in dashed lines. For ease of explanation, the 2D and 3D ground wave (GW) contributions [the second term on the right side of Eq. (37b)] are also illustrated in the plots.

For the ER and HB grounds (Figs. 3.12a and 3.12b, respectively), the GW contributions are relatively small for both 2D and 3D sound fields because the horizontal separation between the moving source and the receiver are restricted to within $\pm 5$ m in the figures. Hence, $Q_{3-d}$ can be approximated by $Q_{2-d}$ without appreciable discrepancies. An inspection of Eqs. 3.122 and 3.123 suggests that $\Gamma_{2-d}$ is only different from $\Gamma_{3-d}$ by a factor of $\lambda^{1/2}$, where $\lambda$ is defined in Eq. 3.124 as the ratio of the Dopplerized divergence factors. The factor, $\lambda^{1/2}$, is generally close to 1 for the near ground sound propagation at long ranges. However, this is not the case when the incident angle of the reflected wave is less than 80 degree. At near fields with a negligible GW term, it is possible to show that $0 \leq \Gamma_{2-d} \leq 1$, $\Gamma_{3-d} = \Lambda^{\frac{1}{2}}\Gamma_{2-d}$, and $\Gamma_{3-d} < \Gamma_{2-d}$. The implication of a non-unity $\lambda^{1/2}$ leads to an expected deviation of $EA_{2-d}$ from $EA_{3-d}$. The discrepancy can become quite significant, especially when the direct wave interferes destructively with the reflected wave at an approximate location of

$$k_s \left(R_+ - R_-\right) + \Phi_{2-d} = \pi. \tag{3.125}$$

With the selected ground parameters and source/receiver heights, the discrepancy in the predicted EA is over 1 dB for the ER ground 3.13a, and is in excess of 6 dB for the HB ground 3.12b. Given the chosen source/receiver heights and ground parameters, Eq. 3.125 is satisfied at a horizontal separation of about 0.6 m (see Figs. 3.12a and 3.12b).

It should also be noted that there are discontinuities in the GW term when the reception time approaches zero where the horizontal separation vanishes. This "error" is introduced largely owing to the approximation in computing the GW term. [48] However, the contribution from the direct wave component is over 25 dB higher than

Table 3.1. Comparison between 2D and 3D expressions

| | 2-d | 3-d | 3-d ($\psi = 0$) |
|---|---|---|---|
| $p_{\mp}$ | $\frac{\rho_0\omega_s}{4} D_{\mp}^{3/2}\sqrt{2/\mathrm{i}\pi k_s R_{\mp}} \times$ $\mathrm{e}^{-\mathrm{i}\omega_s(t-R_{\mp}/c_0)}$ | $\left(-i\rho_0\omega_s D_{\mp}^2/4\pi R_{\mp}\right)\times$ $e^{-i(\omega_s t - k_s R_{\mp})}$ | $\left(-i\rho_0\omega_s D_{\mp}^2/4\pi R_{\mp}\right)\times$ $e^{-i(\omega_s t - k_s R_{\mp})}$ |
| A | $\frac{(r_\beta/r_w)}{\delta_\mu\Delta}$ | $\frac{(r_\beta/r_w)}{\delta_\mu\Delta}\sqrt{\frac{\sin\mu_p - M}{\sin\theta - M}\cdot\frac{D_p}{D_+}}$ | $\frac{(r_\beta/r_w)}{\delta_\mu\Delta}\sqrt{\frac{\sin\mu_p - M}{\sin\theta - M}\cdot\frac{D_p}{D_+}}$ |
| $r_\beta$ | $D_p\beta_p/D_+\beta_+$ | $D_p\beta_p/D_+\beta_+$ | $D_p\beta_p/D_+\beta_+$ |
| $r_w$ | $2\sqrt{D_p/D_+}\times$ $\sin\frac{1}{2}(\mu_p - \theta_+)/(\cos\theta_+ + \beta_+)$ | $(2\gamma/D_+)\times$ $\sin\frac{1}{2}\left(\mu_{L,p} - \theta_L\right)/(\cos\theta_+ + \beta_+)$ | $2\sqrt{D_p/D_+}\times$ $\sin\frac{1}{2}\left(\mu_p - \theta_+\right)/(\cos\theta_+ + \beta_+)$ |
| $\Delta$ | $\sin\mu_p - \beta_p'$ | $\sin\mu_p - \beta_p'$ | $\sin\mu_p - \beta_p'$ |
| $\delta_\mu$ | $D_+/D_p$ | $\frac{D_+\left(1 - D_p\cos^2\mu_p\right)}{D_p\sin\mu_p\sin\mu_{L,p}}$ | $D_+/D_p$ |

the GW term in the near fields. Thus, this apparent error in the GW term will not cause inaccuracies in predicting the total sound fields. There are also small but noticeable discrepancies between $\mathrm{GW}_{2-d}$ and $\mathrm{GW}_{3-d}$ at the approaching time segments for the ER ground. However, the GW term is around 20 dB below the total fields in this situation. Hence, it has an insignificant impact on the overall sound fields for the short-range predictions (less than 5 m horizontal separation).

At far fields when the incident angle of the reflected wave is greater than 85 degree, there is an intrinsic difference between $Q_{2-d}$ (cylindrical wave reflection coefficient) and $Q_{3-d}$(spherical wave reflection coefficient). According to Columns 1 and 3 in Table 3.2.3, all terms involved in the calculation of $Q_{2-d}$ and $Q_{3-d}$ are identical, except for the augmented diffraction factor, A. An extra factor of $\sqrt{D_p(\sin\mu_p - M)/D_+\,(\sin\theta - M)}$ appears in $\mathrm{A}_{3-d}$, but is not present in $\mathrm{A}_{2-d}$. An implicit requirement is that the surface wave component must contribute significantly to the GW term in order to make the extra factor important.

In Figs. 3.13a and 3.13b, far-field comparisons of $EA_{2-d}$ and $EA_{3-d}$ are shown for the same ER and HB grounds as before with the same source/receiver heights. However, the source frequencies of 200 Hz and 400 Hz are used in Figs. 6a and 6b, respectively. To highlight the comparisons at the far fields, a reception time interval between 0.1 and 0.5 s is shown with the source Mach number of 0.3. This is equivalent to a source/receiver separation ranging from approximately 5 to 26 m. The surface wave is triggered in the HB ground but not in the ER ground. [52] Hence, the effect of the extra factor $\sqrt{D_p(\sin\mu_p - M)/D_+(\sin\theta - M)}$ is much more significant in the HB ground (Fig. 3.13b) than the ER ground (Fig. 3.13a), although the GW term is comparable with the direct wave component in both situations.

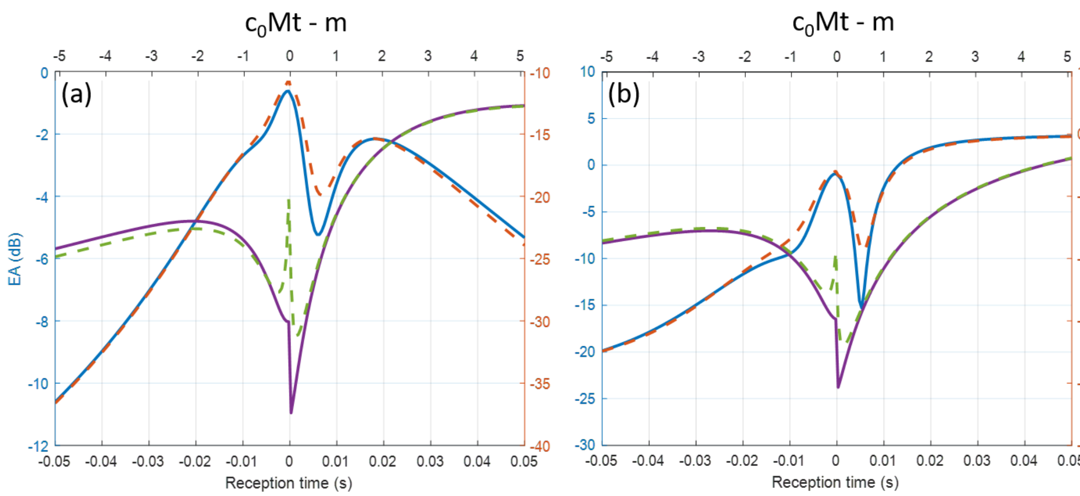


Figure 3.12. Comparisons between time histories of excess attenuation (EA) function of 2d asymptotic solution (solid lines), 3d asymptotic solution (dashed lines). M = 0.3. Source frequency is 300 Hz. Source and receiver heights are set at 0.3 and 0.6 m above the ground. Ground has , , and of 10 kPa m s-2, 1, and 0.9, respectively. Sideline distance is set to 0 m. (a) Semi-infinite ground. (b) hard-backed ground with thickness of the hard-backed layer as 0.05 m.

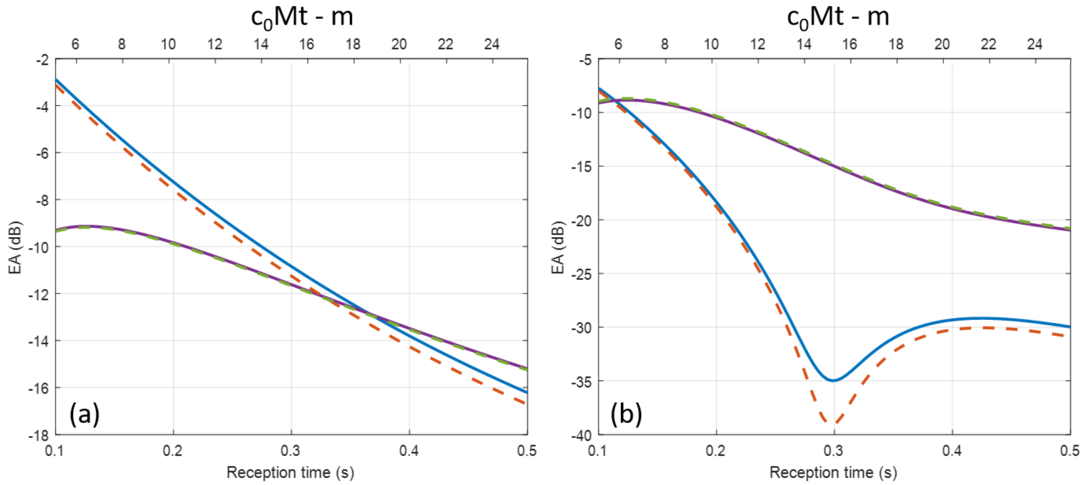


Figure 3.13. Comparisons between time histories of excess attenuation (EA) function of 2d asymptotic solution (solid lines), 3d asymptotic solution (dashed lines). M = 0.15. Source frequency is (a) 200 Hz and (b) 400 Hz. Source and receiver heights are set at 0.3 and 0.6 m above the ground. Ground has , , and of 10 kPa m s-2, 1, and 0.9, respectively. Sideline distance is set to 0 m. (a) Semi-infinite ground. (b) hard-backed ground with thickness of the hard-backed layer as 0.05 m.

### Pole location

Figures 3.14a and 3.14b exemplify the variations in $\mu_p$ and $\psi_p$ for LR, ER, and HB grounds, where a typical source speed (M = 0.3), source frequency (400 Hz is used), and ground parameters ($\sigma_0$, $q^2$, and $\varphi$ of 10 kPa m s-2, 1.25, and 0.9; and HB ground has a layer thickness of 0.05 m) are used. The steepest descent path (SDP) has also been shown in the complex $\mu$-plane for reference (see Fig. 3.14a). The surface wave will be triggered if the pole lies between the SDP and the negative imaginary axis, which is marked as the dashed line shown in Fig. 3.14a. It is apparent from the plot that the surface wave will only be present for the HB ground for the ground parameters used in the present study.

Figure 3.14b traces the locus of $\psi_p$ in the complex $\epsilon$-plane. For the LR, ER, and HB grounds, there is a small but positive imaginary component in $\psi_p$, except when

Re($\psi_p$) is equal to 0 or $\pi$. These two special cases correspond to the situation of a direct overhead flight [with Im $(\psi_p) = 0$], where the locations of the 3D surface wave pole coincide with that of the 2D.

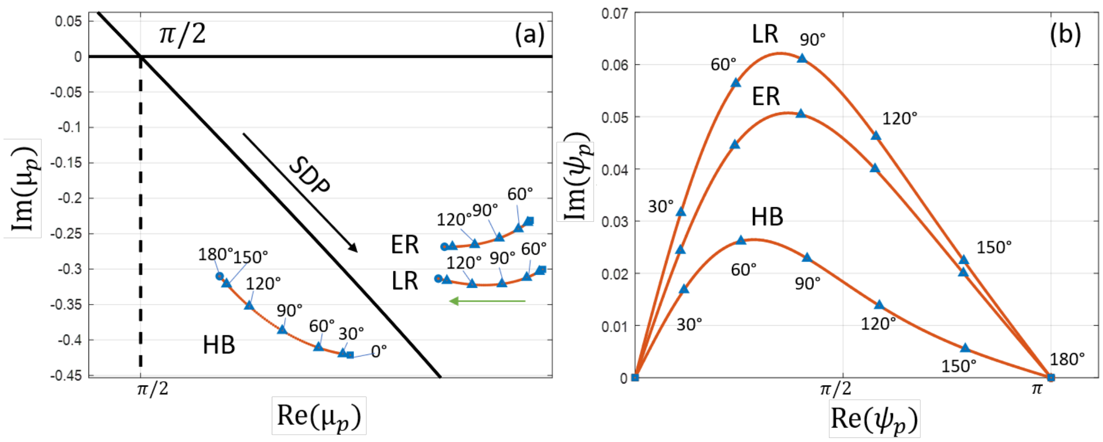


Figure 3.14. Path of (a) $\mu_p$ and (b) $\psi_p$ at different sideline distances and for locally reacting, non-locally semi-infinite and hard-backed ground. M = 0.3. Source frequency is 400 Hz. Source and receiver heights are set at 0.3 and 0.6 m above the ground. Ground has $\sigma_0$ , $q^2$, and $\varphi$ of 10 kPa m s-2, 1.25, and 0.9. The arrows show the direction of increasing reception time. Thickness for hard-backed ground is 0.05 m.

### 3.2.4 Locally vs. non-locally

The difference in the predicted EA values between the locally and non-locally reacting models is small for most acoustic "hard" grounds (e.g., road pavements and sandy grounds). Meanwhile, the use of non-locally reacting boundary conditions is more appropriate for a ground type with the effective flow resistivity of less than 10 kPa m s$^{-2}$ with the Hamet model. The same conclusion applies equally to the moving source problem. A hardback ground with the layer composed of low-resistivity materials is expected to have significant variations in the predicted sound fields between the locally and non-locally reacting models.

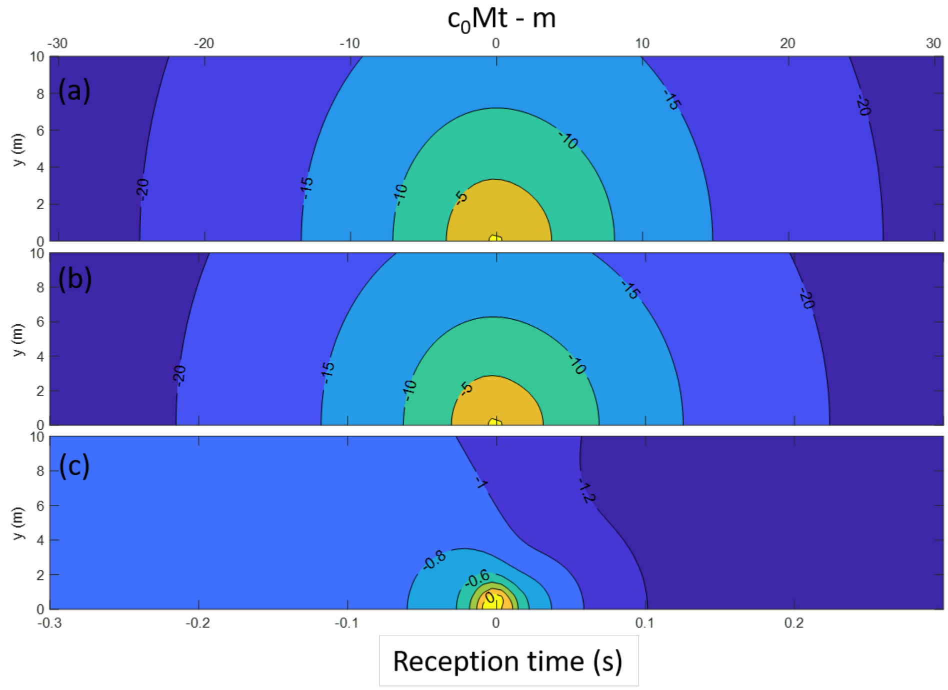


Figure 3.15. Comparison of EA between locally reacting model and non-locally reacting model for semi-infinite ground. Source frequency is 400 Hz. Source and receiver heights are set at 0.3 and 0.6 m above the ground. Ground has : $\sigma_0$ , $q^2$, and $\varphi$, of 10 kPa m s-2, 1.25, and 0.9. (a) Locally reacting model (b) Non-locally reacting model.

A set of three sub-plots, which is shown in Fig. 3.15, is displayed showing the comparison of the predicted EA values of an ER ground calculated with a locally reacting model [see Eq. 3.99] and a non-locally reacting model [see Eq. 3.98]. The Hamet model24 is used here with $q^2$ and $\varphi$ set at 1.25 and 0.9, respectively. The flow resistivity of 10 kPa m s$^{-2}$, which is similar to that of the acoustical properties of snow, [55,56] is used to calculate the ground properties. In the upper two plots (3.15a and 3.15b), the 3D D-WVDP formula is used to compute the sound fields with the sideline distances varying between 0 and 10 m. The third plot shows the difference between these two sets of predicted EA values shown in Figs. 3.15a and 3.15b. The EA contours shown in the upper two plots have comparable shapes. The difference

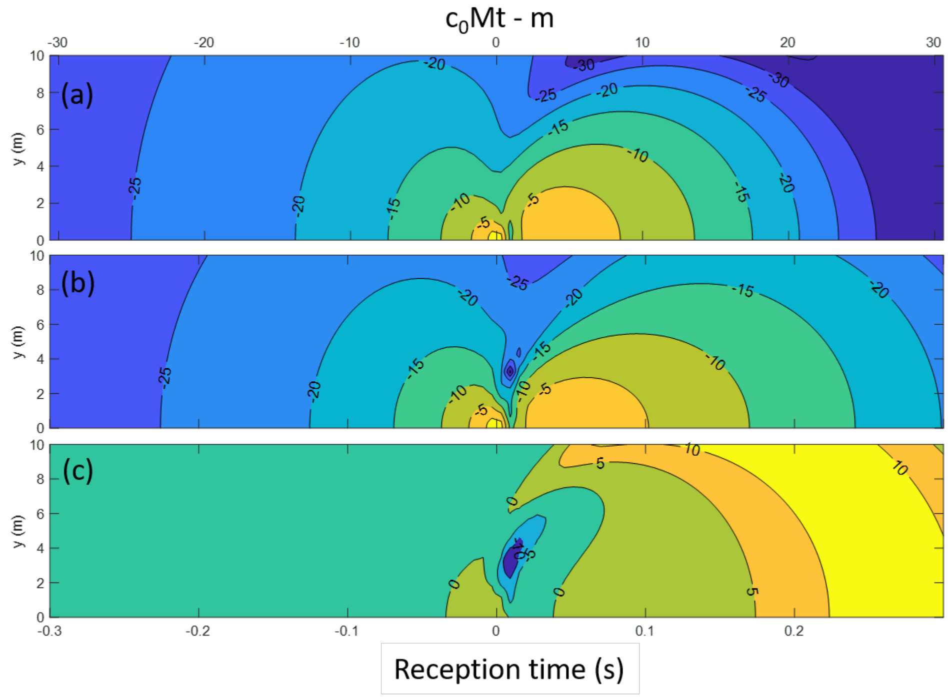


Figure 3.16. Comparison of EA between locally reacting model and non-locally reacting model for hard-backed ground. Source frequency is 400 Hz. Source and receiver heights are set at 0.3 and 0.6 m above the ground. Ground has : $\sigma_0$ , $q^2$, and $\varphi$, of 10 kPa m s-2, 1.25, and 0.9, thickness=.05m. (a) Locally reacting model (b) Non-locally reacting model.

between these two sets of numerical simulations is not obvious even though the flow resistivity has been chosen as low as 10 kPa m s$^{-2}$. The numerical results imply that a locally reacting model can be used in most ER grounds. This point was confirmed in an earlier study [52] in which they investigated the 2D sound fields due to a line source. A locally reacting model can generally be used as a first-order approximation for replacing the non-locally reacting model. A considerable number of studies [4, 48] investigated the differences between the locally and non-locally reacting grounds. No further elaborations will be provided in the present study. However, the above statement cannot be applied for HB ground. Figure 8 shows a comparison between locally and non-locally reacting models for an HB ground with a layer thickness of

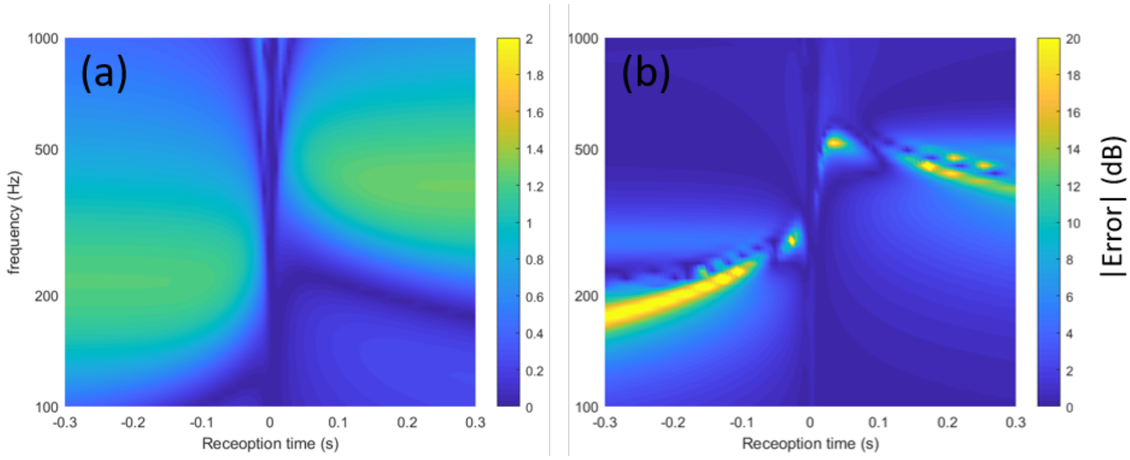


Figure 3.17. Comparison of EA between locally reacting model and non-locally reacting model for hard-backed ground. Source frequency is 400 Hz. Source and receiver heights are set at 0.3 and 0.6 m above the ground. Ground has : $\sigma_0$ , $q^2$, and $\varphi$, of 10 kPa m s-2, 1.25, and 0.9, thickness=.05m. (a) Locally reacting model (b) Non-locally reacting model.

0.05 m. All other parameters are chosen to be the same as those used in the three subplots of Fig. 3.15. Here, the HB boundary conditions for a locally reacting model are the same as the one used by Dragna and Blanc-Benon [35] (see their Eq. (45)). Similar patterns but with noticeable shifts in the approaching and receding segments are displayed in Figs. 3.17a and 3.17(b), respectively. Compared with the non-locally reacting grounds, the locally reacting model overestimates the sound pressure levels in the same locations of the receding region. The difference can be as high as 10 dB at some time segments shown in Fig. 3.17(c). The predicted EA values for different sideline distances are based on a single frequency in each of the plots shown in Figs. 3.14 and 3.17. It is also of interest to present time-frequency contours with the moving source and receiver locating at the $y = 0$ plane, i.e., a direct overhead flight for the 3D sound fields. Using the same source/receiver heights and ground parameters, Figs. 3.17a and 3.17b show the time-frequency analysis for the ER and HB grounds, respectively. The differences in the predicted EA at different frequencies and time segments are shown in these two plots with different scales for the color scheme.

Again, the two time-frequency contours suggest that there are smaller "errors" in the ER ground as opposed to the HB ground. The difference for the HB ground can be as high as 20 dB because of the presence of the Dopplerized surface wave contributions. It is noteworthy that the chosen ground parameters and source/receiver geometries are representative of some of the operating conditions that are due to a high-speed train traveling in the vicinity of snow-covered ground. In fact, the flow resistivity can be even lower with ballast-covered grounds. [39] Hence, it is vitally important to use the non-locally reacting boundary conditions to predict the sound fields for the HB porous ground.

### 3.2.5 Conclusion

The solution of the sound fields generated by a moving point monopole source above a non-locally reacting ground was developed. The property of invariant of phase function was introduced and used to couple the boundary conditions across the plane interface between air and a rigid porous medium below. An accurate asymptotic solution, known as the Dopplerized Weyl-Van Der Pol formula (D-WVDP) was derived using the steepest descent method. The behavior of the pole location, which is crucial to the determination of the surface wave, was analyzed and discussed in the emission time frame. The point source model is distinct from the line source model in both the final expression and the numerical values of the predicted excess attenuation above the ground. The non-locally reacting model is preferred for acoustic "soft" ground (flow resistivity less than about 10 kPa m $s^{-2}$), e.g., snow-covered or ballast-covered grounds, for a better prediction of the overall sound fields.

# 4. DISCOVER-AQ DATA SET AND UNCERTAINTIES IN THE AIRCRAFT NOISE PROPAGTION

## 4.1 Preliminary analysis and directivity

The study of directivity originates in the analysis of the acoustic part in a data set known as "Deriving Information on Surface conditions from Column and Vertically Resolved Observations Relevant to Air Quality" (DISCOVER-AQ) [62]. The DISCOVER-AQ project was originally carried out by the National Aeronautics and Space Administration (NASA) for investigating methods to better distinguish between the pollution high in the atmosphere and that which is near the surface through the use of Earth-observing satellites measuring air quality. The Volpe National Transportation Systems Center (Volpe), in support of FAA AEE, was tasked with measuring in-situ acoustic level data from the flight tests that could then be coupled with corresponding aircraft performance, aircraft position, and meteorological data. The acoustic data sets could be used to investigate, validate, and improve the aircraft acoustic propagation modeling methods in AEDT and other FAA research efforts. Figure 4.1 shows the aircraft used in the Discover-AQ acoustic measurement.

Directivity is one of the most important factors in the prediction of aircraft noise; it could cause large differences in the received noise for receivers at different positions with respect to the aircraft, even if the distance is a constant. The directivity of an aircraft is caused by the engine installation effect, the Doppler effect, and ground effect; among these three, the Doppler effect and the ground effect are independent to the type of aircraft, while the engine installation effect depends highly on the type and configuration of the aircraft.

The extracted data from the DISCOVER-AQ data set show a strong directivity pattern, which needs to be understood before further analysis of propagation effects.


Figure 4.1. NASA P-3B in a typical mission configuration layout during a check flight. (Photo Credit: NASA)

The A-weighted SPL for Event 34 in the DISCOVER-AQ data set is plotted against the time in Figure 4.2. As we can see in the Figure 4.2, the peaks for different frequencies components happen at different moments. The frequency bands centered at 125 Hz, 250 Hz, and 500 Hz have similar peaks, yet the peaks for 63 Hz always happen slightly later than the ones for the other three frequency bands.

At the same time, lower frequencies parts (i.e., 63 Hz and 126 Hz) have more peaks than higher ones. During the event, the aircraft was flying along a spiral path near the receivers on the ground. The locations of the path and the receiver are plotted in Figure 4.3; ; the location where the loudest noise was heard on the ground was also plotted in the figure for the bands centered at 63 Hz and at 500 Hz after adjustments of emission time. It can be observed in the Figures 4.2 and Figure 4.3 that the number of the peaks for 63 Hz is more than those for 500 Hz, and half the peaks for 63 Hz was heard when the aircraft is at the furthest point to the receiver. The phenomenon suggests a strong directivity for the aircraft used in the test since it cannot be explained with any other effects during the propagation.

Directivity pattern for the aircraft used in the test is not available, and a model for the directivity is necessary for a detailed analysis of the propagation effect. Literature

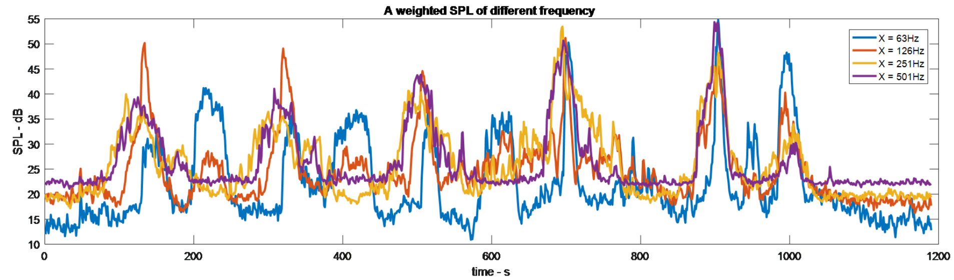


Figure 4.2. A weighting adjusted SPL for different frequencies sound

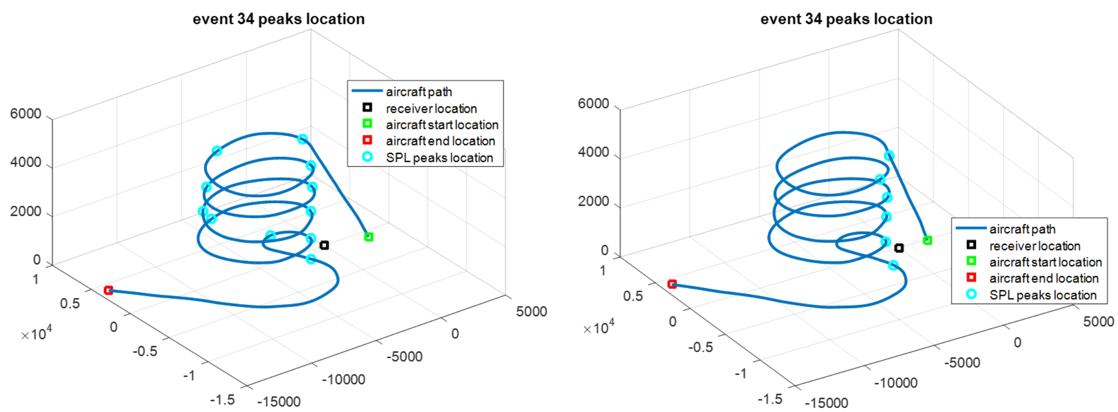


Figure 4.3. Left: 63 Hz peaks locations. Right: 500 Hz peaks locations.

reviews of the directivity pattern show that the azimuthal and the lateral directivity are usually measured and modeled separately. The azimuthal directivity is usually measured with an array of microphones on the aircraft runway in a circular shape, as seen in Figure 4.4 [63]. Lateral directivity was also measured with a set of microphones when the aircraft passed by the array of microphones [64] [65] [66].

The microphones number is not enough for the traditional method of directivity analysis; moreover, the location of the microphones were not properly designed to measure the directivity, due to limitation of available measurement sites. However, there are two very useful features in the DISCOVER-AQ data set. Firstly, the time span of the test in each single event is very long (500 seconds to 1000 seconds), which allows us to gather a large amount of information for the study of directivity. Secondly, the aircraft was flying along a spiral path near the receiver, which provides us with acoustic data and location data for various azimuthal angles and lateral angles. If we can calculate and adjust the relative location of the receiver with respect to the aircraft using the GPS data of the aircraft and the recorded pitch angle, the rolling angle, and the yield angle, most of the area around the lower semi-sphere of the aircraft could be covered with measured data. In the current study, a 3D modeling process is used that could enable the simultaneous modeling of both azimuthal and lateral directivity patterns.

For a curve on a two-dimensional plane, polynomial fitting is enough for the approximation, which is used in many aircraft directivity analyses [63,67–69]. However, for a 3D pattern, a spherical harmonic expansion method should be used instead. A similar method was previously used in reference [64] by subtracting the divergence effects and air absorption effects from the measured data, where the directivity pattern is modeled with spherical harmonic functions. The spherical harmonic functions are a complete set of functions on a sphere, which means any function on a sphere could be constructed with an array of spherical harmonic functions. The first five orders of spherical harmonic functions are used for the approximation to avoid overfitting problems.

The directivity is modeled with the functions:

$$L_{directivity} = \sum_{l=0}^{n} \sum_{m=-l}^{l} {Y_l}^m(\theta, \varphi), \tag{4.1}$$

where $Y_l^m$ is the angle spherical harmonic function on a sphere. The least square method is used for the calculation of the coefficient for each spherical harmonic term. The leading terms of spherical harmonic functions are

$${Y_0}^0(\theta, \varphi) = \frac{1}{2}\sqrt{\frac{1}{\pi}}$$

$$Y_1^{-1}(\theta,\varphi) = \frac{1}{2}\sqrt{\frac{3}{2\pi}}e^{-i\varphi}\sin\theta$$
$$Y_1^{0}(\theta,\varphi) = \frac{1}{2}\sqrt{\frac{3}{2\pi}}\cos\theta$$
$$Y_1^{-1}(\theta,\varphi) = -\frac{1}{2}\sqrt{\frac{3}{2\pi}}e^{i\varphi}\sin\theta$$

where the zero's order represents a mono-pole source, and the rest of the terms are linear dependent to multi-poles. The measured directivity are calculated first from the measured data.

$$L_{directivity} = SPL - L_{air\ absorp} - L_{impedance} - L_{divergence} - L_{doppler} - L_{ground} \quad (4.2)$$

To model the directivity correctly, the propagation effects need to be predicted and subtracted from the measured data; this can be done using the measurements carried out by Volpe. With these measurements, the meteorological data are recorded using a weather balloon together with the acoustic measurement during each event. The location of the aircraft and the receiver are conveniently recorded in every second using a GPS.

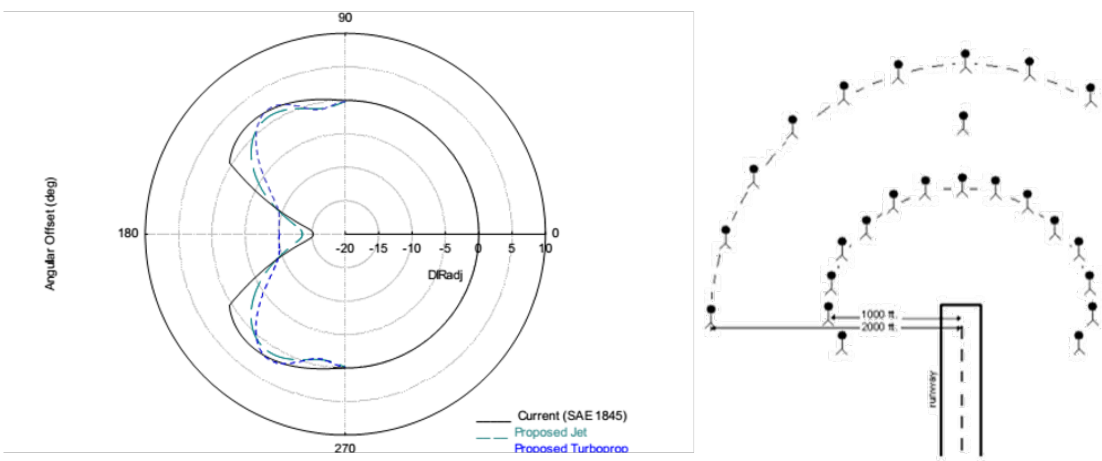


Figure 4.4. The Current and Proposed behind Start of Take-off Roll Directivity Adjustments in Azimuthal Directivity study.

**Air absorption** Air absorption is calculated according to ISO 9613. The atmospheric profile—including the temperature, pressure, and humidity measured using a

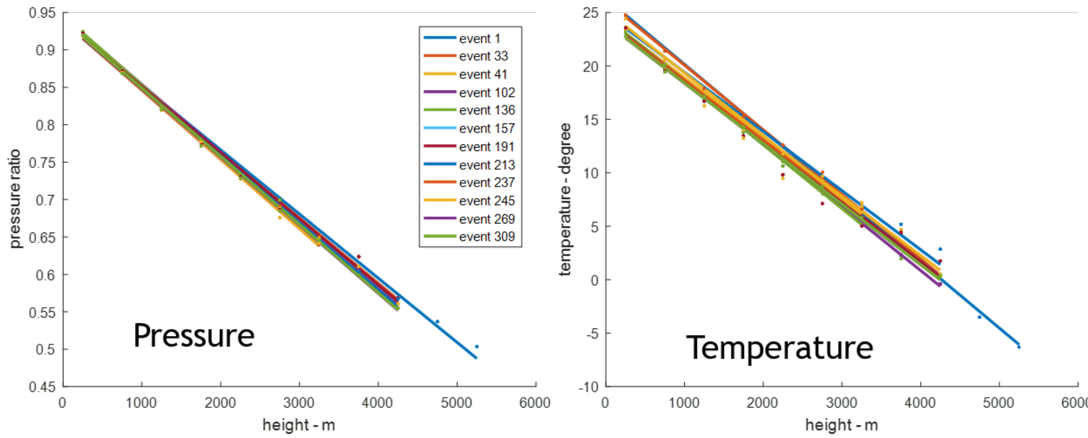


Figure 4.5. Pressure and temperature in discoverAQ data set

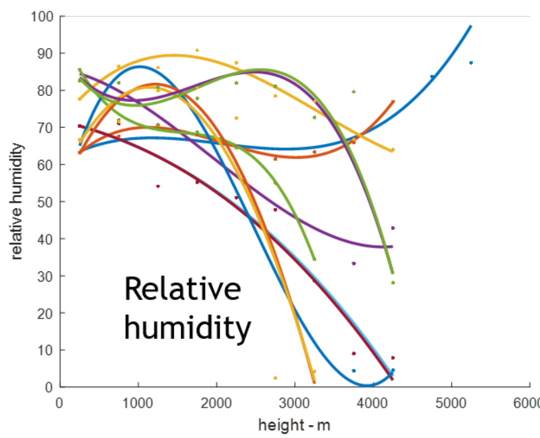


Figure 4.6. Relative Humidity

weather balloon—are modeled into stratified profiles and are used in the prediction of attenuation due to air absorption. In Figure 4.5, we can see that the pressure and temperature as well as the linear functions of height have almost the exact same shape during different events, which can be approximated using linear fits. Figure 4.6 shows both the relative humidity recorded every 500 m during different events and the polynomial fit used in the calculation of air absorption. The measurement of the relative humidity suggests no obvious pattern, and the variation of relative humidity is quite large in almost every event.

The prediction of air absorption with the above collected atmospheric data is plotted in Figure 4.7. The plot suggests that during different tests, the air absorption factors below 3 km are very close to each other in different events. At the same time, the difference could reach 1 dB/km if the sound is emitted above 3 km. The prediction is used in the modeling of directivity by subtracting the attenuation due to the air absorption from the received sound pressure level.

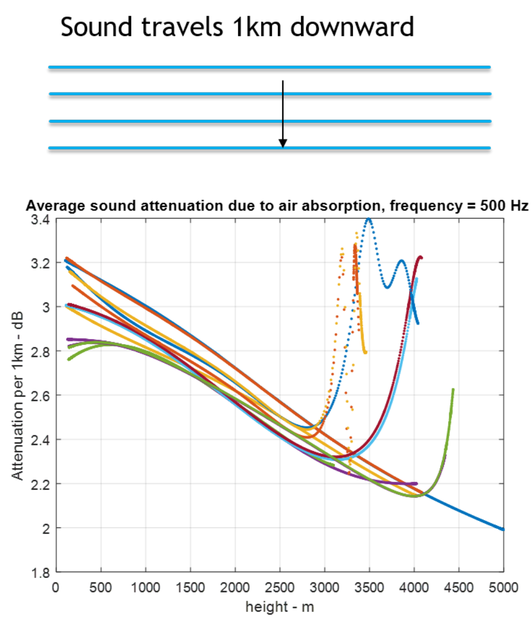


Figure 4.7. Pressure and temperature in the DISCOVER-AQ data set.

**Refraction** Refraction effect is important when either the wind gradient or the temperature is large. Figure 4.8 shows that the sound speed gradient is about 4 m/s per 1 km, and the largest wind speed gradient is 8 m/s per 1 km, which suggests a normal sunny day. Thus, the largest possible effective sound speed gradient is only equal to 12 m/s per 1 km, which is already an overestimation since the direction of the wind gradient is not necessarily the same as the direction of the temperature gradient. However, this is still a rather small gradient for sound propagation with

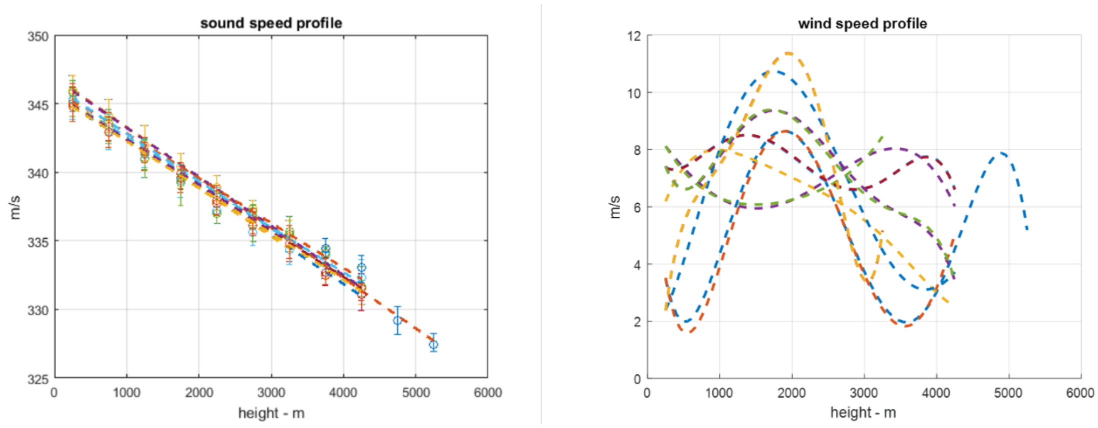


Figure 4.8. Sound speed profile and wind speed profile for downward spiral events.

negligible influence to the total sound field. [26] As the result, the refraction effect is not considered in the prediction.

**Acoustic impedance** Acoustic impedance is calculated according to the AEDT manual [70]. The acoustic impedance is calculated using the temperature and air pressure recorded by the weather balloon every 500 m above the ground. The measured results are plotted in Figure 4.9 and are modeled with a linear function of height. The largest difference caused by acoustic impedance is around 2 dB for a source at 5 km above the ground.

**Divergence** Divergence effect is evaluated with $20log_{10}(1/R)$ where $R$ is the distance from the source to the receiver. The difference between the distances of the direct wave and the reflected wave is ignored due to the lack of interference effect in far range propagation.

Ground effect is calculated with a locally reacting solution due to the point source, as mentioned in Chapter 1; Delany's single parameter impedance model is used with a ground impedance of 200k Pa m s$^{-2}$, which is a common value for grassland [4].

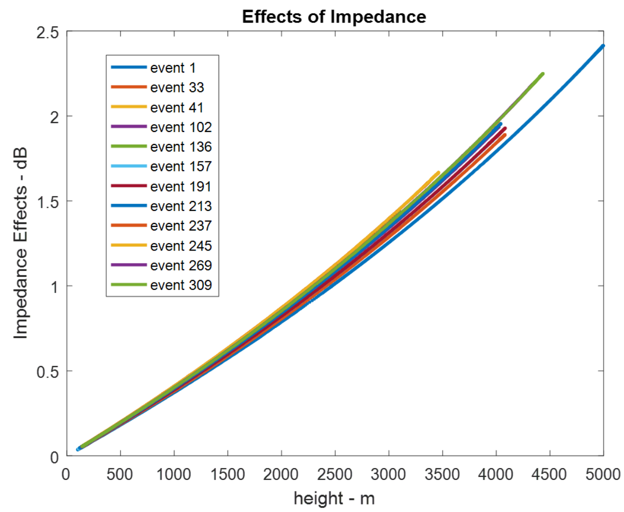


Figure 4.9. Sound speed profile and wind speed profile for downward spiral events

**1/3 octave bands and spherical harmonic regression** The 1/3 octave band provided by the FAA spans from 6 Hz to 20 kHz with 36 bands in total. The bands below 4 kHz are of interest in outdoor sound propagation studies since the air absorption of the noise above 4 kHz is usually much too large for far field propagation. After the analysis of the data set, it can be concluded that the 1/3 bands above 200 Hz can be perfectly modeled using mono-pole, while the part below 200 Hz requires spherical harmonic fitting.

If we set the aircraft's location as the origin of our coordinate system and start to plot the relative locations of the microphone with respect to the aircraft, many of the regions on the lower semi-sphere can be covered with the path, as we can see in Figure 4.10. The acoustic data are then used as the target data for the regression, and the spherical harmonic functions are used as the basis functions for each band with a frequency below 200 Hz. An example is shown in Figure 4.11, in which the 63-Hz band is fitted with spherical harmonic functions. All the comparisons for the other events show similar results and will not be plotted here.

After the modeling with the linear regression, the calculated spherical harmonic coefficients are used for predicting the sound pressure level for other events, and the

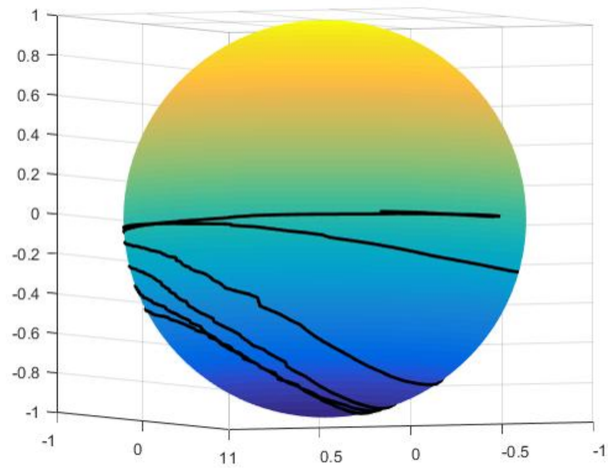


Figure 4.10. Relative location of the Microphone with respect to the aircraft. (Aircraft is at the center of the sphere x,y,z=0)

results are shown in Figure 4.12. The predictions have a good overall agreement with the measurement; however, bad agreement exists at the end when the aircraft is very close to the ground for both events. One possible explanation for the bad fitting at the end is the attenuation caused by the terrain and the forest, but this is difficult to validate due to the lack of ground topological data.

After performing a spherical harmonic fit for all of the bands from 6 Hz to 200 Hz and using a mono-pole fit for the other octave bands, the total sound pressure level could be calculated using their logarithm sum. Figure 4.13 shows the prediction for Events 33 and 41 with the fit from data of event. The agreement is good overall, and the improvement from a mono-pole to spherical harmonic fit is obvious. The directivity of the band centered at 63 Hz is shown in Figure 4.14, where the whole lower sphere is modeled with five orders of spherical harmonic functions. The upper-sphere is not modeled due to the lack of noise data above an aircraft.

After spherical harmonic fitting, the prediction of the total A-weighted noise has been improved by more than 5 dB. At the same time, the model can be used to

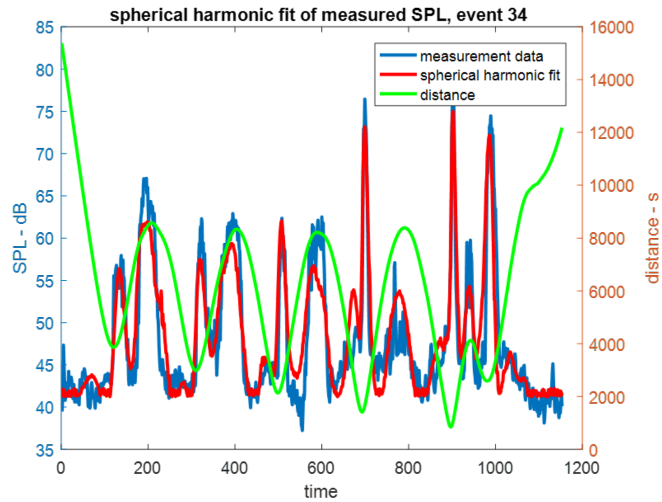


Figure 4.11. Spherical harmonic fit for the band centered at 63Hz

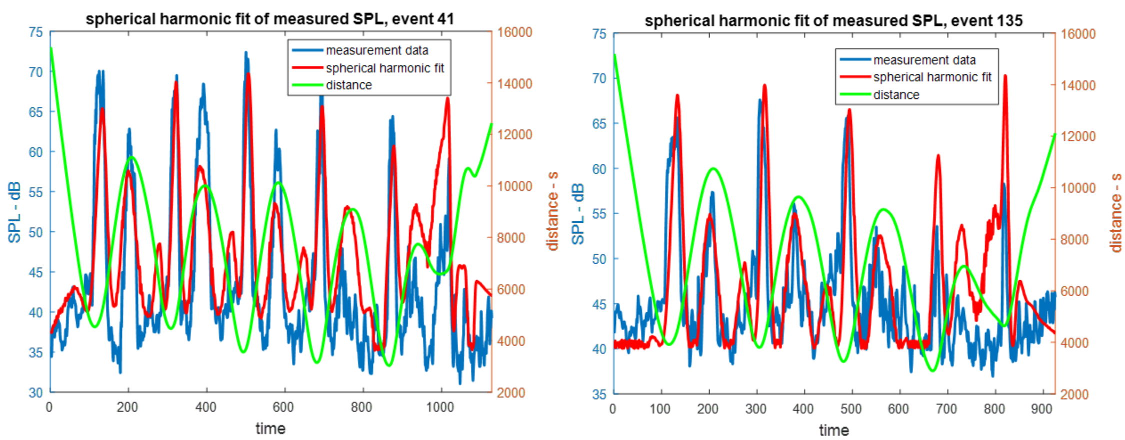


Figure 4.12. Spherical harmonic fit prediction for band centered at 63Hz

predict the noise generated by a same aircraft in a different event. The analysis of a directivity pattern of Lockheed P-3B with spherical harmonic functions is the preliminary study of the DISCOVER-AQ data set. It provides us with a powerful tool to estimate the received noise for different types of events (i.e., upward spiral, downward spiral, and level flight path).

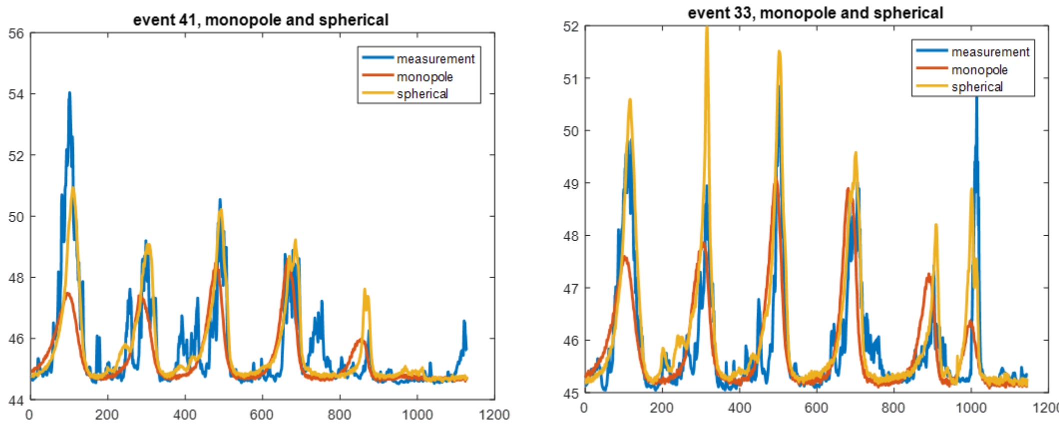


Figure 4.13. Spherical harmonic fit prediction for band centered at 63Hz

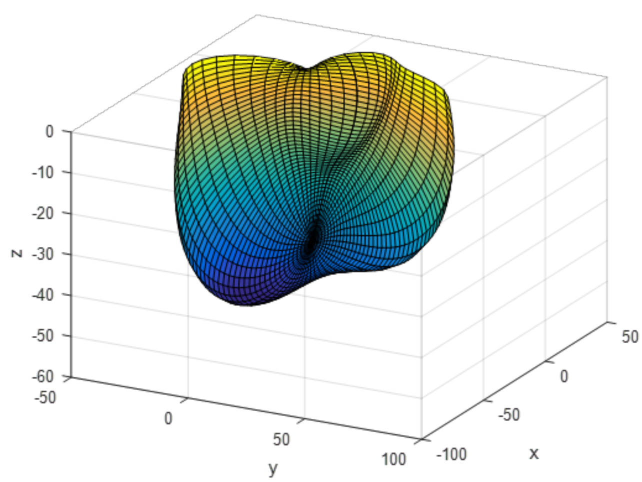


Figure 4.14. Sound speed profile and wind speed profile for downward spiral events

## 4.2 Doppler's shifting effect

After the modeling of aircraft directivity, a hypothesis was made that the strong directivity of Lockheed P-3B Orion is actually due to the Doppler effect. There are several reasons for this. First, the 1/3 octave bands with the strongest directivities are the 63 Hz band and the 78 Hz band; at the same time, the frequency of the first tonal component is about 70 Hz.

Second, the directivity is below 200 Hz, and at the same time the Doppler factor that is predicted from GPS data varies from 0.5 to 1.5, which would shift the 70 Hz sound to a range between 35 Hz and 105 Hz; this frequency range coincides with the range with strong directivity pattern. Third, the 63 Hz band and 78 Hz band have the largest sound pressure level when the aircraft is at the closest point and at the furthest point with respect to the receiver; these locations coincide with the locations with the weakest Doppler effect. All of these observations point to a same possibility that the strong directivity of P-3B Orion is mainly due to the Doppler effect. To validate the assumption and understand the directivity of the aircraft noise better, we perform an analysis around the Doppler factor.

The Doppler effect, which is caused by the motion of the sound source, will change two aspects of the noise emitted by the aircraft. The first aspect is the absolute noise level received. When the aircraft approaches the receiver, the absolute noise level at the receiver's location becomes higher; on the other hand, the noise level decreases as the aircraft recedes. This effect has been studied with theoretical modeling for decades using the Lorentz transform that was introduced from electromagnetics; several scholars have used the Lorentz transform to examine mono-pole sources and line sources above the ground [4, 35, 42]. The other aspect is the shifting effect, which shifts the frequency emitted by the aircraft by a factor that depends on both the relative location of the aircraft to the receiver and the speed of the aircraft. The effect is in the theoretical model of the sound field due to a moving source; however, it is rarely studied using measurements, especially in the area of aircraft noise propagation. Although the Doppler shifting effect cannot change the sound pressure level, it does change the whole spectrum of the noise in relation to human perception. A low pitch noise component generally has a smaller annoyance than a noise component with higher frequencies if A-weighting is used; this approach is considered one of the

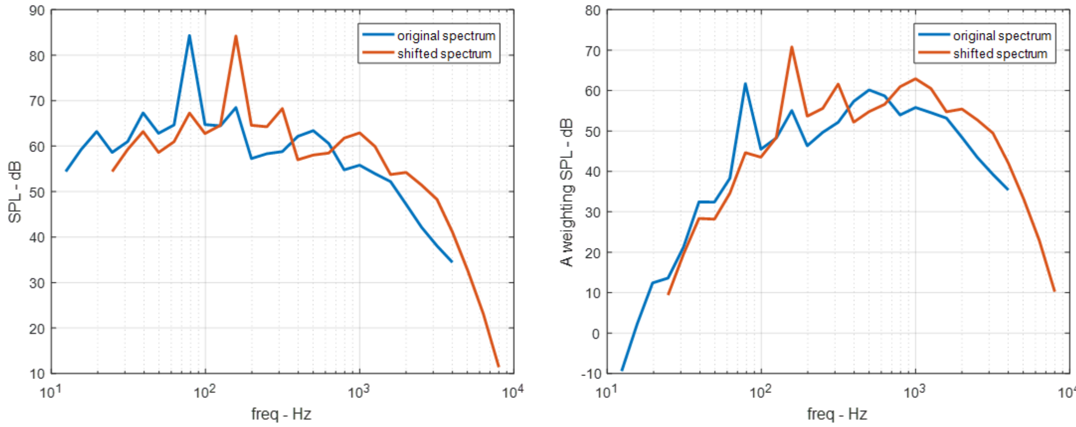


Figure 4.15. Error in A-weighting due to frequency shifting with unweighted 1/3 Octave SPL (left) and A-weighted SPL (right).

most popular methods for including the loudness perceived by the human ear when measuring sound pressure level.

The Doppler shifting effect has a major influence on the noise received on the ground if an A-weighted sound pressure level is applied in the evaluation. The effect is demonstrated in Figure 4.15 with the spectra taken from the Lockheed P-3B Orion. The total A-weighted SPL changed from 62 dB to 66 dB after a positive frequency shifting with a Doppler factor around 2, which is very common for an en-route aircraft. In this section, the analysis focuses on the relationship between the Doppler shifting effect and A-weighting.

### 4.2.1 Calculation of Doppler's factor

The Doppler factor can be calculated using the location data of the sound source and the receiver. When the aircraft's velocity is not available, the value is approximated with a derivative of GPS coordinates. The equations include

$$Mr = \frac{\vec{R}_\tau}{|\vec{R}_\tau|} \cdot \frac{\vec{v}}{c_0} \tag{4.3}$$

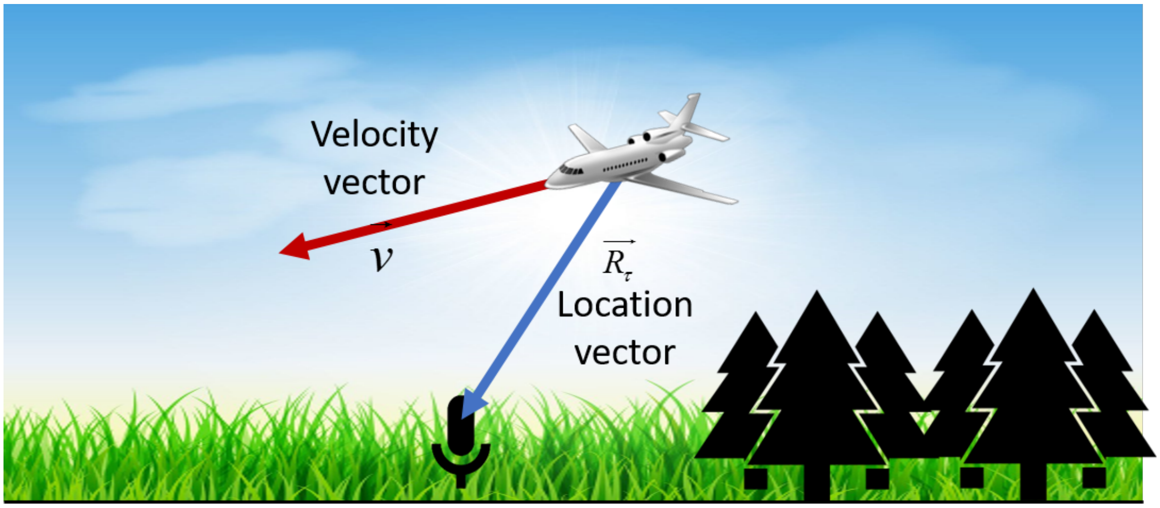


Figure 4.16. Geometrical representation of the problem.

and

$$D = \frac{1}{1 - Mr} \tag{4.4}$$

where $D$ is named as the Doppler factor in the thesis. The Doppler effects—namely the Doppler augmentation and shifting effects—can be calculated using this factor. Acceleration is only added into the equation if it is large enough compared to the absolute speed of the sound source [4]. $\vec{R_\tau}$ is the vector from the sound source to the receiver, while $\vec{v}$ is the velocity vector of the aircraft and $c_0$ is the speed of sound. The two vectors and the geometry can be found in Figure 4.16.

The Doppler shifting effect can be calculated with another simple equation:

$$L_{Dop} = 20log_{10}D^2.$$

Doppler's shifting effect can be calculated with another simple equation

$$f_{shifted} = D \cdot f_{emmitted}$$

It is possible to calculate the effect using this equation, although the theoretical solution for a moving source above a locally reacting ground has already been derived using a fast asymptotic form [71]. The effect of shifting in aircraft noise prediction was always omitted and not properly studied before. In Section 4.2.2, simulation is used for the analysis of this effect.

### 4.2.2 Simulation for flyover events

To analyze the effect on the noise received at ground level due to Doppler shifting, we performed simulations based on the model explained in the last section. Two distinct spectra are used for a detailed analysis; we also used 89 aircraft spectra for different spectral classes provided by FAA to analyze the sound exposure level of simple flyover events. The reason why some spectra are more sensitive to the Doppler effect are explained with these simulation examples.

**Air absorption and Doppler's effect** The Doppler effect changes the frequency of the noise received, meaning that all the propagation effects which depend on the frequency will be changed; such effects include air absorption and ground effect. During the long distance propagation of a sound wave, air absorption is one of the most important factors, and the absorption ratio varies greatly from a low frequency to a high frequency. In this section, the effect relating to air absorption is studied using level-fly simulations. The height of the sound source is set to 1 km above the ground, and the receiver is on the ground with $z = 0m$. The source starts from $x = -6km$, and it then goes toward a positive direction with a Mach number of 0.5. The air absorption is calculated according to ISO-9613 with the temperature set to 15 Celsius degree, the relative humidity at 50%, and the atmospheric pressure ratio at 0.77. In this study, the 500-Hz and 99-Hz sound mono-pole sources are used; results are shown in 4.17. In the approaching region, the air absorption is increased, and in the receding region, the air absorption is decreased. The effect is stronger for the 500-Hz sound due to a higher overall absorption for higher frequency noise. For real world prediction, the air absorption depends highly on the humidity of the air;

as a result, the effect of Doppler shifting on air absorption could be higher or lower depending on the atmospheric condition when the measurement is done.

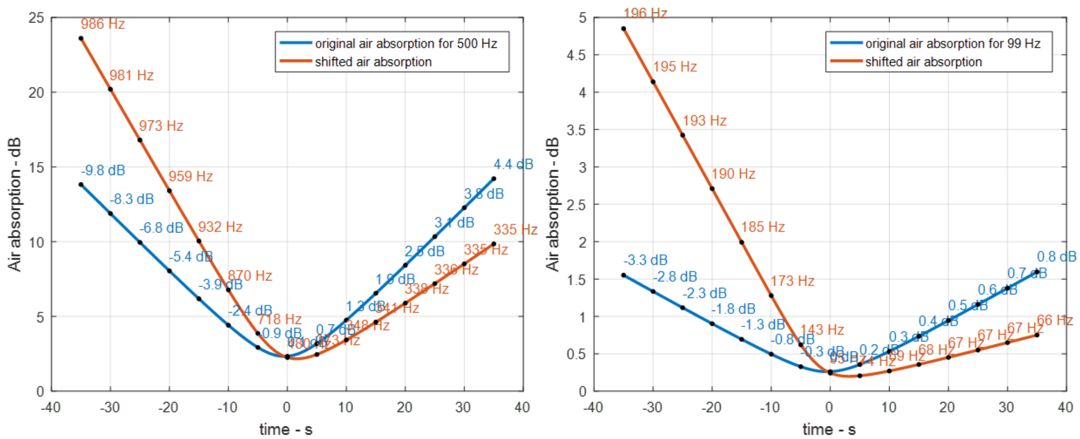


Figure 4.17. The Doppler effect and air absorption at 500 Hz (left) and 99 Hz (right).

**Height, sideline distance and Mach number** The Doppler effect depends on the Doppler factor, which can be calculated using the location vector and the velocity vector. As a result, the height, the sideline distance, and Mach number will have direct influences on the Doppler factor. The spectrum of the P-3B is used in the simulation using Mach numbers 0.5 and 0.8. The atmospheric condition is the same as the one used in Figure 4.17. Figure 4.18 shows that the Doppler shifting effect increases with the Mach number and decreases with height and distance. For aircraft flying with a Mach number of 0.5, the Doppler shifting effect can be basically ignored when is the sideline distance or the height is larger than 10 km. However, during the arrival and departure of the aircraft, the effect is predicted to be very strong for the spectrum of Lockheed P-3B (i.e., the aircraft used in the analysis).

**Spectrum and Doppler's shift** The propagation of aircraft noise depends highly on the spectrum of each type of aircraft, since many effects in the process of prop-

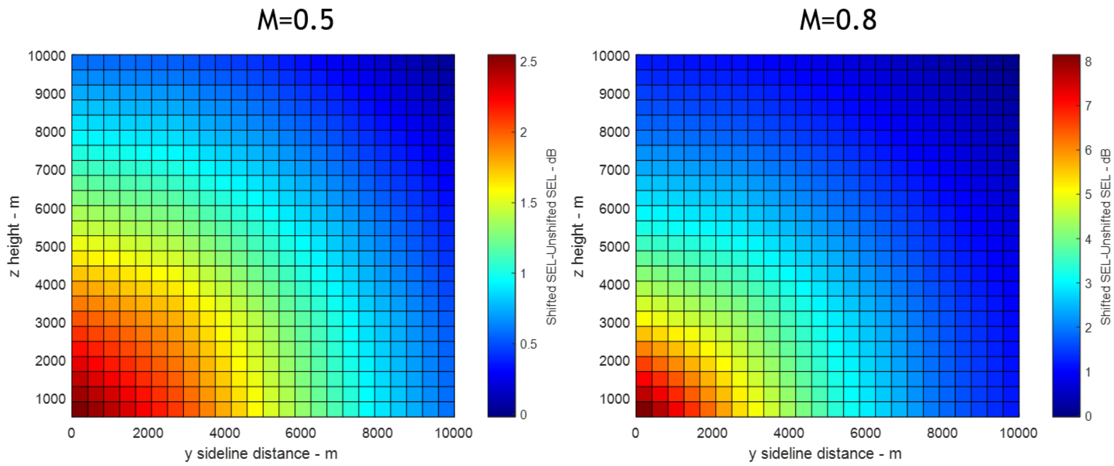


Figure 4.18. The Doppler effect and geometry for Mach numbers 0.5 (left) and 0.8 (right)

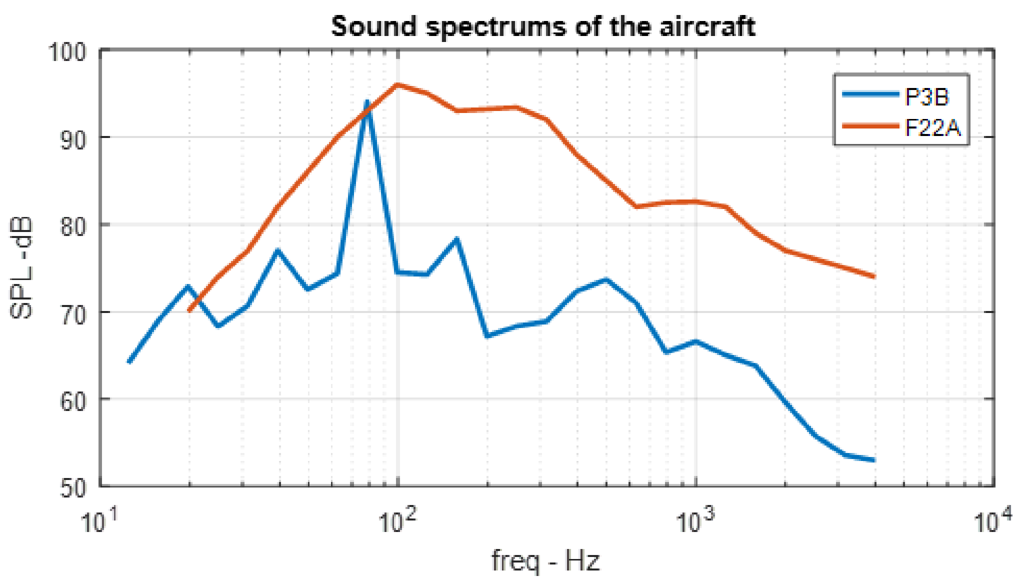


Figure 4.19. spectra of P3B and F22A

agation are frequency dependent. For example, aircraft with jet engines tend to produce more high-frequency noise, which is recognized to be more disturbing with a higher loudness; however, due to the large air absorption coefficient of a high-frequency sound, the high-frequency component will not travel too far away from the noise source. On the other hand, the low pitch noise generated by a modern propeller-driven aircraft could travel miles away without obvious reduction except the divergence effect. To analyze the effect of Doppler shifting on the noise received at ground level, we performed simulations based on the model explained in the last section. Two distinct spectra are used for conducting a detailed analysis, and 89 aircraft spectra with different spectral classes are used for analyzing the sound exposure level of flyover events. The reason why some spectra are more sensitive to the Doppler effect are explained with these simulation examples.

Two aircraft with two distinct spectra are used for comparison in Figure 4.19. Lockheed P-3B has an obvious tonal component of around 70 Hz, while Lockheed F-22A has a very smooth spectrum with no apparent tonal component, which means that none of the sound pressure levels of the 1/3 octave band is obvious enough to surpass the sound pressure level of the adjacent bands. Aside from this, most of the energy for both spectra lies below 1 kHz.

Figure 4.20 shows the predicted A-weighted SPL with the Doppler shifting effect. The 1/3 octave band in red has the largest sound pressure level among all the bands. When time is equal to zero, the aircraft is positioned just above the receiver. When time is a negative value, the aircraft is approaching the receiver, and when time is a positive value, the aircraft is leaving the receiver. It can be observed that the location of the red blocks moves towards the left direction as time increases, which is due to the Doppler shifting effect; consequently, the range of the shifting spans about four blocks. Shifting in the frequency domain will cause the total A-weighted SPL on the ground to change. In contrast to Figure 4.20a, the shifting effect in Figure 4.20b is not as obvious, which is due to a smoother spectrum of F22A.

In Figure 4.21, the prediction with and without the Doppler shifting effect are compared for the two aircraft. The predicted A-weighted SPL with a Doppler shifting effect is larger than that without shifting when the aircraft is approaching. The difference between the two lines reduces to zero when the aircraft is directly above

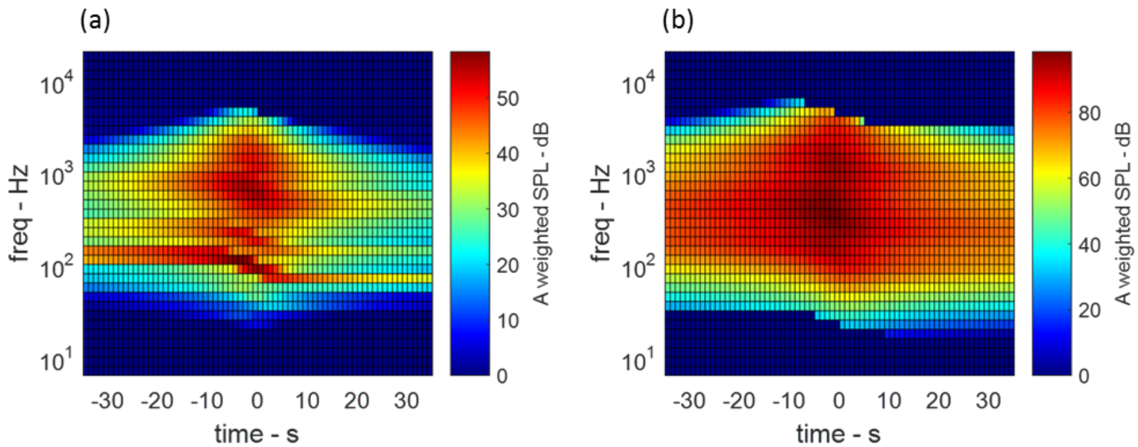


Figure 4.20. Predicted A-weighted spectrograms for (a) Lockheed P3-B Orion and (b) Lockheed Martin F22/A raptor (right). Flyover event with source height at 500 m and receiver height at 1 m, Mach number of 0.3 and sideline distance of 0 m.

the receiver; it continues to decrease to a negative value as the aircraft moves away from the receiver. The comparisons between Figure 4.21 a & b show that the impact of Doppler shifting on the P-3B is larger than that on the F-22A. The reason for the difference in the impacts is due to the shapes of the spectra of the two aircraft; the spectrum of P-3B has an obvious low frequency peak at 70 Hz. When the Doppler effect shifts the peak from 70 Hz to 110 Hz, the weighting factor according to the A-weighting curve changes by 6 dB. This means that a noise component with the same sound pressure level is around 6 dB louder with a frequency of 110 Hz than that with a frequency of 70 Hz. On the other hand, the smooth feature of the spectrum of the F-22A makes the shifting process much gentler. For example, the shifting will have no effect to white noises because the sound pressure level is the same anywhere for white noises.

Since the Doppler shifting effect is decided by the spectrum of the noise source, it might be interesting to analyze the impact of the Doppler shifting effect on different types of aircraft with various shapes of spectra since analyzing the uncertainties due

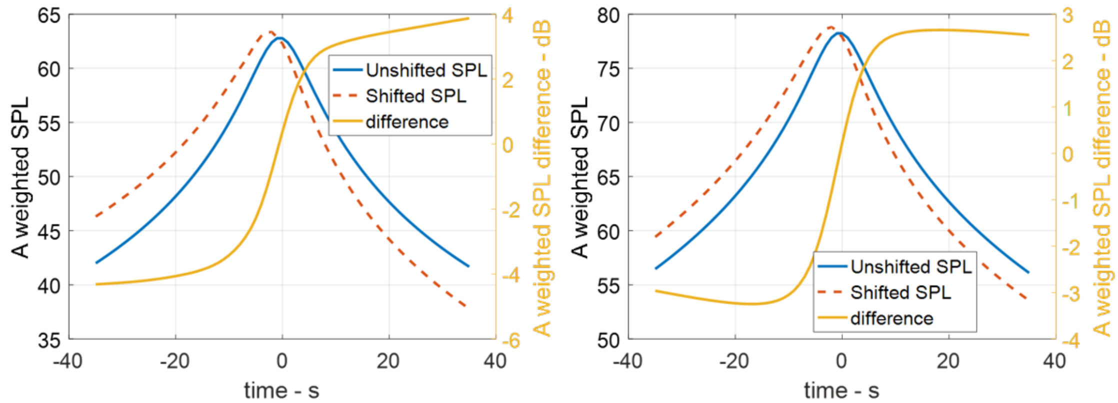


Figure 4.21. Prediction with and without a Doppler shifting effect for the P-3B (left) and F-22A (right) aircraft. Red dash means prediction with shifting effect; yellow solid line shows the difference between the predictions.

to the Doppler shifting effect is one of the main focuses in the current research. In the data set from the FAA with 89 unique spectral classes, each spectral class represents a group of aircraft with similar spectra, and the details about the types of aircraft can be found in the user manual of the INM.

To compare the effect of the Doppler shifting effect to each aircraft class, the sound exposure level is calculate in each simulation. Sound exposure level is a widely used value for evaluating the overall noise impact of one event, and it is an appropriate and convenient value that can be used to perform the comparison. According to an earlier explanation in this section, different spectra tend to produce different results after the Doppler shifting effect is applied to the model. Each of the 89 classes is used as a spectrum of the sound source in the prediction of sound exposure level. The influence from the Doppler effect may not be very prominent if SEL is used as the indicator; this is because the Doppler effect increases the approaching noise and decreases the receding noise at the same time in a whole flyover event. The two types of influences cancel one another out to some extent during the integration of the total

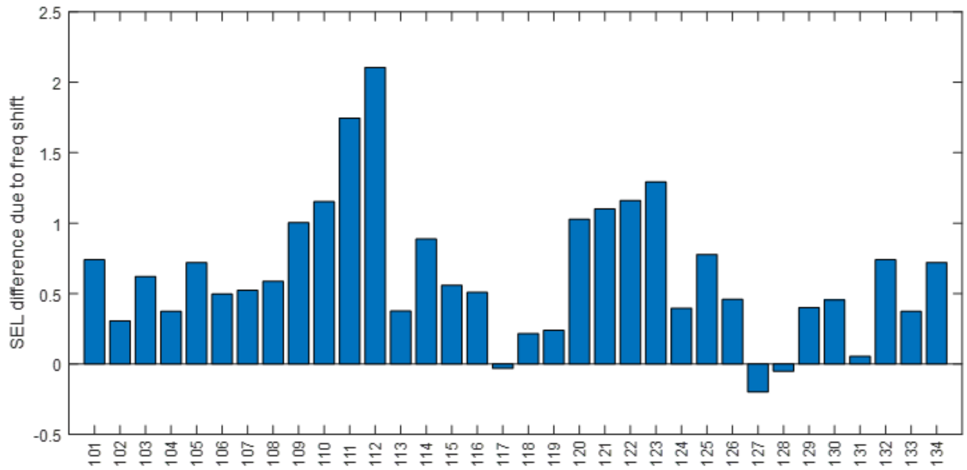


Figure 4.22. Error in A-weighted SPL caused by Doppler's shifting effect for departure classes

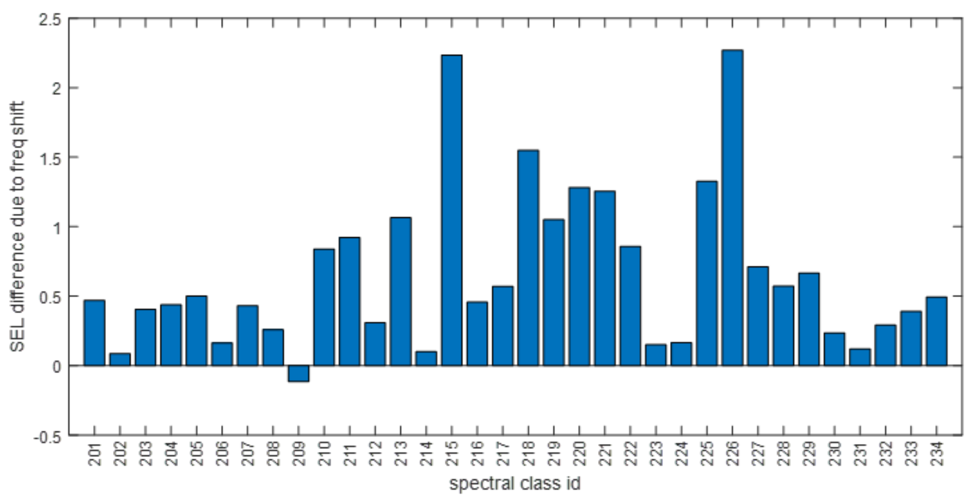


Figure 4.23. Error in A-weighted SPL caused by Doppler's shifting effect for arriving classes

sound exposure level, which gives a smaller total difference in SEL than we initially thought.

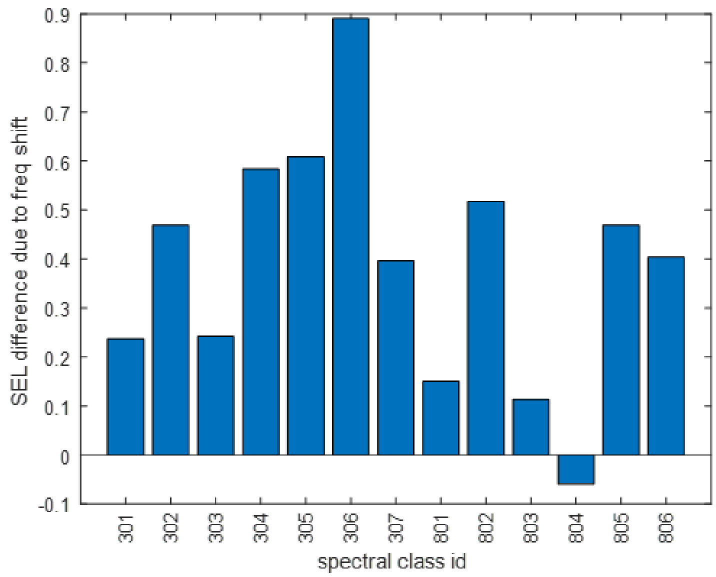


Figure 4.24. Error in A-weighted SPL caused by Doppler's shifting effect for arriving classes

The 89 classes are grouped into three categories, namely departure, arriving, and flyover. For example, class 101 represents the departure event of civil aircraft Boeing 737 and some aircraft with a similar departure spectrum. Each class represents at least one type of aircraft.

Each spectrum of the 89 classes is used as the source spectrum in the prediction of a flyover event. The source height is set to 1 km above the ground, and the Mach number is set to 0.5. For the calculation of air absorption with the temperature set to 15 Celsius degree, the relative humidity at 50% and atmospheric pressure ratio at 0.77. In the calculation of the sound exposure level, we use 200 s before and after the overhead moment in the calculation of SEL. The predicted sound exposure level is compared with the sound exposure level without including the Doppler shifting effect into the model. The difference is calculated using the following: The predicted sound exposure level is compared with the sound exposure level without including the Doppler's shifting effect into the model. The difference is calculated with

$$E = SEL_{shifted} - SEL_{noshifting}$$

Figure 4.22 shows that for the geometrical and atmospheric condition used in the simulation, the total error is between 2 dB to around 0 dB. This indicates an underestimation of the SEL if the Doppler shifting effect is not implemented. Figure 4.23 shows similar information as Figure 4.22. Among the spectra, class 117 and class 209 have the smallest influences that are caused by shifting, while classes 112 and 226 have the largest impacts due to the shifting (see Figure 4.25 for the plots of the four mentioned spectra). The two most affected spectra have obvious peaks around 100 Hz, which could make a great difference in the calculation of the Doppler shifting effect. The two least influenced spectra are relatively smooth, and most of their acoustic energy lies above 1 kHz.

This simulation agrees well with our assumption that the spectra with obvious low frequency peaks are more likely to be influenced by the shifting effect. Additionally, the simulation result of overfly events is shown in Figure 4.24; the error varies from 0.5 dB to 0.9 dB, and no obvious difference is observed in the flyover classes from the departure and arriving sets.

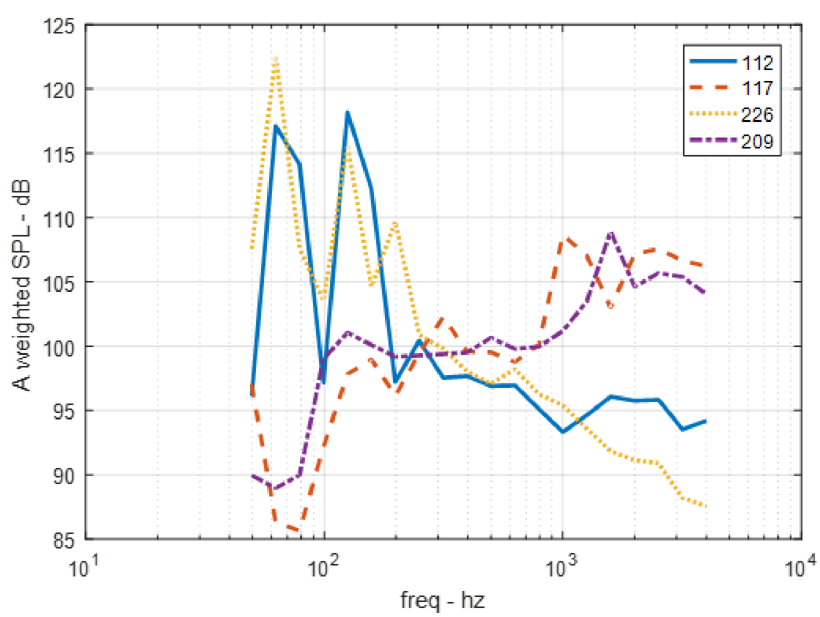


Figure 4.25. spectra of the four classes with maximum and minimum inflences

### 4.2.3 Doppler's effect and discoverAQ dataset

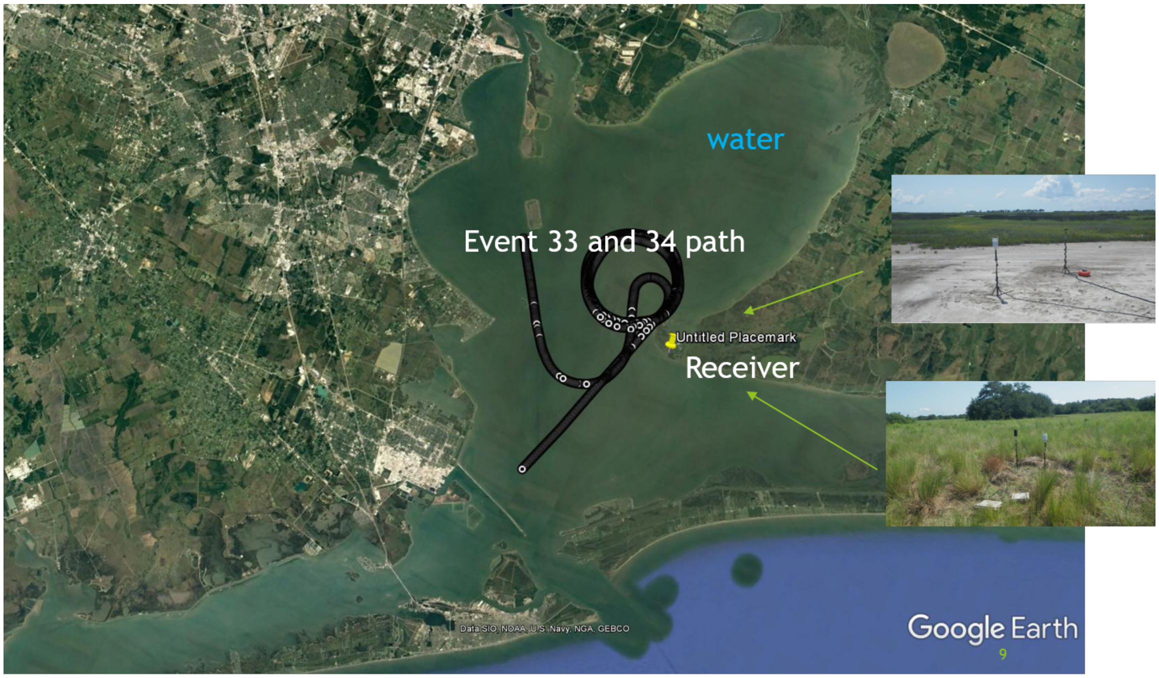


Figure 4.26. Aircraft test path for event 33 and 34

The DISCOVER-AQ data set is a comprehensive data set measured by Volpe Center in support of the Federal Aviation Administration (FAA) in 2013. The high-quality data included 95 events that were collected from a variety of test aircraft operations. The data set also includes meteorological data measured with a weather balloon and with the equipment on the aircraft. Two aircraft were used during the DISCOVER-AQ flight tests: the Lockheed P-3B Orion and the Beechcraft B-200 Super King Air. The air absorption is calculated using stratified the temperature, pressure, and humidity data that were recorded with the weather balloon. The wind is also recorded with the weather balloon in order to analyze the refraction effect together with temperature gradient. The flight tests are recorded on sunny day with a small wind gradient; the average effective sound speed gradient is around $2 \times 10^{-5}$, which is rather small if the ray tracing prediction is used in the calculation. In

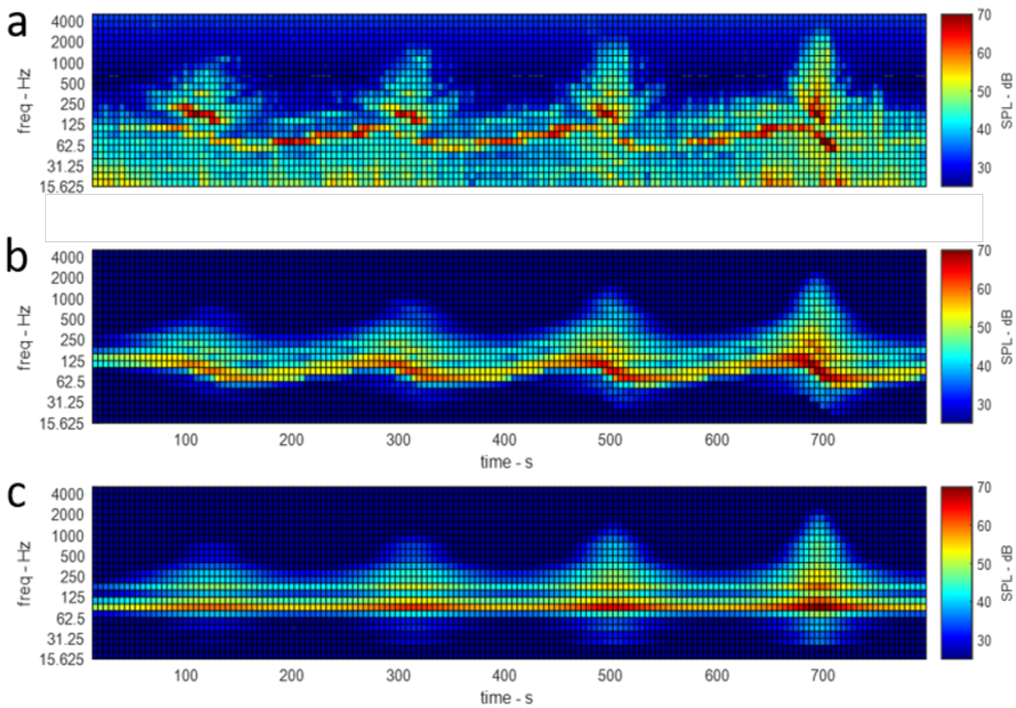


Figure 4.27. Comparison of spectrogram for Event 33. (a) Measurement data; (b) Prediction with Doppler's effect (c) prediction without Doppler's effect.

this simulation, the refraction effect and turbulence are not considered. The air absorption, geometrical attenuation, and impedance difference between the source and the receiver are calculated with the atmospheric data and the GPS data that were collected during the propagation of sound.

The DISCOVER-AQ data set has mainly two types of operational paths in the test—a spiral path and a flyover path. During each event, the sound pressure levels are recorded on the ground at several recording sites. The paths for Events 33 and 34 are shown in Figure 4.26 as an example. Although the aircraft is flying above water, the microphones on the ground are quite far away from the coastline, and no reflection from the water surface needs to be considered. Two measurement sites—namely one on the grassland and one on the hard dirt—are also shown in Figure 4.26.

Figure 4.27 shows that the octave band with the highest SPL varies between 62.5 Hz and 125 Hz in this test operation. Obvious Doppler effects could be observed in the measured data. Subplot c shows the prediction without the Doppler shifting effect; this subplot produces a poor agreement with subplot a. In subplot b, the Doppler shifting effect is used in the prediction. It is obvious that the agreement between a and b is much better than that between a and c. Figure 4.27 also shows that the directivity we observed in Section 4.1 is actually due to the Doppler factor. The disappearance of the 63 Hz band sound could be explained using Figure 4.27b.

In the section, the Doppler shifting effect on an A-weighted sound pressure level is analyzed with a simulation and a comparison using measurement data provided by FAA and Volpe. The difference in the weighted sound exposure level caused by the Doppler shifting is between 0 dB to 2 dB. Doppler shifting is validated with the comparison. A maximum difference of 3 dB due to Doppler shifting is predicted with simulation. There are a few limitations in this study. We use a mono-pole model in the prediction and analysis; however, it should be noted that directivity exists in any aircraft, and it is different for different types of aircraft. Generally, the noise behind the aircraft is larger than that in front of the aircraft due to the engines' layout and shielding effect of the aircraft's body. Most of the available source spectra data measured in the tests have been influenced by the Doppler effect, which makes it difficult to isolate the engine installation effect and the Doppler effect. Thus, it is necessary to include the directivity effect in the prediction model in the future for a more accurate modeling.

The available spectrum data are all 1/3 octave band noise data. The exact location of the tonal component cannot be accurately identified due to the bandwidth of each 1/3 octave noise band. In the modeling of the spectrum, each band is assumed to have the same sound pressure level everywhere within each band, which could sometimes produce large errors if pure-tone noises exist, and pure tonal noises are common for propeller-driven aircraft. It is preferred to use spectra with a better resolution in the future analysis.

## 4.3 Uncertainty analysis

In Sec. 4.2, the measured data in the DISCOVER-AQ were analyzed by comparing the predicted sound pressure level with the measured levels. When analyzing the uncertainty of the propagation effects, a major difficulty found is the varying sound power. Although a constant power setting was required during each flight test, the sound source power changes with time randomly and cannot be accurately predicted. The noise level was recorded in the aircraft cabin during the test. However, the transmission loss between the inter part of aircraft and outer part of it made it impossible to use the cabin noise as the source noise. Another problem of the source is that there is no reliable model to calculate the source power with the available data such as using the power setting, air speed, and aircraft speed; without knowing the accurate sound source, the analysis of the propagation effect is heavily influenced by the source uncertainty.

To deal with these source uncertainties, the method of subtraction is used in this section to minimize the influence of source uncertainties on the propagation uncertainties.

### 4.3.1 Total uncertainties in level flight data

The best test data for uncertainties analysis are level flight measurements. The most important advantage of using level flight data is the similarities between different level flight test. Although the power of the source cannot be kept the same for different level flight tests, the paths are almost the same unlike the spiral events, where the curvature and the radius of the circular paths can be very distinct from each other even for two adjacent loops. It is important to remember that the curvature and radius of the path have a great impact on the total sound exposure level and on the maximum sound pressure level recorded on the ground.

Before and after each upward spiral event, there is a section of level flight event where the P-3B aircraft is moving at a constant speed with an approximately constant height. This type of data is more convenient to use than other types due to its simple feature and its relatively more constant source power. Aside from this, there are more similarities between two different level flight events than between two adjacent loops in a same spiral event.

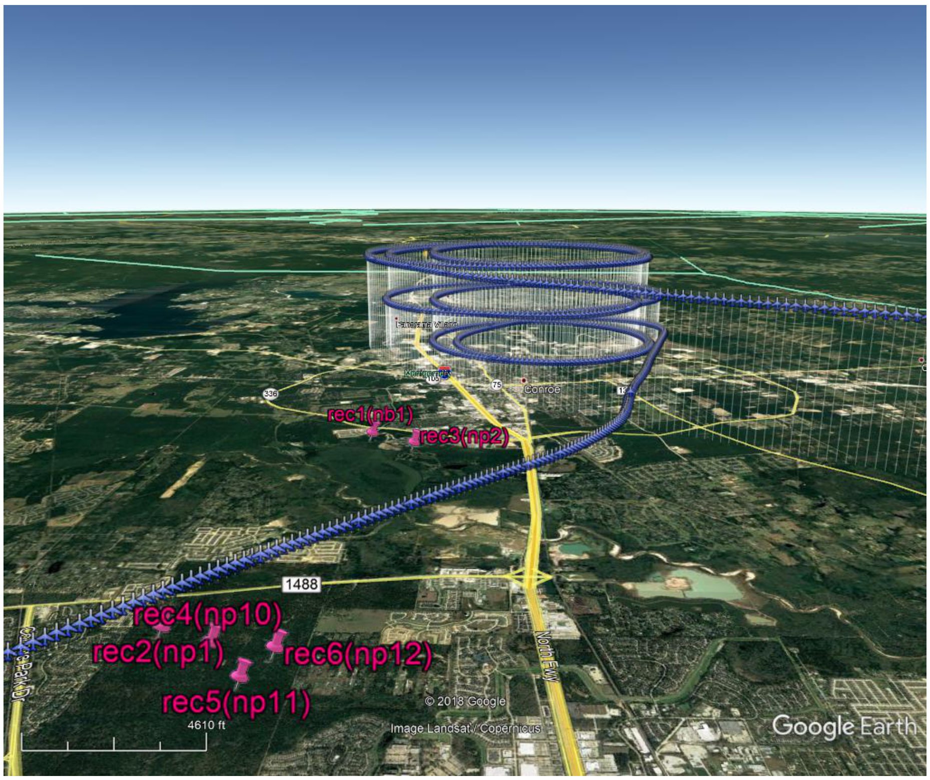


Figure 4.28. Flight path and receivers' locations for the level flight (i.e., Events 279–284) in the DISCOVER-AQ measurement plotted with Google Earth.

Fig. 4.28 presents detailed receiver locations and a 3D level path for an upward spiral event near the city Conroe. There is one level flight path before the spiral section and one after the spiral. The level flight path before the spiral path at low elevation has good signal to noise ratio due to its short distance to all the receivers that are marked with red pins in the figure. There are 11 different groups of similar level flight tests; each was recorded by four to six receivers located in the open area of a forest region in order to avoid the noise of nearby noise activities. The atmospheric profiles are recorded by nearby weather balloons for predicting the air absorption coefficient.

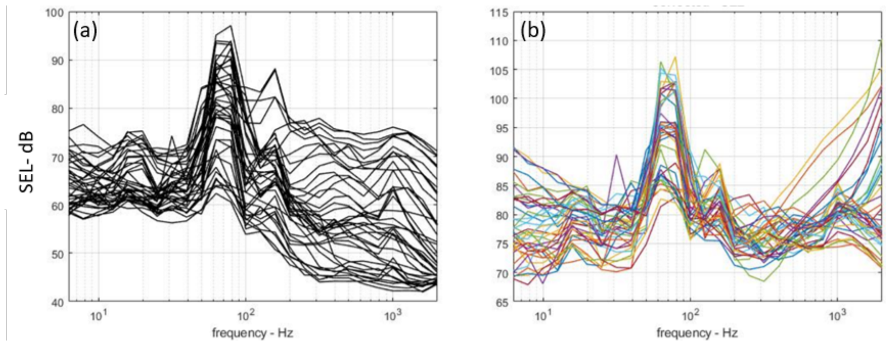


Figure 4.29. Uncorrected (left) and corrected (right) SEL level during level flight of P3B.

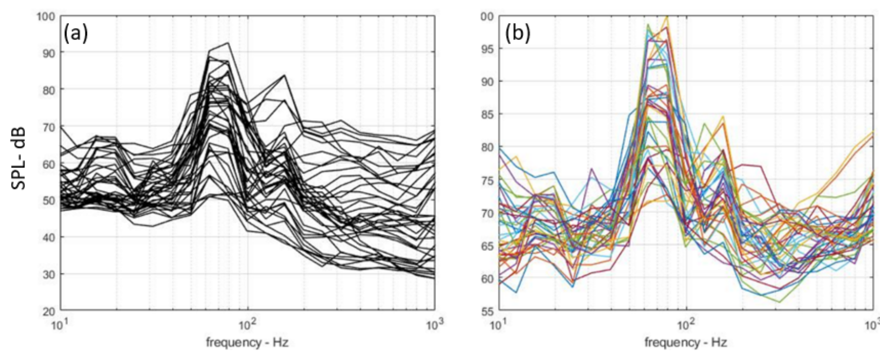


Figure 4.30. Uncorrected (left) and corrected (right) max level during level flight of P3B.

A total of 62 level flights events in the 11 groups were recorded, and 41 of them have satisfying signal to noise ratio. The SEL and max level during each level flight are plotted in Figures 4.29a and 4.30a. Here, it can be observed that the region above 500 Hz is heavily influenced by background noise since the distances between the aircraft and the receivers are between several hundred meters to several thousand meters. On the other hand, the noise components near the blade pass frequency (i.e., roughly 70 Hz) are less influenced by background noise and air absorption due to a much lower attenuation rate for low frequency sound and a much better signal to noise ratio for blade pass frequency. As a result, the blade pass noise could travel a farther distance than the rest part of the emitted noise generated from the P-3B aircraft. The average power setting during the level flights is 1429.2 SHP (shaft horsepower) with a 312.3 SHP standard deviation. The recorded power setting for each event can be found in Table 64 of the DISCOVER-AQ report [62].

The sound pressure level with both divergence and absorption attenuation corrected are also shown in Figures 4.29b and 4.30b. A similar approach was previously used in an analysis on the non-linear effects of jet noise propagation [72]. Although the two types of the most predictable and common attenuation are corrected, the noise level for each level flight still has a large variation near the blade pass frequency—the variation was in fact more than 20 dB for both SEL and the maximum SPL. These uncertainties are most likely caused by both the source uncertainties and the propagation uncertainties at the same time, and there is no practical way to separate them from each other with the available data. However, we can have an overview of the overall uncertainties in the measurement.

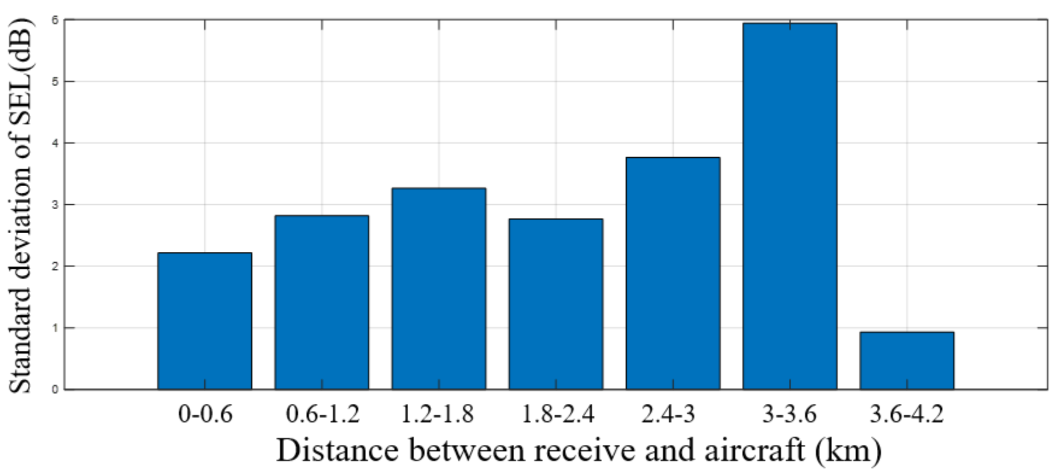


Figure 4.31. Standard deviation vs. distance for level events

In Figures. 4.31, the total standard deviation for the sound exposure level are grouped according to the distance. The increasing trend with distance is obvious; as distance increases, the influences of the propagation effects—such as turbulence, inhomogeneous medium and ground surface—also increase due to a longer propagation distance, and all these contribute to increasing the total variation of the received noise. The sudden drop at 3600 m to 4200 m can be explained by the influence of the background noise in the forest during the test. For distances above 3600 m, the aircraft noise emitted by the P-3B decreases to a level close to the background noise in the area, which is supposed to have a very small variation during the test. The variation in the figure contains not only the propagation effect but also the source uncertainty. This suggests that the total uncertainty of the received noise generally increases with the distance until the aircraft noise becomes indistinguishable from the background noise.

In Figures. 4.29 to 4.31, the analysis includes both the propagation uncertainties and the source uncertainties. Comparing the levels between different group of events will inevitably introduce errors caused by the source uncertainties. Although most of the power setting are recorded during the level flight, there lacks a reliable model to generate the sound field based on the available data. The variance or error in the source modeling will also influence the propagation analysis since there is no practical way to distinguish the source modeling error from the propagation effect based on the available data. One of the best available approaches for propagation analysis is through the method of subtraction within each group of flight events that have a same flight path but with different receiver locations. By doing so, the variation of acoustic source can be minimized since they share the same noise source in the same flight test.

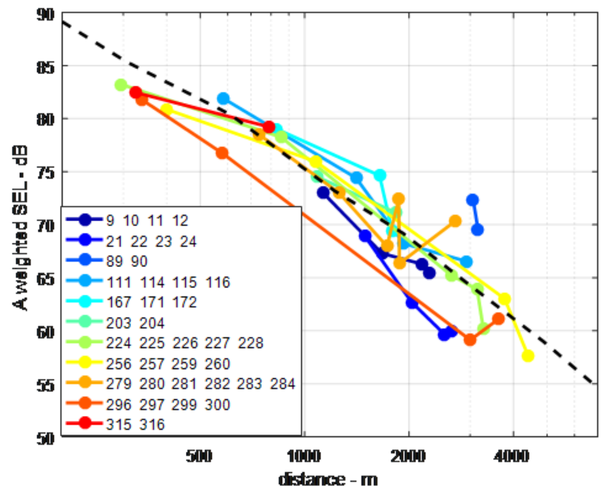


Figure 4.32. Sound exposure level for level flights vs. NPD.

### 4.3.2 NPD and level flight data.

Level flight is widely used for building aircraft noise models. In the AEDT, the prediction process is based on the noise-power-distance (NPD) curve, which contains the maximum sound pressure levels and the exposure-based levels for 10 different reference distances and at least two different power settings. For distance and power settings that are different from those given in the database, interpolation and extrapolation methods are used to generate the required predictions. According to the AEDT user manual, NPD data is extrapolated from one flight test measurement following the procedure in the SAE-AIR-1845 in a situation where there is standard atmosphere condition and aircraft speed. For a comparison, Figure 4.32 shows the NPD curve at the 20% power setting for the P3 aircraft using data extracted from the AEDT database. The focus of the study in this section is the decaying rate of the NPD curve instead of the absolute value of the curve due to the consideration of the source variation.

Four corrections were applied here before comparing the measured data with the NPD data because we need to standardize other data (e.g., geometry, atmosphere profile) to the NPD condition. First, the impedance correction is set to the reference condition based on the procedure in the AEDT technical manual [70]. After this, we applied an atmospheric correction with the temperature, pressure, and humidity that were measured with the weather balloon following Appendix F in the AEDT manual. The atmospheric absorption was first removed with the absorption coefficients for 1/3 octave bands in the ARP5534; it is then added back with the SAE-AIR-1845 absorption coefficients that were used to generate the NPD curve. Atmospheric correction also requires the aircraft spectrum, which is normally measured according to the SAE-AIR-1845 procedure at the LAMAX location; it is also corrected to 305 meters (1000 feet) and normalized to 70 dB at 1000 Hz. The average maximum spectrum that was measured during the DISCOVER-AQ pre-measurement was used; it is supposed to contain a very weak Doppler effect, because it mostly comprises the noise emitted by the aircraft when the Doppler effect is close to zero. We then applied the duration adjustment for the exposure-based metrics using the mean speed during the tests and the reference speed (160 knots). Finally, we applied the lateral attenuation for the AEDT aircraft to account for the ground-to-ground attenuation and the air-to-ground attenuation. The total SEL is equal to

$$L_{ENPD} = L_E - DUR_{ADJ} - AA_{ADJ} - AI_{ADJ} + LA_{ADJ} \tag{4.5}$$

where $L_{ENPD}$ is the sound exposure level corrected to NPD reference condition,$L_E$ is the measured A weighted sound exposure level in the test by integrating the top 10dB sound. $A_{ADJ}$ represents the air absorption correction (SAE-AIR-1845), $AI_{ADJ}$ is the acoustic impedance adjustment, $LA_{ADJ}$ is the lateral attenuation adjustment and $DUR_{ADJ}$ is the duration adjustment. The noise fraction adjustment is not used in our calculation since the flight paths in the test are long enough to be treated as infinite, and only one segment is used in each event. The whole correction part is basically a reverse procedure based on AEDT equations.

The results for 41 different level fight events are plotted in Figure 4.32 and compared with NPD curve. The detailed modeling process for NPD could be found in DISCOVER-AQ report. [62] From Figure 4.32, we could see that the NPD has a similar decaying rate as that of the SEL curves that were measured and corrected in the DISCOVER-AQ test. Furthermore, as distance increases, the uncertainty also increases accordingly. The largest uncertainty is around 15 dB at 3000 m from the receiver.

### 4.3.3 Subtraction analysis for level flight data.

In this section, the method of subtraction is used for minimizing the influence of source uncertainties and for analyzing the pure propagation effects. There are three types of propagation models to be compared, namely the propagation model in the AEDT, the theoretical model with the Doppler effect, and the theoretical model without the Doppler effect. Here, the measured propagation effect is treated as the accurate solution. The difference between the model and the measured data is named as the error in this section.

Propagation factors in AEDT contains three terms: the NPD curve, air absorption, and lateral attenuation. The NPD curve of the P3C is used since it is the closest type available in the AEDT, which is also a P3 family aircraft. The correction of atmospheric absorption is done following the instruction in the AEDT manual. The SAE-AIR1845 atmospheric absorption is removed first, and ARP5534 absorption for 1/3 octave bands are added to each band. The total A-weighted level is then calculated by summing up each frequency band, and correction factor $AA_{ADJ}$ is calculated. (3.4.1 of AEDT technical manual) [70]. The ground effects and other attenuation effects such as refraction are included in the lateral attenuation with the distance and the elevation angle as the two parameters. A soft ground model is assumed, and this is also incorporated in the total lateral attenuation. Other adjustments such as duration adjustment and power adjustment have no influences on the propagation model since they will not change the decaying rate of NPD curve.

Lateral attenuation as a function of slant distance and elevation angle is added to the curve based on AEDT lateral correction equations for AEDT aircraft ($LA_{ADJ}$

3.4.5 of AEDT technical manual). The pure propagation effect can be expressed with the difference between two sound exposure levels:

$$\begin{aligned}\Delta SEL(d_1, d_2) = L_{AE}(d_1) + AA_{ADJ}(d_1) + LA_{ADJ}(d_1) \\ -L_{AE}(d_2) - AA_{ADJ}(d_2) - LA_{ADJ}(d_1)\end{aligned} \tag{4.6}$$

The propagation effects in the measurement and in the theoretical model can be calculated with $\Delta SEL$ directly by eliminating the uncertainty of the sound source using subtraction. All the errors between the propagation models and the measured $\Delta SEL$ with different distance separations are plotted in Figure 4.33. The average error for each 500-m distance is also plotted in the figure. It can be observed that the model with the Doppler effect has a better agreement than the one without the Doppler effect at each group of distances. In addition, the model with the Doppler effect is slightly better than the prediction using the AEDT method. The margin is small mainly due to the small Mach number during the test (i.e., average 70.9 meters/s). By applying the method of point-to-point integration, the error could be minimized to below 2.5 dB within 4000 m. In Figure 4.34, the distributions of the error could be observed: d1 suggests the sideline distance between the aircraft and the receiver of the first SEL used in the subtraction, and d2 suggests the distance of the second SEL. Figure 4.34 shows that the error reaches the maximum value as d2 is close to the maximum distance (4800 m) for all three models. The model without the Doppler effect has the largest mean error, while the model with the Doppler effect has the smallest mean error, and the error of the AEDT model is in the middle. The error is weakly dependent on the distance between the source and the receiver. In addition, the error for the distance below 3 km is generally good for all three models. The observation is consistent with the prediction that the total uncertainty increases with the distance. Moreover, the empirical model of the AEDT is more accurate than the ray model without the Doppler effect and is less accurate than the ray model with the Doppler effect.

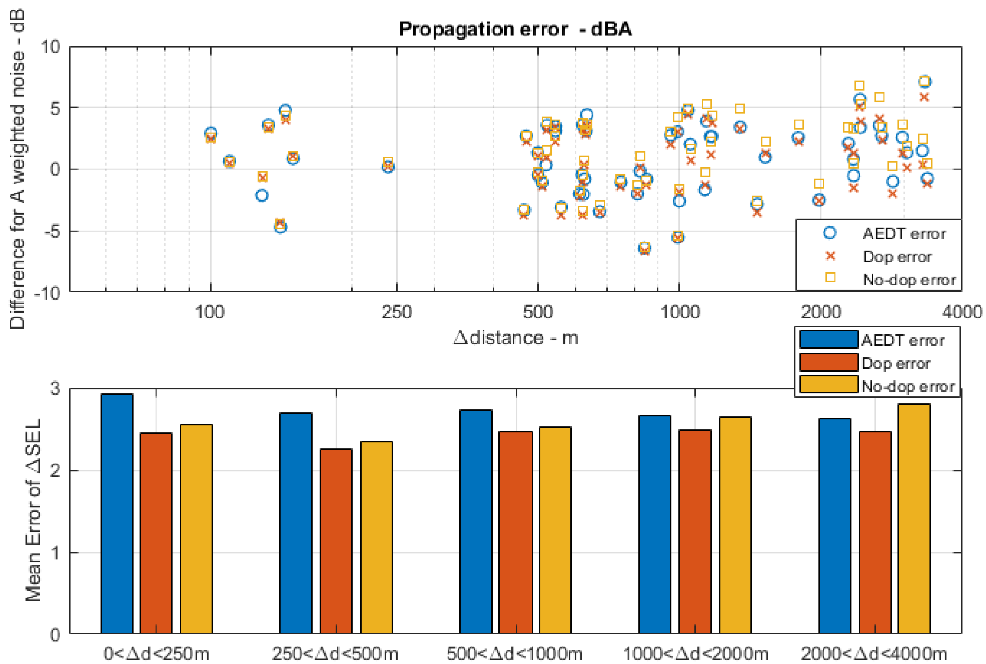


Figure 4.33. SEL difference for different differences of distance.

### 4.3.4 NPD predictions with theoretical model.

The spectral analysis shows the advantage of applying the Doppler effect in the model. In the SEL analysis of the level flight, the improvement of the Doppler effect exists but is small due to the low speed during the test. However, with a higher speed or a different geometry with respect to the reference condition, the Doppler effect will have a very different impact that cannot be predicted with the current model in the AEDT. The decaying rate of the NPD curves are independent of the aircraft speed, and no correction is related to the Doppler effect in the NPD adjustments of the AEDT, which could be problematic for high speed cruising conditions. Based on the ray model with the Doppler effect included in this study, the NPD curve is predicted in this section for a reference speed of 160 knots as well as 300 knots and 500 knots. In Figure 4.35, four aircraft available in the ANP database are used in the

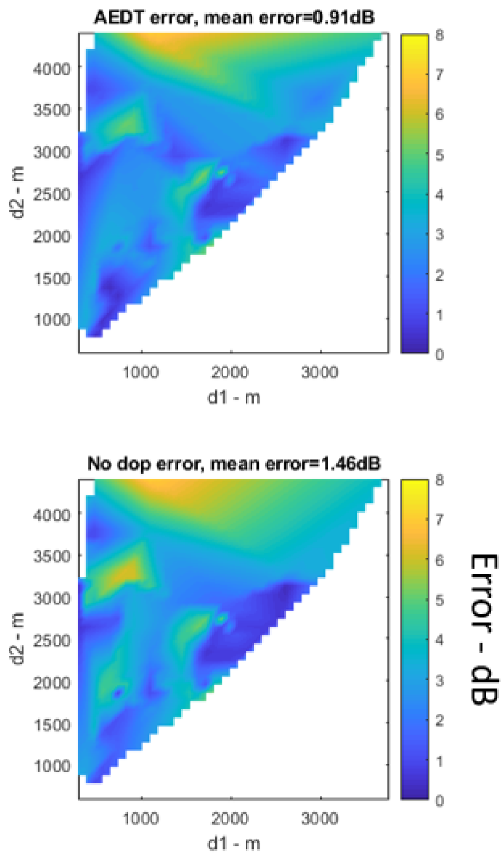


Figure 4.34. Error map of d1×d2 for the AEDT propagation model, theoretical model with Doppler's effect and theoretical model without Doppler's effect.

prediction of the NPD curve with a reference speed 160 knots, 300 knots, and 500 knots; these are compared with the NPD curves of the ones in the ANP database. The power settings in the NPD curve are 600 CNT, 100 CNT (% of the max. static thrust), 16000 CNT, and 6000 CNT. Beech 1900D and Lockheed C-130 are propeller-driven aircraft, while the Boeing 747-100 and Airbus A320232 are jet engine aircraft. The two propeller-driven aircraft both have distinct tonal components, and the two jet engine aircraft have more broadband noise. The departure spectrum is used in the prediction, and the predicted NPD curve is corrected to the same level as the NPD curve at 1000 feet for the analysis of propagation effect, which is a common

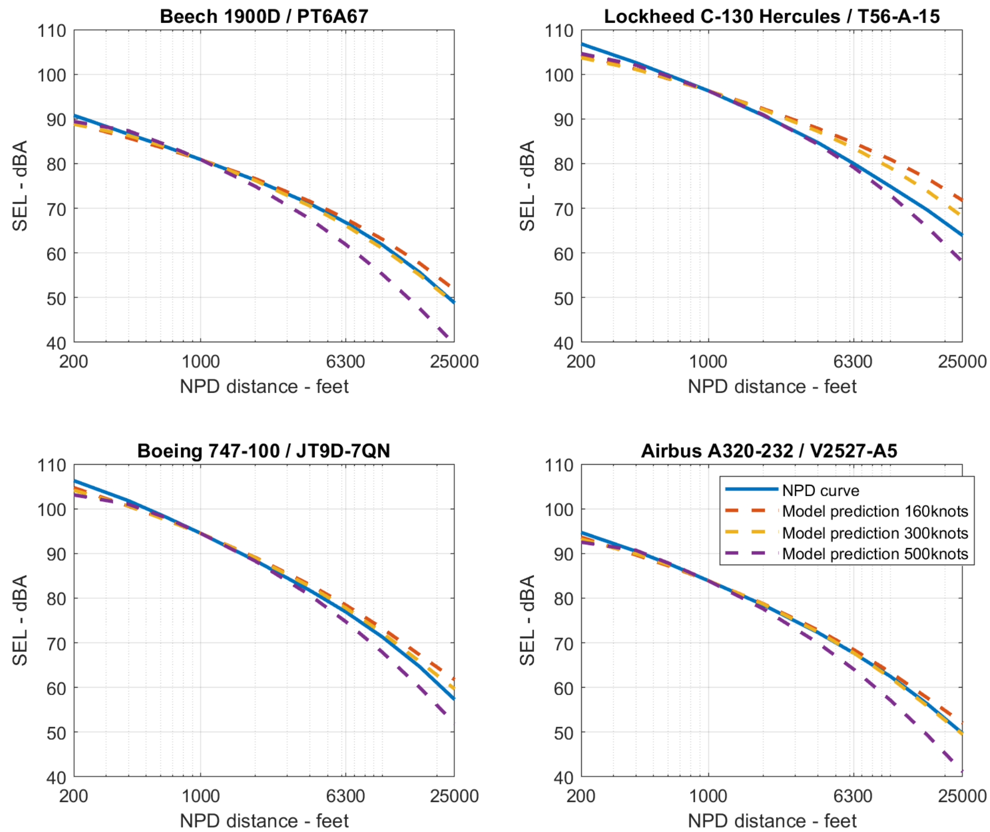


Figure 4.35. NPD curve vs predicted NPD curve with the model.

method used for analyzing the propagation effect [73]. The SAE-AIR-1845 reference absorption is used, and the sideline distance is set to 0.

From Fig. 4.35, it could be observed that the curves for the A320-232 have the best agreement at 160 knots, and the C-130 has the largest disagreement. According to all four subplots, the NPD curve in the ANP database will overestimate the propagation effect for low speed and underestimate the propagation effect for high speed (500 knots). The difference between the predictions is larger for the two propeller-driven aircraft and less so for the two jet engine aircraft. Aside from this, the decaying is higher for all the spectra used at a far distance if the aircraft speed is higher. To summarize, the NPD curves are heavily influenced by the aircraft speed; more than a 10-dB difference is found between the 160 knots curve and the 500 knots curve at 25000 feet above ground according to the theoretical simulation.

### 4.3.5 Conclusion

The propagation effects of aircraft noise are analyzed with the measurements in the DISCOVER-AQ project. The importance of the Doppler effect could be observed in the time-pressure data of the data set. The propagation effects in the measurements are analyzed through the comparison with the AEDT's propagation model using the method of subtraction. A simple model based on the AEDT's noise model with the implementation of the Doppler effect is introduced and compared with the AEDT's propagation model. The model is slightly better than the propagation model in the AEDT.

The current NPD assumes an aircraft speed of 160 knots. Once the speed is changed, the rate of change of the NPD curve should be adjusted due to the Doppler effect according to the prediction of the ray model. However, the adjustment is not implemented in the AEDT's propagation model. One suggestion for possible improvements of the AEDT is to add NPD curves for different aircraft speeds.

# 5. MODIFIED TRAPEZOID METHOD-FAST AND ACCURATE EVALUATION OF SURFACE WAVE TERM

## 5.1 Point source and Modified trapezoid method

The integration of the surface wave term in the sound pressure integral has been one of the most difficult parts in the calculation of the sound field, regardless of the ground type due to the source being spherical in nature. The reason for the difficulty is the existence of a singularity in the integral

$$I = -\frac{i\beta}{2\pi}\int_0^\infty \frac{k_r}{k_z}\frac{e^{ik_z(z+z_s)}}{k_z/k_0+\beta}J_0(\kappa_r r)dk_r \tag{5.1}$$

where $J_0$ is a Bessel $J$ function, which exist in many spherical wave problems. $k_z = \sqrt{k_0^2 - k_r^2}$. Here, $k_0$ is a constant wave number. $z, z_s$ are receiver and source heights. and $r$ is the horizontal distance between the source and the receiver. The same equation can be found in [4]. After the transformation $k_r = k_0 sin\mu$, Equation 5.1 can be rewritten as follows:

$$I = -\frac{ik_0\beta}{4\pi}\int_0^\infty \frac{sin\mu}{cos\mu+\beta}\left[H_0^{(1)}(k_0 r sin\mu)e^{-ik_0 r sin\mu}\right]e^{ik_0 R_2 cos(\mu-\theta)}d\mu \tag{5.2}$$

The term $H_0^{(1)}(k_0 r sin\mu)e^{-ik_0 r sin\mu}$ seems complicated, but it is a smooth function named as the scaled Hankel function on the given integration path. $R_2$ is the distance from source to the image source, and $\theta$ is the angle of incident. The singularity mentioned above is due to the term $cos\mu + \beta$ in the denominator. The location of the pole can be solved with the equation

$$cos\mu + \beta = 0$$

where $\beta$ is the admittance of the ground for locally reacting ground, but its form becomes rather complicated when the ground surface cannot be modeled with a locally reacting model. The details of the term $\beta$ for various types of ground (i.e., infinite, semi-infinite, hard-backed, impedance-backed and multi-layered) can be found in [4, 48].

After evaluation of integral Eq. 5.1 using traditional methods requires the pole subtraction method. [23] A simple function with the same limit at the singularity location is subtracted from the equation and then added back afterwards. The pole subtraction method takes advantage of the fact that the integral of the simple function is much easier to evaluate; it normally has solutions implemented in many software programs (e.g., the complementary error function in MATLAB) so that during the integration, the singularity could be eliminated, and at the same time the subtracted simple integral is added back to the equation at the end, such as with $erfc()$. The pole subtraction method makes it possible to have an asymptotic expansion of the surface wave integral; however, if an accurate solution is required, the pole subtraction method is not the fastest way to fulfill the requirement. The method used in the evaluation of the complementary function could be modified to evaluate any function with a simple singularity directly without using the pole subtraction method.

### 5.1.1 Modified trapezoid rule method for locally reacting ground

We start by using another integral, and we make use of the residue theory, which is inspired by Goodwin and Reichel [74–77]. The method was originally used in the calculation of the complementary error function, and it can be modified and applied directly to calculate the surface wave term without using the pole subtraction method. In this procedure, several branch cuts and singularities are crossed as the integration path changes, which brings about error terms controlled by the step length $h$. An analysis of the following error terms provides us with the information we need for choosing the step length $h$ in an efficient and economical way. Our original integral, which is another form of Eq. 5.1, is

$$I = \frac{e^{ikR_2}}{\pi} \int_{-\infty}^{\infty} \frac{f\left(X\right)}{X^2 - w_+^2} e^{-kR_2 X^2} dX \tag{5.3}$$

Equation 5.3 is derived from a transformation

$$X^2/2 = icos(\mu - \theta) \tag{5.4}$$

which transform the integration path from the original one to the steepest descent path of the integral. The integral in the Equation 5.3 is usually calculated using the pole subtraction method and the Gaussian Hermit quadrature. [8] Here, we introduce a new method that contains some modifications to the simple trapezoid rule will be introduced with the error bound. To analyze the error introduced by the trapezoid rule, the transformation from $X$ to $U$ is made to simplify the process, in this way:

$$X^2 = \frac{U^2}{kR_2}$$

After the transformation, the original integral for the locally-reacting ground becomes the following:

$$I = \int_{-\infty}^{+\infty} \frac{g_{even}(U)}{U^2 + w^2} e^{-U^2} dU \tag{5.5}$$

The even function in the integral can be calculated in the U plane as follows:

$$g_{even}(U) = i\sqrt{kR_2}\frac{e^{ikR_2}}{\pi} \frac{\beta(\cos\theta + \beta + i\frac{U^2}{kR_2}\cos\theta)}{\sqrt{2i - \frac{U^2}{kR_2}}(\frac{U^2}{kR_2} - w_-{}^2)} \tag{5.6}$$

It is necessary to introduce a new integral, which is

$$\begin{aligned} I_c &= \int_C \frac{g_{even}(U)}{U^2 + w^2} e^{-U^2} \frac{1}{1 - e^{-2\pi iU/h}} dU \\ &= h\sum_{-\infty}^{\infty} \frac{g_{even}(nh)}{n^2h^2 + w^2} e^{-n^2h^2} + [\frac{\pi e^{w^2} g_{even}(iw)}{w(1 - e^{2\pi w/h})} - \frac{\pi e^{w^2} g_{even}(iw)}{w(1 - e^{-2\pi w/h})}]\varepsilon \\ &- \int_{B1+B2} \frac{g_{even}(U)}{U^2 + w^2} e^{-U^2} \frac{1}{1 - e^{-2\pi iU/h}} dU - \int_{B3+B4} \frac{g_{even}(U)}{U^2 + w^2} e^{-U^2} \frac{1}{1 - e^{-2\pi iU/h}} dU \end{aligned} \tag{5.7}$$

where h is the step length of the integration, and

$$\varepsilon = \begin{cases} 0 & \pi/h < \mathrm{Im}(U_0) \\ 1/2 & \pi/h = \mathrm{Im}(U_0) \\ 1 & \pi/h > \mathrm{Im}(U_0) \end{cases} \tag{5.8}$$

which can be found in the paper by Matta and Reichel. [77]. $w$ is a term defined as:

$$
{w_+}^2 = -\frac{w^2}{kR_2}, w_- = -w_+ \tag{5.9}
$$

Here, $I_c$ can be broken into two parts

$$
\begin{aligned}
I_c = \int\limits_{C1} \frac{g_{even}(U)}{U^2 + w^2} e^{-U^2} \frac{1}{1 - e^{-2\pi i U/h}} dU + \int\limits_{C2} \frac{g_{even}(U)}{U^2 + w^2} e^{-U^2} \frac{1}{1 - e^{-2\pi i U/h}} dU \\
= I_{C1} + I_{C2}
\end{aligned} \tag{5.10}
$$

Then We can easily get the following:

$$
\int\limits_{C2} \frac{e^{-U^2}}{U^2 + w^2} g_{even}(U) dU = I \mp \frac{\pi e^{w^2}}{w} g_{even}(iw)\varepsilon - \int\limits_{B3+B4} \frac{g_{even}(U)}{U^2 + w^2} e^{-U^2} dU \tag{5.11}
$$

If Im(i$\omega$) $> 0$, we choose the positive sign, otherwise, if Im(iw) $< 0$, we choose the negative sign.

Now we can combine Equations 5.7 to 5.11 to obtain the total expression for the error of the trapezoid rule

$$
I = h \sum_{-\infty}^{\infty} \frac{g_{even}(nh)}{n^2h^2 + w^2} e^{-n^2h^2} + I_{pole} + (-I_{C1} - {I_{C2}}') + I_{branch} \tag{5.12}
$$

The contribution from the pole can be easily added to the trapezoid integration result, and it can be expressed as follows:

$$
I_{pole} = \frac{\pi e^{w^2} g_{even}(iw)}{w(1 - e^{2\pi w/h})} \frac{\pi e^{w^2} g(iw)}{w(1 - e^{-2\pi w/h})} \pm \frac{\pi e^{w^2}}{w} g_{even}(iw) \tag{5.13}
$$

Here, the total error is composed of two different terms. The first error term is an integral along the line $U = i\pi/h$:

$$I_{C1} + I_{C2}' = \int\limits_{C1} \frac{g_{even}(U)}{U^2 + w^2} e^{-U^2} \frac{1}{1 - e^{-2\pi iU/h}} dU + \int\limits_{C2} \frac{e^{-U^2 - 2\pi iU/h}}{(U^2 + w^2)(1 - e^{-2\pi iU/h})} g_{even}(U) dU$$

$$= \int\limits_{C2} \frac{g_{even}(U)}{U^2 + w^2} e^{-U^2} \frac{1}{e^{2\pi iU/h} - 1} dU + \int\limits_{C2} \frac{e^{-U^2}}{(U^2 + w^2)(e^{2\pi iU/h} - 1)} g_{even}(U) dU$$

$$= 2 \int\limits_{-\infty - i\pi/h}^{\infty - i\pi/h} \frac{g_{even}(U)}{U^2 + w^2} e^{-U^2} \frac{1}{e^{2\pi iU/h} - 1} dU$$

$$\approx 2i(\pi k R_2)^{-\frac{1}{2}} e^{-\frac{\pi^2}{h^2}} e^{ikR_2} \frac{\beta(\cos\theta + \beta + i\cos\theta \frac{\pi^2}{h^2 k R_2})}{\sqrt{2i + \frac{\pi^2}{h^2 k R_2}} (\frac{\pi^2}{h^2 k R_2} + w_+^2)(\frac{\pi^2}{h^2 k R_2} + w_-{}^2)} \frac{1}{e^{-2\frac{\pi^2}{h^2}} - 1} \tag{5.14}$$

This error term decreases as h decreases, and the decreasing speed is dominated by the term $e^{\pi^2/h^2}$. There is also another error term introduced by the branch cuts of the square root term $\sqrt{2i - X^2}$, which equals to the following:

$$\begin{aligned} I_{branch} = &- \int\limits_{B1+B2} \frac{g_{even}(U)}{U^2 + w^2} e^{-U^2} \frac{1}{1 - e^{-2\pi iU/h}} dU - \\ &\int\limits_{B3+B4} \frac{g_{even}(U)}{U^2 + w^2} e^{-U^2} \frac{1}{1 - e^{-2\pi iU/h}} dU + \int\limits_{B3+B4} \frac{g_{even}(U)}{U^2 + w^2} e^{-U^2} dU \\ = &- \int\limits_{B1+B2} \frac{g_{even}(U)}{U^2 + w^2} e^{-U^2} \frac{1}{1 - e^{-2\pi iU/h}} dU + \int\limits_{B3+B4} \frac{g_{even}(U)}{U^2 + w^2} e^{-U^2} \frac{1}{1 - e^{2\pi iU/h}} dU \end{aligned} \tag{5.15}$$

In Figure 5.1, the black lines are the branch cut lines in the $U$ plane, which extends to the positive infinity on the right and negative infinity to the left. It can be noted that in the relationship between the integrals on the two paths, the $\frac{g_{even}(U)}{U^2+w^2} e^{-U^2} \frac{1}{1-e^{-2\pi iU/h}}$ on path B3 is equal to $\frac{g_{even}(U)}{U^2+w^2} e^{-U^2} \frac{1}{1-e^{2\pi iU/h}}$ on the path B1, In addition, $dU$ has opposite signs on the two paths. We can conclude that the integral values are the same on B1 and B3, as well as on B2 and B4. The asymptotic solutions for the integrals on B1 to B4 have the same value according to a stationary phase analysis,

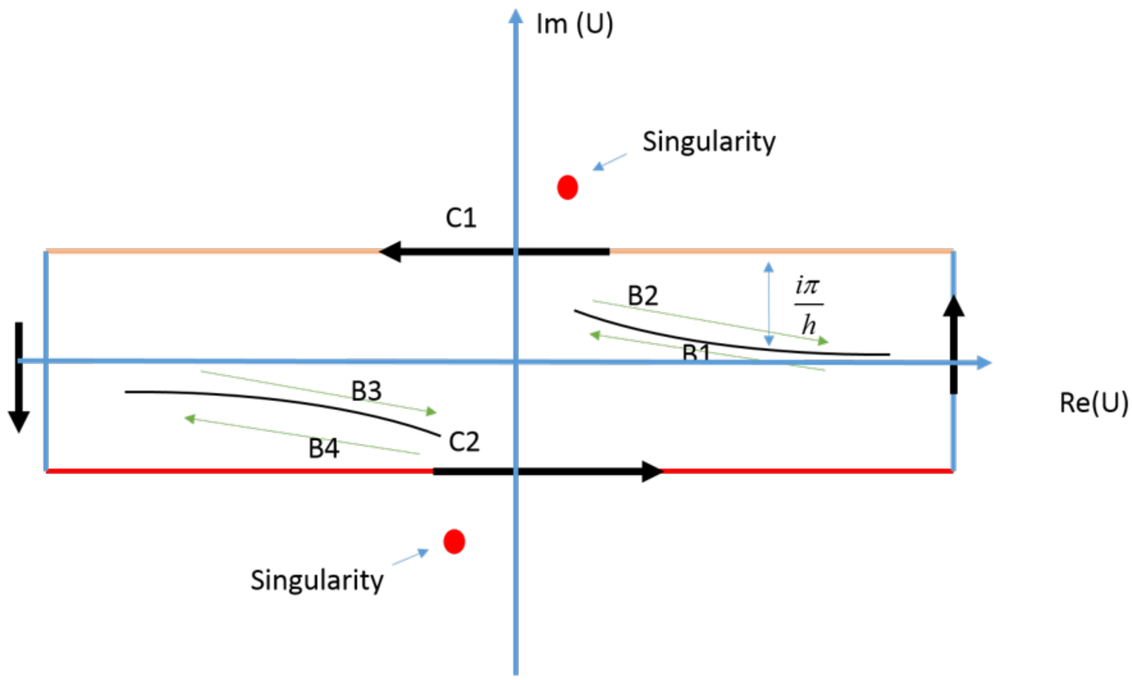


Figure 5.1. Path of the branch cut integrals

since they all can be approximated by the values of the function at the branch points. The total branch cut error can be estimated as follows:

$$I_{branch} = 4 \times \{-\frac{e^{-ikR_2}}{\pi} \frac{\beta(-\cos\theta + \beta)}{(2i - w_-{}^2)(2i - w_+{}^2)\sqrt{2i}(1 - e^{-2\pi\sqrt{kR_2}(i-1)/h})} \sqrt{\frac{\pi}{kR_2}}\} \quad (5.16)$$

**The detail of the branch cut integral** The detailed procedure in the evaluation of the branch cut integral is as follows

$$I_{B1} = \int_{B1} \frac{g_{even}(U)}{U^2 + w^2} e^{-U^2} \frac{1}{1 - e^{-2\pi i U/h}} dU = \int_{B1} \frac{e^{-kR_2X^2}}{\sqrt{2i - X^2}} Y(X) dX \quad (5.17)$$

where

$$Y = i\frac{\beta e^{ikR_2}}{\pi} \frac{\cos\theta + \beta + iX^2\cos\theta}{(X^2 - w_+{}^2)(X^2 - w_-^2)} \frac{e^{-kR_2X^2}}{1 - e^{-2\pi i\sqrt{kR_2}X/h}} \quad (5.18)$$

We choose $(2i - X^2)^{\frac{1}{2}} = +\sqrt{2i - X^2}$ on B1 and $(2i - X^2)^{\frac{1}{2}} = -\sqrt{2i - X^2}$ on B2, where the branch cut is chosen to be on the negative real axis of . In order to handle the singularity at the branch points, we need to make another transformation

$$y^2 = t = 2i - X^2, \tag{5.19}$$

In this way, we can obtain the following:

$$\begin{aligned} I_{B1} &= -\int_0^{i\infty} Y(X = \sqrt{2i - y^2}) \frac{e^{-kR_2(2i-y^2)}}{y} \left(-\frac{y}{\sqrt{2i - y^2}}\right) dy \\ &= \int_0^{i\infty} Y \frac{e^{-2ikR_2} e^{kR_2 y^2}}{\sqrt{2i - y^2}} dy \end{aligned} \tag{5.20}$$

The integral could be approximated with the steepest descent method

$$\begin{aligned} I_{B1} &\approx \int_0^{i\infty} Y(y = 0) \frac{e^{-2ikR_2 kR_2 y^2}}{\sqrt{2i}} dy \\ &= -\frac{e^{-ikR_2}}{\pi} \frac{\beta(-\cos\theta + \beta)}{(2i - w_-{}^2)(2i - w_+{}^2)\sqrt{2i}(1 - e^{-2\pi\sqrt{kR_2}(i-1)/h})} \sqrt{\frac{\pi}{kR_2}} \end{aligned} \tag{5.21}$$

Following the same procedure, we found that the asymptotic solutions on all of the branch cut paths are the same. The total branch cut integral is given in Equation 5.16.

The branch cut error, the error on the straight line $i\pi/h$ and the total error are plotted in Figure 5.2. The two types of errors decay as step length h decreases. The total error becomes a constant when $h$ is less than 0.5 since $10^{-16}$ approaches the limit of MATLAB's default accuracy. We can also observe that in the region with a large step size (h larger than 0.6), the error on the $i\pi/h$ dominates the total error. Most of the time, the error on the branch cut can be ignored due to its complicated feature and its relatively small contribution to the total error.

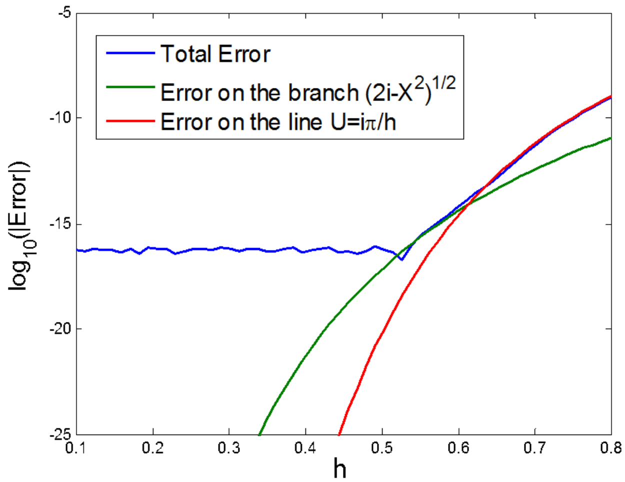


Figure 5.2. The Errors comparison. Frequency=500 Hz, rs=(0,0), rr=(1,0), Admittance=0.3+i0.1 m/(Pa s).

### 5.1.2 Modified trapezoid rule method for non-locally reacting ground

For a non-locally reacting ground surface, the original integral is as follows:

$$I = i\frac{e^{ikR_2}}{\pi}\int_{-\infty}^{+\infty}\frac{(b_+ + b_-)\left[(\cos\theta+\beta_p)+iX^2\cos\theta\right]-i\,(b_+ - b_-)\,X\sqrt{2i-X^2}\sin\theta}{2\sqrt{2i-X^2}(X^2-w_-{}^2)(X^2-w_+)}e^{-kR_2X^2}dX \tag{5.22}$$

Most of the error terms have similar expressions as those in the previous section, except for a new error term that is introduced by a multi-valued function $\sqrt{n^2-\sin^2\mu}$, which brings the lateral wave term into the equation with a certain choice of speed ratio between the air and the underground medium. The total error can be found in this expression:

$$I = h\sum_{-\infty}^{\infty}\frac{g_{even}(nh)}{n^2h^2+w^2}e^{-n^2h^2}+I_{pole}+(-I_{C1}-I_{C2}{}')+I_{branch}+I_{nbranch} \tag{5.23}$$

The branch cut integral is

$$I_{branch} = 4\times\{-\frac{e^{-ikR_2}}{\pi}\frac{b_0(-\cos\theta+\beta)}{(2i-w_-{}^2)(2i-w_+{}^2)\sqrt{2i}(1-e^{-2\pi\sqrt{kR_2}(i-1)/h})}\sqrt{\frac{\pi}{kR_2}}\} \tag{5.24}$$

where

$$b_0 = \frac{\cos\theta + \xi\sqrt{n^2 - sin\theta^2}}{\cos\theta + \beta_p} \tag{5.25}$$

The error integral on the path $U = i\pi/h$ has a similar expression as the one for the

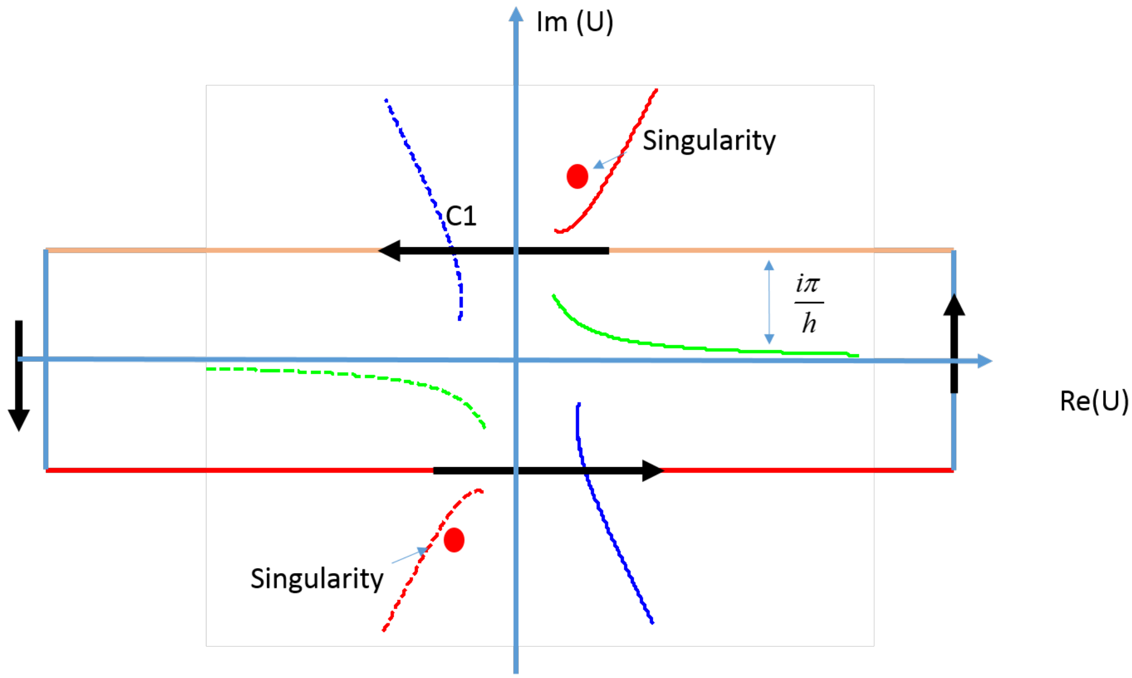


Figure 5.3. Integration path and the branch cuts. Red and blue: Branch cuts for non-locally reacting ground. Green: branch cut for $(2i - X^2)^{\frac{1}{2}}$

locally reacting ground, which is

$$\begin{gathered} I_{C1} + I_{C2}{}' = 2\int_{-\infty - i\pi/h}^{\infty - i\pi/h} \frac{g_{even}(U)}{U^2 + w^2} e^{-U^2} \frac{1}{e^{2\pi i U/h} - 1} dU \\ \approx 2i(\pi k R_2)^{-\frac{1}{2}} e^{-\frac{\pi^2}{h^2}} e^{ikR_2} \\ \frac{(b_+{}' + b_-{}')(\cos\theta + \beta + i\cos\theta\frac{\pi^2}{h^2 k R_2}) - (b_+{}' - b_-{}')\frac{\pi}{h\sqrt{kR_2}}\sqrt{2i + \frac{\pi^2}{h^2 k R_2}}\sin\theta}{2\sqrt{2i + \frac{\pi^2}{h^2 k R_2}}(\frac{\pi^2}{h^2 k R_2} + w_+^2)(\frac{\pi^2}{h^2 k R_2} + w_-{}^2)} \\ \frac{1}{e^{-2\frac{\pi^2}{h^2}} - 1} \end{gathered} \tag{5.26}$$

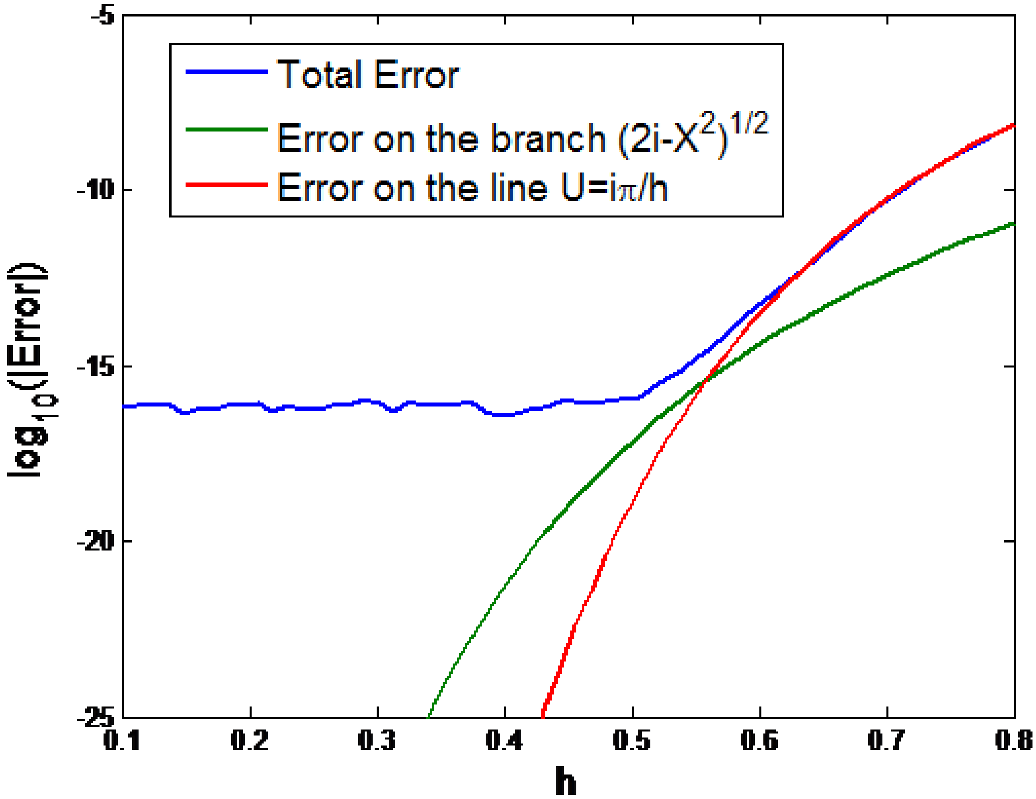


Figure 5.4. Error comparison for non-locally reacting ground surface. Frequency=500 Hz, rs=(0,0), rr=(1,0), Flow resistivity=10 kPa s m-2, Delaney and Bazley's modell is used.

where

$$
\begin{aligned}
b_+{}' &= b_+(X = -i\frac{\pi}{h\sqrt{kR_2}}), \\
b_-{}' &= b_-(X = -i\frac{\pi}{h\sqrt{kR_2}})
\end{aligned}
\tag{5.27}
$$

Another branch cut error exist due to the term $\sqrt{n^2 - \sin^2\mu}$. Exact evaluation of the branch cut integral is complicated and unnecessary, so we only consider the 90 degree incident angle condition, because the error of the surface wave term only matters significantly under near grazing conditions. The branch cut in the X plane is determined by

$$X = \{-i[(n^2 - t)^{\frac{1}{2}} - 1]\}^{\frac{1}{2}} \tag{5.28}$$

where $t$ lies on the negative real axis, and $X_b(t = 0)$ are the branch cut points. The paths are shown in the Figure 5.3. After some tedious calculations, this branch cut integral is found to be equal to zero when the incident angle is 90 degree. For a large speed ratio between the air and the ground medium, the location of these branch cut points are always far from the origin, and the result has a very small error.

Figure 5.4 shows the comparison between the error terms. Similar to locally reacting case, the total error is dominated by $i\pi/h$ error with large $h$.

### 5.1.3 Error analysis for point source

In Figure 5.5, the error of the method is plotted against a different value of admittance. We could observe in the figure that the maximum error is close to $10^{-12}$ if the step size is set to 0.5 and if 13 points are used in the integration. If the step size is decreased to 0.25 and if 26 points are used in the integration, the error at the right edge disappears. In Figure 5.6, similar results could be observed for a non-locally reacting ground. In the lower real plane, a bright line could be observed in Figures 5.5 and 5.6, which is due to the singularity. The accuracy of the integration decreases as the steepest descent path gets closer to the singularity. To handle the case when the pole is positioned just on the real axis, we used the method suggested by Hunter and Regan [76].

The advantage of this new method over the traditional pole subtraction method is that it cuts the calculation time nearly by half. Pole subtraction method always require almost twice the nodes to reach the same accuracy. The error comparison with the same number of points can be found in Figure 5.7. We can see that the error of the new method is smaller than the error of the pole subtraction method if the same number of points are used in the integration. The error bound is also given for the

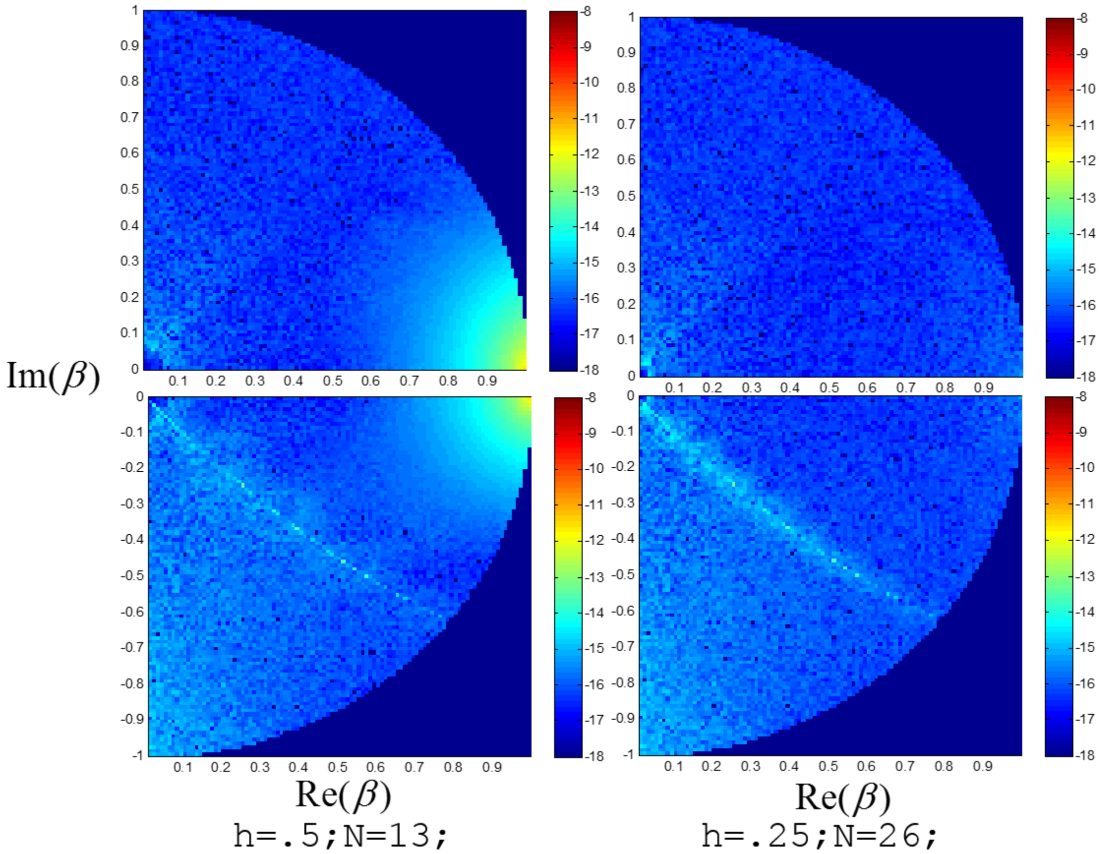


Figure 5.5. Error for locally reacting ground. Log10(Absolute Error). Frequency=500 Hz, rs=(0,0), rr=(1,0) . Same ground property as in Figure 5.2

trapezoid rule method. The sound field above any type of ground with a singularity in the surface wave term can be calculated using the same method mentioned above. The only advantage that the pole subtraction method has is it gives an explanation to the surface wave term in terms of the ray theory, which is not available for the modified trapezoid rule method.

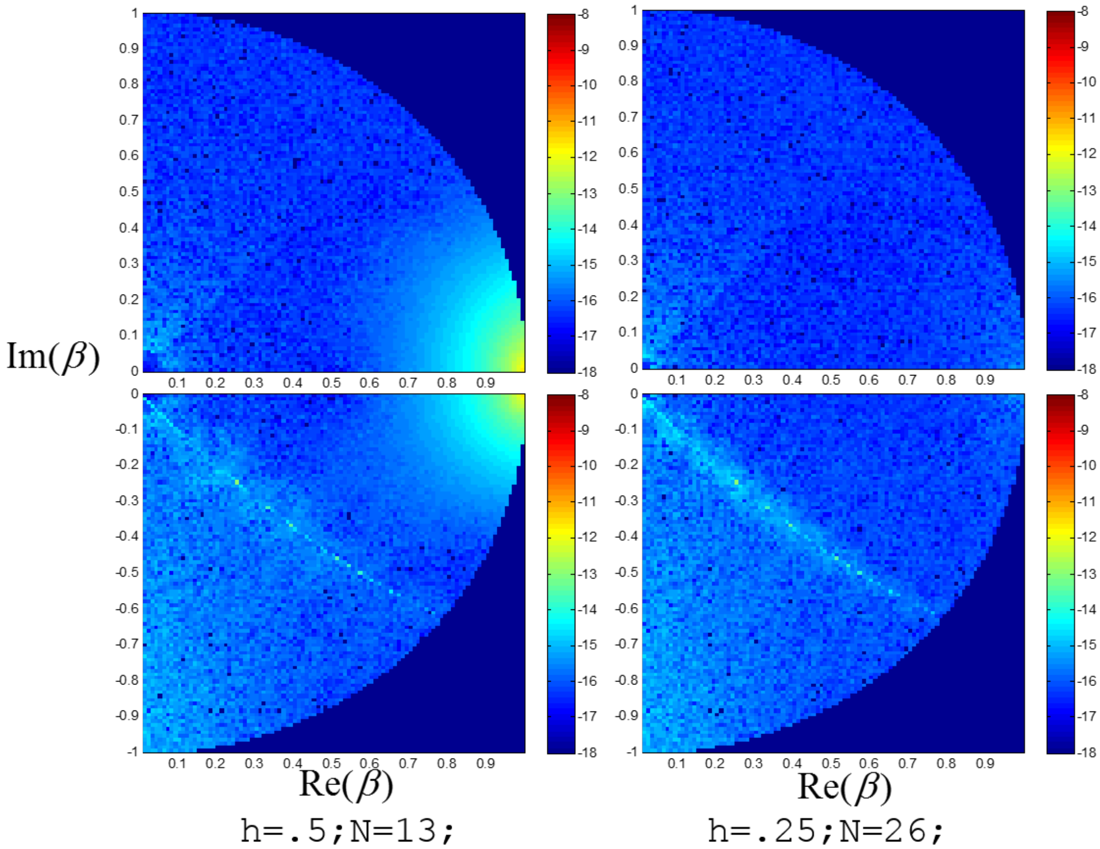


Figure 5.6. Error for non-locally reacting ground. Log10(Absolute Error). Frequency=500 Hz, rs=(0,0), rr=(1,0) . Same ground property as in Figure 5.4

## 5.2 Line source and modified trapezoid method with a simple error bound

In the previous section, the exact error bound is calculated using numerical integration along several path. We found that the error due to the branch cuts has a limited contribution to the total error. An error bound in terms of numerical integration is not useful and not convenient for many purposes; instead, a simple estimation

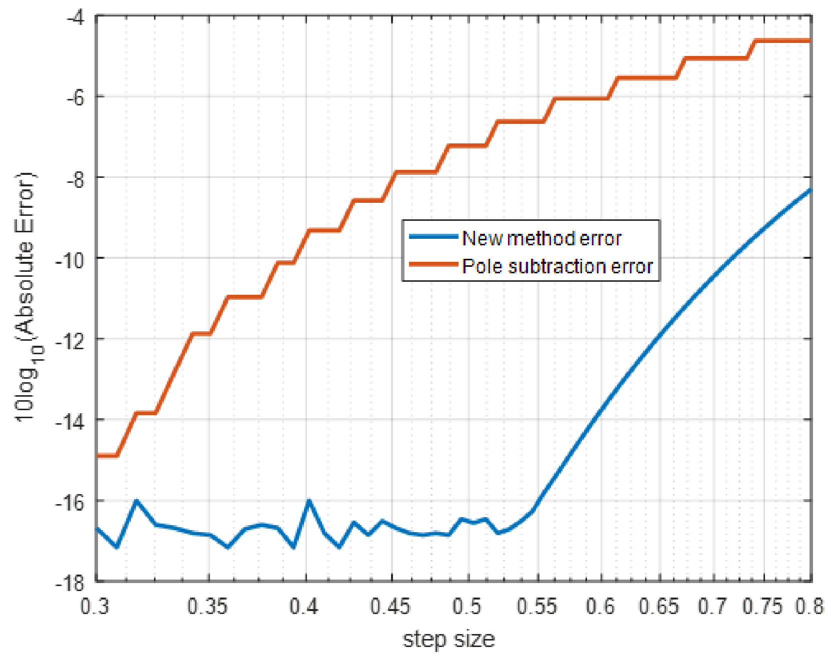


Figure 5.7. Error comparison between traditional pole subtraction method and the new modified trapezoid rule method. r=0.1m; freq=500Hz; $(x, y) = (0, 0)m$; $(x_s, y_s) = (2, 0)m$; porosity=0.3; $q^2$=3.3; $\sigma = 500$ cgs rayls

of the error is more desirable most of the time. Recently, the exact error bound for Fresnel integral of the type

$$w(z) = \frac{i}{\pi} \int_{-\infty}^{+\infty} \frac{e^{-y^2}}{z - t} \mathrm{dt} \tag{5.29}$$

was given by Mohammad Alazah [78]. Equation 5.29 shares many similarities with Equation 5.1; the only difference is that the function to be integrated is more complicated in 5.1. Although it is not easy to give an exact error bound for Equation 5.1, we can assume that the function changes slowly near the integration path with this we can give an approximating error bound.

### 5.2.1 Problem formulation

In this section, an approximated error bound for an integral

$$u_\beta = -\frac{i}{2\pi}\int\limits_C \frac{\beta(\mu)\, e^{ikR_2\cos(\mu-\theta)}}{\cos\mu + \beta(\mu)} d\mu \tag{5.30}$$

will be given based on the complicated and detailed derivation in [78]. The function $\beta$ can be either locally or non-locally. For a local situation, $\beta = \xi n$, while for a semi-infinite ground $\beta = \xi\sqrt{n^2 - sin^2\mu}$. The pole is denoted as $\mu_p$ due to the zero in the denominator. After using simple algebra, Equation 5.30 can be written as

$$u_\beta = -\frac{i}{2\pi}\int\limits_C \frac{a(\mu)\,\beta(\mu)\, e^{ikR_2\cos(\mu-\theta)}}{(1-\zeta^2)(\cos\mu + \beta_p)} d\mu \tag{5.31}$$

where $a(\mu)$—which is referred to as the admittance factor—is given by

$$a(\mu) = \frac{\cos\mu - \beta(\mu)}{\cos\mu - \beta_p} \tag{5.32}$$

for a non-locally reacting interface, and it is unity for a locally reacting one because $\beta(\mu) = \beta_p$. The admittance factor is a complete function because $\cos\mu - \beta_p \neq 0$ in the region of interests. As shown in Eq. 5.30 and 5.31, a locally reacting interface is merely a special case of the non-locally reacting interface with $1 >> \zeta^2$ and $1 << n^2$. We shall not show separately the solution for the locally reacting interface. In our subsequent analysis, the advantage of using Eq. 5.31 instead of Eq. 5.30 becomes more revealing when we present the solution in the next section.

### 5.2.2 The diffraction integral along the steepest descent path

The integrand of Eq. 5.31 is highly oscillatory especially for large $kR_2$ that renders the direct computation of the integral along $C$ to be inefficient. The indentation of $C$ to the steepest descent path $C_\mu$ is a useful remedy to the situation. To determine the steepest descent path, we introduce a new complex variable $W$ to replace $\mu$ in Eq. 5.31 by requiring

$$\cos(\mu - \theta) = 1 + iW^2 \tag{5.33}$$

where $W = X + iY$. This leads to a pair of non-linear simultaneous equations that links $X$ and $Y$ in the $W$-plane [7]. It should be noted that the steepest descent path can be found in any plane. However, in the $W$ plane, the steepest descent path is simply the real axis; this can be convenient in the later evaluation of the integral and helps to give a simpler final asymptotic solution.

We can then determine the steepest descent path in the W-plane by setting $Y = 0$ in Eq. 5.33. We can easily verify that

$$\sin\mu_X = \left(1 + iX^2\right)\sin\theta + iX\sqrt{2i - X^2}\cos\theta \tag{5.34}$$

$$\cos\mu_X = \left(1 + iX^2\right)\cos\theta - iX\sqrt{2i - X^2}\sin\theta \tag{5.35}$$

where $\mathrm{Im}\left(\sqrt{2i - X^2}\right) > 0$, $\sqrt{2i - X^2} = +i\sqrt{X^2 - 2i}$ and the subscript X signify the respective parameters along the steepest descent path $C_\mu$ in the $\mu$-plane. It should be noted that in $\cos\mu_p = -\beta_p$, we can see that the integrand of Eq. 5.31 has a pole at the point $\mu = \mu_p$. In mapping $\beta_p$ in the $W$-plane using Eq. 5.33, we can show that the pole lies on the steepest descent path if $\mathrm{Im}\left(w_+\right) = 0$, where

$$u_\beta = D_X + u_p e^{ikR_2\left(1+w_+^2\right)} H\left[-\mathrm{Im}\left(w_+\right)\right], \tag{5.36}$$

By changing the path from $C$ to $C_\mu$, the pole at $\mu_p$ is crossed if $\mathrm{Im}\left(w_+\right) < 0$. Consequently, the diffraction integral in Eq. 5.31 can be written as

$$u_\beta = D_X + u_p e^{ikR_2\left(1+w_+^2\right)} H\left[-\mathrm{Im}\left(w_+\right)\right], \tag{5.37}$$

where

$$D_X = -\frac{ie^{ikR_2}}{\pi}\int_{-\infty}^{\infty}\frac{a\left(X\right)\beta\left(X\right)}{\left(1-\zeta^2\right)\left(\cos\mu_X + \beta_p\right)}\frac{e^{-kR_2X^2}}{\sqrt{2i - X^2}}dX \tag{5.38}$$

$a\left(X\right)$ and $\beta\left(X\right)$ are obtained by substituting Eqs. 5.34 and 5.35 into Eq. 5.32 and admittance equations to verify

$$a_\pm = a\left(\pm X\right) = \frac{\cos\theta - \beta_\pm + i\left(X^2\cos\theta \pm X\sqrt{2i - X^2}\sin\theta\right)}{\cos\theta - \beta_p + i\left(X^2\cos\theta \pm X\sqrt{2i - X^2}\sin\theta\right)}, \tag{5.39}$$

and

$$\beta_{\pm} = \beta\left(\pm X\right) = \zeta\sqrt{n^2 - \sin^2\theta + X^2\left(2i - X^2\right)\cos 2\theta \pm iX\left(1 + iX^2\right)\left(2i - X^2\right)^{\frac{1}{2}}\sin 2\theta}. \tag{5.40}$$

The second term in Eq. 5.37 is also known as the surface wave contribution [4] where the Heaviside step function is 1, 1/2 or 0, or 0 when $\mathrm{Im}\left(w_{+}\right)$ is either negative, zero, or positive. We can determine this contribution by the calculus of residue to yield

$$u_p = \frac{-\beta_p}{\left(1 - \zeta^2\right)\sqrt{1 - \beta_p^2}}, \tag{5.41}$$

For an arbitrary function $(X)$, the odd and even components are given, respectively, by $\frac{1}{2}\left[\Psi(X) - \Psi(-X)\right]$ and $\frac{1}{2}\left[\Psi(X) + \Psi(-X)\right]$. We can therefore decompose the integrand of Eq. 5.38 and make use of Eq. 5.36 to rewrite Eq. 5.36 as

$$D_X = -\frac{ie^{ikR_2}}{\pi}\int_0^{\infty}\frac{f\left(X\right)}{X^2 - w_+^2}e^{-kR_2X^2}dX \tag{5.42}$$

where f(X) is an even function given by

$$f(X) = \frac{\left(a_+\beta_+ + a_-\beta_-\right)\left[\left(\cos\theta + \beta_p\right) + iX^2\cos\theta\right] - i\left(a_+\beta_+ - a_-\beta_-\right)X\sqrt{2i - X^2}\sin\theta}{\left(1 - \zeta^2\right)\sqrt{2i - X^2}\left(X^2 - w_-^2\right)}, \tag{5.43}$$

because all odd terms vanish in the integral of Eq. 5.38.

In the special case of a locally reacting interface, $\zeta \to 0$, $n \to \infty$ and $\beta_{\pm} = \beta_p = \zeta n$. Here, equation 5.43 is simplified to

$$f(X) = \frac{\beta_p\left[\left(\cos\theta + \beta_p\right) + iX^2\cos\theta\right]}{\sqrt{2i - X^2}\left(X^2 - w_-^2\right)}, \tag{5.44}$$

which is comparable to the expression given in [79]. In this section, Equation 5.42 is the main result; it offers a convenient form for computing the solutions above a non-locally reacting interface and for providing a framework to estimate the error of the numerical solutions.

### 5.2.3 Computation of the diffraction integral with error analysis

In this section, we explore the numerical methods for evaluating the diffraction integral both efficiently and accurately by rewriting Eq. 5.42 as

$$D_X = -\frac{ie^{ikR_2}}{\pi} IF \tag{5.45}$$

where I is an integral operator given by

$$IF = \int_0^\infty F(X)\, e^{-kR_2X^2} dX, \tag{5.46}$$

and

$$F(X) = \frac{f(X)}{X^2 - w_+^2}. \tag{5.47}$$

We therefore seek an approximate solution in a form of

$$IF = I_N F + \varepsilon \tag{5.48}$$

where $\epsilon$ is the error term, and $I_N F$ is represented by a convergent series of N+1 terms:

$$I_N F = \sum_{j=0}^{N} b_j F_j \tag{5.49}$$

with the weighting function $b_j$ and the sampling point $F_j = F(X_j)$ evaluated at the abscissa $X_j \in [0, \infty)$. We choose the abscissas to be: $X_N > X_{N-1} \cdots > X_1 > X_0 = 0$ which may be spaced linearly or non-linearly along the positive real axis of the W-plane. For non-linear spaced sampling points, Liu and Li [7] used the Gaussian-Hermite quadrature of $N+1$ points to compute $I_N F$. An alternative method is to replace $kR_2X^2$ with $t$ in Eq. 5.46 and then use the $N$ point ($j$ starting at 1) Gaussian-Laguerre quadrature with the weight function $e^{-t}\big/\sqrt{t}$. Both Chunrungsikul [80] and Chandler-Wilde [79] used the latter method, and they established rigorous error bounds for their numerical solutions. These two Gaussian quadratures require an analytic function F with no singularity near the integration path. The direct application of the Gaussian quadratures is inaccurate when $w_+$ lies close to the real axis because of the influence of the pole at $X = w_+$. A treatment by the pole subtraction method reduces $F(X)$ to a regular function $F_r(X)$ as follows:

$$F_r\left(X\right) = F\left(X\right) - f\left(w_+\right) / \left(X^2 - w_+^2\right). \tag{5.50}$$

A substitution of Eq. 5.50 into Eq. 5.45 leads to the following:

$$D_X = -\frac{ie^{ikR_2}}{\pi}\left[IF_r + f\left(w_+\right)\int_0^\infty \frac{e^{-kR_2X^2}}{X^2 - w_+^2}dX\right]. \tag{5.51}$$

With a suitable choice of $N$, both Gaussian quadratures offer accurate numerical solutions for $IF_r$ because $F_r(X)$ contains no singularity near the integration path.

The term $f\left(w_+\right)$ in Eq. 5.51 is the residue of F(X) that may be determined by evaluating $f$ at $X = w_+$ in Eq. 5.43. However, we find it more convenient to use the integrand of Eq. 5.38 for deriving $f\left(w_+\right)$ as follows:

$$f\left(w_+\right) = \lim_{X \to w_+} \frac{\left(X^2 - w_+^2\right) a\left(X\right) \beta\left(X\right)}{\left(1 - \zeta^2\right)\left(\cos\mu_X + \beta_p\right)\sqrt{2i - X^2}} = w_+ u_p, \tag{5.52}$$

where $u_p$ is given by Eq. 5.41. Furthermore, the second term of Eq. 5.51 can be identified in terms of the scaled complementary error function [15], which is given as

$$\varpi\left(z\right) = e^{-z^2}\mathrm{erfc}\left(-iz\right) = \frac{2iz}{\pi}\int_0^\infty \frac{e^{-t^2}dt}{z^2 - t^2} \tag{5.53}$$

for Im$(z) > 0$. By combining Eqs. 5.37, 5.41, 5.50-5.53, the diffraction integral becomes

$$u_\beta = \frac{-ie^{ikR_2}}{\pi}\left[IF_r - \frac{\beta_p \varpi\left(w_+\right)}{2\left(1 - \zeta^2\right)\sqrt{1 - \beta_p^2}}\right] \tag{5.54}$$

We are now left with the tasks of evaluating $IF_r$ and $\varpi\left(w_+\right)$ numerically. A close scrutiny of the scaled complementary error function reveals that it merely represents a special case of Eq. 5.46 with the constant $f(X)$. This prompts us to consider tackling Eq. 5.46 directly without resorting to the pole subtraction method for removing the singularity near the integration path.

The scaled complementary error function (or the error function, for short) is also known as the Faddeeva function for the wave propagation of Maxwellan plasmas

[81]. Unsurprisingly, there are many numerical schemes dedicated to calculate the scaled complementary error function as it is one of many special functions [15] with widespread applications. Weideman [82] and Alazah et al [78] provided brief overviews of different schemes for its computation. Among these schemes, the trapezoidal rule is most appropriate because the numerical solution is exponentially convergent when applied to the integral of the form given in Eq. 5.46. More importantly, it leads to a rather simple approximation with an accurate estimation of error bounds [Goodwin [74], Chiraella and Reichel [75], Matta and Reichel [77], and Alazah et al [78]]. The details of the derivation is given in Appendix A but we give the results for applying trapezoidal rule with step-length $h$. The approximation can be written in the form of Eq. 5.49 with

$$\frac{b_j}{h} = \begin{cases} 1/w_+^2 j = 0 \\ 2e^{-j^2h^2} \Big/ \left(j^2h^2 + w_+^2\right) j \neq 0 \end{cases} \tag{5.55}$$

suggested the trapezoidal rule leading.

Here, in Eq. 5.40, the Heaviside step function is unity or zero when $\mathrm{Im}\,(w_+)$ is either negative or positive. However, it should be replaced by the factor $\frac{1}{2}$ when $\mathrm{Im}\,(w_+) = 0$, i.e. the pole is located right on the steepest descent path. The term $D_X$ in Eq. 5.37 can be evaluated with trapezoid rule method with equation:

$$D_x/(-\frac{ie^{ikR_2}}{\pi\sqrt{kR_2}}) = h \sum_{n=-\infty}^{\infty} \frac{f(\frac{n^2h^2}{kR_2})}{n^2h^2/kR_2 - w_+^2} e^{-n^2h^2} + I_{pole} \cdot \epsilon_h + I_{err} \tag{5.56}$$

where $I_{pole}$ is defined with

$$I_{pole} = 2\pi[e^{H[-\mathrm{Im}(w_+)]i\pi\sqrt{kR_2}w_+/h}/(e^{-i\pi\sqrt{kR_2}w_+/h} - e^{i\pi\sqrt{kR_2}w_+/h})]\frac{e^{-kR_2{w_+}^2}}{\sqrt{kR_2}w_+}f(w_+) \tag{5.57}$$

This contribution of the pole is not the same as the surface wave pole contribution even though they are both located at $w_+$. In Eq. 5.37, the existence of the pole is decided by the imaginary part of pole location $w_+$. However, in Eq. 5.58 the existence of the pole contribution is decided by the term $\epsilon_h$, which is a function of the integration step size $h$. To make it clear, $\epsilon_h$ is defined by the following:

$$\varepsilon_h = \begin{cases} 0 & \pi\sqrt{kR_2}/h < \mathrm{Im}(U_0) \\ 1/2 & \pi\sqrt{kR_2}/h = \mathrm{Im}(U_0) \\ 1 & \pi\sqrt{kR_2}/h > \mathrm{Im}(U_0) \end{cases} \tag{5.58}$$

If $\pi\sqrt{kR_2}/h$ is larger than the real part of the pole in the W plane, the equation should include the residue contribution. If $\pi\sqrt{kR_2}/h$ is equal to the real part of the pole, half of the contribution should be included. And if a large $h$ is used, no pole contribution is needed. It might be interesting to point out that since the real part of $w_+$ is always positive, we do not need to consider the condition when it becomes negative. In other words, the existence of the surface wave pole is decided by the ground property and geometry of the problem, but the existence of the pole contribution in Eq. 5.58 is decided by the step size $h$ used in the trapezoid integration process. Moreover, it is independent of the geometry and the ground property. Finally, the error term can be represented by an integral:

$$\begin{aligned} I_{error} &= 2 \int\limits_{-\infty-i\pi\sqrt{kR_2}/h}^{\infty-i\pi\sqrt{kR_2}/h} \tfrac{f(W)}{W^2+w_+{}^2} e^{-kR_2W^2} \tfrac{1}{e^{2\pi i\sqrt{kR_2}W/h}-1} \sqrt{kR_2}dW \\ &\approx 2 \int\limits_{-\infty-i\pi\sqrt{kR_2}/h}^{\infty-i\pi\sqrt{kR_2}/h} \tfrac{f(i\pi\sqrt{kR_2}/h)}{W^2+w_+{}^2} e^{-kR_2W^2} \tfrac{1}{e^{2\pi i\sqrt{kR_2}W/h}-1} \sqrt{kR_2}dW \end{aligned} \tag{5.59}$$

### 5.2.4 A simple error bound

An exact error bound was derived by Alazah et al. [78] for the Fresnel integral. The same process could be used to find the error bound for the modified trapezoid rule method used in this paper. This process is written as:

$$I_{err} < \left|\frac{2\pi f(i\pi\sqrt{kR_2}/h)\hat{c}_N e^{-\pi N}}{\sqrt{kR_2(N+1/2)}w_+}\right| \tag{5.60}$$

where

$$\begin{aligned}
\widehat{c_N} &= c_N + \tfrac{\sqrt{2}(2\pi+1)}{\pi^{3/2}e^{\pi/2}\sqrt{N+1/2}} \\
c_N &= \tfrac{20\sqrt{2}e^{-\pi/2}}{9\pi(1-e^{-2A_N^2})}(1+2\sqrt{\pi}e^{-BA_N{}^2}) + \tfrac{(2\pi+1)e^{-\pi/2}}{2\sqrt{2}\pi^{3/2}A_N} \\
A_N &= \sqrt{(N+1/2)\pi} \\
B &\approx 0.0536
\end{aligned} \tag{5.61}$$

N represents the number of points used in the evaluation using the modified trapezoid rule. To guarantee a fixed error bound, the step size is defined as a function of the number of points used in the integration as:

$$h = \sqrt{\pi/(N+1/2)} \tag{5.62}$$

The final expression of modified trapezoid rule method can then be expressed as

$$u_\beta^* = (-\frac{ie^{ikR_2}}{\pi\sqrt{kR_2}})[h\sum_{n=-\infty}^{\infty}\frac{f(\frac{n^2h^2}{kR_2})}{n^2h^2/kR_2 - w_+^2}e^{-n^2h^2} + I_{pole}\cdot\epsilon_h] + u_p e^{ikR_2(1+w_+^2)}H[-Im(w_+)] \tag{5.63}$$

with the error bound

$$|u_\beta - u_\beta{}^*| = -\frac{ie^{ikR_2}}{\pi\sqrt{kR_2}}I_{err} \tag{5.64}$$

which can be estimated using Eq. 5.60.

### 5.2.5 Numerical analysis.

#### Validation of the modified trapezoid rule method

A simple one parameter model by Delany [83] is used in this process for simple modeling. The result calculated with the modified trapezoid rule method is compared with the Gaussian quadrature method introduced by Li and Liu [8] in Figures 5.8 and 5.9. Twenty points are used in both methods to guarantee an accurate comparison. The agreements are great for both the line source model and the point source model. In the next step, the error for both methods are compared with a different number of points used in the integration.

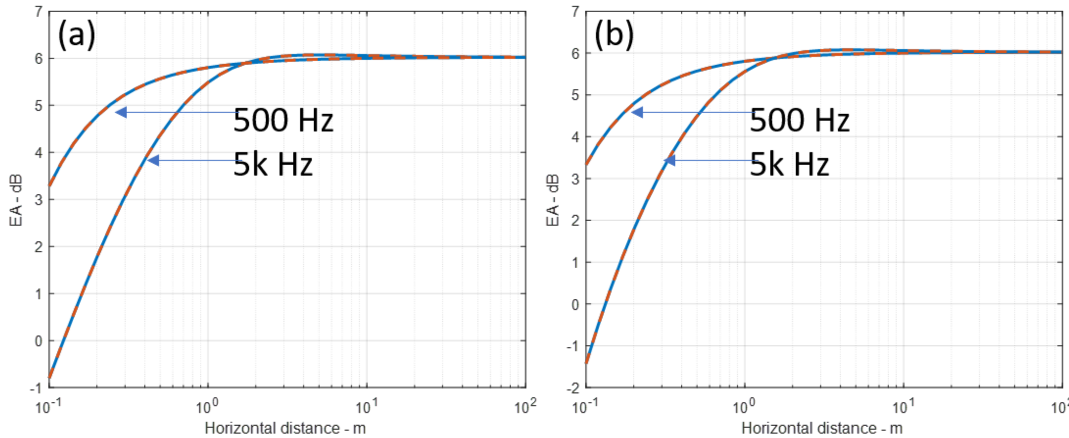


Figure 5.8. Excess attenuation level of refracting wave $u_\beta$. (a) Line source model. (b) Point source model. Source and receiver are both placed on the ground with 0 meter height. Delany's one parameter model is used for the modeling of extend reacting ground. Extend reacting model with flow resistivity = 5k Pa ms$^{-2}$ . Dashed: Modified trapezoid rule. Solid: Gaussian quadrature method

**Error of the method.**

In Figure 5.10, the error of the modified trapezoid rule is compared with both the estimated error bound and the error of the Gaussian-Hermite quadrature method introduced by Li and Liu. We can observe that although the error bound overestimates the error by 3dB in (b), the rate of decaying is well estimated by the bound. The Gaussian quadrature method has a larger error with small number of N, and the errors of both method converge to 10-16 as the number of points surpass 13. The solution are compared with the direct numerical integration solution on the steepest descent path with 2000 points to ensure accuracy.

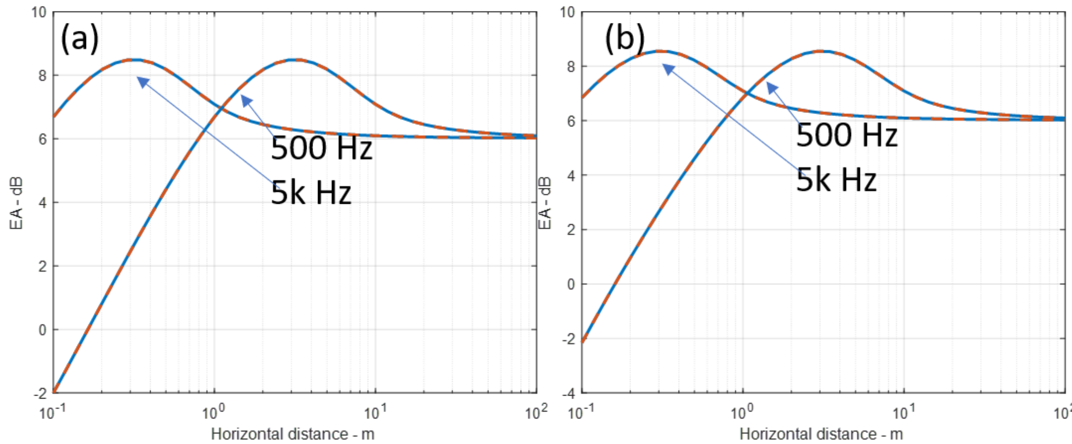


Figure 5.9. Excess attenuation level of refracting wave $u_\beta$. (a) Line source model. (b) Point source model. Source and receiver are both placed on the ground with 0 meter height. Delany's one parameter model is used for the modeling of extend reacting ground. Locally reacting model with constant admittance: 0.25-0.25i. Dashed: Modified trapezoid rule. Solid: Gaussian quadrature method.

## 5.3 Conclusion

The modified trapezoid rule is applied in this chapter to evaluate the refraction wave term for a point source and a line source. The same method can also be applied to similar problems such as a moving source problem due to a point or a line source above a locally and a non-locally reacting ground. The modified trapezoid rule method uses about half of the computational time used in the Gaussian quadrature method with same level of accuracy. This shows that the pole subtraction method is not the only way to solve the refraction wave term. In addition, the behavior of the pole is analyzed in detail with the modified trapezoid rule method. The surface wave pole due to the $cos\theta + \beta$ term is in nature more of a numerical artifact than a physical property of the ground. A different mathematical solution could give different physical explanations to the diffraction wave term. If a low accuracy is required (i.e., error less than 0.5 dB), an asymptotic solution may be the best method to calculate the

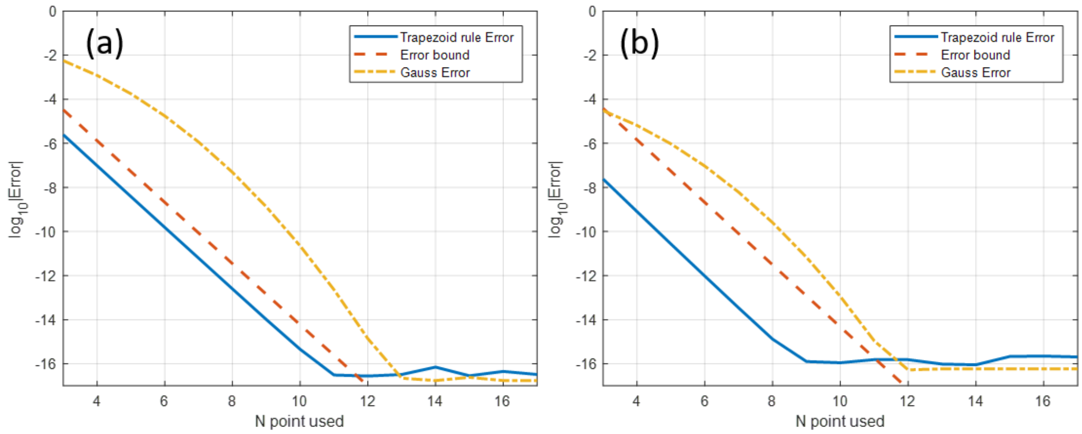


Figure 5.10. Comparison of the error of trapezoid rule, error of Gaussian quadrature method and error bound of trapezoid rule. N indicates the number of point used in the integration. (a) Extend reacting model with flow resistivity = 5k Pa ms$^{-2}$ . (b) Extend reacting model with flow resistivity = 500k Pa ms$^{-2}$ . Horizontal separation = 1m. Both source and receiver are placed on the ground.

reflected wave term. However, if a high accuracy solution is required, the modified trapezoid rule method is faster than the Gaussian quadrature method and the FFP method.

# 6. SOUND PROPAGATION ABOVE GROUND SURFACE WITH TEMPERATURE GRADIENT

## 6.1 Introduction

Meteorological effect is one of the most important effects in the propagation of en-route aircraft noise. The sound speed profile—which is decided by the temperature and the wind speed profile along the propagation path—could influence the arrival time and the power of the sound wave. This effect is known as the refraction effect. With a positive sound speed profile, the refraction is called a downward refraction, which tends to increase the sound pressure level on the ground. On the contrary, an upward refracting medium with a negative sound speed profile tends to decrease the sound pressure level on the ground. The topic has been studied for several decades [84–87]; however, there has not been any accurate and simple asymptotic solution derived which is valid at any range.

There are mainly three methods to predict the sound field due to refraction effects: ray tracing, normal mode, and asymptotic theory. Ray tracing approximates the sound waves in terms of sound rays, and it uses ideas of geometric acoustics to model the problem; however, the method cannot be used to accurately predict the sound field under some circumstances, such as the sound field in the shadow zone [26]. An asymptotic solution based on wave theory has been suggested by Li [88], which is based on WKB approximation for the sound field before the turning point, but the solution has a singularity at the turning point, which makes the solution inaccurate near the turning point.

For upward refracting medium, an approximation based on residue theory is suggested by Pierce in [16] and later studied by Raspet in [17] and Berry in [89] for the sound field in the shadow zone, which is called the normal mode method. This method ignores the contribution of a direct wave and thus is inappropriate for the sound field in the illuminated zone. In this chapter, the asymptotic solution for the sound field above a locally reacting ground in an upward refracting profile is derived based on wave theory and the stationary point method. After that, we compare the asymptotic solution with numerical integration for validation.

The prediction of the sound propagating in an upward refracting medium is of great importance in outdoor sound predictions. The bilinear sound speed profile in the chapter was widely used as a substitution of the linear sound speed profile due to their similarity and the simple expressions of a bilinear profile. The calculation of the sound field in a linear sound speed profile with the turning point theory requires an additional integration step, which is not required for a bilinear profile.

A bilinear upward refracting profile is a very common daytime sound speed profile type. The sound speed is a function of height $c_0/c = \sqrt{1-2az}$, in which the value of a is negative for an upward refracting atmosphere, c0 is the sound speed at height $z = 0$ m, and $c(z)$ indicates the sound speed at height $z$ m. The integral for the sound propagation above an impedance plane for a bilinear sound speed profile can be derived by solving an inhomogeneous Helmhotz equation. The details can be found in [90] and will not be repeated here.

The solution for the sound pressure can be expressed with the integral

$$p = \int_0^\infty J_0(kr)P(z,k_r)k_r dk_r. \tag{6.1}$$

where function $P$ is defined as

$$P = le^{i\pi/6}Ai[(\tau - \frac{z_l}{l})e^{i2\pi/3}][Ai(\tau - \frac{z_s}{l}) - \frac{[Ai'(\tau) - qAi(\tau)]Ai[(\tau - z_s/l)e^{i2\pi/3}]}{e^{i2\pi/3}Ai'(\tau e^{i2\pi/3}) - qAi(\tau e^{i2\pi/3})}] \tag{6.2}$$

where

$$\begin{aligned} q = ik_0 l\rho c/Z,\ l = (R/2{k_0}^2)^{1/3} \\ \tau = ({k_r}^2 - {k_0}^2)l^2,\ k_0 = \omega/c_0 \end{aligned} \tag{6.3}$$

where $J_0$ is a bessel function; $R$ is the radius of curvature of rays, which is equal to $1/|a|$; $\rho$ is the density of the air; and $c$ is the speed of sound and it is a function of height $z$ in the chapter. $Z$ is the specific impedance of the ground. $z_l$ and $z_s$ are the greater and lesser of sound source height and receiver height. $l$ is sometime known as creeping wave layer. *Ai(x)* is the Airy function, which is analytic for any complex value $x$. An similar expression with wind effects and arbitrary sound speed profile was derived by Li [90], which was solved using the normal mode method for the sound field in the shadow zone and was validated with the FFP method [18] .

An evaluation of the integral is difficult due to the highly oscillatory feature of Airy functions, which makes real time calculation of a high-frequency sound field impossible. There have been several attempts to evaluate the integral efficiently using numerical techniques. The FFP method was used by Taherzadeh [18]for the sound field with an arbitrary sound speed profile. The method significantly reduced the calculation time, but the evaluation still requires a larger number of points to converge the solution to a correct value. The derivation of an asymptotic solution was not available due to the complicated behavior of Airy functions. Recently, studies around Airy functions [91] have made their evaluation much simpler using scale factors of an Airy function and the derivative of an Airy function. This advancement provided an new opportunity in deriving an asymptotic solution for the sound field in an upward refracting medium with the help of the development of numerical calculation techniques.

### 6.1.1 Behavior of airy function and its asymptotic expansion

In the process of deriving an asymptotic solution for the aforementioned sound field, a detailed analysis around the behavior of the Airy function is required. One of the mean reasons that there has been no accurate asymptotic solution available for the sound field in a bilinear or linear medium is due to the complicated behavior of the Airy function. The most widely used asymptotic solution of the Airy function is

$$Ai(x) \approx \frac{1}{2}\pi^{(-1/2)}x^{-1/4}e^{-\xi}\sum_{0}^{\infty}(-1)^k c_k \xi^{-k} \qquad (|\arg x| < \pi) \tag{6.4}$$

where $x$ is simply a variable which has no connections to the geometry of our acoustic problem. The formula in Eq. 6.4 is true in most of the regions on the $x$ plane, but there are areas where the formula falls short. For example, on the negative real axis, the above asymptotic solution fails. Another asymptotic solution should be used on the negative real axis:

$$Ai(x) \approx \pi^{(-1/2)}x^{-1/4}\sin(\xi + \frac{\pi}{4})\sum_{0}^{\infty}(-1)^k c_{2k}\xi^{-2k} - \cos(\xi + \frac{\pi}{4})\sum_{0}^{\infty}(-1)^k c_{2k+1}\xi^{-2k-1} \qquad (|\arg x| < \frac{2}{3}\pi) \tag{6.5}$$

This effect with two different asymptotic solutions is known as the Stokes phenomenon. [92] The stokes phenomenon in the Airy's function indicates that the oscillator in the integrand is different for different value of $x$. In $Ai(\tau - \frac{z_s}{l})$, the second expansion (Eq.6.5) should be used when the integration variable $k_r$ is between the two points $\pm\sqrt{z_s/l^3 + k_0^3}$, because the argument of airy function is a negative real number in the interval. Outside of this interval between the two points, Equation 6.4 should be used. At the same time, for $Ai[(\tau - \frac{z_l}{l})e^{i2\pi/3}]$, the first asymptotic solution (Eq.6.4) should be used for any value of $k_r$ on the real axis due to the term $e^{2i\pi/3}$. Choosing the correct asymptotic expansion is one of the most important part in the derivation of the asymptotic solution.

### 6.1.2 Stationary phase approximation

Similar to the equation for the homogeneous atmospheric condition, the integral has two parts. The direct wave component is as follows:

$$p_{dir} = \int\limits_{-\infty}^{\infty} \frac{1}{2} H_0(kr) l e^{i\pi/6} Ai[(\tau - \frac{z_l}{l})e^{i2\pi/3}] Ai(\tau - \frac{z_s}{l}) k_r dk_r \tag{6.6}$$

If the correct asymptotic solution is used for expanding Eq. 6.6, the oscillators of the direct wave term can be found as

$$g_{d1} = \int\limits_{zs}^{zl} kz(kr, z)dz + r \cdot kr - \frac{\pi}{4} \tag{6.7}$$

and

$$g_{d2} = \int\limits_{zt}^{zl} kz(kr, z)dz + \int\limits_{zt}^{zs} kz(kr, z)dz + r \cdot kr + \frac{\pi}{4} \tag{6.8}$$

There are two exponential oscillators since the expansion of the Airy function on the negative real axis is a trigonometric function, which can be expanded using two exponential terms according to Euler's identity. The $Ai[(\tau - \frac{z_l}{l})e^{i2\pi/3}]$ function is expanded with the scaled Airy function, which is $Ais(x) = Ai(x)e^{\frac{3}{2}z^{3/2}}$. (The scaled Airy function can be found in MATLAB) The term $e^{\frac{3}{2}x^{3/2}}$ is highly oscillatory but term $Ais(x)$ is smooth on the real axis of $x$.

The first oscillator $g_{d1}$ corresponds to the path that connects the source point and the receiver point without a turning point, and $\int\limits_{zs}^{zl} kz(kr, z)dz$ corresponds to the integral between $z_s$ and $z_l$ without passing through a turning point. The second oscillator $g_{d2}$ corresponds to the path with a turning point, where $\int\limits_{zt}^{zl} kz(kr, z)dz$ corresponds to the integral from the turning point to $z_l$ and $\int\limits_{zt}^{zs} kz(kr, z)dz$ corresponds to the integral from the turning point $z_t$ to $z_S$.

In Figure 6.1, the source is at $(x_0, z_0) = (0, 20)$ and the receiver is at $(x, z) = (10, 10)$. The sound speed gradient is $a = -3 \cdot 10^{-4}$. There are two possible paths that connect the source point and the receiver point without the ground reflection,

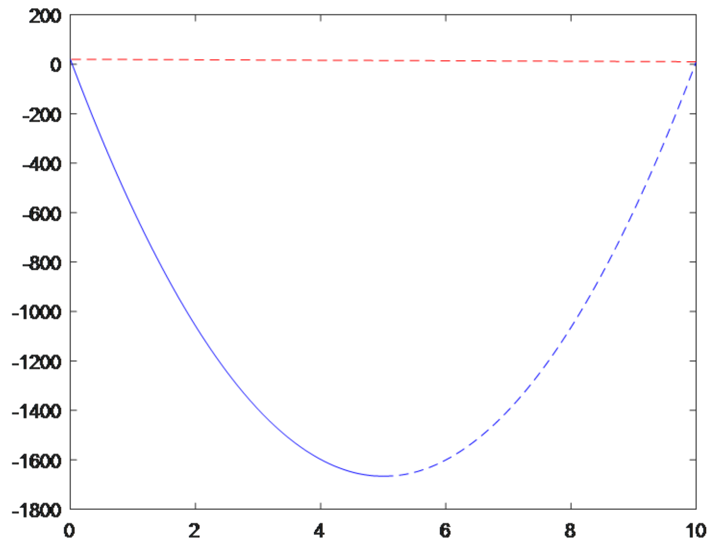


Figure 6.1. Two possible paths for bilinear profile

as seen in Figure 6.1. In reality, the second path is usually not possible due to the existence of the ground surface. The second term exists only when the sound speed below the ground is defined with the function $c_0/c(z) = \sqrt{1-2az}$ as well for negative $z$. This is also true when ray tracing method is used to find the ray paths for a bilinear profile. Using the same sound speed gradient, there are two possible solutions for the ray path if equations

$$r = \int_{z_S}^{z_L} tan\phi dz \tag{6.9}$$

and

$$\frac{c_0}{c} = \frac{sin\phi_0}{sin\phi} = \sqrt{1-2az} \tag{6.10}$$

are used to solve for the paths, where $\phi$ is the angle between the ray path and the $z$ axis, and where $\phi_0 = \phi(z=0)$. However, if the linear sound speed profile is used, there is only one possible path that connects the source and receiver.

**The first term in the direct wave** The first term in the direct wave term is the leading term and is the only term used in many ray tracing methods [26] since the second wave term is not possible in the presence of ground. The full expression of the total direct wave integral is:

$$\int_{-\infty}^{+\infty} k_r {H_0}^{(1)}(kr \cdot r) l e^{i\pi/6} Ai[(\tau - \frac{z_l}{l})e^{i2\pi/3}]\pi^{(-1/2)}(\tau - \frac{z_s}{l})^{-1/4} \sin(\frac{2}{3}(\tau - \frac{z_s}{l})^{3/2} + \frac{\pi}{4}) dk_r$$

$$= I_{d1} + I_{d2} = p_{dir} \tag{6.11}$$

The zero point of the derivative of the phase function with respect to the integration variable ($dg_{d1}/dk_r$=0) is the saddle point for the integral. Instead of using $k_r$, a simpler expression could be obtained by substituting $k_r$ with $k_0 sin\mu$. The derivative of the phase function with respect to $\mu$ is

$$\frac{dg_{d1}}{d\mu_0} = \int_{zs}^{zl} k_0\sqrt{n^2 - \sin{\mu_0}^2} + k_0 \cos\mu_0 r = k_0 \int_{zs}^{zl} \cos\mu_0(\tan\phi - \tan\mu) dz \tag{6.12}$$

where $\phi$ is the incident angle of the direct wave that was solved with ray tracing. Eq. 6.12 is worth mentioning because this equation shows the connection between the ray tracing method and the saddle point method (which is another name for the stationary point method). This indicates that the incident angle on the ground solved with the saddle point method is actually equal to the incident angle solved with the ray tracing method. Here, $\mu_0$ must be equal to $\phi_{10}$ at the stationary point. The two methods using different theories, complex analysis and geometric acoustics, give the same conclusion in Eq.6.12.

The stationary point is

$$kr_{st1} = k_0 \sin\phi_{10} \tag{6.13}$$

Subscription 1 in $\phi_{10}$ suggests it to be the angle in the shorter path, which is named as the first type of path in the thesis; 0 means that the value of the height $z$ is zero, which then means it is the ground incident angle. IN addition $\phi_1$ is a function of the height defined as $\phi_1 = \phi_1(z)$.

By substituting the stationary point into the phase function, we can find a simplified equation:

$$
\begin{aligned}
g_{d1}(\phi_1) &= \int_{zs}^{zl} (\sqrt{{k_0}^2 n^2 - {k_r}^2} dz + k_r \tan\phi_1) dz - \pi/4 \\
&= k_0 \int_{zs}^{zl} \frac{n}{\cos\phi_1} dz - \pi/4 = k_0 R_{d1} - \pi/4.
\end{aligned} \tag{6.14}
$$

Then, substitute the saddle point into the Eq. 6.11. Using stationary phase approximation and Gaussian integral's approximation of $\int_{-\infty}^{+\infty} e^{-x^2/2} \approx \sqrt{2\pi}$, we can obtain the following:

$$
\begin{aligned}
I_{d1} \approx & \sqrt{\frac{1}{2i\pi k_r r}} k_r \frac{1}{2} \frac{1}{\sqrt{\pi}} \frac{1}{[({k_0}^2 - k_r^2) l^2 - z_l/l]^{1/4}} \cdot \frac{1}{\sqrt{\pi}} \\
& \cdot \frac{1}{[-({k_0}^2 - k_r^2) l^2 + z_s/l]^{1/4}} \cdot \frac{i}{2} \\
& \cdot l e^{i\pi/6} e^{i g_{d1}(k_{stp1})} \sqrt{2\pi} \sqrt{i / \frac{d^2 g_{d1}}{d{k_r}^2}|_{k_{stp1}}}
\end{aligned} \tag{6.15}
$$

In the above equation

$$
\frac{d^2 k_z}{d{k_r}^2} = -\frac{{k_r}^2}{({k_0}^2 n^2 - {k_r}^2)^{3/2}} - \frac{1}{\sqrt{{k_0}^2 n^2 - {k_r}^2}} = -\frac{1}{n k_0 \cos^3\phi_1} ({\sin\phi_1}^2 + {\cos\phi_1}^2), \tag{6.16}
$$

so

$$
\frac{d^2 g_{d1}}{d{k_r}^2}(k_{stp1}) = \int_{zs}^{zl} \frac{d^2 k_z}{d{k_r}^2}(k_{stp1}) dz = -\int_{zs}^{zl} \frac{1}{n k_0 \cos^3\phi_1} dz \tag{6.17}
$$

The term with double derivative can be simplified to

$$
\sqrt{i / \frac{d^2 g_{d1}}{d{k_r}^2}|_{k_{stp1}}} = 1 / \sqrt{\int_{zs}^{zl} \frac{i}{n k_0 \cos^3\phi_1} dz} \tag{6.18}
$$

at the stationary point. We can compare Eq.6.18 with the corespondent term for homogeneous medium, which is the following:

$$
\sqrt{i / \frac{d^2 g_{homo}}{d{k_r}^2}|_{k_{stp1}}} = \sqrt{\frac{k_0 \cos^3\phi}{i(zl - zs)}} \tag{6.19}
$$

The similarity is obvious and if $a = 0$, Eq. 6.18 and Eq. 6.19 will be equal to each other.

After substituting Eq.6.18 into Eq.6.15, we can obtain our final solution for the direct wave (without a turning point), which is

$$I_{d1} \approx \frac{1}{4\pi} k_0 \sqrt{\frac{\sin\phi_{10}}{r}} \frac{1}{\sqrt{k z_{zs} k z_{zl}}} e^{ik_0 R_{d1}} / \sqrt{\int_{zs}^{zl} \frac{dz}{n\cos^3\phi_1}} \tag{6.20}$$

where $R_{d1}$ is named as the effective phase distance:

$$R_{d1} = \int_{zs}^{zl} \frac{n}{\cos\phi_1} dz \tag{6.21}$$

Eq.6.21 is slightly different from the path length solved with ray tracing method:

$$R_{ray\,tracing} = \int_{zs}^{zl} \frac{1}{\cos\phi_1} dz \tag{6.22}$$

Here, the difference suggests a slightly different decaying rate between the wave equation approximation and the ray tracing approximation.

It might be interesting to reduce the value of the sound speed gradient $a$ to 0, and it would reduce Eq.6.20 to

$$\begin{aligned} &\frac{1}{4\pi} k_0 \sqrt{\frac{\sin\phi_{10}}{r}} \frac{1}{\sqrt{k z_{zs} k z_{zl}}} e^{ik_0 R_{da}} / \sqrt{\int_{zs}^{zl} \frac{dz}{n\cos^3\phi_1}} \\ \xrightarrow[a=0]{} &\frac{1}{4\pi} k_0 \sqrt{\frac{\sin\phi}{r}} \frac{1}{k_0 \cos\phi} e^{ik_0 R_d} \sqrt{\frac{n\cos^3\phi}{z_l - z_s}} = \frac{e^{ik_0 R_d}}{4\pi R_d} \end{aligned} \tag{6.23}$$

which is the solution of the direct wave for a homogeneous atmosphere. Eq.6.23 shows the relationship between homogeneous solution and the asymptotic solution with sound speed gradient. $R_d$ is the straight distance between the source and the receiver.

**The second term in the direct wave** Come back to Eq.6.11. The phase function of the second term is

$$g_{d2}(\phi_2) = \int_{zt}^{zl} (\sqrt{{k_0}^2 n^2 - {k_r}^2} dz + k_r \tan\phi_2) dz = \int_{zt}^{zs} (\sqrt{{k_0}^2 n^2 - {k_r}^2} dz + k_r \tan\phi_2) dz + \pi/4 \tag{6.24}$$

The horizontal distance can be divided into two parts:

$$r = \int_{zt}^{zs} k_r \tan\phi_2 dz + \int_{zt}^{zl} k_r \tan\phi_2 dz \tag{6.25}$$

where the first term corresponds to the ray section from $z_t$ to $z_s$, and the second term corresponds to the section from $z_t$ to $z_l$. Here, $z_t$ is the height of the turning point, which can be solved geometrically by setting $k_z = 0$. Equation 6.25 indicates that the second path requires a turning point in the path in order to complete the trip from the sound source to the receiver. This hypothesis will be proved in the stationary phase analysis.

A similar approach is used in the derivation of the asymptotic solution for the second term in 6.11. The stationary point also coincides the ray tracing solution. The derivative of the phase term is as follows:

$$\frac{dg_{d2}}{d\mu_0} = \int_{zs}^{zl} k_0 \sqrt{n^2 - \sin{\mu_0}^2} + \int_{zs}^{zl} k_0 \sqrt{n^2 - \sin{\mu_0}^2} + k_0 \sin\mu_0 r = k_0 \int_{zt}^{zl} \cos\mu_0 (\tan\phi_2 - \tan\mu) dz + k_0 \int_{zt}^{zl} \cos\mu_0 (\tan\phi_2 - \tan\mu) dz \tag{6.26}$$

Eq.6.26 suggests that the ray tracing solution coincides with stationary phase solution for the path with one turning point. This is because the stationary point indicates that $\phi_2 = \mu$. An approach similar to the one we did for the path of the first type gives

$$I_{d2} \approx -\frac{1}{4\pi} k_0 \sqrt{\frac{\sin\phi_{20}}{r}} \frac{1}{\sqrt{kz_{zs} kz_{zl}}} e^{ik_0 R_{d2}} / \sqrt{\int_{zt}^{zl} \frac{dz}{n \cos^3\phi_2} + \int_{zt}^{zs} \frac{dz}{n \cos^3\phi_2}} \tag{6.27}$$

where

$$R_{d2} = \int_{zt}^{zl} \frac{n}{\cos\phi_2} dz + \int_{zt}^{zs} \frac{n}{\cos\phi_2} dz \tag{6.28}$$

Eq.6.28 indicates a turning point within the path. It can be observed from the expansion of Eq.6.11 that there are two types of paths for the direct wave. The first one is linked to the path without a turning point and the second one is linked to the path with a turning point. For a short range, the first type of path is possible but when the horizontal distance is larger than $r_{tur}$, the wave can never travel to the predefined receiver location without getting to a turning point first. The $r_{tur}$ for the direct wave is

$$r_{tur} = -\frac{1}{a}\sqrt{-2a(z_{Ls} - z_s)} \tag{6.29}$$

If the horizontal distance is larger than $r_{tur}$, Eq.6.12 has no zeros and Eq.6.26 has two zeros, one of these zeros represents the main path—which is also the path that was solved with the ray tracing method—while the other one zero represents the less important and physically longer path. The total asymptotic solution of Eq.6.6 if the horizontal range is larger than $r_{tur}$ is

$$I_{dtotal} = I_{d2}(\phi_{20a}) + I_{d2}(\phi_{20b})$$

and before the turning point the solution is

$$I_{dtotal} = I_{d1}(\phi_{10a}) + I_{d2}(\phi_{20b})$$

where "2" represents the second path type, "$a$" represents main path and "$b$" represents insignificant path.

It might be interesting to compare this solution with the solution suggested by Li [88] where the WKB method is used. In Li's solution, a singularity exists at the turning point, and the solution start to deviate from the accurate solution as the receiver approaches the turning point. However, the problem does not exist in the current solution. Moreover, the current solution works after the turning point for any value of the horizontal range. Li's work used the steepest descent method in the $\mu$

Table 6.1. Saddle points in each type of path for bilinear profile

| | $r < r_{tur}$ | $r \geq r_{tur}$ |
|---|---|---|
| First path type | 1 saddle point | 0 saddle point |
| Second path type | 1 saddle point | 2 saddle point |

plane and made an assumption of $cos(\mu_0 - \phi_0) = cos(\mu - \phi)$, which is not an accurate approximation for a ong horizontal range. In contrast to Li's work, in this study the steepest descent method is carried out in the $k_r$ plane instead of the $\mu$ plane without making other assumptions except when using the asymptotic form of Airy functions.

The distribution of the saddle points in the two paths is exhibited in Table 6.1; the location of the turning point can be found in Figure 6.2. It is easier for the rays in a profile with a large sound speed gradient to reach the turning point. The insignificant path always contains a turning point, which means that Eq.6.26 has at least one insignificant solution.

Although the exact solutions for most sound speed profiles do not exist, the exact solution for the bilinear profile is available with the method of path integral. According to Eq. (13) in [93], the exact solution for the bilinear profile could be expressed using a multiplication of two Airy functions. Although it is difficult to find any connections between the exact solution and geometric acoustics, the solution could be used to validate the newly derived asymptotic equation. The expression for the exact solution is

$$\begin{aligned}
&G_{ext} = \tfrac{-1}{2|r-r_s|}e^{i(\pi/6)}\{Ai'[-(\tfrac{k_0}{A})^{2/3}(1+\tfrac{A}{2}(z+z_s)-\tfrac{|A|}{2}|r-r_s|)] \\
&\cdot Ai[-e^{i(2\pi/3)}(\tfrac{k_0}{A})^{2/3}(1+\tfrac{A}{2}(z+z_s)+\tfrac{|A|}{2}|r-r_s|)] \\
&-e^{i(2\pi/3)}Ai[-(\tfrac{k_0}{A})^{2/3}(1+\tfrac{A}{2}(z+z_s)-\tfrac{|A|}{2}|r-r_s|)] \\
&\cdot Ai'[-e^{i(2\pi/3)}(\tfrac{k_0}{A})^{2/3}(1+\tfrac{A}{2}(z+z_s)+\tfrac{|A|}{2}|r-r_s|)]\}
\end{aligned} \tag{6.30}$$

where $A = -2a$.

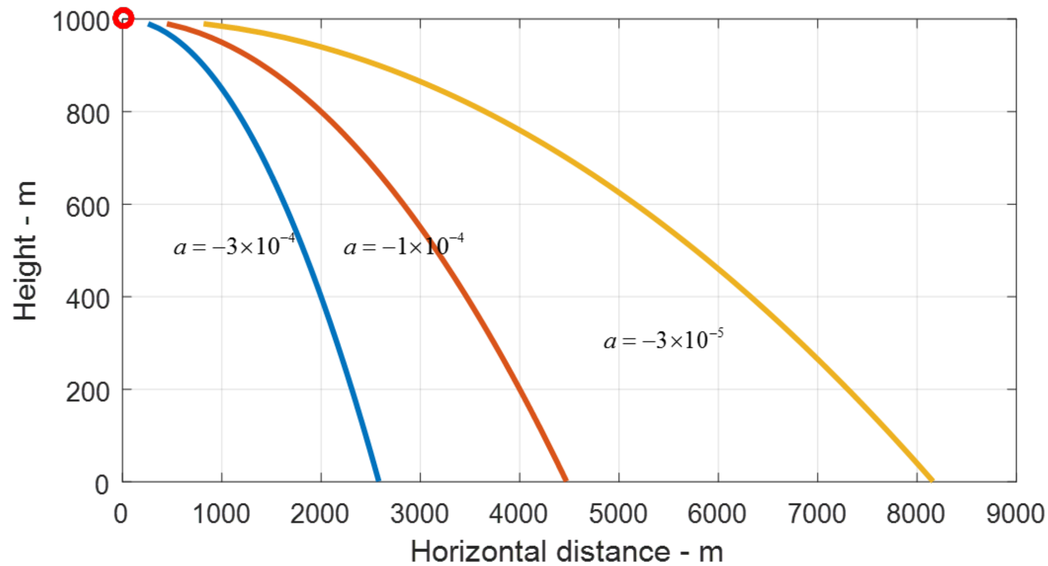


Figure 6.2. Turning line for three different sound speed profiles. Sound source is located at $z_L = 1km$, $x_S = 0m$. Three sound speed gradient $-3 \times 10^{-4}$, $-1 \times 10^{-4}$ and $-3 \times 10^{-5}$ are used in the figure.

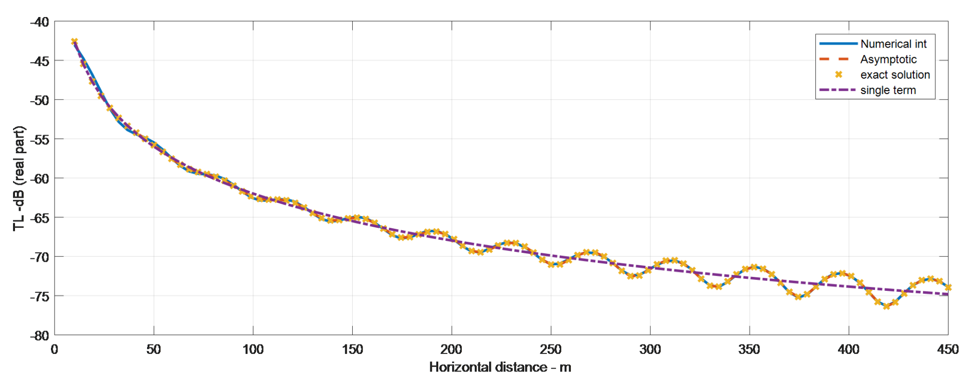


Figure 6.3. a=0.001 s-1, zl=5m, zs=1m, frequency = 10 Hz.

It is important to note that for the bilinear profile, two wave terms exist for the direct wave. In Figures 6.3 and Figure 6.4, we could see that our asymptotic has a good agreement with the exact solution. The dashed dotted line uses only one

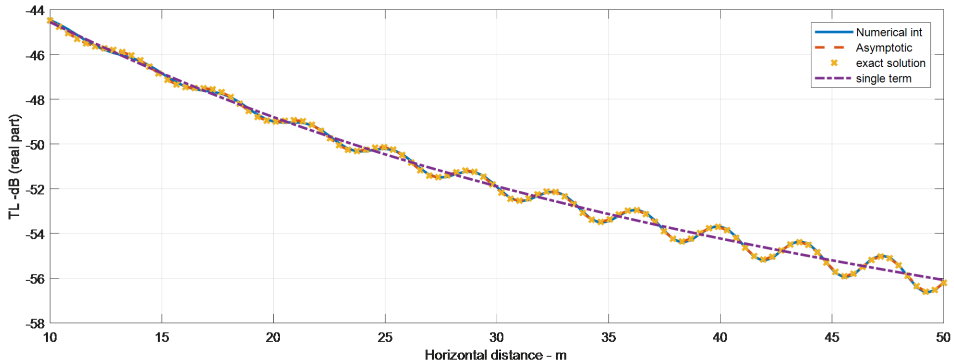


Figure 6.4. a=0.003 s-1, zl=10m, zs=1m, frequency = 100 Hz.

direct wave term and obvious disagreements could be observed in both figures. The curves for the result with only one ray term is very smooth and is actually very close to the solution for the linear sound speed profile. However, if the second term is not included, the oscillations at far range cannot be captured. The reason that the second wave term exists is that the value of speed ratio becomes very large with a large negative z value, as a result, the second wave becomes possible due to the large sound speed gradient.

In the near field, due to the long wave path of the second wave term, the contribution of the term is very small compared to the total wave. However, in the far field, as the magnitude of the first wave term drops to a certain level, the interference effect between the two waves becomes obvious. In real life with a ground surface, the second term is usually not possible most of the time because the depth required for the second wave is larger than 9km for a=$-3 \times 10^{-4}$. The second wave path would normally be blocked by the ground in both outdoor acoustics and underwater acoustics. However, theoretically, the second wave term should always be included if the bilinear profile is used, which explains the existence of the interference effect in the exact solution.

**Reflected wave term** The reflective wave term also comprises two terms. The equation is

$$I_r = \int_{-\infty}^{+\infty} k_r {H_0}^1(kr \cdot r) l e^{i\pi/6} Ais[(\tau - \frac{z_l}{l})e^{i2\pi/3}] Ais[(\tau - \frac{z_s}{l})e^{i2\pi/3}]_r$$
$$(\Gamma_{s1} e^{i(\int_0^{zs} k_z(k_r,z)dz + \int_0^{zl} k_z(k_r,z)dz - \pi/4)} + \Gamma_{s2} e^{i(\int_{zt}^{zs} k_z(k_r,z)dz + \int_{zt}^{zl} k_z(k_r,z)dz + \pi/4)}) dk_r \tag{6.31}$$

where

$$\Gamma_1 = \sqrt{i} e^{i\pi/6} \frac{-(l^2 k_z(z_0))^{1/2} - iq}{(l^2 k_z(z_0))^{1/2} - iq} \tag{6.32}$$

and

$$\Gamma_2 = \sqrt{i} e^{i\pi/6} \frac{-(l^2 k_z(z_0))^{1/2} + iq}{(l^2 k_z(z_0))^{1/2} - iq} = -\sqrt{i} e^{i\pi/6} \tag{6.33}$$

The Airy function with an argument on the real axis (with no $e^{i2\pi/3}$ term in the argument) also has two asymptotic solutions due to the Stokes phenomenon. As a result, a wave term with a turning point and a wave term without a turning point could be found with a similar method. The insignificant wave term always exists as well, the oscillator of which is as follows:

$$g_{r2} = \int_{zt}^{zs} k_z(k_r, z)dz + \int_{zt}^{zl} k_z(k_r, z)dz + \pi/4 + k_r r, \tag{6.34}$$

Eq. 6.34 is exactly the same as the phase function in the second wave term in the direct wave Eq.6.8, which means that their stationary points and their behaviors of the phase function are exactly the same. The terms will cancel out with the insignificant term in the direct wave due to an opposite sign. At the same time, the main term in the reflected wave is a bit different

$$g_{r1} = \int_0^{zs} k_z(k_r, z)dz + \int_0^{zl} k_z(k_r, z)dz - \pi/4 + k_r r. \tag{6.35}$$

Eq. 6.35 has two integrals, one of which is from $z = 0$ to $z = z_s$ while the other one is from $z = 0$ to $z = z_l$. This is similar to the ray tracing solution [26] in which two integrals both start from the ground level; one ends at the location of the source, and the other one ends at the location of the receiver. The derivative of Eq. 6.35 is as follows:

$$\begin{aligned}\frac{dg_{r1}}{d\mu_0} &= \int_0^{zl} k_0\sqrt{n^2-\sin{\mu_0}^2} + \int_0^{zl} k_0\sqrt{n^2-\sin{\mu_0}^2} + k_0 \sin\mu_0 r \\ &= k_0 \int_0^{zl} \cos\mu_0(\tan\theta_1 - \tan\mu)dz + k_0 \int_0^{zl} \cos\mu_0(\tan\theta_1 - \tan\mu)dz\end{aligned} \tag{6.36}$$

Eq.6.36 suggests that the solution based on the stationary phase method and on wave theory coincides with the ray tracing solution once again. Symbol $\theta$ is used for reflection, and symbol $\phi$ is used for the direct wave to indicate two different incident angles. Here, we substitute the stationary point (zeros of Eq. 6.36) into Eq.6.31 to obtain

$$I_{r1} = \frac{1}{4\pi} k_0 \sqrt{\frac{\sin\theta_{10}}{r}} \frac{1}{\sqrt{kz_{zs}kz_{zl}}} \frac{\cos\theta_{10} - \beta}{\cos\theta_{10} + \beta} e^{ik_0 Rr1} / \sqrt{\int_0^{zl} \frac{dz}{n\cos^3\theta_1} + \int_0^{zs} \frac{dz}{n\cos^3\theta_1}} \tag{6.37}$$

and

$$\begin{aligned}I_{r2} &= \frac{1}{4\pi} k_0 \sqrt{\frac{\sin\theta_{20}}{r}} \frac{1}{\sqrt{kz_{zs}kz_{zl}}} \frac{\cos\theta_{20} + \beta}{\cos\theta_{20} + \beta} e^{ik_0 R_{r2}} / \sqrt{\int_{zt}^{zl} \frac{dz}{n\cos^3\theta_2} + \int_{zt}^{zs} \frac{dz}{n\cos^3\theta_2}} \quad ////// \\ &= \frac{1}{4\pi} k_0 \sqrt{\frac{\sin\theta_{20}}{r}} \frac{1}{\sqrt{kz_{zs}kz_{zl}}} e^{ik_0 R_{2b}} / \sqrt{\int_{zt}^{zl} \frac{dz}{n\cos^3\theta_2} + \int_{zt}^{zs} \frac{dz}{n\cos^3\theta_2}}.\end{aligned} \tag{6.38}$$

where

$$R_{r1} = \int_0^{zl} \frac{n}{\cos\theta_1} dz + \int_0^{zs} \frac{n}{\cos\theta_1} dz \tag{6.39}$$

and

$$R_{r2} = \int_{zt}^{zl} \frac{n}{\cos\theta_2} dz + \int_{zt}^{zs} \frac{n}{\cos\theta_2} dz \tag{6.40}$$

Equation 6.27 and Equation 6.38 are exactly the same since $\theta_{20} = \phi_{20}$ and thus they cancel out each other in the total asymptotic solution. If we compare the solution with the homogeneous solution, we get the following

$$I_{r1} = \frac{1}{4\pi} k_0 \sqrt{\frac{\sin\theta_{10}}{r}} \frac{1}{\sqrt{kz_{zs}kz_{zl}}} \frac{\cos\theta_{10} - \beta}{\cos\theta_{10} + \beta} e^{ik_0 R_{r1}} / \sqrt{\int_0^{zl} \frac{dz}{n\cos^3\theta_1} + \int_0^{zs} \frac{dz}{n\cos^3\theta_1}}$$
$$\xrightarrow{a=0} \frac{1}{4\pi} k_0 \sqrt{\frac{\sin\theta}{r}} \frac{1}{k_0\cos\theta} \frac{\cos\theta - \beta}{\cos\theta + \beta} e^{ik_0 R_2} \sqrt{\frac{\cos^3\theta}{z_l + z_s}} = \frac{\cos\theta - \beta}{\cos\theta + \beta} \frac{e^{ik_0 R_r}}{4\pi R_r}. \tag{6.41}$$

Equation 6.41 shows that the asymptotic solution is reduced to the plane wave solution if a is set equal to zero. For the reflected wave, there is also a turning point, or we could call it shadow boundary

$$r_{tur} = 1/a(-\sqrt{1 - (1 + a \cdot zl)^2}) + 1/a(-\sqrt{1 - (1 + a \cdot zs)^2}) \tag{6.42}$$

If the horizontal distance is larger than $r_{tur}$, the receiver goes into the shadow zone, which means there is no direct or reflected ray that could be found for connecting the source and the receiver. The asymptotic solution does not exist in the shadow zone; however, the normal mode method [17] or the direct numerical integration could be used to solve for the sound pressure in the shadow zone. The location of the shadow boundary can be seen in Figure 6.5.

The total asymptotic solution for illuminated zone is given by the following

$$I_{total} = I_{d1} + I_{r1} = \frac{1}{4\pi} k_0 \sqrt{\frac{\sin\phi_{10}}{r}} \frac{1}{\sqrt{kz_{zs}kz_{zl}}} e^{ik_0 R_{d1}} / \sqrt{\int_{zs}^{zl} \frac{dz}{n\cos^3\phi_1}}$$
$$+ \frac{1}{4\pi} k_0 \sqrt{\frac{\sin\theta_{10}}{r}} \frac{1}{\sqrt{kz_{zs}kz_{zl}}} \frac{\cos\theta_{10} - \beta}{\cos\theta_{10} + \beta} e^{ik_0 Rr1} / \sqrt{\int_0^{zl} \frac{dz}{n\cos^3\theta_1} + \int_0^{zs} \frac{dz}{n\cos^3\theta_1}} \tag{6.43}$$

Equation 6.43 is the final asymptotic solution for plane wave, which can be used for en-route aircraft noise propagation since the surface wave term is weak for a sound source with high elevation. However, when both the sound source and the receiver are very close to the ground, the reflection coefficient of plane wave cannot be used to

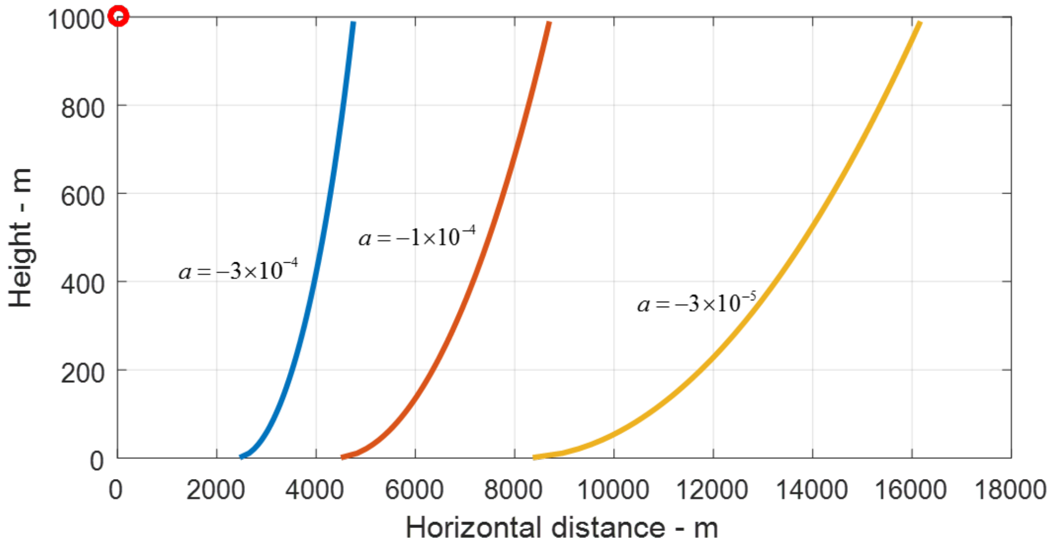


Figure 6.5. Shadow boundary for three different sound speed profiles. Sound source is located at $z_L = 1km$, $x_S = 0m$. Three sound speed gradient $-3 \times 10^{-4}$, $-1 \times 10^{-4}$ and $-3 \times 10^{-5}$ are used in the figure.

substitute the spherical wave reflection coefficient. The asymptotic solution is affected by the singularity in the term $(\cos\theta_{10} - \beta)/(\cos\theta_{10} + \beta)$. One of the methods for dealing with this problem is to substitute the plane wave reflection coefficient with the spherical reflection coefficient borrowed from the homogeneous solution. After the substitution, the reflected wave becomes

$$I_{r1} = \frac{1}{4\pi} k_0 \sqrt{\frac{\sin\theta_{10}}{r}} \frac{1}{\sqrt{kz_{zs}kz_{zl}}} Qe^{ik_0 Rr1} / \sqrt{\int_0^{zl} \frac{dz}{n\cos^3\theta_1} + \int_0^{zs} \frac{dz}{n\cos^3\theta_1}} \tag{6.44}$$

where

$$\begin{aligned} Q &= R_p + (1 - R_p)F_w \\ F_w &= 1 + i\sqrt{\pi} w e^{-w^2} erfc(-iw) \\ w &= \frac{1}{2}(1 + i)\sqrt{kR_r}(\cos\theta_{10} + \beta) \end{aligned} \tag{6.45}$$

where erfc(z) is known as the complementary error function. $R_p$ represents the plane wave reflection coefficient; and $\theta_{10}$ is the incident angle for the reflected wave on the

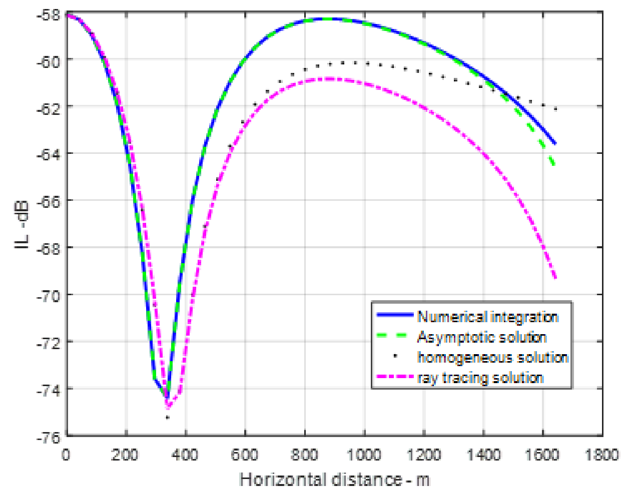


Figure 6.6. Comparison between numerical integration, asymptotic solution, homogeneous solution and ray tracing solution. Frequency= $100hz$, $z_L = 100m$; $zl = 1m$; $a = -3 \times 10^{-4}$. $IL = 20log_{10}[p_{total}/(1/4\pi)]$

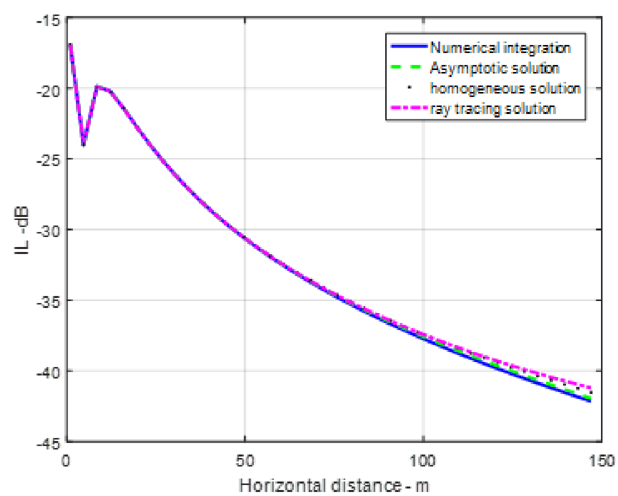


Figure 6.7. Comparison between numerical integration, asymptotic solution, homogeneous solution and ray tracing solution. Frequency= $100hz$, $z_L = 5m$; $zl = 1m$; $a = -3 \times 10^{-4}$. $IL = 20log_{10}[p_{total}/(1/4\pi)]$

ground level, which can be solved with the ray tracing method. $R_r$ represents the path distance for image wave, and $\beta = Z/\rho_0 c_0$.

Figures 6.6 and Figure 6.7 compared four different types of solutions, namely the numerical integration solution, the asymptotic solution, the homogeneous solution (Weyl-Van der Pol formula) and the ray tracing solution. Delany's single parameter model is used and the flow resistivity is euqal to 100 $kPa\,s\,m^{-2}$. [83] Figure 6.6 indicates that the agreement between the asymptotic solution and the numerical integration is very good until the horizontal range is close to the shadow boundary. The difference between the ray tracing solution and the numerical solution is obvious, and the ray tracing solution is closer to the homogeneous solution than to the correct solution with the sound speed gradient. We can conclude that the ray tracing solution tends to underestimate the influence of the temperature gradient and our asymptotic solution has a much better accuracy. In Figure 6.7, a much lower source height was used. The accuracy of the asymptotic solution is slightly better than the ray tracing solution for this geometry.

The asymptotic method introduced in this thesis has several improvements over many existing methods. The solution approximates the sound field within the illuminated zone with an analysis based on wave theory. It also has better theoretical support and it is more accurate than the ray tracing method which approximates the sound field simply with a series of functions such as $e^{ik_0R}/R$. At the same time, there are a few connections between the ray tracing solution and the asymptotic solution because the two methods give the same incident angle on the ground. The method introduced by Pierce [17] based on the residue theory could be used to calculate the sound field in the shadow zone. However, for en-route aircraft noise prediction, the sound field in the illuminated zone is more important for most audiences. The low sound pressure level in the shadow zone is usually less than background noise. For example, according to Figure 6.5, for the sound speed gradient $a = -3 \cdot 10^{-5}$ (which is a typical value during daytime), the shadow boundary is more than 10 km away from the source if the height of aircraft is 1 km above the ground. The divergence effect and the air absorption already have a 100 dB attenuation for most frequency bands at the shadow boundary.

## 6.2 Linear sound speed profile

For a linear profile, the second wave term in the direct wave does not exist since there is only one stationary point in the exponential term. To some extent the asymptotic solution is simpler than that of the bilinear profile. The derivation of the asymptotic solution is almost the same as the part for the bilinear profile and will not be repeated here. The solution for the direct wave term is simply

$$p_{dir} = p_{d1} \approx \frac{1}{4\pi} k_0 \sqrt{\frac{\sin\phi_{10}}{r}} \frac{1}{\sqrt{kz_{zs} kz_{zl}}} e^{ik_0 R_{d1}} / \sqrt{\int_{zs}^{zl} \frac{dz}{n\cos^3\phi_1}} \tag{6.46}$$

where the horizontal range $r$ is less than the turning point range.

Similar to the bilinear profile, this formula reduces to $e^{ik_0R_1}/4\pi R_1$ as the sound speed gradient goes to zero. For $r$ larger than the turning point range, the expression becomes

$$p_{dir} \approx p_{d2} = \frac{1}{4\pi} k_0 \sqrt{\frac{\sin\phi_{20}}{r}} \frac{1}{\sqrt{kz_{zs} kz_{zl}}} e^{ik_0 R_{d2}} / \sqrt{\int_{zt}^{zl} \frac{dz}{n\cos^3\phi_2} + \int_{zt}^{zl} \frac{dz}{n\cos^3\phi_2}} \tag{6.47}$$

It should be noted that the path of the first type has no stationary point after the turning point. The details of the existence of stationary point at different ranges can be found in Table 6.2.

In Figure 6.8a, for the absolute magnitude, the difference between the asymptotic solution and the exact solution is very weak (i.e., less than 0.2 dB). We can also see that the asymptotic solution is much better than the ray tracing method at far range. The ray tracing solution has a 5 dB error at a 1 km horizontal range. If the real part is used for comparison in Figure 6.8b, the advantage of the asymptotic solution is even more obvious. Starting from 150 m, the ray tracing solution cannot match the dips of the exact numerical integration solution, and no obvious error is observed for the asymptotic solution at any range.

In can be seen that, Equations 6.46 and 6.47 are valid for any types of monotonous increasing or decreasing sound speed profiles because no exclusive features of bilinear

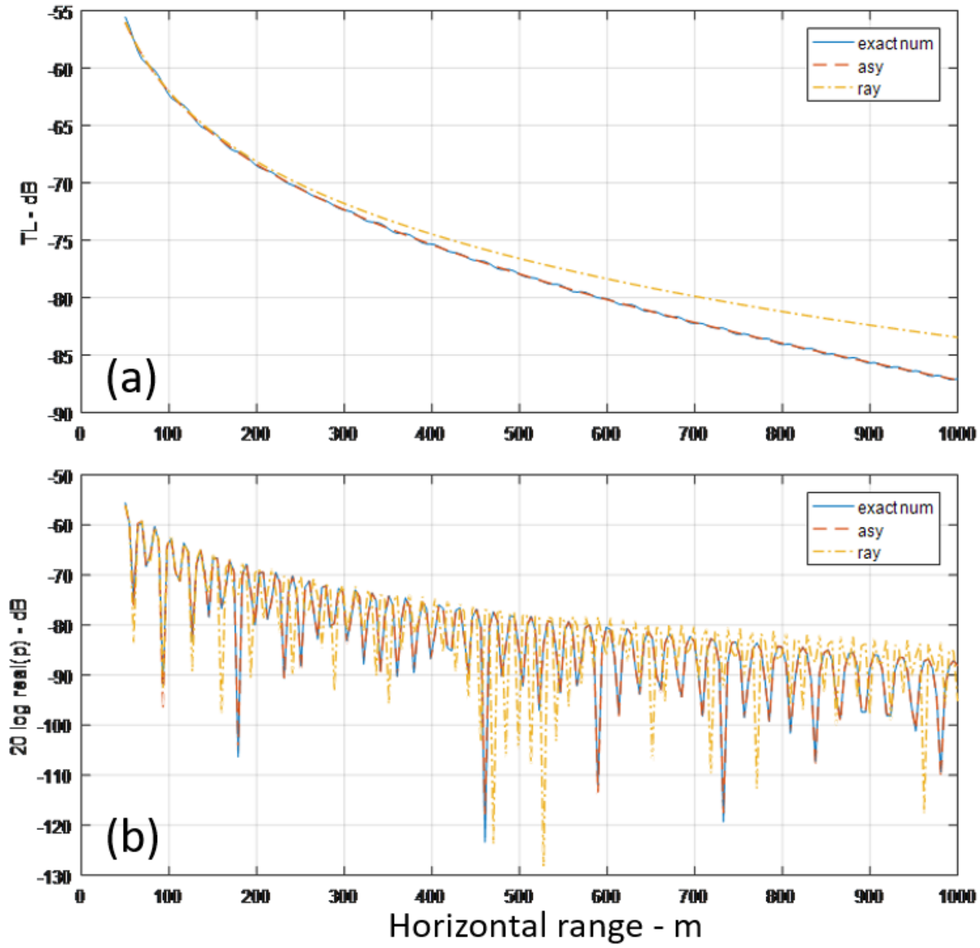


Figure 6.8. Transmission loss and the real part of sound pressure for medium with linear sound speed profile. a=0.003 $s^{-1}$, zl=10m, zs=1m, freq = 100 Hz.

or linear profiles are used in the derivation. For any sound speed profile, we only need to substitute each wave contribution that was solved using the ray tracing method with Equation 6.46 if there is no tuning point and with Equation 6.47 if there is a turning point for the ray.

Table 6.2. Saddle points in each type of path for the linear profile

| | $r < r_{tur}$ | $r \geq r_{tur}$ |
|---|---|---|
| First path type | 1 saddle point | 0 saddle point |
| Second path type | 0 saddle point | 1 saddle point |

## 6.3 Conclusion

The method of asymptotic expansion was used to derive the asymptotic solution for the sound field in a medium with a sound speed gradient. The features of the Airy function and the Stokes phenomenon were analyzed and studied. The direct wave of the asymptotic solution has a great agreement with the exact numerical integration solution; however, the accuracy of the reflected wave term is compromised by the existence of a surface wave at far range. Previously used methods to solve for reflected wave terms (i.e., pole subtraction and the modified trapezoid rule) cannot be applied here due to the different exponential terms used and the Stokes phenomenon. To obtain a fast and accurate solution for the reflected wave term, a new technique is required, which will be explained in the next chapter.

# 7. EVALUATION OF SOUND FIELD WITH TEMPERATURE GRADIENT WITH LEVIN'S COLLOCATION

## 7.1 Introduction

In the previous chapters, asymptotic methods were used for treating different types of sound propagation problems, such as a moving source problem and refraction problems. The most important advantage of the asymptotic method is its calculation speed. At the same time, asymptotic solutions solved using the stationary method can usually give physical meaning for each wave term in the solution.

However, several problems exist in the asymptotic method. First, the singularities in the integrand always influence the accuracy of the asymptotic solution. Although the problem can sometimes be solved using the pole subtraction method, the evaluation requires extensive knowledge of the pole location. Secondly, in problems such as sound field in a medium with a sound speed gradient, the asymptotic solution does not work at a far distance. For upward refracting problems, the asymptotic solution based on a stationary phase method only works in the illuminated zone; it fails as the receiver approaches the shadow boundary. In the shadow zone, there is no ordinary ray path between the source to the receiver, and the asymptotic solution based on steepest descent method does not give the correct solution. The method of normal mode could be used to calculate the sound field in the shadow zone [17,19]. However, the solution does not have the direct wave term, and this is problematic for short range prediction.

Comparing to the asymptotic solution, numerical solutions based on integrations are much slower. However, they converge to the exact solution of the problem as the number of points used in the integration increases. Additionally, these methods are still valid when the asymptotic solution fails due to singularities and branch cuts.

Several methods could be used to evaluate the integral in the wavenumber domain. A direct numerical integration is the most straightforward evaluation method and is used in many studies as the validation benchmark [48, 94]. It calculates the integral using the basic trapezoid rule or other methods such as the adaptive quadrature along the real axis of $k_r$ (or $k_x$ for line source problems) with a small indentation towards $-i$ direction to avoid possible singularities on the real axis. The method is valid universally, but it is also the most inefficient method for obtaining the solution. The number of points that are needed increases with the frequency of the sound source and horizontal distance between source and receiver. At a high frequency, a simple evaluation for the sound pressure level at one point could take more than an hour for some complicated upward/downward refracting problems.

Another method is the FFP [95], which is one of the fastest and most popular numerical integrations method for integrals with Bessel type kernels. The method takes advantage of the fast Fourier transform algorithm to perform a conversion—namely to convert an integral with respect to frequency to an integral with respect to distance. The evaluation with the FFP method requires many points, but at the same time it also provides the sound pressure level many points on a line with the same receiver height. The method is efficient if the sound pressure of many different points on the same horizontal plane are required.

The two aforementioned numerical integration techniques both have an important disadvantage. As the frequency of the sound source increases, the oscillation of the integrand becomes larger due to the $k_0 = 2\pi f/c_0$ term in the exponential oscillator, and the required integration points also increase due to the higher oscillation. The calculation for a long horizontal distance between the source and the receiver will also require much more integration points due to the $k_r{\cdot}r$ term in the exponential oscillator, where $r$ is normally defined as the horizontal distance. These phenomena suggest that the required number of points in the integration depends highly on the frequency and the distance between the source and the receiver. For some high frequency problems, the evaluation becomes extremely slow even with the FFP method.

A third method, which is called Levin's collocation method [28], could also be used in the numerical evaluation along the $k_r$ axis. The most important advantage of this method is that the number of the required integration points is independent of the frequency and distance. However, the integration algorithm with this method requires a thorough understanding of the integrand, which is discussed in this chapter with two types of examples, namely the upward and the downward refracting problems.

## 7.2 Theory of Levin's collocation

Levin's collocation method is a fast integration method for the evaluation of the integral

$$I = \int_a^b f(x)e^{iq(x)}dx \tag{7.1}$$

where $f$ is required to be a smooth function with no obvious oscillation. This requirement is not strict. A lower smoothness for function f only means more integration points. Another requirement is $|q'(x)| \geq (b-a)^{-1}$.

If $f(x)$ can be expressed using

$$f(x) = iq'(x)p(x) + p'(x) = L^{(1)}p(x) \tag{7.2}$$

the integral in Equation 7.1 can be evaluated simply with

$$\begin{aligned} I = \int_a^b(iq'(x)p(x) + p'(x))e^{iq(x)}dx = \int_a^b \frac{d}{dx}p(x)e^{iq(x)}e^{iq(x)}dx \\ = p(b)e^{iq(b)} - p(a)e^{iq(a)}. \end{aligned} \tag{7.3}$$

We could see in Equation 7.3 only the end point and the start point are required in the evaluation of the integral in Equation 7.1. To finish the evaluation, all we need is to find the function $p(x)$, which can be modeled using an n-point collocation approximation algorithm, which was first introduced by Levin [28]. Here, $p(x)$ can be defined as

$$p_n(x) = \sum_{k=1}^{n} \alpha_k u_k(x) \tag{7.4}$$

where $\{u_k\}_{k=1}^{n}$ are linearly independent basis functions such as the Chebyshev polynomial or the simple polynomial basis like $a_k x^k$. The coefficients $\{a_k\}_{k=1}^{n}$ can be calculated with a collocation method:

$$L^{(1)}p_n(x_j) = f(x_j) \qquad , j = 1, 2, ..., n, \tag{7.5}$$

where $\{x_j\}_{j=1}^{n}$ are distinct collocation points between $[a, b]$. The choices of the $n$ distinct points are arbitrary, however, some choices of collocation points could give more stable results for certain physical problems.

The coefficients can be solved with

$$\sum_{k=1}^{n} \alpha_k u_k'(x_j) + iq'(x_j) \sum_{k=1}^{n} \alpha_k u_k(x_j) = f(x_j), \qquad j = 1, 2, ..., n, \tag{7.6}$$

which is equivalent to solving a $n \times n$ linear system. Then the original integral can be solved with

$$I_n = \sum_{k=1}^{n} \alpha_k u_k(b) e^{iq(b)} - \sum_{k=1}^{n} \alpha_k u_k(a) e^{iq(a)} \tag{7.7}$$

The accuracy of the evaluation will not decrease as the oscillation increases according to the error analysis of Levin's method by Olver [96]. The advantage of Levin's collocation method is obvious considering the calculation time. However, there are a few disadvantages of using Levin's method. First, near the stationary point, the method fails, and thus other integration techniques should be used instead. This is not a big issue since near the stationary point (e.g., absolute value of the phase function less than 20), the function varies slowly and a calculation with the simplest trapezoid rule is fast enough. In the study, the adaptive Clenshaw-Curtis quadrature is used because of the accuracy and speed consideration. Second, if function $f$ in Equation 7.1 varies too fast between $[a, b]$, the accuracy of Levin's collocation will drop. We investigate how to increase the accuracy; to do this, the section needs to be divided into two or more subsections. The oscillation of Equation 6.1 is extremely difficult due to the highly oscillatory Airy functions and the term $e^{ik_r r}$. Since Levin's collocation depends on the feature of the oscillator and the function kernel, the strategies of integration are different for the direct wave term and the reflected wave term.

### 7.2.1 Direct wave term

In the equation of 6.11, the integral we need to evaluate is as follows:

$$p_{dir} = \int_{-\infty}^{\infty} \frac{1}{2} H_0(kr) l e^{i\pi/6} Ai[(\tau - \frac{z_l}{l}) e^{i2\pi/3}] Ai(\tau - \frac{z_s}{l}) k_r dk_r. \tag{7.8}$$

For a section of the integral in Eq. 7.8 from $k_r = 1$ to $k_r = 10$, the numerical integration with the trapezoid rule requires around $5 \times 10^4$ sampling points to obtain the seventh digit of $p_{dir}$ correctly; however, with Levin's collocation, only 10 equally spaced sampling points are required to achieve the same accuracy. The trapezoid rule requires 0.052849s and Levin's method only requires 0.001812s using MATLAB on a desktop with i7-4770 CPU 3.40GHz and 16GB memory. Levin's method could noticeably reduce the calculation time, however, better choices of dividing points need to be found for better results due to the stationary points and a lack of smoothness in $f$ at some locations.

The evaluation of equation 7.8 requires information of the stationary point because Levin's collocation fails near the stationary point. According to [97], the problem could be solved by adding a linear function to the exponential term so that we can change the location of the stationary point. However, the method seems to be unstable and will not be used here. Although Levin's collocation fails around the stationary point, the integration around the stationary point is very fast, even with the most basic trapezoid rule method since there is no oscillation near the stationary point. In this study, the Clenshaw Curtis quadrature method is used for the numerical integration near stationary points. As an alternative, the Gaussian quadrature could also be used here with a similar performance. The integrand of Equation 7.8 cannot be expanded with the same expressions for all kinds of $k_r$ value. The asymptotic expansion of the Airy function depends on the argument of Ai() because of the Stokes phenomenon explained in Chapter 6. For a relatively large $l$, the integral could be broken into three regions.

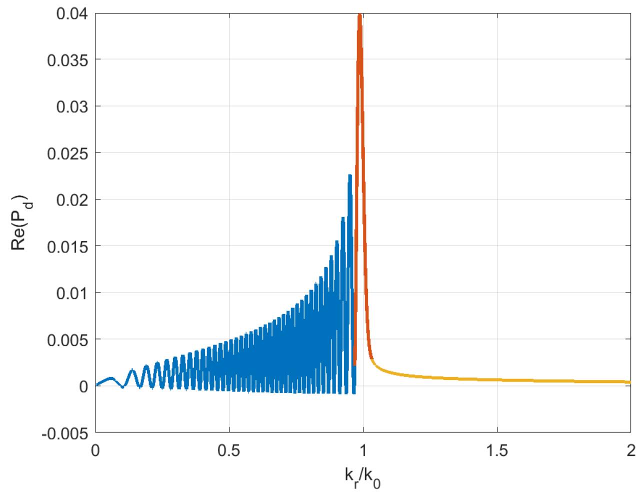


Figure 7.1. Three sections of direct wave integrand

It could be observed in Figure 7.1 that the integrand is divided into three sections: the trigonometric section, the Stokes section and the decaying section. The first section is the most complicated section because it has the most oscillations and contains one or two stationary points. The second section is evaluated using the quadrature method since the oscillation is weak in the region and the only oscillation is caused by $k_r \cdot r$ term. The third section decays fast and can be evaluated with one or two sections using Levin's method.

1. Trigonometric part.

   In this region, the argument of the Ai() function is negative and large. The integral here could be approximated with [15]

$$
\begin{aligned}
I_{sin} \approx -\frac{i}{8\pi} \int_{\epsilon}^{s(s^-,z_s)} & H_0(k_r r) l e^{i\pi/6} (\xi_<)^{-1/4} (-\xi_> e^{i2\pi/3})^{-1/4} \\
\cdot [-e^{-i(\frac{2}{3}\xi_<{}^{3/2}+\pi/4)} & + e^{i(\frac{2}{3}\xi_<{}^{3/2}+\pi/4)}] e^{-\frac{2}{3}(-\xi_> e^{i2\pi/3})^{3/2}} k_r dk_r \\
& = I_{sin1} + I_{sin2} \\
& = \int_{-\infty}^{+\infty} P_d dk_r
\end{aligned} \tag{7.9}
$$

where $s(s^-, z_s)$ is the location of the upper limit of the first section. The function $s$ is defined with

$$s(x,z) = \sqrt{(x+z/l)/l^2 + k_0^2}. \tag{7.10}$$

Here, $s^-$ suggests the value on the negative real axis of Airy function; the value used in the study is -10. It decides the splitting point between section 1 and section 2. The two components in Equation 7.10 have two different oscillators, namely

$$q_{sin1} = \int\limits_{zs}^{zl} k_z(k_r, z)dz + r \cdot k_r - \pi/4$$

and

$$q_{sin2} = \int\limits_{zt}^{zl} k_z(k_r, z)dz + \int\limits_{zt}^{zl} k_z(k_r, z)dz + r \cdot k_r + \pi/4$$

The two integral in Equation 7.10 could be expressed with

$$\begin{aligned} I_{sin1} &= \int_0^{s(s^-,zs)} f_{sin1} e^{iq_{sin1}} dk_r, \\ I_{sin2} &= \int_0^{s(s^-,zs)} f_{sin2} e^{iq_{sin2}} dk_r \end{aligned} \tag{7.11}$$

where

$$\begin{aligned} f_{sin1} &= \frac{i}{8\pi} l e^{i\pi/6} (\xi_<)^{-1/4} \left(-\xi_> e^{i2\pi/3}\right)^{-1/4} k_r, \\ f_{sin2} &= -\frac{i}{8\pi} l e^{i\pi/6} (\xi_<)^{-1/4} \left(-\xi_> e^{i2\pi/3}\right)^{-1/4} k_r \end{aligned} \tag{7.12}$$

According to the Chapter 6. the first oscillator for the bilinear profile has one stationary point when $r < r_{tur}$ and has no stationary points when $r > r_{tur}$. The second oscillator has one stationary point when $r < r_{tur}$ and two stationary points when $r > r_{tur}$. It is important that the Levin's collocation should avoid these stationary points. For the bilinear profile, the analytical solution of the phase function and the derivative of the phase function $g_{d1}$ and $g_{d2}$ are available. These can be expressed as

$$\int_{zt}^{z} k_z(k_r, z) = -\frac{2}{3}\frac{1}{2ak_0^2} k_z^3 \tag{7.13}$$

and

$$\frac{d\int_{zt}^{z} k_z(k_r, z)}{dk_r} = \frac{k_r k_z}{ak_0^2} \tag{7.14}$$

where

$$k_z(k_r, z) = \sqrt{k_0^2(1 - 2az) - k_r^2}. \tag{7.15}$$

The stationary point for $g_{d1}$ is

$$k_{stp1} = \frac{\sqrt{2}}{2}|a|k_0 r\sqrt{1/(\sqrt{4a^2 z_l z_s - 2azs - a^2r^2 - 2az_l + 1} + az_l + az_s - 1)} \tag{7.16}$$

and that of $g_{d2}$ is

$$k_{stp2} = \frac{\sqrt{2}}{2}|a|k_0 r\sqrt{1/(\sqrt{4a^2 z_l z_s - 2azs - a^2r^2 - 2az_l + 1} - az_l - az_s + 1)}. \tag{7.17}$$

The first stationary point is moving in the positive direction on the $k_r$ axis as the horizontal axis increases, and the second one is close to the origin where $k_r = 0$. The region where the absolute value of the derivative is less than 20 is treated as the region with a weak oscillation in this study. In the region, the quadrature method is used for better efficiency.

2. Stokes part.

   The Stokes phenomenon is that the asymptotic behavior of the function can be different in different regions in the complex plane; this was first discovered by G. G. Stokes. [98] For the Airy function, the asymptotic behaviors are different on the negative real axis and on the positive real axis. On the negative real axis, the Airy function oscillates in a way similar to a sine-cosine function, and on the positive real axis, Airy function oscillates like an exponential function. Near the Stokes line of Airy function, the behavior of Airy cannot be described with any simple exponential expansions; a summation of a series of exponential functions are required to describe it.

   The integral in this region can be expressed as

$$I_m = \int_{s(s^-,zs)}^{s(s^+,zl)} \frac{1}{2}H_0(kr)le^{i\pi/6}Ai[(\tau - \frac{z_l}{l})e^{i2\pi/3}]Ai(\tau - \frac{z_s}{l})k_r dk_r \tag{7.18}$$

The quadrature method is used for calculating the integral in this region. Although the quadrature method is not efficient for functions with oscillations, the region has very weak oscillations due to its small span. In addition, the percentage of the region among the whole integration span decreases with the frequency. The span of the region divided by $k_0$ is

$$[s(s^+, z_l) - s(s^-, z_s)]/k_0 = \sqrt{(s^+ + z_l/l)/(l^2k_0^2) + 1} - \sqrt{(s^- + z_s/l)/(l^2k_0^2) + 1} \tag{7.19}$$

which decrease with $k_0$. This suggests that as frequency increases, the calculation time for the region will not increase with it also.

3. Tail of the integral.

   In the region the oscillation is mainly caused by the $e^{ik_r r}$ term. The expression of the integral is

$$I_t = \int_{s(s^+,zs)}^{+\infty} \frac{l}{2} G(k_r) e^{i\pi/6} Ais[(\tau - \frac{z_l}{l})e^{i2\pi/3}] Ais(\tau - \frac{z_s}{l}) k_r e^{iq_t(k_r)} dk_r \tag{7.20}$$

where

$$q_t(k_r) = \int_{zs}^{zl} k_z(k_r, z)dz + r \cdot k_r \tag{7.21}$$

with $Ais(z)$ being a scaled Airy function

$$Ais(z) = Ai(z)e^{\frac{2}{3}z^{2/3}} \tag{7.22}$$

and with $G(k_r)$ as the scaled Hankel function

$$H_0^{(1)}(k_r r) = G(k_r)e^{ik_r r}. \tag{7.23}$$

Unlike the Hankel function, $G(k_r)$ has no oscillation on the real axis of $k_r$. By separating the exponential term from the Airy function, the error of numerical calculation becomes much smaller. The derivative of the phase function could be calculated with Eq. 7.14 easily:

$$\frac{dq_t}{dk_r} = \frac{k_r}{ak_0^2}[k_z(z_l) - k_z(z_s)]. \tag{7.24}$$

The value of $s^+$ used in this study is 2, and truncation is needed to avoid integration into infinity. The magnitude of the integrand decreases with $k_r$ and the converging speed increases with the vertical separation between $z_l$ and $z_s$. The integral from truncation point $k_t$ to infinity could be approximated with the asymptotic expansion as follows:

$$I_\infty \approx \frac{l}{2i}\frac{dk_r}{dq_r}|_{k_t} G(k_t)e^{i\pi/6}Ais[(\tau - \frac{z_l}{l})e^{i2\pi/3}]Ais(\tau - \frac{z_s}{l})k_r e^{iq_t(k_t)}dk_r \quad (7.25)$$

The truncation point could be estimated using Eq. 7.25. Summing up the integral in each section, the total direct wave can be expressed as

$$p_d = I_{sin} + I_m + I_t + I_\infty \quad (7.26)$$

### 7.2.2 Reflected wave term

A similar process could be applied to the reflected wave term. The details will not be repeated and only the necessary equations are given in this section. The reflected wave term can be expressed as

$$p_{re} = -\int_{-\infty}^{\infty} \frac{1}{2}H_0(kr)k_r l e^{i\pi/6}Ai[(\tau - z_s/l)e^{i2\pi/3}]Ai[(\tau - z_l/l)e^{i2\pi/3}]\Gamma dk_r \quad (7.27)$$

where

$$\Gamma = \frac{Ai'(\tau) - qAi(\tau)}{e^{i2\pi/3}Ai'(\tau e^{i2\pi/3}) - qAi(\tau e^{i2\pi/3})} \quad (7.28)$$

1. Trigonometric part.

   The integral can be split into two components, namely

$$I_{rsin} = I_{rsin1} + I_{rsin2} \quad (7.29)$$

   where

$$\begin{aligned} I_{rsin1} &= \int_{\epsilon}^{s(s^-,0)} f_{rsin1}e^{iq_{rsin1}}dk_r, \\ I_{rsin2} &= \int_{\epsilon}^{s(s^-,0)} f_{rsin2}e^{iq_{rsin2}}dk_r \end{aligned} \quad (7.30)$$

and

$$f_{rsin1} = \frac{1}{2} H_0^{(1)}(k_r r) k_r e^{-ik_r r} Ais[(\tau - z_l/l)e^{i2\pi/3}] Ais[(\tau - z_s/l)e^{i2\pi/3}]\Gamma_1,$$
$$f_{rsin2} = \frac{1}{2} H_0^{(1)}(k_r r) k_r e^{-ik_r r} Ais[(\tau - z_l/l)e^{i2\pi/3}] Ais[(\tau - z_s/l)e^{i2\pi/3}]\Gamma_2, \qquad (7.31)$$

where

$$q_{rsin1} = \int_{zt}^{zl} k_z(k_r, z)dz + \int_{zt}^{zs} k_z(k_r, z)dz + k_r r + \pi/4 \qquad (7.32)$$

and

$$q_{rsin2} = \int_{0}^{zl} k_z(k_r, z)dz + \int_{0}^{zs} k_z(k_r, z)dz + k_r r - \pi/4. \qquad (7.33)$$

The term $\Gamma_1$ and $\Gamma_2$ acting similar to reflection coefficients are defined as

$$\Gamma_1 = \frac{1}{2} \frac{(-1 + iq)\pi^{-1/2}(-\tau)^{1/4}}{e^{i2\pi/3} Ais'(\tau e^{i2\pi/3}) - qAis(\tau e^{i2\pi/3})} \qquad (7.34)$$

and

$$\Gamma_1 = \frac{1}{2} \frac{(-1 - iq)\pi^{-1/2}(-\tau)^{1/4}}{e^{i2\pi/3} Ais'(\tau e^{i2\pi/3}) - qAis(\tau e^{i2\pi/3})} \qquad (7.35)$$

The same process is used in a way similar to what was done for the direct wave term.

2. Stokes part

   A quadrature method is used in this region because Levin's collocation is not efficient when function $f()$ is varying at a fast rate without an exportable oscillator. Eq. 7.27 can be used in the Clenshaw-Curtis quadrature integration. The integration limit is set to be from $s(s^-, 0)$ to $s(s^+, zl)$ for a monotonic sound speed profile. The definite integral in the region is defined as

$$p_{re} = -\int_{s(s^-,0)}^{s(s^+,zl)} \frac{1}{2} H_0(kr) l e^{i\pi/6} Ai[(\tau - z_s/l)e^{i2\pi/3}] Ai[(\tau - z_l/l)e^{i2\pi/3}]\Gamma dk_r \qquad (7.36)$$

3. Tail of the integral.

   The region can be integrated with Levin' collocation using this equation

$$I_{rt} = \int_{s(s^+,zl)}^{\infty} f_{rt} e^{iq_r t} dk_r \qquad (7.37)$$

where

$$f_{rt} = -\frac{1}{2}G(k_r)k_r l e^{i\pi/6} k_r Ais[(\tau - z_s/l)e^{i2\pi/3}]Ais[(\tau - z_l/l)e^{i2\pi/3}] \\ \frac{Ais'(\tau) - qAis(\tau)}{e^{i2\pi/3}Ais'(\tau e^{i2\pi/3}) - qAis(\tau e^{i2\pi/3})} \tag{7.38}$$

where the oscillating phase function is

$$q_{rt} = \int_0^{zl} k_z(k_r, z)dz + \int_0^{zs} k_z(k_r, z)dz + k_r r \tag{7.39}$$

The part after the truncation point can be approximated as this:

$$I_{r\infty} \approx \frac{l}{2i}\frac{dk_r}{dq_r}|_{k_t} G(k_r)k_r e^{i\pi/6} Ais[(\tau - z_s/l)e^{i2\pi/3}]Ais[(\tau - z_l/l)e^{i2\pi/3}] \\ \cdot \frac{Ais'(\tau) - qAis(\tau)}{e^{i2\pi/3}Ais'(\tau e^{i2\pi/3}) - qAis(\tau e^{i2\pi/3})} e^{iq_{rt}(k_t)} \tag{7.40}$$

The total reflected wave term is as follows:

$$p_{re} = I_{rsin} + I_{rm} + I_{rt} + I_{r\infty} \tag{7.41}$$

Similar to the direct wave, term $I_{r\infty}$ can be used as an estimation of the truncation error to decide the required truncation point.

### 7.2.3 Upward Linear profile

For the linear profile, the overall process is the same. Apart from the different equations that should be used, the only difference is the stationary point. It is actually simpler because the linear sound speed profile has only one stationary point for both the direct wave and the reflected wave. Fewer integration sections are needed, which makes the algorithm simpler. However, the calculation time is longer for the linear speed profile due to the complicated $\xi$ function. The process will not be shown here because it repeats most of the work in Section 7.2.

## 7.3 Downward refracting medium

The same approach could be used for the direct wave in a downward refracting medium since it is the same as the direct term in the upward refracting medium with the only difference being an opposite sign. The sound pressure for the sound field above impedance ground in a downward refracting medium is as follows:

$$p \approx \frac{e^{i\pi/6}}{2} \int_0^\infty H_0(k_r r) k_r [\frac{\xi_< \xi_>}{k_<^2 k_>^2}]^{1/4} \\ \{Ai(-\xi_< e^{i2\pi/3}) - \Gamma Ai(-\xi_<)\} Ai(-\xi_>) dk_r \tag{7.42}$$

The reflection coefficient is slightly different from that of the upward medium, which is defined as the following:

$$\Gamma = \frac{e^{i2\pi/3} Ai'(-\xi_0 e^{i2\pi/3}) + qAi(-\xi_0 e^{i2\pi/3})}{Ai'(\xi_0) + qAi(-\xi_0)} \tag{7.43}$$

The dimensionless scale factor is defined as

$$\xi(k_r; z) = \begin{cases} [\frac{3}{2} \int_z^{z_t} \sqrt{k_0^2 n^2 - k_r^2} dz]^{2/3}, & if z_t > z, \\ -[\frac{3}{2} \int_z^{z_t} \sqrt{k_r^2 n^2 - k_0^2} dz]^{2/3}, & if z_t < z, \end{cases} \tag{7.44}$$

where the sound speed gradient can be described with

$$n = c_0/c(z) = 1/(1 + az). \tag{7.45}$$

In contrast to the upward refracting case, $a$ is a positive number for the downward refracting medium.

### 7.3.1 Reflected term

The integral expression for the reflected wave term is

$$p_{re} \approx -\frac{e^{i\pi/6}}{2} \int_\epsilon^\infty H_0(k_r r) k_r [\frac{\xi_< \xi_>}{k_<^2 k_>^2}]^{1/4} \Gamma Ai(-\xi_<) Ai(-\xi_>) dk_r \tag{7.46}$$

As usual, the integral could be spitted into three parts

1. Trigonometric part.

   The most distinct difference between the applications of Levin's collocation for upward and downward refracting media is in the trigonometric part. Unlike the upward refracting medium, the reflection coefficient cannot be easily expressed as a term comprising a smooth function and an oscillating exponential term on the real axis of $k_r$. However, with binomial series, the reflection coefficient could be expanded with a series of exponential functions; each exponential term can have connections with each acoustic ray term solved in geometric acoustics due to the same incident angle solved with both methods.

The integral in the region can be expressed as

$$I_{sin} = -\frac{e^{i\pi/6}}{2} \int_{\epsilon}^{s(s^+, z_s)} H_0(k_r r) k_r [\frac{\xi_< \xi_>}{k_<^2 k_>^2}]^{1/4} \Gamma Ai(-\xi_<) Ai(-\xi_>) dk_r. \tag{7.47}$$

According to geometric acoustics, there could be an infinite number of ray paths from the source to the receiver after $n_r$th reflections from the ground. Here, $n_r = 0$ suggests a direct wave from the source to the receiver, which disappears after the turning point. All the ray paths could be found using the basic algebra described in [86]. By defining the horizontal distance of the first strike of a ray from the source to the receiver as $x$, we can solved it using [99] as

$$\begin{gathered} n_r(n_r+1)x^4 - (2n_r+1)rx^3 + [b_2^2 + (2n_r^2 - 1)b_1^2 + r^2]x^2 \\ -(2n_r - 1)b_1^2 r x + n_r(n_r - 1)b_1^4 = 0, \end{gathered} \tag{7.48}$$

where $b_1$ and $b_2$ are functions of the source, the receiver heights and sound speed gradient. They are defined as

$$b_1^2 = z_s^2 + 2z_s/a \tag{7.49}$$

and

$$b_2^2 = z_l^2 + 2z_l/a. \tag{7.50}$$

The number of possible ray paths is decided by the number of real roots in Eq. 7.48. For each $n_r$, there are four possible ray path types, namely $C_{du}, C_{dd}, C_{uu}$ and $C_{ud}$, which are the same as those defined by Hidaka in [26]. The first subscript indicates the ray path type at the source and the second one indicates the type at the receiver; $u$ denotes the up-going ray and $d$ denotes the downgoing ray. After solving for the possible rays between source and receiver with Eq. 7.48, the stationary points could be found with equation

$$sin(\phi(n_r, r_n)) = \frac{2r_n}{\sqrt{(r_n^2 + z_s^2)(a^2r_n^2 + a^2z_s^2 + 4az_s + 4)}} \tag{7.51}$$

where $r_n$ is the id number of the ray path type that has a possible value of 1,2,3, or 4. On the $k_r$ plane, the stationary point of each possible reflected ray between the source and the receiver can be calculated with $k_{stp} = k_0 sin(\phi)$. For each $n_r$, there are also four possible types of stationary points $k_{stp}^{I,II,III,IV}$. The location of the stationary points are required for the evaluation with Levin's method since the stationary points need to be avoided in the integration.

**Reflection coefficient and Binomial theorem** The oscillating terms in the reflection coefficient and the two Airy functions cannot be separated from the integrand directly, much like in the upward refracting case. However, we can achieve it with the help of the binomial theorem. For simplicity, we can first define the plane wave reflection coefficient as follows:

$$V = \frac{k_z(k_r, 0) - k_0\beta}{k_z(k_r, 0) + k_0\beta} \tag{7.52}$$

The integral in Eq. 7.47 can be expressed as

$$\begin{aligned} I_{sin} = -\int_{\epsilon}^{s(s^+, z_s)} \frac{1}{2}\sqrt{\frac{2}{i\pi k_r r}}[\frac{\xi_< \xi_>}{k_<^2 k_>^2}]^{1/4} k_r e^{ik_r r} Ais[-\xi_>(k_r)]Ais[-\xi_<(k_r)] \\ e^{i(\int_{z_l}^{z_t} k_z dz + \int_{z_s}^{z_t} k_z dz - 2\int_0^{z_t} k_z dz)} V B_n(k_r) dk_r \end{aligned} \tag{7.53}$$

where $B_n$ is the binomial expansion of the reflection coefficient, which is defined as

$$B_{n_b} = \sum_{n_b=0}^{\infty} [-V e^{-2i\int_0^{z_t} k_z dz + i\pi/2}]^{n_b} \tag{7.54}$$

where $n_b$ is the binomial expansion order. The larger $n_b$ is, the more accurate the approximation will be. The required number of $n_b$ increases with the frequency;

an order of five is generally enough for 1000 Hz source frequency. If we simplify the equation with a first term expansion for Airy scale functions, we could get

$$\begin{aligned} I_{sin} = & \int \frac{1}{4\pi}\sqrt{\frac{ik_r}{2\pi r}}[\frac{\xi_<\xi_>}{k_<^2 k_>^2}]^{1/4} V B_n e^{ik_r r - 2i\int_0^{z_t} k_z dz} \\ & [e^{i(-\int_{z_l}^{z_t} k_z dz - \int_{z_s}^{z_t} k_z dz)} + i e^{i(-\int_{z_l}^{z_t} k_z dz + \int_{z_s}^{z_t} k_z dz)} \\ & + i e^{i(\int_{z_l}^{z_t} k_z dz - \int_{z_s}^{z_t} k_z dz)} - e^{i(\int_{z_l}^{z_t} k_z dz + \int_{z_s}^{z_t} k_z dz)}] dk_r \end{aligned} \tag{7.55}$$

$n_b$ is also directly related to $n_r$ since the connection could be observed from Eq. 7.55. The four exponential terms represent four possible stationary points in the integration. At this point, the integral $I_{sin}$ can be separated into four parts, and each part represents a possible ray path. The number $n_r = n_b$ represents the binomial expansion order, and it is also the reflection number on the ground. The four types of rays can be treated separately:

(a) Ray type 1. Downward at source and upward at receiver. In the region

$$f_{sin1} = -\frac{1}{4\pi}\sqrt{\frac{ik_r}{2\pi r}}[\frac{\xi_<\xi_>}{k_<^2 k_>^2}]^{1/4} V \cdot [V e^{-i\pi/2}]^{n_r}, \tag{7.56}$$

and the phase term is

$$q_{sin1} = \int_{z_l}^{z_t} k_z dz + \int_{z_s}^{z_t} k_z dz - 2\int_0^{z_t} k_z dz + k_r r - 2n_r \int_0^{z_t} k_z dz. \tag{7.57}$$

(b) Ray type 2. Downward at source and downward at receiver. In the region

$$f_{sin2} = -\frac{1}{4\pi}\sqrt{\frac{k_r}{2i\pi r}}[\frac{\xi_<\xi_>}{k_<^2 k_>^2}]^{1/4} V \cdot [V e^{-i\pi/2}]^{n_r}; \tag{7.58}$$

The phase term is

$$q_{sin2} = -\int_{z_l}^{z_t} k_z dz + \int_{z_s}^{z_t} k_z dz - 2\int_0^{z_t} k_z dz + k_r r - 2n_r \int_0^{z_t} k_z dz \tag{7.59}$$

(c) Ray type 3. Upward at source and upward at receiver. In the region

$$f_{sin3} = -\frac{1}{4\pi}\sqrt{\frac{k_r}{2i\pi r}}[\frac{\xi_<\xi_>}{k_<^2 k_>^2}]^{1/4} V \cdot [V e^{-i\pi/2}]^{n_r}; \tag{7.60}$$

The phase term is

$$q_{sin3} = \int_{z_l}^{z_t} k_z dz - \int_{z_s}^{z_t} k_z dz - 2\int_0^{z_t} k_z dz + k_r r - 2n_r \int_0^{z_t} k_z dz \tag{7.61}$$

(d) Ray type 4. Upward at source and downward at receiver.

$$f_{sin4} = \frac{1}{4\pi}\sqrt{\frac{ik_r}{2\pi r}}[\frac{\xi_<\xi_>}{k_<^2 k_>^2}]^{1/4}V \cdot [Ve^{-i\pi/2}]^{n_r}; \tag{7.62}$$

The phase term is

$$q_{sin4} = -\int_{z_l}^{z_t} k_z dz - \int_{z_s}^{z_t} k_z dz - 2\int_0^{z_t} k_z dz + k_r r - 2n_r \int_0^{z_t} k_z dz \tag{7.63}$$

The total integral expression for trigonometric part of the integral is

$$I_{sin} = \int f_{sin1}e^{iq_{sin1}} + f_{sin2}e^{iq_{sin2}} + f_{sin3}e^{iq_{sin3}} + f_{sin4}e^{iq_{sin4}}dk_r \tag{7.64}$$

It should be mentioned that although the lower limit and the upper limit are the same for the four types of integrals, the location of the stationery points are different, and in all the integrals the stationary point should be avoided. It is also worth mentioning that stationary point does not always exist for each wave type. At a very short range, there is usually only one possible wave. Even if some integral terms do not have any stationary points, the contribution of the integrals still exist, although they are generally smaller than the integrals with existing stationary points. There has been several studies [88, 99, 100] ] conducted that are related to an asymptotic solution based on the ray tracing method for a sound field in a downward refracting medium. However, there are still inevitable discontinuities when the number of possible rays from the source to the receiver is increased. For example, if we increase the horizontal range between the source and the receiver from 0 m to infinity, the change in sound pressure from one possible ray to three possible rays is not continuous. If the binomial expansion is used to understand the contribution of each ray, we can observe that the contribution of each ray always exists, even though some rays cannot reach the receiver geometrically. As we increase the horizontal range, the contribution of the ray—which originally has no viable path to the receiver—begins to increase until the ray becomes possible geometrically.

We return to the calculation of integral; for the linear case, an analytical solution of the integral of $k_z$ with respect to $z$ does exist as follows:

$$\int_{z}^{z_t} k_z dz = -\{k_0 ln[\frac{k_0 + \sqrt{k_0^2 - k_r^2(1+az)^2}}{k_r(1+az)}] - \sqrt{k_0^2 - k_r^2(1+az)^2}\}/a; \quad (7.65)$$

The turning point could be solved with

$$z_t = \frac{k_0}{(k_r - 1)a}; \quad (7.66)$$

The same strategy could be used in this region; The lower and upper limit can be set to $s(s^+, z_l)$ and $s(s^-, z_s)$ where $s$ is defined with this equation:

$$-\xi[s(x,z), z] = x \quad (7.67)$$

For the linear profile, the solution of the bilinear profile in Eq. 7.10 is accurate enough for the numerical purpose. For a more complicated profile, the value of $s$ could be solved using Newton-Raphson method with a few iterations. The integral could be defined with

$$I_m = -\frac{e^{i\pi/6}}{2} \int_{s(s^+,z_l)}^{s(s^-,z_s)} H_0(k_r r) k_r [\frac{\xi_< \xi_>}{k_<^2 k_>^2}]^{1/4} \Gamma Ai(-\xi_<) Ai(-\xi_>) dk_r \quad (7.68)$$

Same as the bilinear profile, the percentage of the region among the whole integration range decreases as the frequency of the sound source increases and a weak oscillation is observed. The quadrature method is used to evaluate the integral in the region.

2. Tail part

   Here, the integral used is

$$I_{rt} = \int_{s(s^+,zl)}^{\infty} f_{rt} e^{iq_r t} dk_r \quad (7.69)$$

where

$$f_{rt} = -\frac{1}{2} G(k_r) k_r [\frac{\xi_< \xi_>}{k_<^2 k_>^2}]^{1/4} e^{i\pi/6} Ai(-\xi_<) Ai(-\xi_>) \Gamma' \quad (7.70)$$

and where the scaled reflection coefficient is

$$\Gamma' = \frac{e^{i2\pi/3}Ais'(-\xi_0 e^{i2\pi/3}) + qAis(-\xi_0 e^{i2\pi/3})}{Ais'(\xi_0) + qAis(-\xi_0)} \tag{7.71}$$

with the oscillating phase function being

$$q_{rt} = \int_0^{zl} k_z(k_r, z)dz + \int_0^{zs} k_z(k_r, z)dz + k_r r \tag{7.72}$$

The part after the truncation point can be approximated as follows:

$$\begin{aligned} I_{r\infty} \approx & \frac{1}{2i}[\frac{\xi_< \xi_>}{k_<^2 k_>^2}]^{1/4} \frac{dk_r}{dq_r}|_{k_t} G(k_r) k_r e^{i\pi/6} Ais(-\xi_<) Ais(-\xi_>) \\ & \cdot \frac{e^{i2\pi/3}Ais'(-\xi_0 e^{i2\pi/3}) + qAis(-\xi_0 e^{i2\pi/3})}{Ais'(\xi_0) + qAis(-\xi_0)} e^{iq_{rt}(k_t)} \end{aligned} \tag{7.73}$$

The total reflected wave term is given as

$$p_{re} = I_{rsin} + I_{rm} + I_{rt} + I_{r\infty} \tag{7.74}$$

## 7.4 Numerical example

### 7.4.1 Upward refraction

The results is compared with the numerical integration results calculated using direct numerical integration at short range and using the FFP at far range. In Figure 7.2, we could see that the agreement is great at any frequency shown in the graphs from 10 Hz to 2000 Hz. The interference effect can be captured perfectly with Levin's collocation method. At the same time, the calculation time is around 100 times faster than the direct numerical integration at 2 kHz. The value of the ground properties and the geometric parameters used are the same as the benchmark case in [6]. It is also worth mentioning that the direct wave can be substituted using the asymptotic solution without losing any accuracy, which can easily cut the calculation time by half.

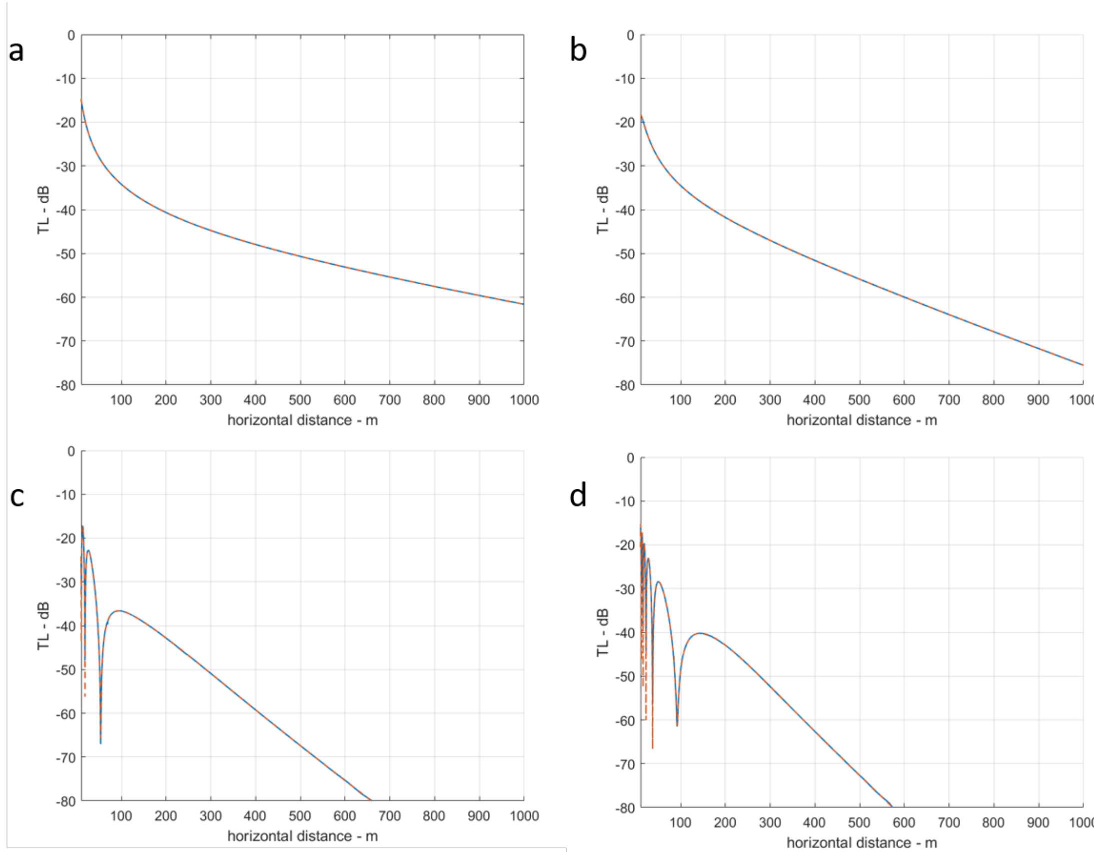


Figure 7.2. Direct numerical integration vs. Levin collocation. $a = -3 \cdot 10^{-4}$. distance = 100 m, 1000 m and 10000 m. $z_l = 5m$, $z_s = 1m.$, a, b, c, d: 10Hz, 100Hz, 1000Hz and 2000Hz.

### 7.4.2 Downward refraction

Figure 7.3 shows the contribution of each ray term from the trigonometric part. When the distance between the source and the receiver is short, the magnitude of the first tray term is significantly larger than the rest term. The magnitude of the first ray term decreases very quickly as the horizontal range increases; in addition, the contribution of the other ray terms become more significant. At 10000 m from the source, the contribution of each type of wave is significant until the eighth reflected term appears.

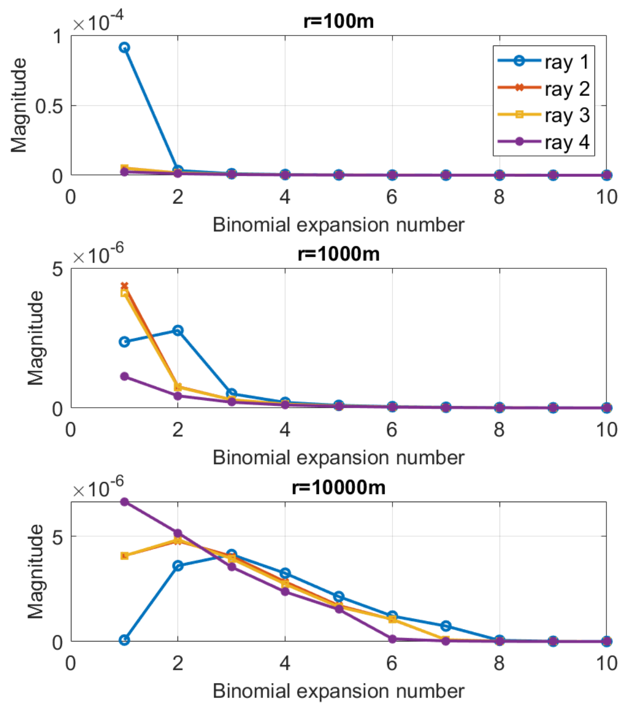


Figure 7.3. Binomial expansion number and magnitude of each term. $a = 3 \cdot 10^{-4}$. distance = 100 m, 1000 m and 10000 m. $z_l = 5m$, $z_s = 1m.$, Frequency=100Hz

Based on the information, we can conclude that as the horizontal distance between the source and the receiver increases, the contribution of each ray term increases with range. As a result, proper integration requires more binomial expansion terms.

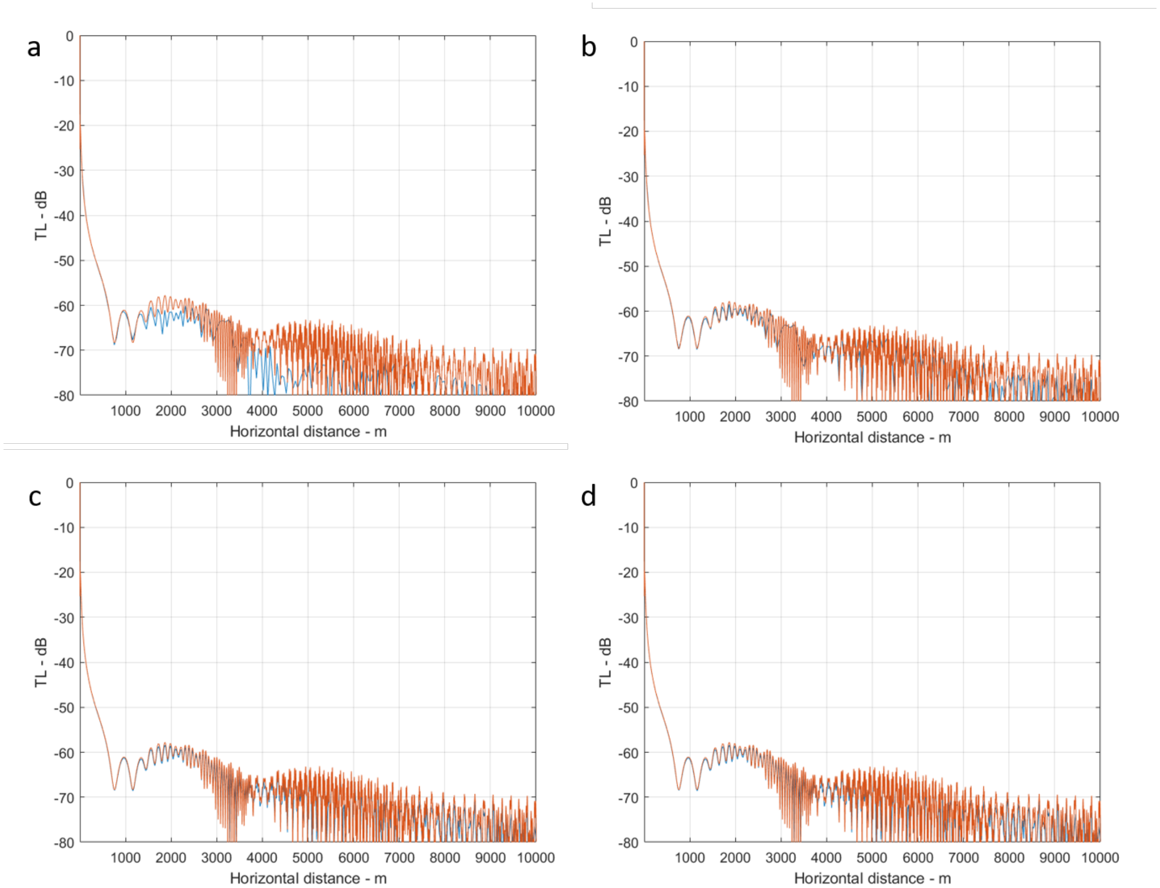


Figure 7.4. Direct numerical integration vs. Levin collocation. $a = 3 \cdot 10^{-4}$. distance = 100 m, 1000 m and 10000 m. $z_l = 5m$, $z_s = 1m.$, Frequency=100Hz. a, b, c, d: 1 term, 5 terms, 10 terms and 20 terms in binomial expansion.

Figure 7.4 shows the influence of the number of wave terms used in the binomial expansion for a 100-Hz sound source. If one term is used in the integration, the accuracy is very weak with an overestimation of transmission loss. As we increase the number of terms used in the expansion, the agreement becomes better at the same

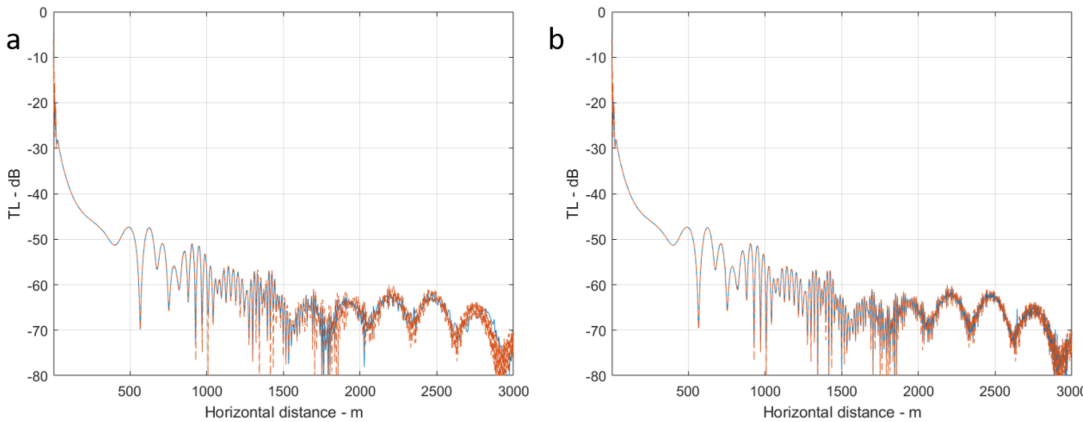


Figure 7.5. Direct numerical integration vs. Levin collocation. $a = 3 \cdot 10^{-4}$. distance = 100 m, 1000 m and 10000 m. $z_l = 5m$, $z_s = 1m.$, Frequency=1000Hz. a, b: 1 term, 5 terms in binomial expansion.

time. The disagreement increases with the distance if only one term is used; this is consistent with the conclusion in Section 7.3.

Similar results could be found for 1000 Hz in Figure 7.5. As the frequency increases, the decaying rate of the sound field with respect to the horizontal distance increases as well. The results for one term and five terms are shown in the figure. For a 1000-Hz sound source, five terms are enough since there is no observable difference between 10 terms expansion and five terms expansion in this case. The contribution of each ray term is shown in Figure 7.6 for a 1000-Hz sound source, and a similar conclusion could be made.

## 7.5 Conclusion

The method of Levin's collocation was used to calculate the sound pressure level in an upward or downward refracting medium above a locally reacting ground. The features of the integral for both cases were studied in detail. Levin's collocation is found to be significantly faster than a direct numerical integration or the FFP method,

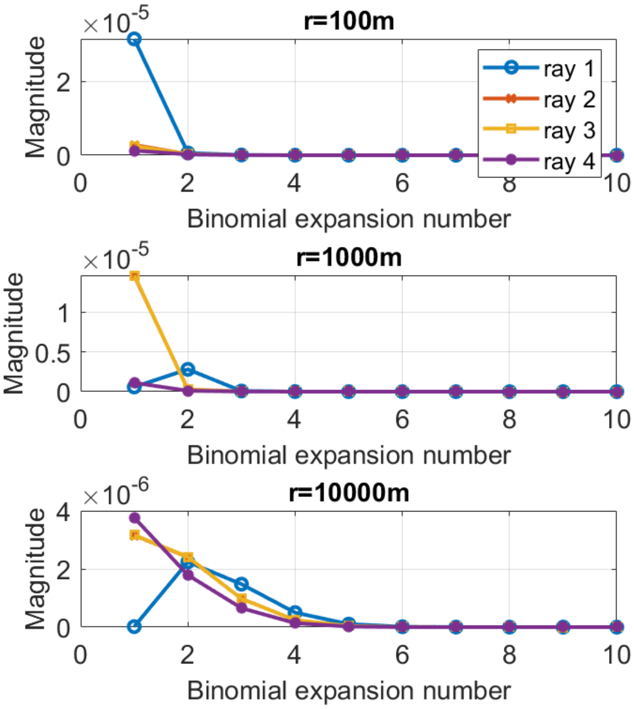


Figure 7.6. Binomial expansion number and magnitude of each term. $a = 3 \cdot 10^{-4}$. distance = 100 m, 1000 m and 10000 m. $z_l = 5m$, $z_s = 1m.$, Frequency=1000 Hz

especially for high-frequency sound and far field prediction because the calculation time of Levin's collocation is almost a constant for different source frequencies and horizontal ranges. The region near the stationary point should be integrated with other integration techniques, such as the Gaussian quadrature, since Levin's method fails near the point. Levin's method could be applied to many other problems in the outdoor sound propagation problems related to integration of oscillatory functions.

# 8. CONCLUSION AND FUTURE WORK

**Conclusion** In the thesis, we studied several common propagation effects of aircraft noise. We derived an asymptotic solution for the sound field above a non-locally reacting ground due to a moving line source using a double convolution method (see Chapter 2). This solution was extended to a point source in Chapter 3. A new method based on a variant of variable was introduced and then used to match the boundary condition, which is the first time the method has been applied in the acoustic area according to the author's knowledge. The model in Chapter 2 and 3 can be used to solve moving source problems above "soft" grounds (e.g., snow, sand, and ballast along railroad). This is the first time the asymptotic solution for the sound field above a non-locally reacting ground is given for a spherical source. In Chapter 4, the influence of the Doppler effect on the propagation of aircraft noise was studied using data provided by the Federal Aviation Administration. A suggestion to add noise-power-distance curves for different aircraft speeds was made at the end of the chapter. In Chapter 5, a modified trapezoid method was introduced for an accurate evaluation of the reflected wave term for line source and point source problems. The error bound was given with detailed analysis. The method could also be applied to moving source problems and other similar problems. In Chapter 6, an asymptotic solution for the sound field in an upward refracting medium was derived and compared using a numerical integration solution. The asymptotic solution is found to be accurate for a direct wave. For a reflected wave, the solution is accurate before the shadow boundary. To obtain a fast and accurate solution for the reflected wave term, Levin's collocation method was used, and the details of the algorithm for the evaluation of reflected wave term are discussed in Chapter 8 for the upward/downward refracting medium.

**Future work** Several possible directions can be considered. First, an accurate asymptotic solution for reflected wave term in upward/downward refracting medium is still not available. The method based on pole subtraction and steepest descent [4] fails in these problems at far range. A new or an improved asymptotic approach for an Airy type oscillator is required to solve the problems.

Secondly, Levin's collocation has great potential in many acoustic problems involving integration in the wavenumber domain. The method has several unique advantages over the asymptotic method and the FFP method. Building a Levin's collocation algorithm for different types of acoustic problems could be an interesting research topic for future studies. Optimization and machine learning techniques could be used to find the best splitting points between different Levin collocation sections.

Another direction can involve investigating the source. The study of aircraft noise propagation requires a better treatment of the sound source. The directivity and source power both influence the analysis of the propagation effects. There still lacks a reliable way to isolate propagation uncertainties from source uncertainties. An artificial sound source different from the aircraft noise could be used as the sound source for research in order to improve the accuracy of aircraft noise studies.

Lastly, the range of this study is within the scope of subsonic problems. In the near future, supersonic aircraft could become popular for public. A sound propagation model for supersonic aircraft may be an interesting research topic for future studies.

# LIST OF REFERENCES

# LIST OF REFERENCES

[1] Charlotte Clark, Rosanna Crombie, Jenny Head, Irene Van Kamp, Elise Van Kempen, and Stephen A Stansfeld. Does traffic-related air pollution explain associations of aircraft and road traffic noise exposure on children's health and cognition? a secondary analysis of the united kingdom sample from the ranch project. *American journal of epidemiology*, 176(4):327–337, 2012.

[2] Mary M Haines, Stephen A Stansfeld, RF Soames Job, Birgitta Berglund, and Jenny Head. Chronic aircraft noise exposure, stress responses, mental health and cognitive performance in school children. *Psychological medicine*, 31(2):265–277, 2001.

[3] EAM Franssen, CMAG Van Wiechen, NJD Nagelkerke, and E Lebret. Aircraft noise around a large international airport and its impact on general health and medication use. *Occupational and environmental medicine*, 61(5):405–413, 2004.

[4] K. Attenborough, K. M. Li, and K. Horochenkov. *Predicting Outdoor Sound*. Taylor & Francis, 2007.

[5] H.E. Bass, L.C. Sutherland, A.J. Zuckerwar, D.T. Blackstock, and D.M. Hester. Atmospheric absorption of sound: Further developments. *Journal of the Acoustical Society of America*, 97:680–83, 1995.

[6] K. Attenborough, S. Taherzadeh, H.E. Bass, X. Di, R. Raspet, G.R. Becker, A. Gudesen, A. Chrestman, G.A. Daigle, A. L'Esperance, Y. Gabillet, K.E. Gilbert, Y.L. Li, M.J. White, P. Naz, J.M. Noble, and H.A.J.M. van Hoof. Benchmark cases for outdoor sound propagation models. *Journal of the Acoustical Society of America*, 97(1):173–91, 1995.

[7] K. M. Li and S. Liu. Propagation of sound from a monopole source above an impedance-backed porous layer. *Journal of the Acoustical Society of America*, 131:4376–88, 2012.

[8] K. M. Li and S. Liu. Fast asymptotic solutions for sound fields above and below a rigid porous ground. *Journal of the Acoustical Society of America*, 130:1103–14, 2011.

[9] K. M. Li and H. Tao. A modified saddle point method for predicting sound fields above a non-locally reacting porous medium. *Wave Motion*, 51:229–39, 2014.

[10] M. Buret, K.M. Li, and K. Attenborough. Optimisation of ground attenuation for moving sound sources. *Journal of Applied Acoustics*, 67:135–56, 2006.

[11] Martin Ochmann. Exact solutions for sound radiation from a moving monopole above an impedance plane. *The Journal of the Acoustical Society of America*, 133(4):1911–1921, 2013.

[12] R. Cheng, P.J. Morris, and K.S. Brentner. A 3d parabolic equation method for sound propagation in moving inhomogeneous media. *Acoustical Society of America*, 126:1700–1710, 2009.

[13] B. Tong and K. M. Li. Sound field of a fast moving source in a horizontally stratified medium above and impedance plane. *Journal of the*, 129:2479, 2011.

[14] Yiming Wang, Bao Tong, and Kai Ming Li. Sound fields generated by a monopole point source moving above a locally reacting surface. In *INTER-NOISE and NOISE-CON Congress and Conference Proceedings*, volume 252, pages 683–694. Institute of Noise Control Engineering, 2016.

[15] M. Abramowitz and I. A. Stegun. *Handbook of mathematical functions with formulas, graphs and mathematical tables.* Dover Publications, New York, 1972.

[16] Allan D Pierce and Robert T Beyer. Acoustics: An introduction to its physical principles and applications. 1989 edition, 1990.

[17] R. Raspet, G.E. Baird, and W. Wu. The relationship between upward refraction above a complex impedance plane and the spherical wave evaluation for a homogeneous atmosphere. *Journal of the Acoustical Society of America*, 89:107–14, 1991.

[18] S. Taherzadeh, K.M. Li, and K. Attenborough. Some practical considerations for predicting outdoor sound propagation in the presence of wind and termperature gradients. *Journal of the Applied Acoustics*, 54(1):27–44, 1998.

[19] R. Raspet, G.E. Baird, and W. Wu. Normal mode solution for low frequency sound propagation in a downward refracting atmosphere above a complex impedance plane. *Journal of the Acoustical Society of America*, 91:1341–52, 1992.

[20] AN Sommerfeld. Propagation of waves in wireless telegraphy. *Ann. Phys.(Leipzig)*, 28:665–737, 1909.

[21] I. Rudnick. The propagation of an acoustic wave along a boundary. *Journal of the Acoustical Society of America*, 9:348–356, 1947.

[22] U. Ingard. On the reflection of a spherical sound wave from an infinite plane. *Journal of the Acoustical Society of America*, 23(3):329–35, 1951.

[23] C.F. Chien and W.W. Soroka. Sound propagation along an impedance plane. *Journal of Sound and Vibration*, 43(1):9–20, 1975.

[24] Kai Ming Li, Tim Waters-Fuller, and Keith Attenborough. Sound propagation from a point source over extended-reaction ground. *The Journal of the Acoustical Society of America*, 104(2):679–685, 1998.

[25] L. M. Brekhovskikh. *Waves in Layered Media*. Academic Press, New York, second edition, 1980.

[26] T. Hidaka, K. Kageyama, and S. Masuda. Sound propagation in the rest atmosphere with linear sound velocity profile. *Journal of the Acoustical Society of Japan*, 6(2):117–125, 1985.

[27] David Levin. Analysis of a collocation method for integrating rapidly oscillatory functions. *Journal of Computational and Applied Mathematics*, 78(1):131–138, 1997.

[28] David Levin. Procedures for computing one-and two-dimensional integrals of functions with rapid irregular oscillations. *Mathematics of Computation*, 38(158):531–538, 1982.

[29] Louis Napoleon George Filon. Iii.on a quadrature formula for trigonometric integrals. *Proceedings of the Royal Society of Edinburgh*, 49:38–47, 1930.

[30] S.J. Franke and G.W. Swenson Jr. A brief tutorial on the fast field program (FFP) as applied to sound propagation in the air. *Journal of Applied Acoustics*, 27:103–15, 1989.

[31] Daan Huybrechs and Sheehan Olver. Highly oscillatory quadrature. *Highly oscillatory problems*, (366):25–50, 2009.

[32] Didier Dragna and Philippe Blanc-Benon. Towards realistic simulations of sound radiation by moving sources in outdoor environments. *International Journal of Aeroacoustics*, 13(5-6):405–426, 2014.

[33] Timothy Van Renterghem. Efficient outdoor sound propagation modeling with the finite-difference time-domain (fdtd) method: A review. *International Journal of Aeroacoustics*, 13(5-6):385–404, 2014.

[34] Didier Dragna, Philippe Blanc-Benon, and Franck Poisson. Modeling of broadband moving sources for time-domain simulations of outdoor sound propagation. *AIAA Journal*, 52(9):1928–1939, 2014.

[35] Didier Dragna and Philippe Blanc-Benon. Sound radiation by a moving line source above an impedance plane with frequency-dependent properties. *Journal of Sound and Vibration*, 349:259–275, 2015.

[36] O Buser. A rigid frame model of porous media for the acoustic impedance of snow. *Journal of Sound and Vibration*, 111(1):71–92, 1986.

[37] Prem Datt, JC Kapil, Ashavani Kumar, and PK Srivastava. Experimental measurements of acoustical properties of snow and inverse characterization of its geometrical parameters. *Applied Acoustics*, 101:15–23, 2016.

[38] K. Attenborough. Acoustical impedance models for outdoor ground surfaces. *Journal of Sound and Vibration*, 99(4):521–44, 1985.

[39] Kurt Heutschi. Sound propagation over ballast surfaces. *Acta acustica united with acustica*, 95(6):1006–1012, 2009.

[40] S Oie and R Takeuchi. Sound radiation from a point source moving in parallel to a plane surface of porous material. *Acta Acustica united with Acustica*, 48(3):123–129, 1981.

[41] TD Norum and CH Liu. Point source moving above a finite impedance reflecting plane—experiment and theory. *The Journal of the Acoustical Society of America*, 63(4):1069–1073, 1978.

[42] P.M. Morse and K.U. Ingard. *Theoretical Acoustics*. McGraw & Hill, New York, 1968.

[43] Keith Attenborough, Sabih I Hayek, and James M Lawther. Propagation of sound above a porous half-space. *The Journal of the Acoustical Society of America*, 68(5):1493–1501, 1980.

[44] SN Chandler-Wilde and DC Hothersall. Sound propagation above an inhomogeneous impedance plane. *Journal of Sound and Vibration*, 98(4):475–491, 1985.

[45] Kai Ming Li, Shahram Taherzadeh, and Keith Attenborough. Sound propagation from a dipole source near an impedance plane. *The Journal of the Acoustical Society of America*, 101(6):3343–3352, 1997.

[46] Kai Ming Li and Shahram Taherzadeh. The sound field of an arbitrarily oriented quadrupole near ground surfaces. *The Journal of the Acoustical Society of America*, 102(4):2050–2057, 1997.

[47] KM Li and H Tao. Reflection and transmission of sound from a dipole source near a rigid porous medium. *Acta Acustica united with Acustica*, 99(5):703–715, 2013.

[48] Kai Ming Li and Hongdan Tao. Heuristic approximations for sound fields produced by spherical waves incident on locally and non-locally reacting planar surfaces. *The Journal of the Acoustical Society of America*, 135(1):58–66, 2014.

[49] H. Tao, B. N. Tong, and K. M. Li. Sound penetration into a hardbacked rigid porous layer: theory and experiments. *Journal of the Acoustical Society of America*, 136(2), 2014.

[50] Keith Attenborough, Imran Bashir, and Shahram Taherzadeh. Outdoor ground impedance models. *The Journal of the Acoustical Society of America*, 129(5):2806–2819, 2011.

[51] MC Berengier, MR Stinson, GA Daigle, and JF Hamet. Porous road pavements: Acoustical characterization and propagation effects. *The Journal of the Acoustical Society of America*, 101(1):155–162, 1997.

[52] Y Wang, KM Li, D Dragna, and P Blanc-Benon. On the sound field from a source moving above non-locally reacting grounds. *Journal of Sound and Vibration*, page 114975, 2019.

[53] Didier Dragna, Pierre Pineau, and Philippe Blanc-Benon. A generalized recursive convolution method for time-domain propagation in porous media. *The Journal of the Acoustical Society of America*, 138(2):1030–1042, 2015.

[54] K. Attenborough. Review of ground effects on outdoor sound propagation from continuous broadband sources. *Journal of Applied Acoustics*, 24:289–319, 1988.

[55] Donald G Albert. Acoustic waveform inversion with application to seasonal snow covers. *The Journal of the Acoustical Society of America*, 109(1):91–101, 2001.

[56] Laurens Boeckx, Gert Jansens, Walter Lauriks, and DG Albert. Modelling acoustic surface waves above a snow layer. *Acta Acustica United with Acustica*, 90(2):246–250, 2004.

[57] M Buret, KM Li, and K Attenborough. Optimisation of ground attenuation for moving sound sources. *Applied acoustics*, 67(2):135–156, 2006.

[58] Bao Tong and Kai Ming Li. Atmospheric effects on noise propagation from an en-route aircraft. In *INTER-NOISE and NOISE-CON Congress and Conference Proceedings*, volume 248, pages 656–663. Institute of Noise Control Engineering, 2014.

[59] D Keith Wilson. Sound field computations in a stratified, moving medium. *The Journal of the Acoustical Society of America*, 94(1):400–407, 1993.

[60] Changbiao Wang. Wave four-vector in a moving medium and the lorentz covariance of minkowski's photon and electromagnetic momentums. *ArXiv e-prints*, 2011.

[61] Aleksandar Gjurchinovski. Is the phase of plane waves a frame-independent quantity? *arXiv preprint arXiv:0801.3149*, 2008.

[62] Eric Boeker, Jordan Cumper, Amanda Rapoza, Chris Cutler, Noah Schulz, Joyce Rosenbaum, Robert Samiljan, Christopher Roof, Kevin P Shepherd, Jacob Klos, et al. Discover-aq acoustics: Measurement and data report. Technical report, John A. Volpe National Transportation Systems Center (US), 2015.

[63] Michael C Lau, Christopher J Roof, Gregg G Fleming, Amanda S Rapoza, Eric R Boeker, David A McCurdy, and Kevin P Shepherd. Behind start of take-off roll aircraft sound level directivity study-revision 1. *FAA Report*, 2015.

[64] W Krebs and G Thomann. Aircraft noise: New aspects on lateral sound attenuation. *Acta Acustica united with Acustica*, 95(6):1013–1023, 2009.

[65] Kenneth J Plotkin, Christopher M Hobbs, Kevin A Bradley, and Kevin P Shepherd. Examination of the lateral attenuation of aircraft noise. *NASA Report*, 2000.

[66] Gregg G Fleming, David A Senzig, and John-Paul B Clarke. Lateral attenuation of aircraft sound levels over an acoustically hard water surface: Logan airport study. *Noise Control Engineering Journal*, 50(1):19–29, 2002.

[67] Gregg G Fleming, David A Senzig, David A McCurdy, Christopher J Roof, and Amanda S Rapoza. Engine installation effects of four civil transport airplanes: Wallops flight facility study. *NASA Report*, 2003.

[68] David A Senzig, Gregg G Fleming, and Kevin P Shepherd. Measured engine installation effects of four civil transport airplanes. *NASA Report*, 2001.

[69] Christopher Menge, Bradley Nicholas, and Robert Miller. Attachment b: Noise analysis of taxi queuing alternatives for taxiway november at logan international airport. *HMMH Report*, (300280.003), 2006.

[70] Jonathan Koopmann, Meghan Ahearn, Eric Boeker, Andrew Hansen, Sunje Hwang, Andrew Malwitz, David Senzig, Gina Barberio Solman, Eric Dinges, Michael Yaworski, et al. Aviation environmental design tool (aedt): Technical manual, version 2a. Technical report, FAA, 2012.

[71] Bao N Tong. *Prediction and reduction of aircraft noise in outdoor environments.* PhD thesis, Purdue University, 2015.

[72] CL Morfey and GP Howell. Nonlinear propagation of aircraft noise in the atmosphere. *AIAA Journal*, 19(8):986–992, 1981.

[73] Technical report.

[74] ET Goodwin. The evaluation of integrals of the form. In *Mathematical Proceedings of the Cambridge Philosophical Society*, volume 45, pages 241–245. Cambridge University Press, 1949.

[75] C Chiarella and A Reichel. On the evaluation of integrals related to the error function. *Mathematics of Computation*, 22(101):137–143, 1968.

[76] DB Hunter and T Regan. A note on the evaluation of the complementary error function. *Mathematics of Computation*, 26(118):539–541, 1972.

[77] F Matta and A Reichel. Uniform computation of the error function and other related functions. *Mathematics of computation*, 25(114):339–344, 1971.

[78] Mohammad Alazah, Simon N Chandler-Wilde, and Scott La Porte. Computing fresnel integrals via modified trapezium rules. *Numerische Mathematik*, 128(4):635–661, 2014.

[79] SN Chandler-Wilde and DC Hothersall. Efficient calculation of the green function for acoustic propagation above a homogeneous impedance plane. *Journal of Sound and Vibration*, 180(5):705–724, 1995.

[80] Sumlearng Chunrungsikul. *Numerical quadrature methods for singular and nearly singular integrals*. PhD thesis, Brunel University, School of Information Systems, Computing and Mathematics, 2001.

[81] E Atlee Jackson. Drift instabilities in a maxwellian plasma. *The Physics of fluids*, 3(5):786–792, 1960.

[82] J Andre C Weideman. Computation of the complex error function. *SIAM Journal on Numerical Analysis*, 31(5):1497–1518, 1994.

[83] M.E. Delaney and E.N. Bazley. Acoustical properties of fibrous absorbent materials. *Journal of Applied Acoustics*, 3(2):105–16, 1970.

[84] P.H. Parkin and W.E. Scholes. The horizontal propagation of sound from a jet engine close to the ground at Radlett. *Journal of Sound and Vibration*, 1:1–13, 1965.

[85] Isadore Rudnick. Propagation of sound in the open air. *Handbook of noise control*, page 3, 1957.

[86] TFW Embleton, GJ Thiessen, and JE Piercy. Propagation in an inversion and reflections at the ground. *The Journal of the Acoustical Society of America*, 59(2):278–282, 1976.

[87] KB Rasmussen. Outdoor sound propagation under the influence of wind and temperature gradients. *Journal of sound and vibration*, 104(2):321–335, 1986.

[88] Kai Ming Li. On the validity of the heuristic ray-trace-based modification to the weyl–van der pol formula. *The Journal of the Acoustical Society of America*, 93(4):1727–1735, 1993.

[89] Alain Berry and GA Daigle. Controlled experiments of the diffraction of sound by a curved surface. *The Journal of the Acoustical Society of America*, 83(6):2047–2058, 1988.

[90] Kai Ming Li and Qiang Wang. Analytical solutions for outdoor sound propagation in the presence of wind. *The Journal of the Acoustical Society of America*, 102(4):2040–2049, 1997.

[91] Olivier Vallée and Manuel Soares. *Airy functions and applications to physics*. World Scientific Publishing Company, 2010.

[92] Michael V Berry. Stokes phenomenon; smoothing a victorian discontinuity. *Publications Mathématiques de l'Institut des Hautes Études Scientifiques*, 68(1):211–221, 1988.

[93] YL Li, CH Liu, and Steven J Franke. Three-dimensional green's function for wave propagation in a linearly inhomogeneous medium—the exact analytic solution. *The Journal of the Acoustical Society of America*, 87(6):2285–2291, 1990.

[94] K.M. Li, K. Attenborough, and T. Walter-Fullers. Sound propagation from a point source over extended reaction ground. *Journal of the Acoustical Society of America*, 104(2):1–7, 1998.

[95] H. Schmidt and J. Glattetre. A fast field model for three-dimensional wave propagation in stratified environment based on the global matrix method. *Journal of the Acoustical Society of America*, 78(6):2105–14, 1985.

[96] Sheehan Olver. *Numerical approximation of highly oscillatory integrals*. PhD thesis, University of Cambridge, 2008.

[97] Konstantin Lovetskiy, Leonid Sevastianov, and Nikolai Nikolaev. Regularized computation of oscillatory integrals with stationary points. *Procedia computer science*, 108:998–1007, 2017.

[98] George Gabriel Stokes. On the discontinuity of arbitrary constants which appear in divergent developments. *Transactions of the Cambridge Philosophical Society*, 10:105, 1864.

[99] A. L'Esperance, P. Herzog, G.A. Daigle, and J. R. Nicolas. Heuristic model for outdoor sound propagation based on an extension of the geometrical ray theory in the case of a linear sound speed profile. *Applied Acoustics*, 37:111–139, 1992.

[100] Erik M Salomons. Caustic diffraction fields in a downward refracting atmosphere. *The Journal of the Acoustical Society of America*, 104(6):3259–3272, 1998.

# APPENDICES

# A. METHOD OF SHIFTING AN AIRCRAFT SPECTRUM WITH 1/3 OCTAVE BAND

The algorithm in the evaluation of frequency shifting effect is based on 1/3 octave bands instead of narrow band due to limitation of source data. The frequency range after the shift is limited to 6.3 Hz to 20 khz and the source spectra have a range between 50 Hz to 10 kHz. The shifted frequency could reach out of the upper or lower limit of frequency. The part of energy out of the limit are ignored due to small contributions to the total A weighted noise. Sound with frequency below 6.3 Hz has less than -50 dB A weighting gain factor and can be ignored for majority of aircraft source. For sound above 20k Hz, the high attenuation makes the noise irrelevant to the total sound pressure level received on the ground. Lower limit and upper limit of each band can be calculated with

$$\begin{aligned} f_{lower}(n) &= f_{center}(n) \cdot 2^{-1/6} \\ f_{upper}(n) &= f_{center}(n) \cdot 2^{1/6} \end{aligned} \tag{A.1}$$

Bandwidth of each 1/3 octave band band can be calculated with

$$BW_n = f_{upper}(n) - f_{lower}(n) \tag{A.2}$$

The sound pressure level is assumed to be a constant in each band. The band level in each band is first transformed to sound pressure level by subtracting the bandwidth:

$$L_{SPL}(f) = L_{BSPL}(n) - 10\log_{10}(BW_n) \tag{A.3}$$

After the shifting, the sound pressure level of each 1/3 octave band are integrated with equation

$$L_{SBSPL}(n) = 10\log_{10}[\int_{f_{lower}}^{f_{upper}} 10^{L_{SPL}(f/D)/10} df] \tag{A.4}$$

For example, with a Doppler's factor of 2, the $SPL$ of 100Hz sound at the receiver should be equal to the sound pressure of 50Hz sound at the source if shifting is the only change to be considered in this calculation. For numerical calculation, 0.1 Hz step size is used in the integration over the frequency domain. Numerical integration is necessary because the Doppler's factor D is not always a multiple of 21/3, so it is possible that in the same 1/3 octave band the sound pressure level is not a constant after the shifting. $L_{SBSPL}$ is then used in Eq. A.4 as $L_{ps}$ to add up with the attenuation terms to give the sound pressure level at the receiver. Shifted frequency should be used in the calculation of each attenuation term such as air absorption and ground attenuation for aircraft noise propagation model.

The A weighted $SPL$ $L_A$ can then be calculated with $L_{pr}$ by applying A weighted factor to each band and incoherent summing up each band from 6.3 Hz to 20k Hz. Besides, the band with SPL less or equal to 0 due to the attenuation terms are assumed to have no contribution to the total $SPL$. The overall A weighting sound pressure level can be calculated with each 1/3 octave band level with equation

$$L_A = 10^{\sum_{n=1}^{n=36}[L_{receiver}(n)+A_{weight}(n)]/10} \tag{A.5}$$

And the sound exposure level can be calculated with

$$SEL = 10\log_{10}(\int_{t_0}^{t} \frac{L_A}{10} dt) \tag{A.6}$$

Sound exposure level could be defined with different rules. In the paper, only the 10dB down noise are used in the calculation of sound exposure which is the same as the one defined in SAE-AIR-1845 document. The definition may raise questions because for aircraft events with different distances to the receiver, the time spans for 10dB noise are very different. The noise level for aircraft operating at 10km above the ground varies much slower than the one at several hundred meters above the ground. As the result, the time span for high elevation flight is much longer and top 10 dB sound exposure level may not be a proper way to calculate the SEL in this case. Unless another more appropriate definition is defined, our study will stick to the 10dB down exposure level used in SEA-AIR-1845.

# B. MATCHING BOUNDARY CONDITION OF NON-LOCALLY REACTING GROUND WITH CONVOLUTION

The boundary condition for point source can also be solved with convolution method similar to the process in the 2-d case in Chapter 2. The continuities of surface pressure and normal velocity are:

$$\rho_0 \hat{\phi}_0(k_x, k_y, 0, \omega) = \rho_1(\omega)\, \hat{\phi}_1(k_x, k_y, 0, \omega) \tag{B.1}$$

and

$$\partial_z \hat{\phi}_0(k_x, k_y, 0, \omega) = \partial_z \hat{\phi}_1(k_x, k_y, 0, \omega), \tag{B.2}$$

It follows from Eqs. 3.55 and B.2 that

$$\partial_z \hat{\phi}_0(k_x, k_y, 0, \omega) = -\mathrm{i} k_z \hat{\phi}_1(k_x, k_y, 0, \omega). \tag{B.3}$$

Application of Eq. B.3 into Eq. B.1 leads to the following boundary condition:

$$c_0 \partial_z \hat{\phi}_0(k_x, k_y, 0, \omega) + \mathrm{i}\omega\beta\, \hat{\phi}_0(k_x, k_y, 0, \omega) = 0, \tag{B.4}$$

where $\beta\,[\equiv \beta(k_x, k_y, \omega)]$, which is the apparent surface admittance of the extended reaction ground, is given by

$$\beta = \zeta\sqrt{n^2 - (k_x/k_s)^2 - (k_y/k_s)^2}, \tag{B.5}$$

Defining an impulse response in space-time for the apparent surface admittance:

$$\beta(k_x, k_y, \omega) = \int_{-\infty}^{\infty}\int_{-\infty}^{\infty}\int_{-\infty}^{\infty} \hat{\beta}(x, y, t) \mathrm{e}^{\mathrm{i}(\omega t - k_x x - k_y y)} \mathrm{d}x dy \mathrm{d}t, \tag{B.6}$$

the boundary condition [Eqs. B.4 and B.5] can be converted to a convolution integral in terms of the surface potential

$$\phi_g(x, y, t) \equiv \phi_0(x, y, 0, t)$$

:

$$c_0\partial_z\phi_g(x,y,t) - \int_{-\infty}^{\infty}\int_{-\infty}^{\infty}\int_{-\infty}^{\infty} \hat{\beta}(x',y',t')\partial_t\phi_g(x-x',y-y',t-t')\mathrm{d}t'\mathrm{d}x'\mathrm{d}y' = 0. \quad \text{(B.7)}$$

The next step is to derive the corresponding boundary condition in the Lorentz space from Eq. B.7. According to Eqs. 3.45 and B.5, the differentiation with respect to t, x, y and z in the physical space can be written in the Lorentz space as

$$\partial/\partial t = \gamma^2\left(\partial/\partial t_L - c_0M\partial/\partial x_L\right), \quad \text{(B.8)}$$

$$\partial/\partial x = \gamma^2\left[\left(-M/c_0\right)\partial/\partial t_L + \partial/\partial x_L\right], \quad \text{(B.9)}$$

$$\partial/\partial y = \gamma\partial/\partial y_L \quad \text{(B.10)}$$

$$\partial/\partial z = \gamma\partial/\partial z_L. \quad \text{(B.11)}$$

And it is convenient to define a Doppler factor for the x directional wave number according to Eq. 3.57:

$$\Gamma_x\left(L_x,\omega_L\right) = M + L_x/k_L. \quad \text{(B.12)}$$

which is different from Eq. 2.15 in Chapter 2 by only a factor of $\gamma^2$. Another difference from 2-d case is that there is also a Dopplerized component in the $k_y$ direction. We can name it as

$$\Gamma_y = L_y/\gamma k_s \quad \text{(B.13)}$$

And the temporal component is defined as:

$$\Omega_L\left(L_x,\omega_L\right) = 1 + ML_x/k_L \quad \text{(B.14)}$$

It is important to note that Eq. B.14 is same as Eq. 3.61. Also, Eqs. B.12 and B.13 are same as Eq. 3.61. They are defined here again for convenience since they are crucial to the following derivations.

In the Lorentz space, the two surface potentials in Eq. B.7 can be expressed as

$$\phi_L = \frac{1}{(2\pi)^3}\int_{-\infty}^{\infty}\int_{-\infty}^{\infty}\int_{-\infty}^{\infty}\hat{\phi}_L e^{i(L_x x_L + L_y y_L - \omega_L t_L)}dL_x dL_y d\omega_L \quad \text{(B.15)}$$

and

$$\phi_g(x-x',y-y',t-t')$$
$$=\frac{1}{(2\pi)^3}\int\limits_{-\infty}^{\infty}\int\limits_{-\infty}^{\infty}\int\limits_{-\infty}^{\infty}\hat{\phi}_L(L_x,L_y,0,\omega_L)\mathrm{e}^{\mathrm{i}(L_xx_L+L_yy_L-\omega_Lt_L)-\mathrm{i}\gamma^2(\Gamma_xk_sx'+\Gamma_yk_sy'-\Omega\omega_Lt')}\mathrm{d}L_x\mathrm{dL}_y\mathrm{d}\omega_L \quad . \tag{B.16}$$

where Eq. B.16 is obtained by using the Lorentz transform [Eq. 3.45] with the temporal and spatial Doppler terms defined in Eqs. B.12 to B.14. Substitute Eqs. B.8 to B.16 into Eq. B.7, apply the convolution identity of Eq. B.6, and manipulating the resulting expression, the boundary condition for an extended reaction ground in the Lorentz frame is then given by

$$\partial\hat{\phi}_L(L_x,L_y,0,\omega_L)\Big/\partial z_L+\mathrm{i}k_0\left(\gamma\Omega_L\right)\beta(\gamma^2\Gamma_{Lx}k_s,\gamma^2\Gamma_{Ly}k_s,\gamma^2\Omega\omega_L)\hat{\phi}_L(L_x,L_y,0,\omega_L)=0, \tag{B.17}$$

where

$$\beta(\gamma^2\Gamma_{Lx}k_s,\gamma^2\Gamma_{Ly}k_s,\gamma^2\Omega_L\omega_L)=\zeta\sqrt{n^2-\left(\Gamma_{Lx}/\Omega_L\right)^2-\left(\Gamma_{Ly}/\Omega_L\right)^2}, \tag{B.18}$$

For semi-infinite ground type. Eq. B.17 is same as Eq. 2.36. The density ratio and speed ratio are functions of Dopplerized frequency:

$$\zeta\equiv\zeta\left(\gamma^2\Omega_L\omega_s\right)\text{ and }n_L\equiv n\left(\gamma^2\Omega_L\omega_s\right). \tag{B.19}$$

To couple with Eq. B.17, Eq. 3.60 needs to be converted to Lorentz frame with Eq. 3.57 as:

$$\phi_0=\frac{\rho_0\gamma^2e^{-i\omega_st_L}\omega_s}{8\pi^2}\int\limits_{-\infty}^{\infty}\int\limits_{-\infty}^{\infty}\frac{\gamma^2\Omega_L}{L_z}[e^{iL_z\Delta z_{L-}}+V_+e^{iL_z\Delta z_{L+}}]e^{iL_xx_L+iL_yy_L}dL_xdL_y \tag{B.20}$$

Combining Eq. B.17 and Eq. B.20, we can get the diffraction term $I_b$ in the Lorentz frame:

$$\frac{I_b}{\rho_0c_0}=\frac{-\gamma^2k_se^{-i\omega_st_L}}{4\pi^2}\int\limits_{-\infty}^{\infty}\int\limits_{-\infty}^{\infty}\frac{\gamma^3k_s\Omega_L^2\beta(\gamma^2\omega_s\Omega_L,\gamma^2k_s\Gamma_r)e^{i(L_xx_L+L_yy_L+\gamma L_z\Delta z_+)}}{L_z\left[L_z+\gamma k_s\Omega_L\beta(\gamma^2k_s\Omega_L,\gamma^2k_s\Gamma_r)\right]}dL_xdL_y, \tag{B.21}$$

which is same as Eq. 3.77.

VITA

# VITA

Yiming Wang was born in Lanzhou, Gansu, China. He studied automotive engineering in Tongji University in Shanghai and graduated in 2012. After obtaining his bachelor's degree he came to United States and attended Purdue University in West Lafayette, Indiana. He received his Master's degree in acoustics in 2015 and continued to pursue his PhD's degree in acoustics in Ray W. Herrick Laboratories at Purdue University.